PhD Thesis

The Surface Chemistry of Metal Fluoride Nanocrystals

Jordi Martínez Esaín

Supervised by:

Dr. Ramón Yáñez

Dr. Susagna Ricart

Dr. Jordi Faraudo

PhD program in Chemistry

Chemistry department – Science faculty

2018

Report submitted for the achievement of the Doctor degree in Chemistry by:

Jordi Martínez Esaín

Checked and accepted:

Dr. Ramón Yáñez   Dr. Susagna Ricart   Dr. Jordi Faraudo

Bellaterrra, September 2018

"The important thing is not to stop questioning. Curiosity has its own reason for existence."

Albert Einstein

Acknowledgements

Considering the personal character of this part, I would express myself in my tongue language, trying to use the desired words in each moment. Thus, this part is written, almost totally, in Spanish.

Curiosamente, cada vez que he leído los agradecimientos de una tesis doctoral siempre se comenta que ésta es la última página escrita o la dificultad que presenta escribirla. Ahora, a una semana de depositar la tesis veo que todos tenían razón.

En primer lugar, me gustaría agradecer a mis directores de tesis: Dr. Ramón Yáñez, Dra. Susagna Ricart y Dr. Jordi Faraudo por dirigirme en este camino. Tener tres directores puede parecer complicado (imaginad tener tres puntos de vista a parte del tuyo propio), pero creo que cada uno ha sido un punto clave para mi desarrollo y el diseño de esta tesis. Ramón ha conseguido hacer volar más mi mente, planteándome todas las opciones a mi alcance y abriendo (casi cada día) un camino diferente a investigar. Susagna ha sabido en cada momento frenar las ideas locas para no dispersarme, aunque también me ha dado alas para volar en diferentes direcciones. Jordi me ha dejado ver el mundo atómico desde un punto de vista que ha enriquecido exponencialmente esta tesis y mi formación. También recordar al Prof. Josep Ros, Prof. Teresa Puig y Prof. Xavier Obradors, que aun no siendo mis directores han seguido este trabajo y se han involucrado en discusiones científicas que me han hecho cuestionar cada paso dado, llegando finalmente a una mejor comprensión de todo el trabajo realizado.

La realización de una tesis no sería posible sin la ayuda del personal administrativo y técnico, por ello quiero agradecer al personal del Departamento de Química toda la ayuda con el papeleo de estos años y por encontrarme siempre una sonrisa cuando entraba de la forma más caótica. También quiero agradecer a los servicios técnicos, tanto de UAB como de ICMAB, por toda la ayuda y su tiempo analizando muestras.

Pasando a la parte más personal de los agradecimientos, recordar a todas aquellas personas que desde un ámbito personal/profesional han sido clave para el desarrollo de esta tesis. Especialmente, me gustaría recordar al Dr. Eduardo Solano ya que podríamos decir que fue él quien me enseño a trabajar en un laboratorio de investigación. Cuando pasas tanto tiempo en el mismo grupo ("veranito", máster y tesis), ves llegar e irse a mucha gente, y como es normal en la vida algunos dejan huella y otros solo son parte del camino.

Pensando en estos agradecimientos, me doy cuenta de que toca acabar esta etapa y cambiar el rumbo en el momento en que me siento más a gusto. Aunque en el fondo sea un trabajo o una etapa formativa, se crean vínculos personales que repercuten directamente en tu día a día, haciendo que tu entorno sea un punto crucial en tu investigación. Llegados a este punto se te presenta el dilema de tener ganas de avanzar y cambiar de aires e incluso de temática de investigación para abarcar más pero, por la gente y el entorno de trabajo, me gustaría quedarme un tiempo más aquí, creyendo firmemente que sería otra grandísima etapa tanto profesional como personal. ¿Quiere decir eso que solo pienso en trabajo? Diría que no, creo que como en todo hay una parte de ti mismo que se queda dónde has estado a gusto.

Algunos podrán pensar que nunca desconectamos de nuestro trabajo, que en muchas ocasiones sacrificamos lo personal por lo profesional, aunque desde dentro todo tiene matices. Cuando nos ponemos a corregir TFGs/TFMs de estudiantes de otros grupos, no es solo profesional, lo hacemos por la persona que hay detrás y el vínculo que se ha formado en poco tiempo. Cuando sacrificamos parte de nuestro tiempo en una investigación ajena, lo hacemos para dar a la persona otra perspectiva. Cuando nos ofrecemos a leer el manuscrito de una tesis para ver si hay fallos, lo hacemos por quién hay detrás. Cuando nos llevamos un capitulo de una tesis a Budapest para mirarlo, no lo hacemos para tener lectura en el avión, lo hacemos por la persona. Cuando pedimos perdón por no haber podido ayudar durante una temporada porqué estábamos inmersos en otras cosas, lo decimos de corazón por haber "fallado" a la otra persona. Nos gusta hablar de ciencia, discutir, dar puntos de vista, aprender a cada paso, pero todo adquiere un carácter personal en el fondo. No creo que necesite enumerar vuestros nombres uno a uno, ya sabéis perfectamente que estáis incluidos aquí. Solo puedo deciros una cosa: Gracias, gracias por ser grandes científicos y mejores personas, creedme que sin vosotros este trabajo no hubiera acabado de la misma forma.

También quiero recordar a los estudiantes que he tenido durante este tiempo (tanto TFGs y TFMs como los alumnos a los que he impartido alguna clase). Cuando nos ponemos delante de una clase para dar una explicación o enseñamos un protocolo a seguir en el laboratorio, nos parece que somos nosotros los que estamos enseñando. Durante este tiempo me he dado cuenta

de que ambas partes aprenden en el camino, ellos de nuestras explicaciones o consejos y nosotros de sus preguntas e inquietudes científicas. Espero haber enseñado tanto como lo que he aprendido durante este camino.

Now, I would like to thank Prof. Isabel Van Driessche and SCRiPS group to give me the opportunity to stay in her research group at Ghent University for 3 months. To Dr. Katrien De Keukeleere and Dr. Jonathan De Roo for the scientific discussions that make Chapter 5 of this thesis one of the pillars of my research, being applicable in several fields. Specially, I would like to thank Dr. Katrien De Keukeleere for her support and for all these hours of discussion. She brought about that my chaotic mind become ordered after her contribution to my experimental results, for all, Thank you!

Como olvidarme de ti, poco a poco te has hecho indispensable en el desarrollo de este trabajo y en mi día a día. Ya ves que te debo mucho más que la portada de esta tesis. Como ya sabes que opino solo te diré algo que te recuerdo a menudo, "De mayor quiero ser como tú".

Finalmente, agradecer a mi gente fuera del ámbito científico, ya sabéis que me cuesta bastante desconectar de ciencia, pero con vosotros ha sido posible. Hemos brindado por los éxitos y por los fracasos tratando de acabar siempre riendo y pensando que mañana será otro día. Como no, a mi familia, por estar siempre ahí, por confiar en mi y por todo lo que me han dado durante todo este camino, este trabajo también os pertenece.

Motivation

"I am among those who think that science has great beauty. A scientist in his laboratory is not only a technician: he is also a child placed before natural phenomena which impress him like a fairy tale."

Marie Curie, 'The Future of Culture' (1933)

Currently, researchers from different areas (chemists, physicists, engineers, biologists, …) work together to enhance our facilities and living standards. Among the different topics, nanoscience englobes several disciplines that are prone to be merged, developing new devices or reaching new frontiers to make science for society. From "There's plenty room at the bottom" of Richard Phillips Feynman (1959) to our days, nanoscience has emerged to be studied in detail covering all the scientific fields. The main goal is the applicability of nanoscaled devices in a deep range of areas, because of their promising properties compared with their bulk analogues.

This work started with the aim of obtaining metal fluoride nanocrystals, to expand the previous knowledge of our research group after the synthesis of metal and metal oxide nanocrystals. Our first goal was: are we able to obtain YF_3 nanocrystals with a small size to be applied in antibacterial fields? After some years, YF_3 nanocrystals have been obtained successfully but any evidence of antibacterial effect was found. However, each wrong step or different result as expected, were converted in a new question to give answer. All these new questions make that our first goal became in new topics to be explored and investigated, giving a new point of view and hence, producing a different, but not worse, research line as is presented in this thesis.

Contents

5.   Selective ligand exchanges in LaF₃ nanocrystals 119

Abbreviations

ABF	Adaptive biasing force
Ac	Acetate anion
AFM	Atomic force microscopy
Amm	Ammonium cation
ATR	Attenuated total reflection
CBC	Covalent bond classification
CHARMM	Chemistry at Harvard macromolecular mechanics
Cin	3,4-Dihydroxyhydrocinnamic acid
Cit	Citrate anion
DFT	Density functional theory
DLS	Dynamic light scattering
DMF	N,N-Dimethylformamide
DNA	Deoxyribonucleic acid
Dop	Dopamine
DOSY	Diffusion-ordered spectroscopy
EDTA	Ethylenediaminetetraacetic acid

EGA	Evolved gas analysis
ESI	Electrospray ionisation
FTIR	Fourier-transform infrared spectroscopy
HRTEM	High-resolution transmission electron microscopy
IR	Infrared
LAO	$LaAlO_3$
Lys	L-Lysine
MAS NMR	Magic angle spinning nuclear magnetic resonance
MD	Molecular dynamics
MRI	Magnetic resonance imaging
MS	Mass spectrometry
MW	Microwave
NAMD	Nanoscale molecular dynamics
NC	Nanocrystal
NMR	Nuclear magnetic resonance
NOE	Nuclear Overhauser effect
NOESY	Nuclear Overhauser effect spectroscopy
NPT	Isothermal-isobaric conditions
PET	Positron emission tomography
PME	Particle-mesh Ewald
PMF	Potential of mean force
QM	Quantum mechanics
SAED	Selected-area electron diffraction
SI	Supporting information

TEM	Transmission electron microscopy
TGA	Thermogravimetric analysis
Tma	Tetramethylammonium cation
UV-Vis	Ultraviolet-Visible
VMD	Visual molecular dynamics
XPS	X-ray photoelectron spectroscopy
XRD	X-ray diffraction
YBCO	$YBa_2Cu_3O_{7-\delta}$

Abstract

Starting from the synthesis of fifteen different types of inorganic nanocrystals, the general trends of metal fluoride nanocrystals have been successfully unravelled. Using the co-precipitation method, we reported the easy, fast and reproducible synthesis of LnF_3 nanocrystals and the detailed mechanistic studies of different synthetic conditions.

Through the complete study of the surface chemistry, a new kind of ionic self-assembly in colloidal systems has been proposed. Using experimental techniques and molecular dynamics simulations, we postulated this self-assembly mechanism not only specific for the studied case but also applicable to other kind of systems. In addition, thermodynamically stable patchy nanocrystals have been also obtained using an easy, fast and reproducible method. The behaviour of these patchy nanocrystals has been investigated in detail using this dual approximation, from experimental techniques to all-atomistic molecular dynamics simulations. Our results revealed the spontaneous and selective attachment of cations and anions in their different exposed faces, as well as, selective solvent interactions.

 Going one step further in patchy nanocrystals, we demonstrated that the different facets of the obtained nanocrystals can be modified selectively. Cations and anions can be removed from nanocrystal surface via the addition of a new molecule containing an amino group or a carboxylate respectively. Likewise, using a zwitterionic molecule, the homogenisation of the surface was possible releasing at same time cations and anions. Additionally, some growing process were carried out to enhance the obtained particles, allowing bigger hexagonal-faceted nanocrystals while trying to modify the organic stabilisers.

In addition, EGA-MS technique has been tested to simplify the complex pathway to full-characterise colloidal systems. We demonstrated that using a

simple experimental technique, the full characterisation of a colloidal system is possible, comparing the results with our previous characterisations.

This thesis is mainly based on the mechanistic understanding of the synthesis and the final behaviour of the surface of LnF_3 nanocrystals. In consequence, this knowledge will allow the control and manipulation of the bridge between synthesis and applications, currently called surface chemistry. Finally, some initial applications will be presented as different pathways emerged from the manipulation of the unravelled systems, being promising candidates for material science and medical fields.

1
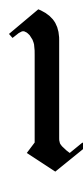
Introduction
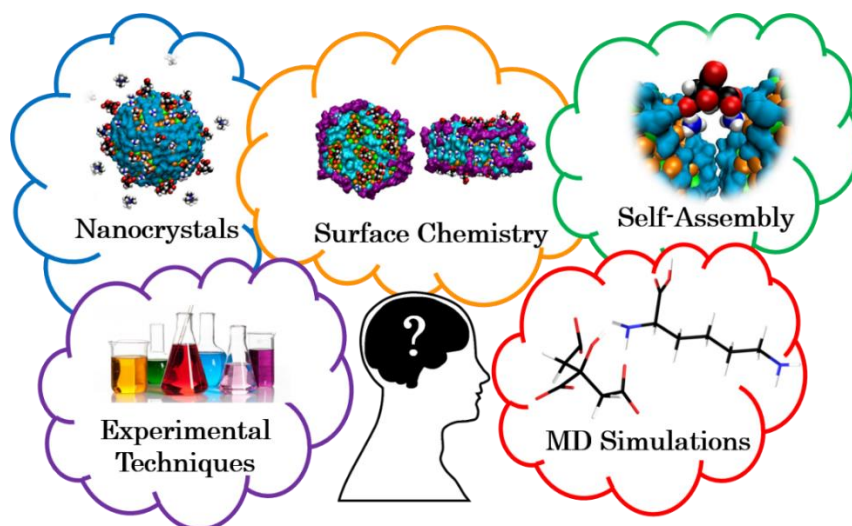
The objective of the first chapter is to situate the reader in the importance of nanoscience, nanochemistry, surface chemistry and the necessity of an accurate investigation in the general interface mechanisms related to colloids. From a chemical point of view, the knowledge obtained through a deep investigation of the main mechanism involved in controlling and tuning the colloidal surface is a challenge to open the window to design accurately our own system. Currently, the importance of metal fluoride nanocrystals has increased exponentially because they are prone to be applied in several material/medical fields. In this thesis, a dual approximation has been applied to full-characterise in all-atomic detail the mechanism involved in the colloid interface. Aimed by experimental techniques and molecular dynamics simulations, we were able to: unravel new ionic self-assembled colloidal systems, uncover the general behaviour of fifteen lanthanide fluoride nanocrystals, prepare thermodynamically-stable patchy nanocrystals, perform selective ligand exchange in aqueous and non-aqueous systems, the use of a thermogravimetric technique to unravel the detailed surface chemistry and start to apply these nanocrystals in different fields.

1.1 Current context

Have you ever thought about the possibility to develop a system able to be used to enhance human facilities or their living standards? Could be possible to create a system to be functionalised depending on the final application? Nowadays, these questions are in the scientist's mind when they want to start a new project. But, what are the most promising fields of science to focus our efforts?

Among the different current trending topics, nanoscaled systems applied in material science, chemistry and medical purposes are those with a major relevance (Figure 1.1).[1] As example, the achievement of ceramic nanocomposites with nanocrystals (NCs) in their matrix is currently under deep interest to enhance the properties of ceramic materials (e.g. superconducting $YBa_2Cu_3O_{7-\delta}$ layers).[2,3] Focusing on medical applications, LnF_3 and $MLnF_4$ (where M is a metallic monovalent cation) doped with different lanthanide cations are rising importance in bioimaging, optical and medical applications.[4]
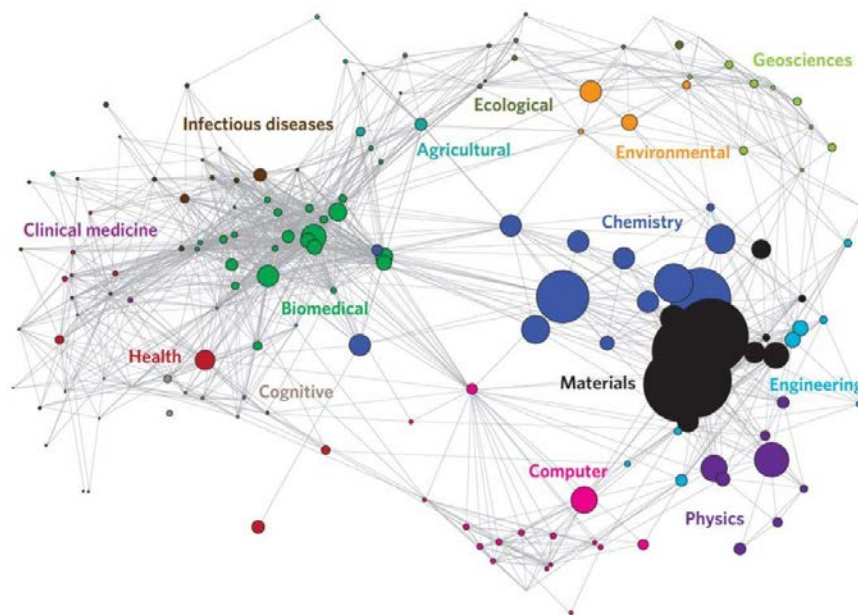
Figure 1.1. Representation of the different areas in which NCs are applied. The size of each node is proportional to the number of papers published in journals in each subject category during the period January–July 2008.[1]

NCs are highlighted to be used in several applications because of their enhanced properties compared with their bulk analogous. Currently, nanoscience is more focused on the study of the complete surface chemistry to control and predict efficiently the insights of these promising systems.[5–7] However, nanoscaled systems present some drawbacks, especially when trying to use the obtained NCs with a determinate methodology in a broad

range of fields. During several years, the efforts in nanoscaled systems were focused to obtain high crystalline NCs via high-temperature synthetic methodologies. When a specific methodology is used to obtain nanoscaled systems, the procedure and reactants define the final properties and the behaviour of the surface chemistry.[8] In addition, the nature of the capping agent determines the final stability of these systems in specific solvents or environments.[9] Ligand exchange methodologies have been applied in several systems, emerging as a suitable pathway to obtain the desired ligands onto the surface, where surface chemistry techniques are used to unveil the commonly complex and unknown NC interface.[10–13]

In consequence, this thesis is centred on a deep investigation of the surface chemistry of metal fluoride NCs to understand and control their behaviour. This knowledge allows the implementation of these NCs in several scientific areas through the controlled surface functionalisation.

1.2   State of the art

1.2.1 General trends in NCs

Nanoscaled systems present promising properties compared to their bulk analogues. When the size of a material decreases from micro to nanoscale, the electrons confined in this material are quantified because the size of the particle is too small to be compared with the wavelength of the electron, affecting to its final electronic configuration. At this scale, the electrons show an organisation from continuous band configuration to discrete energy levels, as in the case of small molecules.[14] The quantification confinement effect becomes important in quantum dots[15] and in any nanoscaled systems able to tune their emission by size modifications.[16] In the specific case of metal fluoride NCs, the confinement of the energetic levels in our systems becomes a key factor in the selection of metal cation for doping final host-NCs. The interactions between the energetic levels of the different metal cations in the quantified levels of NCs, gives the broad range of applications of these up/down-conversion systems.[17]

Other important property that share all NCs is their high surface-to-volume ratio.[18] If decreasing the size of a cubic box, for instance break apart this box in smaller ones, new cubes are obtained with more surface area compared with the new volume of the smaller cubes. From the same initial volume, the exposed surface has been increased exponentially. If we consider that these surfaces are formed by atoms with deficiencies in coordination, external atoms will be more reactive compared with the internal ones. This property shed light to use these systems in fields where the exposed surface

is the key factor as in catalysis,[19] solar cells,[20] biosensors,[21] adsorption of pollutants[22] and batteries.[23] Although the surface-to-volume ratio is one of the key properties of nanoscaled systems, also is their major drawback. The direct consequence of a high-reactive surface is that NCs tend to aggregate to reduce their intrinsic energy (thermodynamic process).[24] However, if the NC synthesis has been carried out with a stabiliser able to bind onto NC surface (kinetic stabilisation process), they will remain stable in the colloidal solution without evidence of aggregation.[25]

In consequence, the use of inorganic NCs has raised in the development of nanoscaled devices to enhance our living standards. They allow the use of an inorganic core (e.g. metal, metal oxide, metal fluoride, …) combined with a stabiliser (organic and/or inorganic ligands).[26] The combination of both open an exceptional way to use these NCs in a broad range of application using the stabiliser as biosensor, the photoluminescent core as labelling agent or the combined effect of both in cancer therapy.[4,27,28]

1.2.2   Lanthanide (III) fluoride NCs

Among the different kind of NCs, metal fluorides have been deeply investigated during the last decades due to their applicability in several areas of science.[29] $LnF_3/MLnF_4$ nanoscaled systems are currently under a deep study because they are prone to be applied in medical fields.[4,30–32] There are several highlighted applications such as, Photodynamic Therapy,[33,34] Positron Emission Tomography (PET) imaging using ^{18}F as radionuclei,[35] contrast agents by their up/down-conversion fluorescence properties[4,36] and Magnetic Resonance Imaging (MRI).[37] Their low solubility in water and their biocompatible functionalisation of the surface make them suitable for fighting cancer.[38,39]

In materials science, LnF_3 NCs can be used in the synthesis of superconducting $YBa_2Cu_3O_{7-\delta}$ (YBCO) layers. It is well known that ceramic nanocomposites as YBCO can incorporate NCs in their matrix to enhance their physical properties (e.g. high critical current density). In the specific case of YBCO, NCs are able to produce a vortex pinning enhancing the superconducting property.[2] During the thermal treatment to produce YBCO from the precursor solution, it is needed the presence of some amount of fluorine to produce BaF_2 instead of the undesired $BaCO_3$.[40] For this purpose, some efforts have been performed to include fluorine-based precursors (e.g. trifluoroacetates). However, fluorine-free solutions are highlighted from an environmental point of view.[3] In this thesis, we are intended to use LnF_3 NCs into YBCO layers. During the thermal process, LnF_3 decompose to Ln_2O_3 NCs releasing the fluorine in the matrix which is expected to form BaF_2, without the use of fluorinated organic precursors.

Focusing to their up/down-conversion properties when LnF$_3$ NCs are doped with other lanthanide cations, these fluorescents materials are also applied in materials fields. In a recent work, the combination of up-converting NCs and dithienylethene is used for optical memory applications and remote-control photoswitching.[41]

1.2.3 Synthetic strategies of LnF$_3$ NCs

In general terms, the synthetic strategies to develop NCs could be divided in two pathways: top-down and bottom-up approaches (Figure 1.2). Top-down consist of big crystal splitting (bulk material) to obtain nanoscaled systems, in general using physic methods (e.g. laser ablation).[42] In contrast, bottom-up approach uses chemical precursors to build up nanoscaled systems using chemical reactions from atoms, molecules or clusters to NCs. Bottom-up approach had been highlighted if we want a homogeneous and a controllable size and shape of the final NCs, although currently both methods seem to allow similar systems.[43]
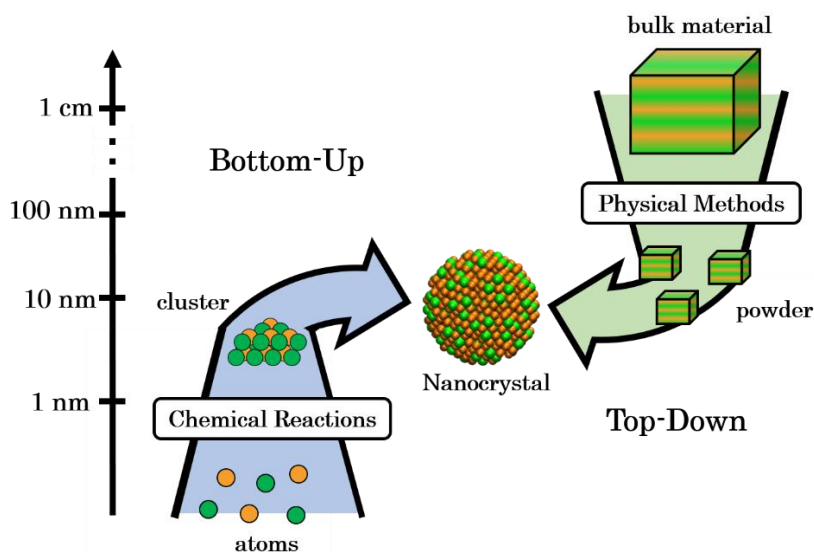
Figure 1.2. Schematic representation of Bottom-Up and Top-Down approaches in the synthesis of NCs.

In the literature, there are several reported methods, normally divided in high-temperature (thermal) and low-temperature (soft) processes. Thermal processes are claimed to form more homogeneous, high-crystalline and fast colloidal suspensions through the decomposition of precursors and/or the application of high temperatures and pressures.[44,45] In contrast, soft methods are labelled of poor-crystalline colloidal suspensions which requires post-thermal processes, non-reproducible and sluggish (several hours of reaction to allow significance growth and/or crystallinity).[4] All these considerations depend on the final system that one expects, but normally the

used methodology is claimed to be the most adequate to this aim. Consequently, we investigated the most convenient synthetic approach to prepare LnF_3 NCs.

Among the different reported routes, co-precipitation method is claimed as easiest and most convenient for working with LnF_3 NCs, due to their low solubility in water, easy protocols and low-cost equipment.[4] This methodology was developed by van Veggel et al.[46] preparing doped LaF_3 NCs with ammonium di-n-octadecyldithiophosphate (as stabiliser) in ethanol−water solution at 75 °C.[46,47] After this point, several methodologies have been developed based on the co-precipitation to allow reproducible and homogeneous colloidal dispersions of LnF_3 NCs. Our work started with the optimisation of a previously reported work,[35] in which the authors used citric acid, sodium hydroxide, yttrium (III) chloride and ammonium fluoride as reactants. They obtained a set of quasispheroidal supraparticles of different sizes if time, temperature and ligand concentration are modified. The evidence of supraparticles (controlled aggregation of small NCs) is not limited on YF_3 and some evidences have been encountered in other LnF_3 NCs.[48,49] In addition, when working in aqueous media, subtle changes in the synthetic parameters could allow the presence of different sized, shaped and structured colloidal systems.[29,35,50]

Hydrothermal treatment is other interesting aqueous based method to synthesise this kind of NCs at high temperatures and pressures. Carrying out this method, bigger and more crystalline NCs will be obtained compared with the common co-precipitation method. Wang et al.[51] reported the hydrothermal (water/ethanol) synthesis of LnF_3 NCs using chloride precursors, linoleate as stabiliser and the fluorinating agent ($NH_4F \cdot HF$ or NaF). The authors stated the formation of single LnF_3 NCs dispersion from La to Nd, but they failed to obtain the same kind of particles for the rest of the series. Here, this tendency is also verified, some metals tend to aggregate in spherical or rod-like shapes if they are synthesised in aqueous medium.

1.2.4 Basic characterisation techniques

During several years, NCs were synthesised and characterised to know their size and crystalline structure. The main interests during the firsts trials in obtaining nanoscaled system were to obtain small-sized and homogeneous colloidal systems with a high crystallinity and defined crystalline structure.[52–54]

Transmission Electron Microscopy (TEM) and in general electronic microscope techniques could be considered the first approximation to uncover the nanoworld. The use of an electron beam instead of the typical visible light

increases the resolution because electrons wavelength is 100,000 times shorter than photon wavelengths. Using electronic microscopes, the size and shape of nanoscaled systems can be measured in a range between few nanometres to microns. Additionally, with the same electron beam can be analysed the crystalline structure (electron diffraction), atomic composition (energy-dispersive X-ray spectroscopy) and the oxidation state of metal ions (electron energy loss spectroscopy), among others.

Concerning crystallinity, powder X-ray Diffraction (XRD) has been used to analyse the crystalline structure of synthesised NCs. With the obtained experimental diffractogram, we can compare the pattern with the database of the expected compounds and conclude which crystalline structure has our system. Additionally, XRD pattern could give us information about the crystalline coherent domain (τ) of the analysed NCs. Using Scherrer equation:

$$\tau = \frac{K\lambda}{\beta\cos\theta} \tag{1.1}$$

it is possible to calculate the crystalline size of the NCs to know if these values match well with the obtained with TEM. This equation depends on the shape-parameter K (0.9 for spherical particles), λ (wavelength of X-ray diffraction), β (full width at half maximum of the most intense peak) and θ (the angle between the incident and the dispersed rays).

In addition, UV-Visible (UV-Vis) spectroscopy has been emphasised for those NCs with surface plasmon resonance (e.g. gold and silver NCs). Using this technique, the main size of the colloidal solution could be determined easily without the use of microscope techniques.[55]

During the last years, the necessity to explore deeply nanoscaled systems promoted the incorporation of other techniques to fully characterise NCs and to be able to adapt them being applied in several fields. In consequence, surface chemistry became the new frontier to be explored.

1.2.5 Models in surface chemistry

As said before, the study of the surface chemistry in NC design has risen importance due to their potential implications in the final applicability. Nanoscaled systems are considered hybrid materials with a core and surface, which determine the final properties of the NC.[56] Surface in this case means the interface between the core and solvent, in this region, capping agents (organic/inorganic molecules) stabilise kinetically the NC. The nature of the stabilisers and their interactions with NC surface are key factors in the final colloidal stability, properties and usability of the as-synthesised NCs. In

addition, the complete knowledge of the stabiliser attached onto NC surface and their NC-interface interaction allow the surface chemistry modification, opening a wide range of applications and new properties.

Concerning the high interest to study the surface chemistry in NCs, it is mandatory to use a model in which we could rationalise the key aspects of interface. Recently, Owen and co-authors[57] discussed the surface-ligand chemistry of NC trying to understand the insights of the interface between the NC surface and the solvent. Covalent Bond Classification[58] (CBC) has been postulated as an useful analogy between coordination chemistry and NC surface, due to the similitude of surface atoms with classical coordination complexes. It considers each interaction as two-centres with two-electrons, the classical covalent bond.[58] First CBC considers L-type ligands as Lewis bases with two-donor electrons (e.g. H_2O, NH_3 and PR_3) interacting with metal atoms, Z-type ligands as Lewis acids with zero-donor electrons (e.g. BF_3 and Me_3Al) interacting with non-metal atoms. Finally, X-type ligands are formally considered radicals with single-donor electron (H, Cl and CH_3) interacting with metal and/or non-metal atoms (Figure 1.3, Model I).
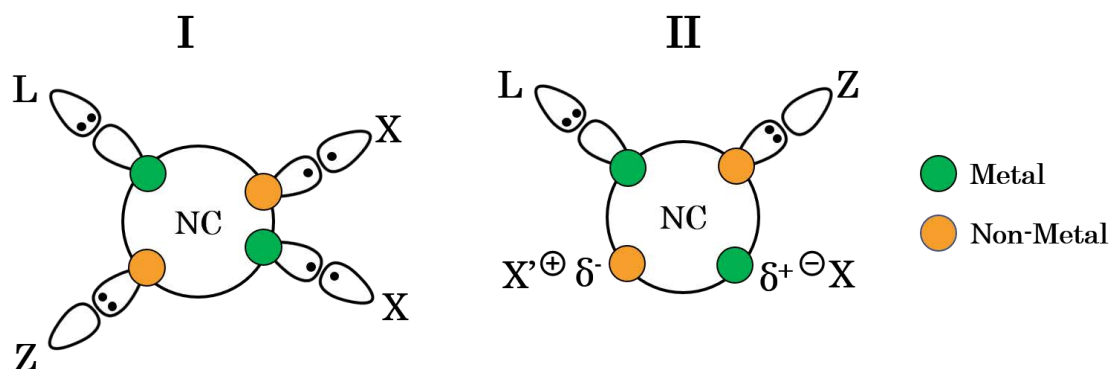
Figure 1.3. CBC classification to describe the NC-surface interactions. (I) L-type are Lewis bases, Z-type are Lewis acids and X-type are radicals. In case (II) X/X'-type are ligands with a real ionic charge (anionic or cationic ligands) interacting electrostatically with metal and non-metal atoms onto surface.

Focusing on X-type ligands, in Owen's classification these ligands are considered formally as radicals interacting with one single electron with metal or non-metal atoms onto the NC surface. In our case, we adapted the CBC to our observations (Figure 1.3, Model II), defining X-type ligands as anions interacting electrostatically with metal atoms (e.g. carboxylates and phosphates) and X'-type ligands, formally cations (e.g. ammonium salts), interacting electrostatically with non-metal atoms. In consequence the presence of two X-type ligands (Model I) or X-type and X'-type ligands (Model II) could be easily exchanged by L-type ligands (two-donor electrons).[56] CBC classification provides a broad description of the different scenarios that we could encounter in NC surface characterisation. Although, this is a useful model, the complete characterisation of surface chemistry is sometimes a

hard work and requires several techniques to unveil the complete surface image.

1.2.6 Analysing the surface chemistry

Commonly, surface chemistry is divided in three different subsections: (i) NC-ligand interface, (ii) ligand and (iii) entire particle (ligand + NC). This division is focused to study the different parts of the NCs observing first the core, then focusing on the shell and final observing the overall system (core and shell). In Figure 1.4, it is shown the categories and which techniques are claimed to be applied to unravel the specific insights of each section.[59]
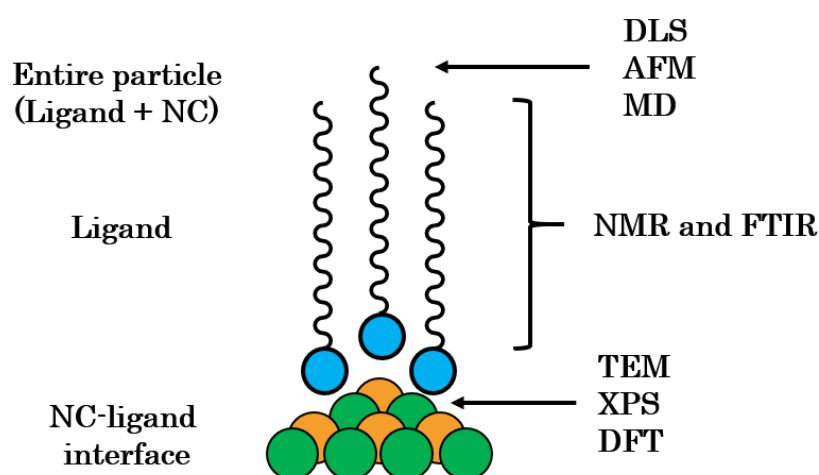
Figure 1.4. Sketch of the used techniques to full-characterise the surface chemistry of NCs divided in the three main parts: NC-ligand interface, ligand and the entire particle. Green spheres represent metal atoms and orange spheres the non-metal atoms of NC surface. Blue spheres represent the ligand headgroup atoms.

Concerning to category (i), NC-ligand interactions could be understood as the chemical bond between the NC core and surface ligands. In consequence, it is possible to study these interactions from an experimental point of view using X-ray Photoelectron Spectroscopy (XPS) to see the effect of the coordination of ligands onto the surface atoms of the core and TEM to see the real-space imaging of the NCs.[60]

To see the ligand category (ii), two experimental techniques are highlighted: Fourier Transform Infrared Spectroscopy (FTIR) and nuclear Magnetic Resonance (NMR). Vibrational spectroscopy, FTIR, is a simple way of proving information on the structure of the molecules capped onto NC surface. It is easy to see the stretching and bending modes of simple organic molecules such as oleic acid[61] or to observe different chain conformations and molecular order by the displacement of the observed bands.[62]

Concerning NMR spectroscopy, it allows a characterisation using the fingerprints of spin-active nuclei (commonly ^{1}H, ^{13}C and ^{31}P).[63] Using one-dimensional (1D) ^{1}H NMR, the information of which stabilisers are coordinated onto NC surface can be obtained. In contrast with a common ^{1}H NMR, if the molecule is attached onto a surface, signals of the hydrogens are broadened and show a downfield shift. These characteristic effects in the NMR signals are common and observed in a several papers.[56,64,65] Theoretically,[66] the broadening in magnetic resonance peaks is inversely proportional to transverse relaxation time (T_2), as it is observed in equation 1.2. In consequence, the transversal interproton dipolar relaxation is usually more efficient if the mobility of the ligands decreases, in our case, when the ligands are attached onto NC surface.

$$\Delta \upsilon_{1/2} = \frac{1}{\pi T_2} \tag{1.2}$$

Although, 1D experiments could shed light on NC-ligand interface, if broader signals are observed, 2D NMR experiments are highlighted to know if ligand is attached onto NC surface. Diffusion-ordered spectroscopy (DOSY) relates a diffusion coefficient with each signal of capping agent, while nuclear Overhauser effect spectroscopy (NOESY) allows to know if the capping agent is attached onto the surface by the presence of a negative cross-peak.[11,64,67] This could be understood considering that NOE effect finally depends on the molecular tumbling, in other words, NOE effect is affected by the molecular weight or how voluminous is the analysed molecule. In consequence, small molecules (organic free molecules in a solvent) show a positive NOE effect, while big molecules (polymers, micelles or stabilisers anchored onto NC surface) present a negative NOE effect.

As NMR technique has raised importance in the last years to full-characterise NC surfaces, currently the study of each different system provides new challenges in the interpretation and study of NMR data. Unfortunately, the information obtained by this technique is not always reliable and often, new strategies and different techniques must be performed.

Finally, category (iii) is based on uncovering information related with the entire particle (inorganic core and organic/inorganic shell). Dynamic light scattering (DLS) technique allows to obtain the hydrodynamic diameter of the NCs in solution (Figure 1.5A). If this measure is compared with the obtained with TEM technique (in which only the core is observable), the thickness of the shell could be calculated.[68] In addition to DLS, using the same instrumentation, ζ-Potential can be calculated by the measure of electrophoretic mobility, obtaining the charge of colloids in their Slip plane (Figure 1.5B).
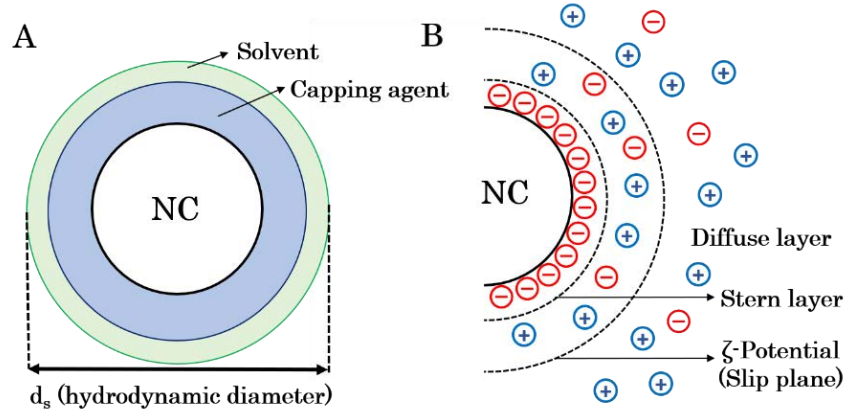
Figure 1.5. (A) Schematic representation of the hydrodynamic diameter (d_s) of a NC and (B) the schematic interpretation of which part measures the ζ-Potential in a solution of NCs.

ζ-Potential values[69] could be obtained by the following equations:

$$u_e = \frac{\varepsilon_{rs}\varepsilon_0}{\eta}\xi_S \tag{1.3}$$

$$u_e = \frac{2}{3}\frac{\varepsilon_{rs}\varepsilon_0}{\eta}\xi_H \tag{1.4}$$

where u_e is the electrophoretic mobility, ε_0 and ε_r are the relative dielectric constant and the electrical permittivity of a vacuum respectively, μ is the solution viscosity. We can calculate this value using Smoluchowski equation 1.3 or Hückel equation 1.4, depending basically on the size of the colloids. ζ-Potential from Smoluchowski (ξ_S) equation becomes a good approximation for colloids larger to 100 nm, while we must use Hückel (ξ_H) approximation for those comprised in few nanometres.

As the instrument automatically perform the conversion from electrophoretic mobility to ξ_S, if the conversion to ξ_H is needed in the case of small colloids, this could be calculated from:

$$\xi_H = \frac{3}{2}\xi_S \tag{1.5}$$

When experimental techniques are not enough to obtain a complete surface characterisation for associated difficulties, computational methods allow the all-atomic-detailed screening to uncover the insights concerning surface interaction (see Section 1.3).

1.2.7 General trends in ligand exchanges

The knowledge obtained through a full characterisation of the surface chemistry allows the control and prediction of the surface insights in several nanoscaled systems. In addition, if the composition of the NC-ligand interface is completely uncovered, we can rationalise the most efficient way to exchange the capping agent introducing a new kind of molecule. These ligand exchange methodologies are raising importance due to the possibility to design the properties onto the surface on request depending on the final application.[26,56,65] In accordance with the thermodynamic instability of the NC surface, the exchange process should be efficient and fast to promote the release of the ligand and the direct attachment of the new one without the unprotection of the surface.[10,70] If the exchange methodology becomes inefficient or slow, the high reactive unprotected surface will tend to collapse with other free-NC surfaces promoting the formation of agglomerates. However, ligand exchange methodologies are useful to obtain an homogeneous colloidal dispersion from an aggregated system. Recent works reported the stabilisation, from aggregates to homogeneous colloidal suspensions, of ZrO_2 and HfO_2 NCs using an easy exchange method in chloroform, obtaining finally oleic acid coated NCs.[11,64]

Analysing the CBC in more detail, it is easy to see that it provides some assumptions derived from the classification model of the ligands onto the surface. Concerning L- and Z-type ligands, they involve the modification of two neutral moieties, which could be exchanged by the surface-ligand affinity.[26] We could expect that L-type ligands (two-electrons donors) will be easily exchanged by other L-type ligands to be anchored onto metallic surface positions.[56] Z-type ligands are expected to stabilise non-metal position onto NC surface due to their acidic role (zero-electron donors) and could be exchanged by other Z-type ligands. The cross exchange between Z- and L-type ligands could be possible, because their exchange do not imply the formation of charged positions. However, depending on their nature they are stabilising metal or non-metal atomic positions, the exchange between them seems to be considerably harder due to the thermodynamics onto the surface.

In contrast, the desorption of X-type ligands implies the formation of charged species in the system. This process is generally thermodynamically unfavourable in non-polar solvents due to the low dielectric constant of these kind of solvents. In aqueous media, the exchange of X-type ligands becomes easier and thermodynamically favourable due to water can solvate released ions allowing the exchange by electrostatic interactions. In general terms, it would be impossible to exchange X-type ligands for L-type ligands.[56] Using our CBC nomenclature, X-type (anions) and X'-type (cations) ligands would be exchanged using analogous ligands to allow an electrostatic exchange onto NCs surface without a notable modification of ligand-NC interface. However,

the addition of a L-type ligand could release two X-type ligands (X and X'-type) as X_2-type bond ion pair, achieving again the neutrality of the NC surface.

1.2.8 Ligand exchange methodologies

There are several standard procedures to perform ligand exchange reactions onto NC surface, being difficult to use one single classification to englobe them. They could be divided considering the number of phases in which the exchange is carried out, the nature of the exchange (if the binding motif is maintained or replaced) and if the exchange implies a chemical reaction during the process. In this thesis, four ligand exchange procedures have been presented in more detail to give an overview of those used currently in the literature (Figure 1.6). Concerning the number of phases, monophasic and biphasic procedures are exposed to be useful to transfer NCs from polar to non-polar solvent or vice versa. In contrast, the exchanges which imply a chemical reaction during their process are divided in striping exchange and chemical reaction, depending if the exchange maintain the original binding motif or not.
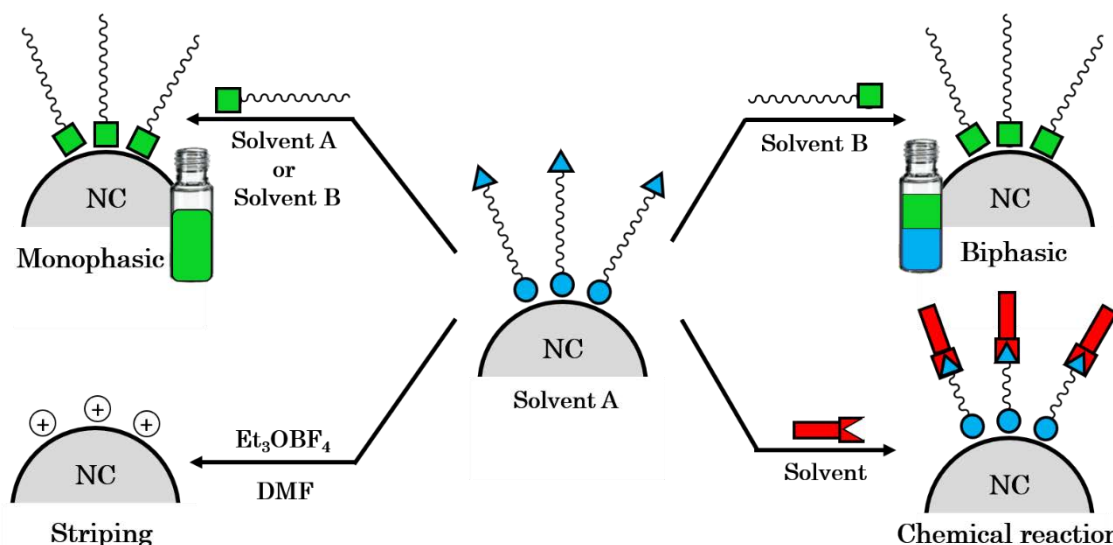
Figure 1.6. Schematic representation of the four-claimed general ligand exchange processes. monophasic, biphasic, striping and by chemical reaction. Solvent A and solvent B must be immiscible to achieve a biphasic system. In striping method, triethyloxonium tetrafluoroborate in DMF has been selected as example.

Monophasic procedures imply firstly the precipitation of the NCs using a non-solvent, after that the new solvent and the desired capping agent are introduced allowing that the initial milky dispersion becomes transparent due to the stabilisation of the surface by the new capping agent.[11,64,71] This methodology could be used to transfer NCs from aqueous (hydrophilic) to non-aqueous dispersions (hydrophobic), as well as, to modify the shell of the NC

changing the capping agent being stable in the same solvent (see Chapter 5). In contrast, biphasic methodologies are highlighted to be controlled upon visual inspection. They consist in blend two immiscible solvents, usually aqueous and non-aqueous, in which NCs start in one of these phases and, after the exchange, are transferred into the other phase.[72–74]

Alternatively, one could perform ligand exchanges based on two steps, the striping of the native ligand and then the attachment of the new capping agent. Commonly, triethyloxonium tetrafluoroborate (Et_3OBF_4)[10] or nitrosonium tetrafluoroborate ($NOBF_4$)[75] compounds are used to strip the native ligand (in hydrophobic colloidal suspensions), through the cleavage of NC-carboxylate interaction, stabilising finally the NC by charge (BF_4^- anions) and adsorbed DMF in polar solvents. At the end, NC surface is able to bind new capping agents through a biphasic or monophasic methodology, depending on the desired solvent.

The last approximation to modify the surface chemistry of the as-synthesised NCs is performing a chemical reaction between one free binding motif of the attached ligand with a new organic molecule. Some ligands have a tether point in their chain or as terminal group, this position is active to react achieving a covalent bond through a chemical reaction.[59] Blanco-Canosa et al.[76] reported an easy covalent linkage based on aldehyde-hydrazine coupling using the well-known "click" reactions. Other approximation has been reported by Kim et al.[77] based on an amide coupling between an oligomeric phosphine containing a carboxylic acid with 2,6-diaminopimelic acid via amide coupling.

1.2.9 Self-assembly

Currently, the interest in self-assembled structures is raising importance to open a deep range of applications. Self-assembly concept is based on the process by which single structures arrange themselves into ordered superstructures. Accordingly to this, these systems commonly are assembled through weak intermolecular forces (e.g. electrostatic, van der Waals and hydrogen bonding interactions)[78] In addition, considering the general definition of self-assembly, it is also included those organisations mediated by external forces as electric/magnetic fields. In terms of energy, the interactions involved in the self-assembly process should be sufficiently strong (of the order of k_BT, being k_B the Boltzmann constant and T the absolute temperature) to provide enough stability, but not so strong to promote an irreversible first-interaction. In other words, the final system should be enough stable to self-assemble and enough flexible to achieve the best energetic configuration.[79]

There are several classifications concerning self-assembly processes, they could be classified considering the kind of interaction (e.g. hydrogen bonding and van der Waals interactions), the nature of the system (e.g. molecular self-assembly, NC self-assembly), among others. A recent review of Boles et al.,[80] classifies the self-assembly of NCs considering the chemical processes onto the surface, usually promoted by the capping agents. In this classification, a surface chemistry containing aliphatic ligands (C_8 to C_{18} length chains) is considered, where the effect or modification of these ligands promotes different self-assembled structures. A review of Min et al.[78] explains accurately the main interparticle forces, which can stabilise or promote the self-assembly process in NCs if they are understood and controlled. The most relevant interparticle forces include van der Waals interactions, internal and external magnetic or electrostatic forces, repulsive steric forces and solvation forces.

Van der Waals interactions are present in all molecules and particles, which are attractive between identical materials and repulsive between dissimilar materials in the presence of a third component (normally a liquid). Typically, metal and metal oxide NCs tend to aggregate in nonpolar solvents if their surface is not sterically stabilised by long-chains or polymers. By this mechanism, quantum dots as PbS or PbSe can aggregate from nanorods to nanowires.[81,82] When NCs are stabilised by steric forces (using a long-chain molecule attached onto their surfaces), they present high-repulsive forces (linear or exponential)[83] between particles avoiding the self-assembly processes.

Magnetic NCs can mutually orient their dipoles producing a self-assembly via magnetic dipole-dipole interactions. These magnetic NCs typically show two different self-assembled structures: (i) the inner one when the different dipoles of these particles interact between them and (ii) if any external magnetic field is applied. In the case (ii), NC dipoles are oriented along the external field, allowing a "directed assembly" induced by external forces.[84] Concerning charged NCs, it is known that these particles repeal each other in aqueous electrolytic solution by the so called electric double-layer force. As the electrostatic interaction promoted by ions are easily tuned by changing ionic strength, pH and involved ions,[60,85,86] these modifications are pivotal aspects to promote self-assembled systems.

Finally, solvation forces (or hydration forces in water) are promoted by the orientation of solvent (or water molecules) between two NCs avoiding their aggregation. In this field, we demonstrated the role of adsorbed water molecules in YF_3 NCs preventing the high-ionic condensation of different ions onto NC surface.[60]

1.2.10 Ionic self-assembly

As in this thesis is presented a new kind of self-assembly process, ion-mediated, between different NCs, is mandatory an overview of the main ionic self-assembled systems mediated by Coulombic interactions, called also ionic self-assembly.[87]

In contrast with the common Coulombic interaction between the ions of a salt, ionic self-assembly process is usually accompanied by a cooperative binding mechanism between the different "building blocks", in which the first interaction promotes further bonding to form the final self-assembled system. Due to the flexibility of ionic self-assembly, its applicability in a deep range of areas is expected in contrast with common hydrogen bonding or stable metal coordination. In contrast with common salt association, which is defined as non-selective and have a long-range character, ionic self-assembly can form defined shape structures, functional patterns and cohesion energies along the charged objects driven by short-range charge-charge couplings. In this case,[88,89] although ions play an important role, the essence of the method is not based on ions. The self-assembly method is based on using building blocks of different charge and different chemical properties.

Other interesting case is the so called self-assembly by ionic bridges, in which usually one has typically a multivalent ion that binds simultaneously to two chemical groups, but each one belonging to a different molecule. For example, divalent ions such as Ca^{2+} are able to bind to anionic groups in biomolecules such as lipids or DNA and induce a variety of self-assembled structures.[90,91]

1.3 Molecular dynamics simulations to surface chemistry

Computer simulations is a widely used approach to provide a theoretical framework to study from ideal systems to realistic models in several research areas. In recent years, computational approaches have been used to investigate in all-atomistic detail the insights which could not be deeply study experimentally due to the limitations of these techniques.[92] In this sense, the combination of computational and experimental approaches gives us the perfect match to rationalise the main insights of our systems.[93]

Concerning the different simulation techniques, they can be divided considering the time scales and the length resolution. Taking into account the dimension of nanoscaled systems, quantum mechanics and classical mechanics are those simulation techniques comprised in the scale between

angstroms and nanometres. At these dimensions, we can use Density Functional Theory (DFT) to optimise the electronic configuration of involved molecules to know structure and charge parameters (Quantum Mechanics). Then, system can be bought with all optimised parts to start Molecular Dynamics (MD) simulations, based on atomic/molecular force fields. During this thesis, MD simulations have been used in all cases in which an atomistic/molecular interpretation was needed to understand the obtained experimental results.

1.3.1 The concept

MD simulations provide us exact results for the position and velocity of our system (composed by several number of atoms) solving the Newtonian equations. These simulations can be performed in a two different detail levels: (i) considering the role played by electrons (e.g. breaking or formation of covalent bonds) by *ab initio* MD simulations or (ii) ignoring the role of electrons and considering only atomic interactions by classical MD simulations. In case (i), Schrödinger equation is solved in each time step before the application of Newtonian equations. This method is normally used in small-scaled systems in which a chemical reaction is the key factor under study. This theory level is applied when the system is composed by ~100 atoms and in a short time scale (~10 ps). Case (ii) is based on the calculation of atomic interactions using the obtained approximations from theoretical or semiempirical methods, which are commonly called force fields. In this case, as electronic interactions are not considered, simulations could be performed in large-scaled (10-100 ns) and complex systems in solution (~10^5 atoms).

1.3.2 Newtonian equation

The method is based on the numerical solution of the motion equation under thermodynamic conditions.[94,95] Considering a system with N atoms, the Newton's equation of motion can be summarised as:

$$m_\alpha \ddot{\vec{r}}_\alpha = -\frac{\partial}{\partial \vec{r}_\alpha} U_{total} (\vec{r}_1, \vec{r}_2, \dots, \vec{r}_N), \qquad \alpha = 1,2,\dots,N \qquad (1.6)$$

where m_α is the mass of atom α, $\vec{r}_1$ is its position and U_{total} is the total potential energy (representing the interactions of all atoms). In general terms, this kind of simulations (based on Newton's equation) consider atoms as classical entities, which interact between other by electrostatic interactions. Concerning U_{total}, this could be calculated by quantum mechanics or using force fields, as will be discussed in section 1.3.3. In all the

simulations performed in this thesis, U_{total} in equation (1.6) was computed using the standard CHARMM force field.[96]

Newtonian equation cannot be solved directly using a computer to obtain an analytical numerical solution. To this end, time must be discretised using several small-scaled time intervals (Δt), allowing a system of nonlinear algebraic equations, which can be numerically solved. In this way, the solving of Newtonian equation can be performed by numerical methods (Euler, Leapfrog, Verlet and velocity Verlet, among others).[94] In view of the advantages and drawbacks of each method, some conditions must be followed to achieve a realistic solution. For instance, Euler algorithm cannot be used because presents problems with the energy conservation (not suitable for real systems). Among the different options, velocity Verlet is the most used method to solve numerically the Newtonian equation of motion.[97] The algorithm is based on time expression of the coordinates of each atom using the Taylor expansion. Position is calculated in each step from the position of the two earliest steps with:

$$\vec{r}(t + \Delta t) \simeq 2\vec{r}(t) - \vec{r}(t - \Delta t) + \frac{f(t)}{m}\Delta t^2 \qquad (1.7)$$

In this equation, $f(t)$ is the total force interaction produced by all elements in the system to each individual atom at instant t. When the position is defined by equation 1.7 in the current step, velocity is obtained from:

$$\vec{v}(t + \Delta t) = \vec{v}(t) + \frac{f(t+\Delta t)+f(t)}{2m}\Delta t \qquad (1.8)$$

As it is required in MD simulations, the velocity Verlet algorithm is completely reversible in time, which implies the conservation of the energy (Noether´s theorem[98]).

To consider the time scale used in the simulations, we need to choose a value smaller than the time for typical physical processes in MD simulations (see Table 1.1), but without reducing a lot this scale because the computational cost increases. In all simulations performed in the present thesis, a time step of 2 fs ($2 \cdot 10^{-15}$ s) was used to be appropriated according to Table 1.1.

Finally, an initial condition of the atomic positions must be defined to solve Newton's laws. Initial position of all molecules or particles are defined with a random distribution but maintaining the atomic connectivity and the crystalline structures. As MD simulations are performed in a determined temperature, the velocities of all involved molecules/particles are randomly generated following a Maxwell-Boltzmann distribution.

Table 1.1. Standard time steps for atoms and different type of molecules in MD simulations.

System	Type of motion	Time step (s)
Atoms	Translation	10^{-14}
Rigid molecules	Translation and rotation	$5 \cdot 10^{-15}$
Flexible molecules with rigid bonds	Translation, rotation and torsion	$2 \cdot 10^{-15}$
Flexible molecules with flexible bonds	Translation, rotation, torsion and vibration	$5 \cdot 10^{-16} - 10^{-15}$

1.3.3 CHARMM force field

As commented before, to perform the MD simulations carried out in this thesis, the use of force fields is enough. There are several common force fields (AMBER, CHARMM or OPLS, for instance)[99,100] In our case, we used CHARMM (Chemistry at Harvard Macromolecular Mechanics) force field[96,101,102] in all simulations because it is implemented by NAMD (Nanoscale Molecular Dynamics), which is the software used to solve the equation of motion. In addition, CHARMM force field is the most widely employed for those simulations containing ions in aqueous systems. To obtain this force fields, it is necessary to determine the parameters of the intramolecular interactions using *ab initio* calculations (Quantum Mechanics). After that, the force field is tested to reproduce well-known molecules or the properties of the solvent. This force field is suitable for systems containing molecular systems as organic molecules, ions or surfaces, because all these parameters are implemented in CHARMM force field.

Used potential are composed by intramolecular interactions and intermolecular interactions as it is indicated by:

$$U_{total} = U_{bond} + U_{angle} + U_{dihedral} + U_{vdW} + U_{Coulomb} \qquad (1.9)$$

where intramolecular part is referred to these interactions between atoms of the same molecule, including bonds, angles between covalent bonds and dihedral (angles formed by planes containing atoms connected by three covalent bonds):

$$U_{bond} = \sum_{bonds} k_{ij}^{bond}(r_{ij} - r_0)^2 \qquad (1.10)$$

$$U_{angle} = \sum_{angles} k_{ijk}^{angle}(\theta_{ijk} - \theta_0)^2 \qquad (1.11)$$

$$U_{dihedral} = \sum_{dihedrals} \begin{cases} k_{ijkl}^{dihedral}\left[1 + \cos\left(n\Phi_{ijkl} - \Phi_0\right)\right] & n \neq 0 \\ k_{ijkl}^{improper}\left(\psi_{ijkl} - \psi_0\right)^2 & n = 0 \end{cases} \quad (1.12)$$

where r_{ij} is the distance between atoms i and j bonded covalently and θ_{ijk} is the angle formed by two covalent bonds connecting atoms i, j and k. If the system is formed by four atoms (i, j, k and l) linearly connected by three bonds, Φ_{ijkl} is the dihedral angle (between plane containing atoms i, j, k and plane formed by atoms j, k and l). Additionally, ψ_{ijkl} is the improper angle between the plane formed by atoms i, j, k and the plane formed by atoms j, k, l in which atoms j, k, l are bonded separately to atom i (see Figure 1.7).
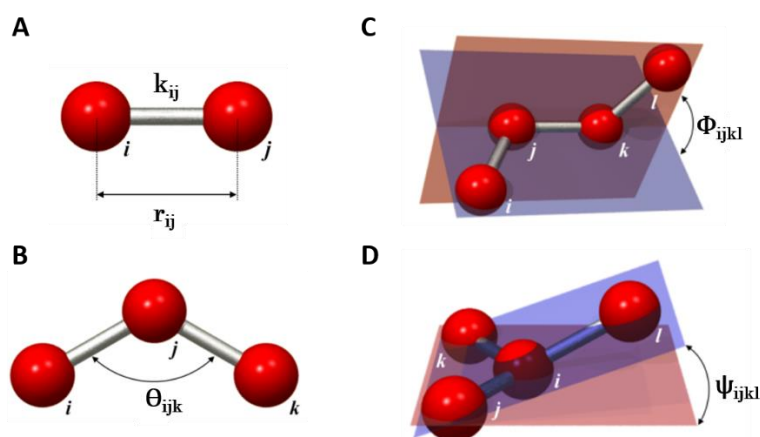
Figure 1.7. Coordinates for the intramolecular interactions between covalently bonded atoms. (A) Bond stretching, (B) Bond angle, (C) Dihedral angle and (D) Improper angle.[103]

Equation 1.10 represents the covalent bond between atoms i and j by elastic constant k_{ij}^{bond} from Taylor approximation. Real positions of the atoms are obtained from the small deviation from their equilibrium position r_0. The same principle is assumed for the angle between two covalent bonds, with a force constant k_{ijk}^{angle} and reference value of θ_0. (see equation 1.11).

As dihedral angle can oscillate between different reference values (Φ_0), in equation 1.12, n indicates the different energy minima and $k_{ijkl}^{dihedral}$ is the constant force. It is easy to understand the different energy minima of a dihedral angle as the case of cis/trans isomers of a molecule.

Finally, in improper angles, the harmonic potential has only an energy minimum in ψ_0. This parameter is related to planarity in the molecular structure. In consequence, ψ_{ijkl} value has small deviations from its reference value and has a constant force of $k_{ijkl}^{improper}$ (equation 1.12).

The interactions between non-bonded atoms (intermolecular interactions), are displayed by two different contributions in equation 1.9. Atoms are considered as rigid spheres by Lennard-Jones potentials (van der Waals forces) and by electrostatic interactions (Coulombic forces) as follow:

$$U_{vdW} = \sum_i \sum_{j>i} 4\epsilon_{ij} \left[\left(\frac{\sigma_{ij}}{r_{ij}} \right)^{12} - \left(\frac{\sigma_{ij}}{r_{ij}} \right)^6 \right] \qquad (1.13)$$

$$U_{Coulomb} = \sum_i \sum_{j>i} \frac{q_i q_j}{4\pi\varepsilon_0 r_{ij}} \qquad (1.14)$$

These interactions consider the characteristics of the individual atoms as the size, electrostatic charge and polarizability. Periodic boundary conditions, introduced in the system, produce a problem related with the intermolecular interactions. In consequence, each atom should be exposed to the potential force of infinitive number of particles being impossible to calculate. To solve this, intermolecular interactions are limited at certain distance due to the potential associated to van der Waals forces is quickly decreased with the distance ($U_{vdW} \, \alpha \, r^{-6}$), thus a limit is established in these interactions. In contrast, electrostatic interactions can not be truncated by the same way, due to long range interactions are essential because the potential is inversely proportional to the distance between particles. To this end, the computing of Coulomb interactions is performed by Ewald summation method. This is based on considering the electrostatic interactions as a sum of screened charges instead of individual charges, due to screened charges decay quickly with the distance and can be easily computed.[104]

In the simulations presented in this thesis, equations from 1.9 to 1.14 have been used to obtain the force field of ions and NCs in aqueous solution. In the experimental part of each chapter is explained the modelling of the used ions and particles, while CHARMM force field of water has been modelled in TIP3P model in all cases.[100] Water is represented as an entity with one oxygen and two hydrogen atoms (explicit solvent). The O-H bonds are covalent and H-O-H angle is maintained at 104.52 °, in consequence, intramolecular interactions are not calculated for this case.

Intermolecular interactions are defined by parameters (see equations 1.13 and 1.14) of van der Waals (Lennard-Jones potential) and electrostatic interactions (Coulomb) as it is shown in Table 1.2. In addition, there is no an internal redistribution of the electric charges because it is based on a non-polarisable model. Model allows the free orientation of the molecules, as well as, the formation of hydrogen bonds between the different molecules. This water model is the best option to maintain an agreement between computational cost and its validity for liquid water. In addition, TIP3P model

has a suitable approximation of the interactions of ions and molecules with water.

Table 1.2. Parameters for van der Waals and Coulomb forces (intermolecular interactions) for water TIP3P model used in the simulations.

Atom	ϵ_i (kcal/mol)	σ_i (Å)	q_i (e)
O	0.1521	3.5364	-0.8340
H	0.0460	0.4490	0.4170
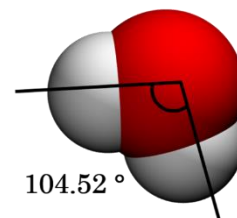
1.3.4 Isothermal-isobaric ensemble

All simulations performed in this thesis are under isothermal-isobaric ensemble (NPT), which means that the simulation is performed under conditions of number of atoms, pressure and temperature constants during the simulation. This ensemble (Figure 1.8) is highlighted to be compared with experimental systems because these usually work at NPT conditions. As the simulated system is not isolated, external energy can be added or removed by a thermostat and a barostat maintaining constant the temperature and the pressure of the system, respectively.

Concerning temperature, the most reasonable idea is simulating a large system (at a constant temperature) in contact with our system, like a thermal bath. However, this approximation implies high computational cost, so it is necessary the implementation of other kind of thermostat. Basically, we have two different options: stochastic (e.g. Langevin)[104] and deterministic (e.g. Nosé-Hoover).[94] As mentioned before, initial velocities of atoms are generated following Maxwell-Boltzmann distribution with a desired temperature. After that, the temperature is maintained fixed following the Langevin thermostat because it is based on the Brownian motion of particles in contact with a large heat bath. Our system is considered as a Brownian particle, where all its atoms are immersed in an imaginary fluid (the thermostat). This system is subjected to the friction force produced by the thermostat and the thermal noise.[105–107]

Pressure is maintained at a desired value, applying an external force, where the volume is adjusted by a "piston" (Figure 1.8). In our simulations, we used the Nosé-Hoover-Langevin barostat to adjust the pressure constant.[94] To this end, an extra parameter is incorporated to motion equations, this corresponds to the "piston" that allows the volume changes in the simulation box.
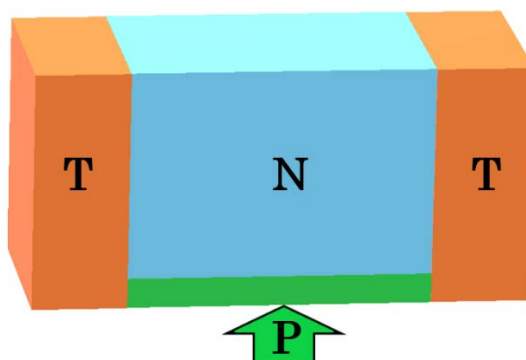
Figure 1.8. Schematic representation of NPT ensemble of a system of N atoms in which temperature (T) is controlled through a thermal bath (thermostat) and pressure (P) is regulated by a barostat.

Currently, there are several open code programs for a scientific usage to solve the algorithms of MD simulations with Langevin thermostat and Nosé-Hoover-Langevin barostat. In this thesis, we used NAMD[104] and VMD[108] developed by the Theoretical and Computational Biophysics Group of the University of Illinois. NAMD program is used to solve the equation of motion and with VMD we can visualise and analyse the results of the simulations.

1.3.5 Radial pair correlation function g(r)

As usual in MD simulations,[94] the identification of the different coordination shell is based on the radial distribution function (Figure 1.9). In general terms, radial pair correlation function is used to know the order, adsorption and correlation of the considered system.

In general terms, g(r) consist of to know the correlation between one atom with the other atoms of the system. This is performed by a screening of the system in a radial movement from the desired atom. Finally, the graph represents the correlation in arbitrary units (as more atoms at the same distance bigger the correlation is) in front of the distance.
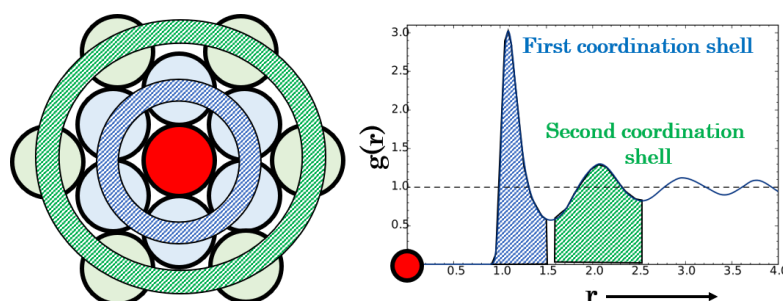
Figure 1.9. Radial distribution function, g(r), in which is represented the correlation between the selected atom (red) with the analysed atoms in their different shells.

In this thesis, g(r) has been used to know the correlation between atoms in NC (metal or fluorine) with the binding motifs of the different ions. Carboxylic oxygen atoms (from anions) and nitrogen atom (from cations) are assigned to the first coordination shell of the NC if their separation is smaller than the distance r corresponding to the first minimum of the g(r) function between these two types of atoms. In our case, the other peaks (other shells) have been assigned to be in the diffuse double layer. Radial distribution function, g(r), describes the correlations between different atoms defined by the equation:

$$\delta N(r) = g(r)4\pi r^2 \rho \delta r \qquad (1.15)$$

where $\delta N(r)$ is the number of oxygen and nitrogen atoms from ionic molecules in a small shell of size δr around given metal or fluorine atoms and ρ is the number density of the oxygen or nitrogen atoms

1.3.6 Adaptive biasing force MD simulations

Specific methods are required to perform free-energy calculations, due to thermodynamic free energy cannot be obtained from a combination between positions and velocities of a single equilibrium MD simulations. The use of adaptive biasing force (ABF) method[109] (implemented in NAMD) allows the calculation of the free energy from a biased MD simulation. A set of atoms (usually one molecule) has a biased motion following a predefined pathway while the rest of the simulation box is maintained without restrictions, moving according to their motion equations. The movements of the constrained molecule, along the predefined pathway, must be very slow, allowing that the system achieves the equilibrium under the effects of thermostat and barostat.

The force needed to constrain the trajectory of the molecule is computed following an adaptive way to obtain an approximation for the reversible work:

$$W_{rev} = \sum_i \vec{F}_i \cdot \Delta \vec{r}_i \qquad (1.16)$$

This reversible work is usually called potential of mean force (PMF). In NPT ensemble under thermodynamic equilibrium, reversible work is interpreted as the Gibbs free energy for this process.

1.4 Objectives and Outline

Although it could be tautological, the first objective of a PhD thesis is to obtain the PhD. degree through the accurate investigation of the main goals proposed to enhance a specific topic. Moreover, the classical objectives that are not directly written in a thesis must be also considered as: to learn, to enhance the scientific criteria, to take decisions, to explore the scientific options, choosing the most adequate and to be able to follow your own scientific career.

The main objective of this PhD. study is based on the easy and reproducible synthetic methodology and the complete understanding of the surface chemistry of metal fluoride NCs, specifically lanthanide (III) fluorides. This thesis has been performed to shed light on the general mechanism related with the synthesis and surface chemistry of metal fluoride NCs.

The current interest of these NCs remains in their applicability as hosts of up/down-conversion devices and to their final application in material science and medical fields. In this vein, a general route to synthesise these NCs is mandatory with some requirements as: low reaction times, high reproducibility, low cost precursors and well-characterised and tuneable systems. The most complex requirement resides in the deep characterisation of the surface chemistry and its manipulation. Using the well-known co-precipitation method, we are aimed to fully characterise both, the core and the surface chemistry of metal fluoride NCs. After this knowledge, the secondary goal is the functionalisation or manipulation of the interface to adapt the final system to all possible applications.

After this work, it could be possible synthesise, characterise and functionalise metal fluoride NCs to be applied in a broad range of fields without the common limitations of nanoscaled systems. Thanks to the better understanding of the insights concerning surface chemistry of these NCs, new frontiers should be attained. In consequence with the main objectives described above, this thesis is divided in different independent chapters with the same guiding thread, the better understanding of LnF$_3$ NCs from synthesis to the complete system image.

In Chapter 2, using YF$_3$ as model system we tried to rationalise the aggregation phenomenon observed when we performed the co-precipitation method. We uncover an ionic self-assembled system mediated by the formation of citrate bridges between cations adsorbed onto different NCs. The formation of these bridges is highly temperature-dependent, at 5 °C this self-assembly is not observed while at 25 and 100 °C NCs tend to assemble in big and temperature-size dependent supraparticles. This interaction has been

stated as one of the strongest ionic interaction ever observed in colloids and rationalised as a new kind of self-assembly ever described. Finally, we were able to extend these conclusions to other metal fluoride NCs and using other polydentate ligands.

Chapter 3 optimise and compare the synthesis of fifteen LnF_3 NCs with a well-known method. Using co-precipitation method, we allowed the easy, fast and reproducible synthesis of all NCs (including the as-synthesised YF_3). After that, some modifications and different studies have been performed to know the insights concerning these NCs. The effect of pH is stated as key factor in the control of the crystalline structure, while the nature of the fluorinating agent seems to be not relevant although their mechanism has been studied. Finally, two different behaviour was unravelled: single-hexagonal dispersed NCs and big assembled systems.

Chapter 4 is focused on the complete study of these hexagonal-NCs that are forming homogeneous colloidal dispersions without aggregation. After a deep study from experimental techniques to MD simulations, the insights of why these NCs remains stable as single particles have been unravelled. A new model of faceted-charge patchy NCs is presented, where ions (cations and anions) and solvents interact selectively in the different surface patches. In addition, we also adapt the MW and hydrothermal treatment (alone and in combination with co-precipitation method) to tune these patchy NCs.

Chapter 5 explains the selective ligand exchange mechanisms performed in aqueous media to LaF_3 NCs. These patchy NCs are excellent candidates to investigate selective ligand exchange in their dual faceted surface. Cations and anions could be replaced selectively and investigated in all-atomic detail by MD simulations. Moreover, the use of a zwitterionic molecule (e.g. L-Lysine) allowed the total exchange replacing all stabilising ions (cations and anions) by a zwitterionic and high biocompatible molecule.

In Chapter 6, we employed Evolved Gas Analysis by Mass Spectrometry (EGA-MS) to uncover experimentally the surface image of a set of NCs. Usually, this technique is applied to uncover the amount of organic matter of a sample with their decomposition mechanism. Aimed by an experimental full-characterisation, we used this technique to YF_3 NCs/supraparticles and LaF_3 NCs to study their surface chemistry. Obtained results have been compared with the obtained by other experimental techniques and MD simulations. At the end, we were able to unravel the image of the surface chemistry, as well, the coordination of multidentate ions using a single technique.

Finally, after the general conclusions and the specific perspectives of each chapter, some preliminary applications are introduced. Currently, we

are using the obtained NCs in three different areas: (i) to enhance YBCO superconducting layers, (ii) as up-converting devices by doping host LaF$_3$ and YF$_3$ systems and (iii) preliminary toxicity assays in cancer cells to unveil their potential application in medical fields.

1.5 References

[1]   A. L. Porter, J. Youtie, *Nat. Nanotechnol.* **2009**, *4*, 534–536.

[2]   A. Llordés, A. Palau, J. Gázquez, M. Coll, R. Vlad, A. Pomar, J. Arbiol, R. Guzmán, S. Ye, V. Rouco, et al., *Nat. Mater.* **2012**, *11*, 329–336.

[3]   X. Obradors, T. Puig, Z. Li, C. Pop, B. Mundet, N. Chamorro, F. Vallés, M. Coll, S. Ricart, B. Vallejo, et al., *Supercond. Sci. Technol.* **2018**, DOI: 10.1088/1361-6668/aaaad7.

[4]   S. Gai, C. Li, P. Yang, J. Lin, *Chem. Rev.* **2014**, *114*, 2343–2389.

[5]   M. Shi, K. L. De Mesy Bentley, G. Palui, H. Mattoussi, A. Elder, H. Yang, *Nanoscale* **2017**, *9*, 4739–4750.

[6]   Y. He, X. Pang, B. Jiang, C. Feng, Y. W. Harn, Y. Chen, Y. J. Yoon, S. Pan, C. H. Lu, Y. Chang, et al., *Angew. Chemie - Int. Ed.* **2017**, *56*, 12946–12951.

[7]   E. Song, A. Gaudin, A. R. King, Y. E. Seo, H. W. Suh, Y. Deng, J. Cui, G. T. Tietjen, A. Huttner, W. M. Saltzman, *Nat. Commun.* **2017**, *8*, 1–14.

[8]   J. Conde, J. T. Dias, V. GrazÃº, M. Moros, P. V. Baptista, J. M. de la Fuente, *Front. Chem.* **2014**, *2*, 1–27.

[9]   B. D. Johnston, W. G. Kreyling, C. Pfeiffer, M. Schäffler, H. Sarioglu, S. Ristig, S. Hirn, N. Haberl, S. Thalhammer, S. M. Hauck, et al., *Adv. Funct. Mater.* **2017**, *27*, 1–9.

[10]   E. L. Rosen, R. Buonsanti, A. Llordes, A. M. Sawvel, D. J. Milliron, B. a Helms, *Angew. Chem. Int. Ed. Engl.* **2012**, *51*, 684–9.

[11]   K. De Keukeleere, J. De Roo, P. Lommens, J. C. Martins, P. Van Der Voort, I. Van Driessche, *Inorg. Chem.* **2015**, *54*, 3469–3476.

[12]   V. Chechik, *J. Am. Chem. Soc.* **2004**, *126*, 7780–7781.

[13]   M. Kluenker, M. Mondeshki, M. Nawaz Tahir, W. Tremel, *Langmuir* **2018**, *34*, 1700–1710.

[14]   T. Y. Kim, N. M. Park, K. H. Kim, G. Y. Sung, Y. W. Ok, T. Y. Seong, C. J. Choi, *Appl. Phys. Lett.* **2004**, *85*, 5355–5357.

[15]   T. Takagahara, K. Takeda, *Phys. Rev. B* **1992**, *46*, 15578–15581.

[16] H. S. Zhou, I. Honma, H. Komiyama, J. W. Haus, *Phys. Rev. B* **1994**, *50*, 12052–12056.

[17] R. Naccache, Q. Yu, J. A. Capobianco, *Adv. Opt. Mater.* **2015**, *3*, 482–509.

[18] G. Guisbiers, *Nanoscale Res. Lett.* **2010**, *5*, 1132–1136.

[19] S. Drouet, J. Creus, V. Collière, C. Amiens, J. García-Antón, X. Sala, K. Philippot, *Chem. Commun.* **2017**, 1–4.

[20] H. Jiang, K.-S. Moon, H. Dong, F. Hua, C. P. Wong, *Chem. Phys. Lett.* **2006**, *429*, 492–496.

[21] H. Aldewachi, T. Chalati, M. N. Woodroofe, N. Bricklebank, B. Sharrack, P. Gardiner, *Nanoscale* **2018**, *10*, 18–33.

[22] F. Brandl, N. Bertrand, E. M. Lima, R. Langer, *Nat. Commun.* **2015**, *6*, 1–10.

[23] J. Lu, Z. Chen, F. Pan, L. A. Curtiss, K. Amine, *Nat. Nanotechnol.* **2016**, *11*, 1031–1038.

[24] N. T. K. Thanh, N. Maclean, S. Mahiddine, *Chem. Rev.* **2014**, *114*, 7610–7630.

[25] X. Wang, J. Zhuang, Q. Peng, Y. Li, *Nature* **2005**, *437*, 121–124.

[26] J. De Roo, K. De Keukeleere, Z. Hens, I. Van Driessche, *Dalt. Trans.* **2016**, *45*, 13277–13283.

[27] M. Wang, G. Abbineni, A. Clevenger, C. Mao, S. Xu, *Nanomedicine* **2011**, *7*, 710–29.

[28] G. Chen, H. Qiu, P. N. Prasad, X. Chen, *Chem. Rev.* **2014**, *114*, 5161–5214.

[29] P. P. Fedorov, A. A. Luginina, S. V. Kuznetsov, V. V. Osiko, *J. Fluor. Chem.* **2011**, *132*, 1012–1039.

[30] J. Zhou, Q. Liu, W. Feng, Y. Sun, F. Li, *Chem. Rev.* **2015**, *115*, 395–465.

[31] H. Dong, S. R. Du, X. Y. Zheng, G. M. Lyu, L. D. Sun, L. D. Li, P. Z. Zhang, C. Zhang, C. H. Yan, *Chem. Rev.* **2015**, *115*, 10725–10815.

[32] G. Chen, H. Qiu, P. N. Prasad, X. Chen, *Chem. Rev.* **2014**, *114*, 5161–5214.

[33] E. Ruggiero, S. Alonso-de Castro, A. Habtemariam, L. Salassa, *Dalt. Trans.* **2016**, *45*, 13012–13020.

[34] H. Y. Peng, B. Bin Ding, Y. C. Ma, S. Q. Sun, W. Tao, Y. C. Guo, H. C. Guo, X. Z. Yang, H. S. Qian, *Appl. Surf. Sci.* **2015**, *357*, 2408–2414.

[35] L. Xiong, B. Shen, D. Behera, S. S. Gambhir, F. T. Chin, J. Rao, *Nanoscale* **2013**, *5*, 3253–3256.

[36]   X. Li, S. Gai, C. Li, D. Wang, N. Niu, F. He, P. Yang, *Inorg. Chem.* **2012**, *51*, 3963–3971.

[37]   T. Paik, A.-M. Chacko, J. L. Mikitsh, J. S. Friedberg, D. A. Pryma, C. B. Murray, *ACS Nano* **2015**, *9*, 8718–8728.

[38]   F. Ai, T. Sun, Z. Xu, Z. Wang, W. Kong, M. W. To, F. Wang, G. Zhu, *Dalt. Trans.* **2016**, *45*, 13052–13060.

[39]   Z. Zhang, X. Ma, Z. Geng, K. Wang, Z. Wang, *RSC Adv.* **2015**, *5*, 33999–34007.

[40]   Z. A. C. Schnepp, S. C. Wimbush, S. Mann, S. R. Hall, *Adv. Mater.* **2008**, *20*, 1782–1786.

[41]   C. Carling, J. Boyer, N. R. Branda, *J. Am. Chem. Soc.* **2009**, *131*, 10838–10839.

[42]   F. Mafuné, J. Kohno, Y. Takeda, T. Kondow, H. Sawabe, *J. Phys. Chem. B* **2001**, *105*, 5114–5120.

[43]   Y. Wang, Y. Xia, *Nano Lett.* **2004**, *4*, 2047–2050.

[44]   N. L. Y, D. Yb, J. Zhuang, L. Liang, H. H. Y. Sung, X. Yang, M. Wu, I. D. Williams, S. Y. Zhongshan, V. Uni, *Inorg. Chem.* **2007**, *46*, 5404–5410.

[45]   Q. Wang, Y. You, R. D. Ludescher, Y. Ju, *J. Lumin.* **2010**, *130*, 1076–1084.

[46]   J. W. Stouwdam, F. C. J. M. Van Veggel, *Nano Lett.* **2002**, *2*, 733–737.

[47]   V. Sudarsan, F. C. J. M. van Veggel, R. A. Herring, M. Raudsepp, *J. Mater. Chem.* **2005**, *15*, 1332–1342.

[48]   D. Zhang, T. Yan, H. Li, L. Shi, *Microporous Mesoporous Mater.* **2011**, *141*, 110–118.

[49]   S. Rodriguez-liviano, N. O. Nun, S. Rivera-ferna, J. M. De Fuente, M. Ocan, *Langmuir* **2013**, *29*, 3411–3418.

[50]   Z.-L. Wang, Miao; Huang, Qing-Li; Hong, Jian-Ming; Chen, Xue-Tai and Xue, *Cryst. Growth Des.* **2006**, *9*, 2169–2173.

[51]   X. Wang, J. Zhuang, Q. Peng, Y. Li, T. U. V, *Inorg. Chem.* **2006**, *45*, 6661–6665.

[52]   A. Garzón-Manjón, E. Solano, M. de la Mata, R. Guzmán, J. Arbiol, T. Puig, X. Obradors, R. Yáñez, S. Ricart, J. Ros, *J. Nanoparticle Res.* **2015**, *17*, 1–11.

[53]   L. Pérez-Mirabet, E. Solano, F. Martínez-Julián, R. Guzmán, J. Arbiol, T. Puig, X. Obradors, A. Pomar, R. Yáñez, J. Ros, et al., *Mater. Res. Bull.* **2013**, *48*, 966–972.

[54]   E. Solano, L. Perez-Mirabet, F. Martinez-Julian, R. Guzmán, J. Arbiol,

T. Puig, X. Obradors, R. Yañez, A. Pomar, S. Ricart, et al., *J. Nanoparticle Res.* **2012**, *14*, 1034–1049.

[55] W. Haiss, N. T. K. Thanh, J. Aveyard, D. G. Fernig, *Anal. Chem.* **2007**, *79*, 4215–4221.

[56] J. De Roo, Y. Justo, K. De Keukeleere, F. Van den Broeck, J. C. Martins, I. Van Driessche, Z. Hens, *Angew. Chemie - Int. Ed.* **2015**, *54*, 6488–6491.

[57] J. Owen, *Science.* **2015**, *347*, 615–616.

[58] M. L. H. Green, G. Parkin, *J. Chem. Educ.* **2014**, *91*, 807–816.

[59] M. A. Boles, D. Ling, T. Hyeon, D. V. Talapin, *Nat. Mater.* **2016**, *15*, 141–153.

[60] J. Martinez-Esain, J. Faraudo, T. Puig, X. Obradors, J. Ros, S. Ricart, R. Yáñez, *J. Am. Chem. Soc.* **2018**, *140*, 2127–2134.

[61] M. J. Hostetler, J. J. Stokes, R. W. Murray, *Langmuir* **1996**, *12*, 3604–3612.

[62] A. Badia, L. Cuccia, L. Demers, F. Morin, R. B. Lennox, *J. Am. Chem. Soc.* **1997**, *119*, 2682–2692.

[63] Z. Hens, J. C. Martins, *Chem. Mater.* **2013**, *25*, 1211–1221.

[64] J. De Roo, F. Van Den Broeck, K. De Keukeleere, J. C. Martins, I. Van Driessche, Z. Hens, *J. Am. Chem. Soc.* **2014**, *136*, 9650–9657.

[65] J. De Roo, I. Van Driessche, J. C. Martins, Z. Hens, *Nat. Mater.* **2016**, *15*, 517–521.

[66] T. D. W. Claridge, *High-Resolution NMR Techniques in Organic Chemistry*, **2009**.

[67] J. De Roo, S. Coucke, H. Rijckaert, K. De Keukeleere, D. Sinnaeve, Z. Hens, J. C. Martins, I. Van Driessche, *Langmuir* **2016**, *32*, 1962–1970.

[68] R. Chaves, D. Cavalcanti, L. Davidovich, J. Kempe, J. H. Eberly, P. Milman, N. Zagury, I. Chuang, Q. Computation, R. Laflamme, et al., *Science.* **2009**, 1417–1420.

[69] A. V. Delgado, F. González-Caballero, R. J. Hunter, L. K. Koopal, J. Lyklema, *Pure Appl. Chem.* **2005**, *77*, 1753–1805.

[70] J. Aldana, Y. A. Wang, X. Peng, *J. Am. Chem. Soc.* **2001**, *123*, 8844–8850.

[71] J. S. Owen, J. Park, P. Trudeau, a P. Alivisatos, *J. Am. Chem. Soc.* **2008**, *130*, 12279–12281.

[72] J. M. Zemke, J. Franz, *J. Chem. Educ.* **2016**, *93*, 747–752.

[73] L. Su, S. Hu, L. Zhang, Z. Wang, W. Gao, J. Yuan, M. Liu, *Small* **2017**, *13*, 1–9.

[74] M. S. Bootharaju, V. M. Burlakov, T. M. D. Besong, C. P. Joshi, L. G. AbdulHalim, D. M. Black, R. L. Whetten, A. Goriely, O. M. Bakr, *Chem. Mater.* **2015**, *27*, 4289–4297.

[75] A. Dong, X. Ye, J. Chen, Y. Kang, T. Gordon, J. M. Kikkawa, C. B. Murray, *J. Am. Chem. Soc.* **2011**, *133*, 998–1006.

[76] J. B. Blanco-Canosa, I. L. Medintz, D. Farrel, H. Mattoussi, P. E. Dawson, *J. Am. Chem. Soc.* **2010**, *132*, 10027–10033.

[77] S. Kim, M. G. Bawendi, *J. Am. Chem. Soc.* **2003**, *125*, 14652–14653.

[78] Y. Min, M. Akbulut, K. Kristiansen, Y. Golan, J. Israelachvili, *Nat. Mater.* **2008**, *7*, 527–538.

[79] M. Antonietti, C. Göltner, *Angew. Chemie - Int. Ed.* **1997**, *36*, 910–928.

[80] M. A. Boles, M. Engel, D. V Talapin, *Chem. Rev.* **2016**, *116*, 11220–11289.

[81] K. S. Cho, D. V. Talapin, W. Gaschler, C. B. Murray, *J. Am. Chem. Soc.* **2005**, *127*, 7140–7147.

[82] I. Patla, S. Acharya, L. Zeiri, J. Israelachvili, S. Efrima, Y. Golan, *Nano Lett.* **2007**, *7*, 1459–1462.

[83] S. Hyun, L. Pei, J. F. Molinari, M. O. Robbins, *Phys. Rev. E* **2004**, *70*, 26117.

[84] S. L. Tripp, S. V. Pusztay, A. E. Ribbe, A. Wei, *J. Am. Chem. Soc.* **2002**, *124*, 7914–7915.

[85] G. B. Sukhorukov, A. A. Antipov, A. Voigt, E. Donath, H. Möhwald, *Macromol. Rapid Commun.* **2001**, *22*, 44–46.

[86] J. Kolny, A. Kornowski, H. Weller, *Nano Lett.* **2002**, *2*, 361–364.

[87] C. F. J. Faul, M. Antonietti, *Adv. Mater.* **2003**, *15*, 673–683.

[88] T. Zhang, J. Brown, R. J. Oakley, C. F. J. Faul, *Curr. Opin. Colloid Interface Sci.* **2009**, *14*, 62–70.

[89] J. Shen, X. Xin, T. Liu, S. Wang, Y. Yang, X. Luan, G. Xu, S. Yuan, *Langmuir* **2016**, *32*, 9548–9556.

[90] J. Faraudo, A. Martin-Molina, *Curr. Opin. Colloid Interface Sci.* **2013**, *18*, 517–523.

[91] H. Liang, D. Harries, G. C. L. Wong, *Proc. Natl. Acad. Sci. U. S. A.* **2005**, *102*, 11173–8.

[92] M. Fyta, D. Lu, A. Aksimentiev, A. Y. Shih, E. Cruz-chu, P. L. Freddolino, A. Arkhipov, K. Schulten, *Phys. Biol.* **2006**, *3*, S40–S53.

[93] Danylo Zherebetskyy, M. Scheele, Y. Zhang, N. Bronstein, C. Thompson, D. Britt, M. Salmeron, P. Alivisatos, Lin-WangWang, *Science.* **2014**, *346*, 1380–1384.

[94]   D. Frenkel, B. Smit, *Understanding Molecular Simulation*, Academic Press, San Diego, **2002**.

[95]   J. Saiz-Poseu, A. Martínez-Otero, T. Roussel, J. K.-H. Hui, M. L. Montero, R. Urcuyo, M. J. MacLachlan, J. Faraudo, D. Ruiz-Molina, *Phys. Chem. Chem. Phys.* **2012**, *14*, 11937.

[96]   J. A. D. Vanommeslaeghe, K. Hatcher, E. Acharya, C. Kundu, S. Zhong, S. Shim, J. E. Darian, E. Guvench, O. Lopes, P. Vorobyov, I. and MacKerell, *J. Comput. Chem.* **2009**, *31*, 671.

[97]   W. C. Swope, H. C. Andersen, P. H. Berens, K. R. Wilson, *J. Chem. Phys.* **1982**, *76*, 637–649.

[98]   H. Goldstein, C. Poole, J. L. Safko, *Classical Mechanics*, Addison Wesley, New York, **2001**.

[99]   R. Salomon-Ferrer, D. A. Case, R. C. Walker, *Wiley Interdiscip. Rev. Comput. Mol. Sci.* **2013**, *3*, 198–210.

[100] W. L. Jorgensen, J. Chandrasekhar, J. D. Madura, R. W. Impey, M. L. Klein, *J. Chem. Phys.* **1983**, *79*, 926–935.

[101] A. D. Mackerell, M. Feig, C. L. Brooks, *J. Comput. Chem.* **2004**, *25*, 1400–1415.

[102] A. D. MacKerell, D. Bashford, R. L. Dunbrack, J. D. Evanseck, M. J. Field, S. Fischer, J. Gao, H. Guo, S. Ha, D. Joseph-McCarthy, et al., *J. Phys. Chem. B* **1998**, *102*, 3586–3616.

[103] "http://cbio.bmt.tue.nl/pumma/index.php/Theory/Potentials," **n.d.**

[104] J. C. Phillips, R. Braun, W. Wang, J. Gumbart, E. Tajkhorshid, E. Villa, C. Chipot, R. D. Skeel, L. Kalé, K. Schulten, *J. Comput. Chem.* **2005**, *26*, 1781–1802.

[105] F. A. Atkins, P.W. Overton, T.L. Rourke, J.P. Weller, M.T. and Armstrong, *Inorganic Chemistry*, Oxford University Press, **2010**.

[106] J. Kohanoff, A. Caro, M. W. Finnis, *ChemPhysChem* **2005**, *6*, 1848–1852.

[107] R. Kubo, *Rep. Prog. Phys.* **1966**, *26*, 255.

[108] W. Humphrey, A. Dalke, K. Schulten, *J. Mol. Graph.* **1996**, *14*, 33–38.

[109] J. Henin, G. Fiorin, C. Chipot, M. L. Klein, *J. Chem. Theory Comput.* **2010**, *6*, 35–47.

2

Unravelling the self-assembly in LnF₃ nanocrystals
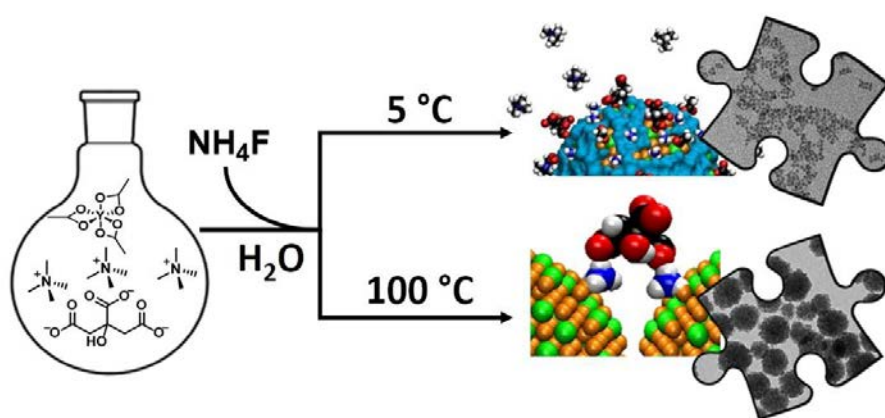
Using YF₃ as model system, here is presented the self-assembly of citrate-stabilised nanostructures tuneable by temperature. Obtained results from several experimental techniques and molecular dynamic simulations suggest that the self-assembly of nanocrystals into supraparticles is due to ionic bridges between different nanocrystals. These interactions were caused by ions (e.g. ammonium cations) strongly adsorbed onto the nanocrystal surface that interact strongly with non-bonded citrate anions, creating ionic bridges in solution between nanocrystals. At higher temperatures (100 °C) this citrate-bridge self-assembly mechanism is more efficient, giving rise to larger supraparticles. At low temperatures (5 °C), this mechanism is not observed and nanocrystals remain stable. Molecular dynamics simulations show that the free energy of a single citrate bridge between nanocrystals in solution is much larger than the thermal energy and in fact is much larger than typical adsorption free energies of ions on colloids. This new citrate mediated self-assembly mechanism is not specific of YF₃ or citrate, so it will be possible to employ it in other multidentate-stabilised colloidal systems.

2.1 Introduction

Nanoscaled structures present multiple edge positions, which play the pivotal role on the tailoring and control of the physicochemical properties. However, their characteristic large surface-to-volume ratio entails difficulties on the stabilisation and lifetime for characterisation and potential applications.[1] Small particles are prone to aggregate as consequence of the intrinsic high thermodynamic energy, reducing the surface-to-volume ratio and hence, the surface energy.[2]

Surface chemistry plays a significant role on understanding and controlling the nanocrystal (NC) aggregation and instability. Coagulation (i) and self-assembly (ii) are the main mechanisms for aggregation of colloidal NCs. The first process (i) involves a non-controlled growth process,[3] whereas the second proposed route (ii) entails an ordered organisation. The high interest in the self-assembly route has been stated during the last years due to its broad possibilities,[4,5] while the uncontrolled coagulation route must be avoided in nanomaterials design.

As mentioned before, aggregation is the first drawback when someone is synthesising colloidal systems, LnF_3 NCs are not an exception. In the literature is not so hard to find several cases where LnF_3 NCs are interacting between them forming assemblies, clusters, aggregates or agglomerates. In a reported work, YF_3 irregular aggregated particles were obtained using a standard co-precipitation method in water in presence of ionic system.[6] These supraparticles change their size depending on concentration of citrate, the temperature and time during the reaction. Doped YF_3 particles synthesised in presence of ethylenediaminetetraacetic acid (EDTA) also showed nanospindles formed by the aggregation of small NCs.[7] Here, the molar ratio Y:stabiliser is the key factor to control the size of these nanospindles in the described hydrothermal method. EuF_3 NCs synthesised in ionic liquids using europium (III) acetate in ethylene glycol as metal precursor was reported by Lorbeer et al.,[8] where they obtained different aggregated systems. They stated that the main reason to promote the aggregation and its behaviour is the ions of the used ionic liquids. Wang et al.[9] reported a general hydrothermal route to synthesise LnF_3 NCs, in which some metal fluoride NCs tend to aggregate in the presence of linoleic acid as stabiliser and sodium fluoride or ammonium fluoride as fluorinating agents. Finally, high aggregation of YF_3 NCs is reported by Zhong et al.[10] formed via the mixture of yttrium (III) nitrate with potassium fluoride as precursors. In this case, the presence of ionic molecules and the absence of a stabilising agent promotes the uncontrollable agglomeration of the colloidal systems.

After this overview, it seems that there is a direct correlation between the described aggregation process with the presence of ions in the system. Ionic strength mediated aggregation is a common effect reported in NC synthesis but normally implies irreversible and uncontrollable processes.[11,12] In addition, the routes that are governing the mechanisms involved in the aggregation or self-assembly are not so clear. The accurate investigation of our situation is mandatory to explore and rationalise the insights involved in the aggregation process of LnF$_3$ NCs.

In this chapter,[13] we propose a new mechanism for the tuneable self-assembly of NCs in water media: the formation of an ionic bridge (mediated by citrate) between NCs stabilised by ionic ligands. This mechanism (the appearance of self-assembled supraparticles and their sizes) is found to be controlled by temperature and the ionic behaviour. This new mechanism could be of interest for a wide class of NCs, stabilised by ionic ligands or in a presence of ionic molecules during their synthesis. The combination of both experimental characterisation and MD simulation methodologies allows a detailed knowledge of NC surface, useful for a rational design in biological applications.[14,15] In addition, the dual approximation reported in this chapter, will provide information of the surface at atomic level useful to understand general self-assembly mechanisms.[16–19]

2.2 Experimental

2.2.1 Particle synthesis

In a 50 mL round-bottom flask equipped with a condenser and a magnetic stirring, citric acid (2.25 mmol) in 16 mL of MilliQ water was neutralised with tetramethylammonium hydroxide (6.75 mmol), followed by the addition of Y(CH$_3$COO)$_3$ · H$_2$O (1.5 mmol). The initial solution was heated until 100 °C or cooled down to 5 °C, and then NH$_4$F (4.5 mmol) in 4 mL of MilliQ water was injected dropwise. After 2 h of reaction, the final mixture was allowed to reach room temperature. YF$_3$ particles were separated from the reaction media by the addition of 10 mL of ethanol (supraparticles) or acetone (NCs), followed by centrifugation at 10,000 rpm for 20 minutes. Separated particles were re-dispersed in 20 mL of MilliQ water forming a stable dispersion.

2.2.2 Characterisation

Dynamic Light Scattering (DLS) and ζ-Potential analyses have been carried out in Characterisation of Soft-Materials Services at ICMAB using a

Zetasizer Nano Zs with measurement range of 0.3 nm – 10.0 µm and sensitivity of 0.1 mg/mL. X-ray powder diffraction (XRD) patterns of the samples were recorded using a Phillips XPert diffractometer equipped with a two circle diffractometers and Cu tube. Transmission Electron Microscopy (TEM) micrographs were obtained on a 120 kV JEOL 1210 TEM, which has a resolution point of 3.2 Å. High Resolution Transmission Electron Microscopy (HRTEM) micrographs were obtained on a 200 kV JEOL 2011 TEM, which has a resolution point of 1.8 Å at 200 kV. Samples for TEM analysis were prepared by spreading a drop of as-prepared NC diluted dispersion on amorphous carbon-coated grids and then dried in air. NMR analyses were recorded with a Bruker Advance II 400 spectrometer in D_2O at 298 K. Samples for NMR were prepared washing the colloidal solution five times before drying NCs. Finally, the powder was dispersed in D_2O. XPS measurements were performed with a Phoibos 150 analyser (SPECS GmbH, Berlin, Germany) in ultra-high vacuum conditions (base pressure $4 \cdot 10^{-10}$ mbar) with a monochromatic aluminum K_α X-ray source (1486.74 eV). The energy resolution as measured by the FWHM of the Ag $3d_{5/2}$ peak for a sputtered silver foil was 0.62 eV.

2.2.3 Computer simulations

All chemical species were described with full atomistic detail. The species included in the simulations are an YF_3 NC, four ionic species (citrate, acetate, ammonium and tetramethylammonium) and water. The force field employed for the molecules was the standard CHARMM force field.[20,21] In this force field, interatomic non-bonding interactions are given by electrostatic and Lennard-Jones 12-6 potentials. Bonded interactions in molecules include harmonic bonds, harmonic angle and dihedral potentials. The molecular models and values of the parameters employed for citrate, acetate, ammonium and tetramethylammonium are the standard in CHARMM. For water, we employed the TIP3P water model with CHARMM parameters. The modelling of an YF_3 NC, so it is consistent with the CHARMM force field, was done as follows. First, we start building the atomic coordinates of a NC based on the experimental crystallographic information. The experimental X-ray diffraction pattern was compared with standard (04-007-2483) reference of the International Centre for Diffraction Data. Once the structure was verified, the unit cell was obtained using the software Eje-Z.[22] Using this unit cell, we employed the program Rhodius[23] to generate the atomic coordinates of Y and F for YF_3 bulk material, which was cut to obtain a spherical NC. We decided to consider a particle of 3 nm diameter, since a larger particle will need the use of extremely large simulation box which also include ions and water. The obtained 3 nm particle had 240 yttrium atoms and 922 fluorine atoms, which does not have the correct 3:1 ratio (occupation

factor for F in the pattern = 0.75). To correct this structure, we assumed an occupation number of 1 for yttrium and an occupation number for fluorine given by 240×3/922≈ 0.780911. Therefore, in the simulations was assigned a partial charge of +3e to the yttrium atoms and a partial charge of -0.780911e to the fluorine atoms to avoid the selective elimination of atoms in this NC. The model of the NC obtained in this way had a zero-net charge. During the MD simulations, the atomic positions of Y and F atoms were maintained fixed at their initial values, avoiding the need of considering explicitly the interaction between yttrium and fluorine. The interaction of yttrium and fluorine atoms with all other atoms of the system (atoms from water or ions) was modelled with the CHARMM force-field with electrostatic interactions (due to particle charges) and Lennard-Jones interactions. The Lennard-Jones parameters employed for fluorine were standard CHARMM values. For yttrium, CHARMM does not provide standard values for Lennard-Jones parameters, so we had to derive appropriate values. To this end, we have considered a previous work[24] in which the force field for yttrium and in particular for yttrium-oxygen interactions was studied and modelled using a Buckingham potential. We converted the Buckingham potential parameters considered in that work to parameters for a Lennard-Jones potential. We have found a good agreement between the two potentials (Buckingham potential employed by Busker et al.[24] and the Lennard-Jones potential employed in CHARMM) by assigning the following Lennard-Jones parameters to yttrium Rmin= 0.3420 nm and ε= -0.001298 Kcal/mol. We performed three main MD simulations summarised in Table 2.1 using a spherical NC of 3 nm.

❖   Preparation of Sim1

The first simulation system (denoted as Sim1 in Table 2.1) corresponds to an YF_3 particle in ionic solution with an excess of ions. The number of ions were selected after trials with smaller number of ions, with the goal of obtaining a NC saturated of ions while, at the same time, having ions in solution with a high concentration like that of the experimental conditions. The ions were randomly introduced in the simulation box containing a NC (initially unprotected onto its surface) and the whole system was solvated with water using the VMD program.[25] In this way, we generated a big simulation box (~10 nm size in each direction) containing about ~10^5 atoms. Sim1 system was suitable for the study of ion-NC interactions.

❖   Preparation of Sim2

We also wished to study the interaction between NCs in the presence of ions, but the direct simulation of many NCs in ionic solution is unfeasible with current computational resources. However, it is still possible to obtain information about NC-NC interaction by considering an infinite array of NCs

with a given separation by employing periodic boundary conditions. To do this, we modified the simulation box of Sim1 to prepare a system which effectively correspond to an infinite bidimensional square lattice of NCs with different lattice constant. The initial configuration is build up as in the case of Sim1 but using a simulation box with shorter length in the x and y axis and larger length in the z axis, see system Sim2 in Table 2.1. In this way, we obtain effective lattices with particle centre-to-centre distances of ~3.7 nm (Sim2), and surface-to-surface of ~7 Å. Sim2 system is presented to study the interface between two different NCs.

❖   Preparation of Sim2B

Finally, to study the role of the explicit water in our system, we performed simulations with implicit water (Table 2.1, Sim2B) in which water is substituted by dielectric constant ($\varepsilon = 80$). The rest of parameters are equal to described in Sim2. Sim2B is suitable to uncover the role of adsorbed water onto NC surface.

Table 2.1. Number of organic molecules, total number of atoms (including NC atoms), distance between NCs in simulations and size of the water box in each simulation.

	Sim1	Sim2	Sim2B
Citrate	20	20	20
Acetate	40	40	40
Ammonium	40	40	40
Tetramethylammonium	60	60	60
Water	33,173	12,520	-
Total Atoms	102,541	40,582	3,022
NCs distance	73.86	6.78	6.78
Box size (Å)	103 x 108 x 99	35 x 35 x 380	35 x 35 x 380

All MD simulations were performed using the NAMD program, version 1.9.[26] In all cases, before running the actual MD simulations, we performed an energy minimisation of the initial configurations using NAMD to solve possible bad contacts between atoms. We have performed MD simulations of all the systems described in Table 2.1, at two different temperatures 5 °C and 100 °C. The Newton equation of motion were solved using a time step of 2 fs in all simulations. Electrostatic interactions were computed using the particle-mesh Ewald (PME) method with the standard settings in NAMD (1 Å resolution, updated each 2 time steps). Lennard-Jones interactions were truncated at 1.2 nm employing a switching function starting at 1.0 nm.

Periodic boundary conditions were employed in all directions. Temperature was fixed at the desired value (278 K or 373 K) using the Langevin thermostat (relaxation time 1 ps). Pressure was kept constant at 1 atm using the Nosé-Hoover-Langevin piston barostat (oscillation period of 100 fs and decay time of 50 fs). In Sim1, we employed the isotropic version of the barostat. In Sim2 and Sim2B we maintained the pressure constant by applying the barostat only in the Z direction.

For each case, simulation times were selected to achieve the maximum information with the minimum computational consume. Sim1 at 5 °C (56.7 ns), Sim1 at 100 °C (55.4 ns), Sim2 at 5 °C (20.2 ns), Sim2 at 100 °C (20.2 ns), Sim2B at 5 °C (22 ns) and Sim2B at 100 °C (22 ns).

2.3 Results and discussion

2.3.1 Nanocrystal synthesis and characterisation

Co-precipitation method was employed at two temperatures (5 and 100 °C) to study if the temperature changes the crystallinity and the behaviour of these NCs. Preliminary, different appearance of the colloidal solution was observed after their synthesis: NCs synthesised at 5 °C showed a transparent-colourless solution while those obtained at 100 °C were transparent and pearl-coloured NCs dispersion. To full-characterise these dispersions, we performed TEM, DLS and XRD experiments to know size, shape, homogeneity and crystalline structure (Figure 2.1).

At 5 °C we obtained a distribution of small NCs with a size average centred at 5 nm by TEM and ~8 nm by DLS, showing a high monodispersed colloidal solution (Figure 2.1A). Particles show a pure cubic crystalline structure with a crystalline coherent domain of 4.4 nm calculated by Scherrer equation of their main diffraction peak (101).[27] Considering the low temperature during the synthesis, obtained NCs present a high crystallinity and good dispersion values.
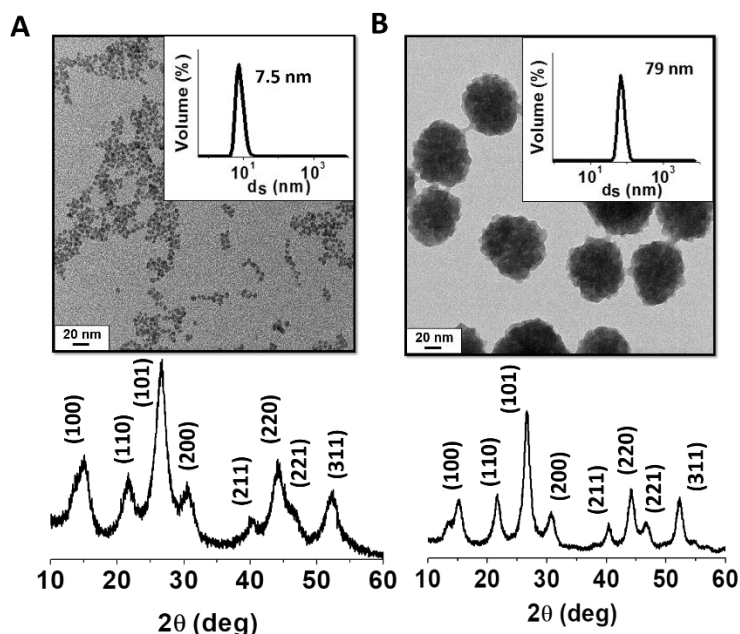
Figure 2.1. Particle size DLS measurements (% in volume) with the corresponding TEM micrographs and powder XRD pattern of the as-synthesised nano/supraparticles at (A) 5 °C and (B) 100 °C. Planes of the cubic crystalline structure assigned with reference pattern (04-007-2483) of the International Centre for Diffraction Data.

When the synthesis is carried out at 100 °C, the system is composed by the self-assembly of small NCs forming spherical supraparticles dispersion of 80 nm approximately (Figure 2.1B). Powder XRD shows a pure cubic crystalline structure (as those obtained at 5 °C), with a high coherent crystalline domain of 6.5 nm.

Electrokinetic measurements were performed to know the electrical nature of these NCs, their values indicate that both, NCs at 5 °C and supraparticles at 100 °C are negatively charged, with values of ζ-Potential that ensure the colloidal stability in water (Table 2.2).

Table 2.2. ζ-Potential using the corresponding equation (see Equation 1.3 and 1.4) of as-synthesised YF$_3$ NCs and supraparticles.

YF$_3$	ζ-Potential	Equation
Nanocrystals	-44.1 mV	Hückel
Supraparticles	-39.2 mV	Smoluchowski

After the primary characterisation of the obtained particles, we want to know the effects controlling the temperature-mediated self-assembly. To this aim, some experimental approaches must be adopted to extract more information of the observed behaviour.

2.3.2 Tuning the parameters in NC synthesis

Synthetic methodology is based on the use of different ionic precursor to achieve the controlled precipitation of YF_3 at nanometric scale. The ionic media, as well as, the kind of ions present in nanoscaled dispersion are claimed to affect directly the stability, aggregation and final behaviour.[28,29] Considering the used synthetic methodology and the observed effect, the self-assembly process could be controlled by two key factors: (i) the temperature during the synthesis and (ii) the ions present in the media and/or the ones adsorbed onto NC surface.

2.3.2.1 Temperature effect

After the self-assembly observed at 100 °C, a comparison of the obtained particles at three different temperatures were performed. To this aim, we chose an intermediated temperature to complete the study (room temperature, approximately 25 °C).

In Figure 2.2 is stated again the temperature effect in YF_3 NC synthesis. At 5 °C the system is formed by single NCs dispersion while at room temperature, the formation of supraparticles is achieved. If in the synthetic procedure the temperature is increased from 25 °C to 100 °C, the size of supraparticles also increases.
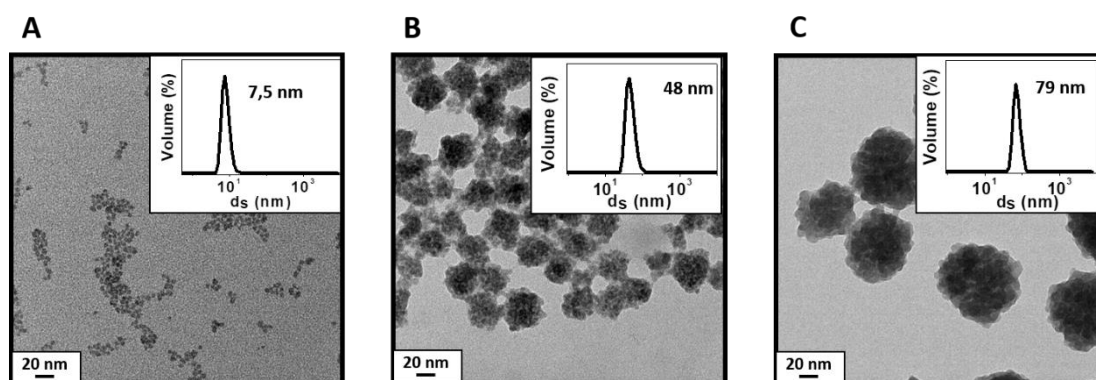
Figure 2.2. TEM and DLS comparison between NCs synthesised at different temperatures. (A) YF_3 NCs obtained at 5 °C, (B) YF_3 supraparticles synthesised at room temperature and (C) YF_3 supraparticles obtained at 100 °C. All images have the same scale bar.

Once the evidence of the effect of temperature have been stated, a size comparison of particles was performed with different techniques. DLS to see the behaviour of the as-synthesised particles in aqueous media and TEM to know the size of the obtained supraparticles. Finally, Scherrer size was calculated to obtain the crystalline coherent domain of the single NCs, regardless if they are aggregated in bigger supraparticles or free in colloidal

dispersion. All these values are presented in Table 2.3. Results of DLS are bigger than those obtained by TEM as we expect, due to DLS includes NC's core and organic shell (adsorbed ions and solvent). However, DLS values show a good correlation with those obtained in microscope technique. Scherrer equation was used to see if the size of monocrystalline NCs increases with temperature as in the case of supraparticle size. It is clear the correlation of Scherrer size with temperature, high reaction temperature promotes the formation of big NCs.

Table 2.3. Size of the obtained particles at different synthetic temperatures by DLS, TEM and Scherrer equation applied to powder XRD

YF$_3$ Particles	DLS (% volume)	TEM histogram	Scherrer size
5 °C	7.5 nm	5.0 ± 0.8 nm	4.4 nm
Room Temp.	48 nm	38 ± 5 nm	5.1 nm
100 °C	79 nm	72 ± 12 nm	6.5 nm

To conclude, the present study supports interesting results not only for the formation of bigger supraparticles at higher reactions temperatures, but specifically for the achievement of NCs, in which their crystalline coherent domain depends directly of the reaction temperature. The temperature is stated as one key factor in the self-assembly process.

2.3.2.2 Effect of the ionic precursors

To discover if the ionic behaviour is other pivotal factor in the self-assembly, some modifications based on the use of different cations and anions in synthetic methodology were performed. Firstly, we consider different salts of Y^{3+} to replace yttrium (III) acetate. Due to the synthesis is performed in water, yttrium (III) trifluoroacetate, nitrate and chloride were selected because they are ionic and soluble in water. Results are presented in Figure 2.3 and Table 2.4, where it can be observed the formation of spherical supraparticles as in the case of yttrium (III) acetate. The size of obtained supraparticles is ~100 nm by DLS, larger than those obtained via standard precursor (~80 nm). This means that acetate anions stabilise better the supraparticle surface compared with trifluoroacetate, nitrate and chloride. In addition, we can conclude that acetate anions are not involved in the self-assembly process, due to, in the presence of other ions, we obtained the same type of supraparticles.

Table 2.4. Size of the obtained particles using different precursors (anionic and cationic) by DLS, TEM and Scherrer equation applied to powder XRD only in cation precursor.

Precursor	DLS (% volume)	TEM histogram	Scherrer size
$Y(CF_3COO)_3$	109	84 ± 10 nm	-
$Y(NO_3)_3$	114	92 ± 11 nm	-
YCl_3	102	87 ± 12 nm	-
Bu_4NF	190 nm	179 ± 26 nm	3.8 nm

Once we concluded that the acetate precursor is not involved in self-assembly process, the cation of fluorinating agent was replaced, using NBu_4^+ instead of ammonium to be more hydrophobic. Note that in the standard synthesis, NMe_4^+ is used in all synthesis as tetramethylammonium hydroxide to neutralise citric acid.
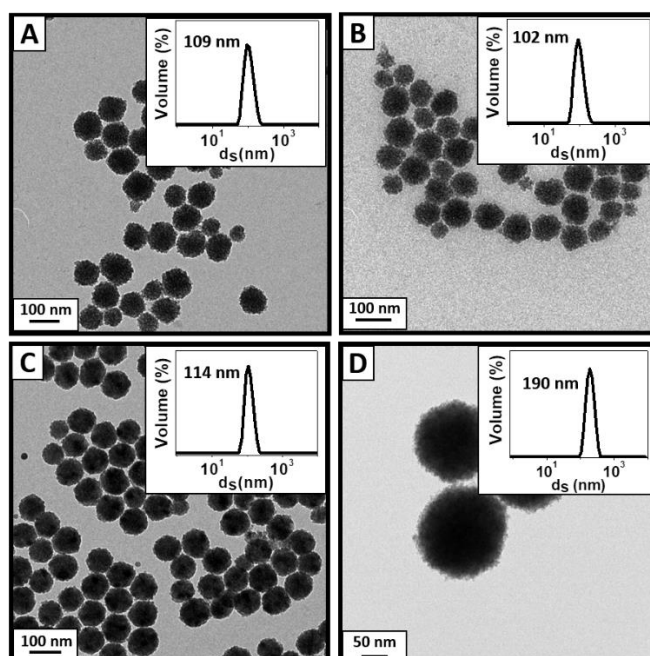

Figure 2.3. TEM and DLS comparison between NCs synthesised with different metallic precursors: (A) $Y(CF_3COO)_3$ (B) $Y(NO_3)_3$ and (C) YCl_3. Finally, is presented the TEM and DLS of YF_3 supraparticles using Bu_4NF instead of NH_4F (D).

Here, we compared the effect of NMe_4^+ as hydrophilic cation compared with NBu_4^+, considering that in the standard synthesis is ammonium which plays the hydrophilic cation role. After the use of tetrabutylammonium fluoride as precursor, supraparticles of 190 nm by DLS was obtained (Figure 2.3D). As the size of supraparticles is increased significantly, we investigate their powder XRD, shown in Supporting Information (SI), to know the crystalline coherent domain. A value of 3.8 nm was obtained, smaller than the achieved with the standard synthesis with ammonium fluoride as precursor (Table 2.3). This means that the role played by ammonium cations is important in NC self-assembly and growth.

After analysing the effects produced by the presence of different ions in the system, we can conclude that the counter ion of the Y^{3+} salt is not involved directly in the self-assembly process. However, it seems that the process is mediated by the cations present in the system because if we change the cation of fluorinating source, the final size of supraparticles and NCs are modified.

2.3.2.3 Effect of the free ions with temperature

Finally, after the statement that the self-assembly process is mediated by the two-postulated key factor: (i) temperature and (ii) ions in the system, we want to know if there is a cooperative effect between these two factors. To do this, we performed the synthesis of YF_3 NCs at 5 °C following the standard protocol, without washing the final solution (solution A). Hereafter, we divided the 20 mL colloidal dispersion in two vessels (10 + 10 mL), the first one was washed twice with acetone and re-dispersed in 10 mL of MilliQ water and heated up at 100 °C for two hours (solution B). The other fraction of 10 mL was heated up at 100 °C directly without washing (solution C). This process is summarised in Figure 2.4 to clarify the steps carried out in each solution.
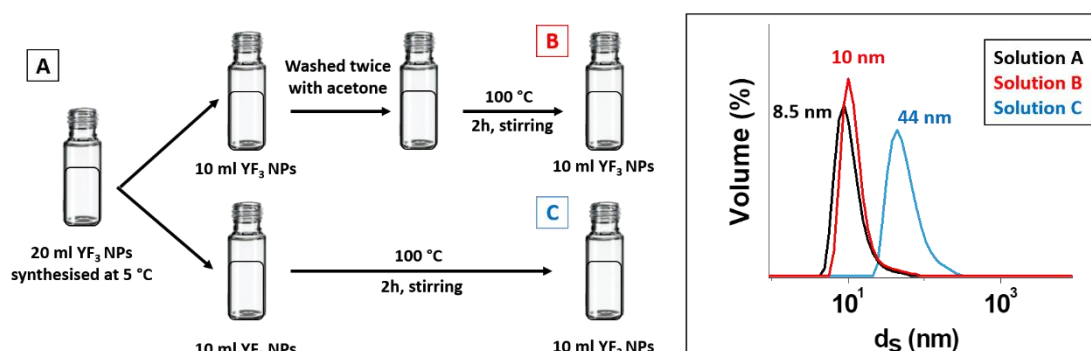

Figure 2.4. Schematic representation of followed process to know the effect of the free ions in the system with temperature with the corresponding DLS measurements in volume of solution A, B and C described in the scheme.

When the three-colloidal solution were obtained, we performed DLS measurements to know their final behaviour. Solution A showed a DLS value of 8.5 nm, compatible with the obtained in the synthesis at 5 °C, after washing twice the solution, its size increases to 10 nm (solution B). Little deviations between a washed and unwashed system could be rationalise considering the surface reorganisation when a colloidal system is exposed to non-solvents, reducing their stability and hence, promoting some surface modifications. The qualitative change in this study was observed in solution C, when the as-synthesised NCs at 5 °C were exposed at 100 °C without a previous washing process. In Figure 2.4 is clearly observed as YF_3 NCs are aggregated in a new family of 44 nm supraparticles by the combined effect of temperature and the

ions in the media (TEM images are shown in SI). After this study we could state that the controlled self-assembly process is not only produced by the synthesis of these particles directly at 100 °C, we are able to obtain NC dispersion at 5 °C and then increasing the temperature to promote self-assembled systems.

2.3.3 Analysing the surface chemistry

As the ions are stated to be a pivotal factor in the self-assembly process, NC surface must be studied to know which ions are adsorbed onto the surface and which are not involved in NC stabilisation. To this aim, we employed the combination of three surface-techniques: solution ^{1}H Nuclear Magnetic Resonance (NMR), powder Attenuated Total Reflection (ATR) Infrared spectroscopy (IR) and powder X-ray Photoelectron Spectroscopy (XPS). All techniques were performed with powder NCs after five washing steps with ethanol to ensure a clear identification of directly-attached molecules to avoid overlapping of free ions. In the case of NMR, obtained NCs at 5 °C were washed five times with acetone and those obtained at 100 °C five times with ethanol. Finally, the dried powder was dispersed in D_2O before the solution analysis.

2.3.3.1 Nuclear magnetic resonance

^{1}H NMR has become a suitable technique to characterise the surface chemistry of nanocolloids in solution. For a complex surface chemistry, this technique allows the identification of all adsorbed species onto NCs surface in comparison with other common techniques (e.g. IR), where the identification is carried out by the presence of the main functional groups. In our case, the presence of different ions containing the same functional groups (e.g. carboxylates) difficult their assignation using other techniques.

Spectrum of both, NCs obtained at 5 °C and supraparticles obtained at 100 °C, were recorded at room temperature (Figure 2.5). Results show the presence of citrate and tetramethylammonium at 5 °C (Figure 2.5A) while at 100 °C, citrate, acetate and tetramethylammonium were observed (Figure 2.5B).
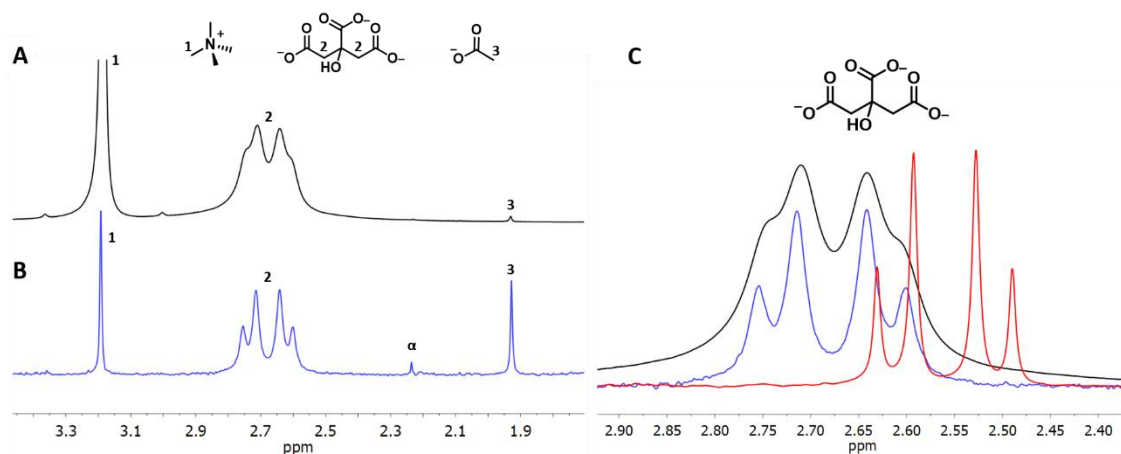
Figure 2.5. ¹H NMR of YF₃ NCs synthesised at 5 °C (A) and YF₃ supraparticles synthesised at 100 °C (B). In the upper part of the spectra, there are the assignations of the peaks (black numbers) related with the ions present in the system for both cases. (α) Corresponds to non-solvent impurity. (C) Comparison of citrate signal of YF₃ NCs synthesised at 5 °C (black), YF₃ supraparticles synthesised at 100 °C (blue) and free citrate (red).

Comparing citrate peaks, produced by the ionic attachment onto particles surface with the reference citrate free anion, we observed a displacement to low fields (Figure 2.5C). This effect is commonly produced by the carboxylic-to-metal interaction, note that both citrate peaks showed the same displacement due to the carboxylic interactions occurs with the same surface metal cation. Considering the different broadness of citrate peaks (see Equation 1.2), two different binding modes were postulated, by one carboxylic moiety at 5 °C and by two carboxylic groups at 100 °C. The freedom movement that allows the coordination by one carboxylic moiety, while other two carboxylic moieties are exchanging their coordination onto NC surface, could produce a broader signal. Ammonium cation is not visible using ¹H NMR due to the experiments were carried out in D₂O, in which deuterium exchange ammonium protons in a fast equilibrium. Trying to detect indirectly this cation, we integrate the peaks observed in NMR to see the charge balance of all species. In Table 2.5 is represented the relative amounts of each detected ion corresponding to the integrations. The number of molecules in Table 2.5 was obtained considering the first enter number of protons for each species. We also compared the effect of washing supraparticles once or five times, concluding the necessity of several washing steps to avoid the presence of free ions (see SI).

Table 2.5. Number of ions present in ¹H NMR obtained to relative integration in each spectrum. Residual charge is indicated to achieve a neutral powder.

Particles		Tetramethylammonium	Citrate	Acetate	Residual Charge
5 °C	*integration*	12.00	13.67	0.04	-27
	number	3	~10	-	
100 °C	*integration*	5.47	27.12	3.00	-43
	number	~1	~14	2	

It is clear the presence of ammonium in both colloidal solutions to achieve the neutrality of -27e and -43e in particle solutions obtained at 5 °C and 100 °C respectively. Although, we could postulate the presence of ammonium cations in the system only with this charge balance, other technique should be performed to ensure the presence of ammonium onto NCs surface.

2.3.3.2 Infrared spectroscopy

IR spectroscopy was performed with the aim to know the behaviour of carboxylic ligands anchored onto NC surfaces. The coordination mode of carboxylates could be identified by the study of $\Delta(v_{asym}- v_{sym})$. In Table 2.6 is reported the common bands of the different coordination modes of carboxylic based compounds,[30,31] giving the overview of the different attachments of citrate and acetate depending on the final IR spectroscopy of as-synthesised particles.

Table 2.6. Comparison of the principle bands presented by carboxylic moieties with their behaviour depending on the difference between asymmetric and symmetric stretching of (OCO) group (Δ ($v_{asym}- v_{sym}$)).

	v_{asym} (cm^{-1})	v_{sym} (cm^{-1})	Δ ($v_{asym}- v_{sym}$) (cm^{-1})
Bidentate (bridge)	1580	1410-1440	**140-170**
Bidentate	1510-1550	1450-1470	40-80
Monodentate	1600-1725	1267-1380	220-460
Ionic	1578	1414	**164**

Considering the integrations and relative amounts obtained in ^{1}H NMR, citrate will be the unique carboxylic-based specie that we could find in IR due to the molar ratio of 14:2 citrate:acetate at 100 °C and 10:0 in the case of 5 °C. After the analysis (Figure 2.6), we could assign the band of ~3260 cm^{-1} to the combination of $v_{str}(N^+-H)$ and $v_{str}(O-H)$ while bands at ~1580 cm^{-1} and ~1420 cm^{-1} were assigned to $v_{asym}(OCO)$ and $v_{sym}(OCO)$ of citrate respectively.
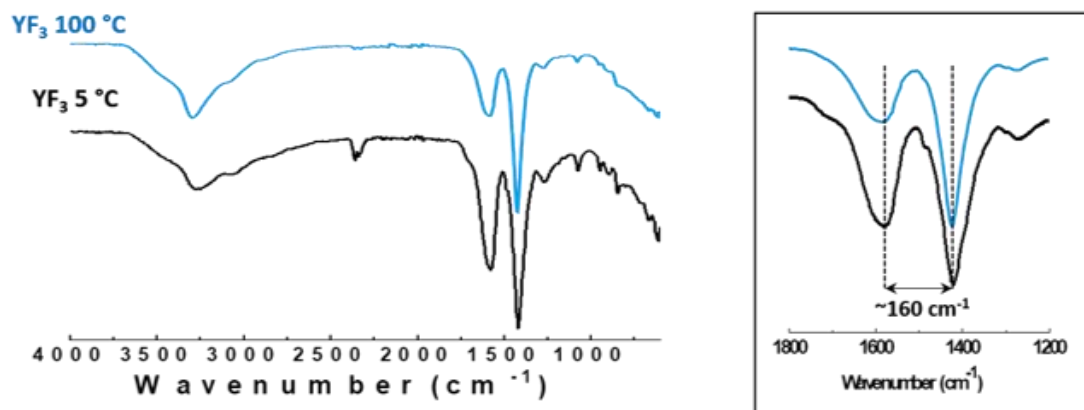
Figure 2.6. FTIR-ATR spectra of YF₃ NCs (synthesised at 5 °C) and supraparticles (synthesised at 100 °C). Ampliation of carboxylate-based bands with the corresponding $\Delta(\nu_{asym} - \nu_{sym})$ is also present to know the behaviour of these interactions.

Finally, in both cases, a $\Delta(\nu_{asym} - \nu_{sym})$ of ~160 cm^{-1} were calculated, giving an ionic behaviour of the carboxylates in our powder NCs. A preference ionic role of carboxylic moieties could be attributed to the free carboxylates of citrates while the direct coordination to NC surface is overlapped in these bands. Taking into account that bidentate bridging carboxylic moieties are close to the ionic in terms of $\Delta(\nu_{asym} - \nu_{sym})$, with these spectrum we can postulate a bidentate bridging moieties attached onto NC surface, while the non-attached carboxylates are ionically stabilised by a cation (ammonium or tetramethylammonium).

2.3.3.3 X-ray photoelectron spectroscopy

XPS technique was performed to YF₃ supraparticles obtained at 100 °C to observe the Y and F interactions with the attached ions onto the surface. Figure 2.7 shows the results of XPS analysis where yttrium signal is composed by two peaks ($3d_{3/2}$ and $3d_{5/2}$) for each interaction, as expected. YF₃ $3d_{5/2}$ peak at 160 eV and $3d_{5/2}$ Y-OOC- interaction at 158 eV.[32] Concerning the last broad peak, this could encompasses acetate, citrate and water (all Y-O interactions). Fluorine spectra shows three different peaks: YF₃ at higher energy (686 eV),[33] F-+NH₄ at 684 eV and at 683 eV a broad peak of F-H₂O, produced by solvated water directly adsorbed onto NC surface. In addition, nitrogen region was analysed, seeming to be compatible with the presence of two different species: one as counter ion and the other attached directly onto NC surface at higher binding energy. We postulate the adsorption of ammonium cations onto NC surface to be small and hydrophilic compared with tetramethylammonium, while the last one should play the counter ion role. The other peak observed at this region corresponds to the 3s Y signal,[34] which is overlapped with the nitrogen signals, interfering with the direct assignment.
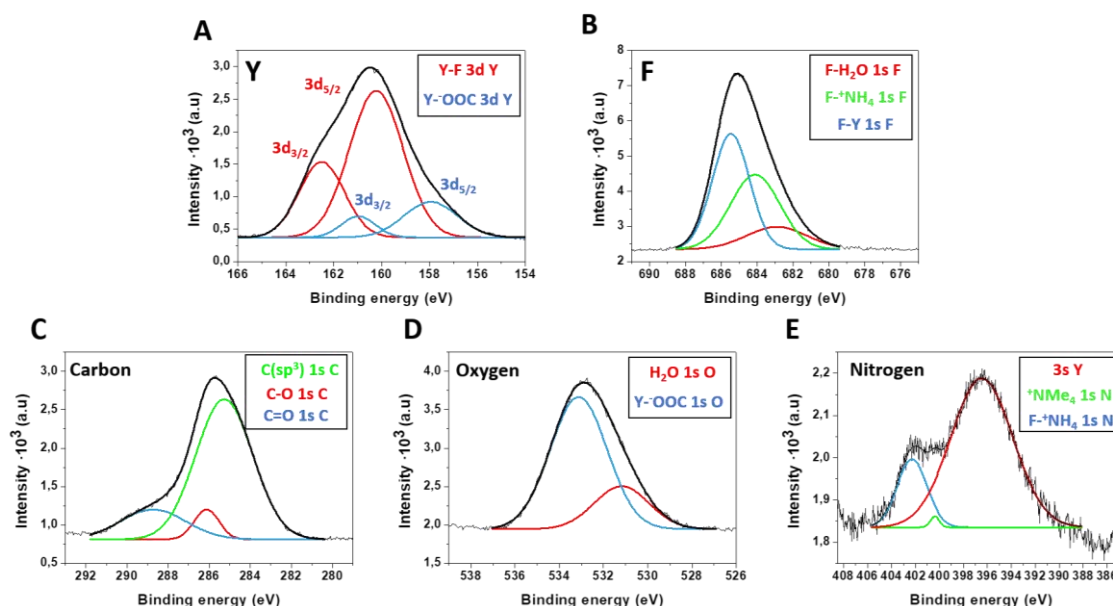
Figure 2.7. XPS of YF₃ supraparticles synthesised at 100 °C. Deconvoluted regions of XPS with their corresponding assignation to each gaussian function of: Yttrium (A), Fluorine (B), Carbon (C), Oxygen (D) and Nitrogen (E). All peaks were deconvoluted using the minimum number of gaussians necessary to obtain the same signal.

These results are compatible with the conclusions obtained from ^{1}H NMR and ζ-Potential experiments. A system with citrate, acetate and ammonium directly adsorbed onto the NC surface was uncovered with tetramethylammoniums as free ions. XPS results suggest the interaction of yttrium with carboxylates and fluorine with nitrogen quaternary cation, as could be expected due to the charge density of Y and F atoms.

2.3.4 Surface image by MD simulations

Once the surface system of the washed-particles was uncovered in detail, large-scale all-atomic MD simulations were performed to extract crucial information of the unwashed system. Simulations were carried out at both temperatures, 5 and 100 °C, including one YF₃ NC electrically neutral. System was designed, starting to build the spherical 3 nm NC, due to large size NC will increase a lot the simulation times. We introduce all ions present in the experimental synthesis (citrate, acetate, ammonium and tetramethylammonium), all of them randomly oriented through the simulation box without contact with the NC. We perform the initial conditions with an uncovered NC with all the ions free in the system to extract crucial information about the affinity of these ions to NC surface and to observe the progressive evolution with time. Finally, we full all the system with a water explicit box (TIP3 model), to simulate solvent interactions. Note that the common reported studies start from a full-covered NC to see the interaction

of capping agent with itself, without making attention to ligand-surface interactions with time.[35,36]

To consider an ion directly attached to the NC surface, radial pair correlation function g(r) was calculated between organic ions and atoms of NC surface (see section 1.3.5). In the case of anions (citrate and acetate), the correlation was performed between carboxylic oxygens with yttrium cations. In the case of cations (ammonium and tetramethylammonium) analysis were performed using nitrogen atoms with fluorides. Citrates and acetates up to a distance of 2.15 Å (carboxylic oxygen – yttrium distance) were accepted as attached. In the case of ammonium, a distance of 3.15 Å (nitrogen – fluoride) was considered. Tetramethylammonium did not present correlation with NC surface (Figure 2.8).
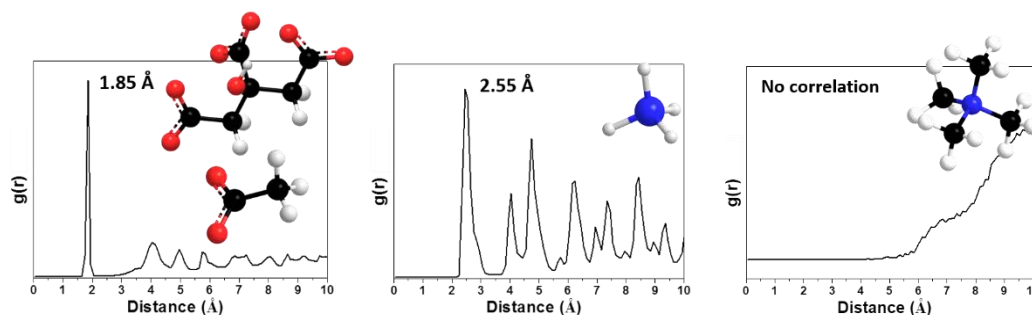

Figure 2.8. Plots of the radial pair correlation function or g(r) of the directly adsorbed ions: acetate and citrate, ammonium and tetramethylammonium.

Equilibrium configurations predict that at 5 °C, system is spontaneously covered by the irreversible attachment of acetate, citrate and ammonium ions while tetramethylammonium has not affinity to NC surface. Our MD simulation also predict that a neutral YF_3 NC will be negatively charged due to the ion adsorption, since negative charge from attached anions is larger than the charge of attached cation, giving a final charge-stabilised system. In addition, results from simulation at 100 °C also showed the attachment of citrate, acetate and ammonium onto NC surface (with an excess of anionic over cationic charge), although larger amounts of adsorbed ions than those obtained at 5 °C were observed (see Table 2.7 and Figure 2.9). These results agree with the electrokinetic experimental results, giving a negative charge in Stern layer, neutralised by the presence of cations (e.g. tetramethylammonium) in the diffusion layer.
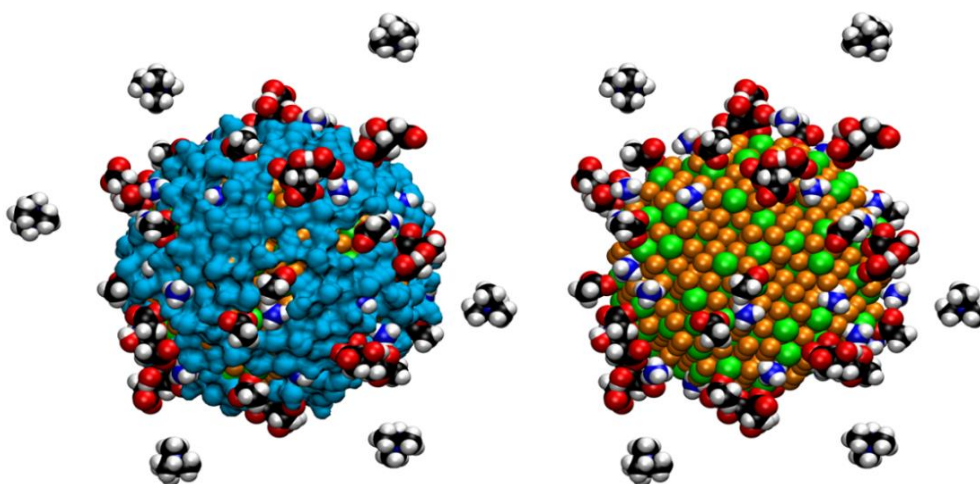
Figure 2.9. Snapshots of final Sim1 at 100 °C where all ions (black spheres are C, red are O, blue are N and white are H), yttrium and fluoride are shown in van der Waals representation (Y in green and F in orange). The left snapshot contains water directly adsorbed onto NC surface with surf representation (made using the surface algorithm of VMD).

The unravelled composition is a clear X-type (bound ion pair) stabilisation,[37] in which acetate and citrate are compensated by the ammonium directly attached and by the tetramethylammonium in the diffuse layer. Formally, we could talk about a charge stabilisation due to the adsorbed ions are not enough large to consider a steric stabilisation, in addition, the high negative charge onto NC surface is guaranteeing the colloidal stability.

Table 2.7. Number of ions directly attached onto the NCs surface (in Sim1) at both experimental temperatures with the relative charge that these ions add to the system. The number of ions presented here corresponds to the obtained in the equilibrium configuration of Sim1.

Ions	Simulation at 5 °C		Simulation at 100 °C	
	Molecules	Charge	Molecules	Charge
Citrate	8	-24e	10	-30e
Acetate	16	-16e	19	-19e
Ammonium	32	+32e	39	+39e
Tetramethylammonium	0	0	0	-
Total	56	-8e	68	-10e

Analysing the carboxylate moieties of citrate, we observed that approximately the 70 % of citrates are adsorbed onto yttrium surface atoms employing two carboxylic groups at both temperatures, 5 and 100 °C. Interestingly, these results are not in the same way that the obtained with

NMR technique, where we postulated two different binding motifs depending on the used temperature. This contradiction could be rationalised considering the two natures of exposed techniques: (i) the characterisation by ^{1}H NMR was performed to the five-steps washed system while, (ii) MD simulations provide information about the unwashed system, giving the surface image directly after the synthesis.

In MD simulations we observe the last surface distribution of our system before the washing-steps, but the procedure to release the excess of ions in our system could modify the surface chemistry, which will be reorganised in a new stable configuration. However, we could also expect that some ions will be released from NC surface after this procedure. Finally, we postulate that the fraction of strongly adsorbed citrate (those that remains absorbed after the washing process), that coordinated with two yttrium atoms is higher at 100 °C than at 5 °C (as we observed in NMR). Thus, we postulated that after the synthesis, this fraction is approximately the same at both synthetic temperatures.

2.3.5 Self-assembly mechanism

After the complete surface image of YF_3 NCs was successfully uncovered, we need to follow with the main question of this chapter, to unravel the self-assembly mechanism observed in several LnF_3 NCs. To study the interaction between two different NCs we performed further MD simulations containing two NCs close to contact at different distance. To summarise, we only shown the simulation with relevant information to our study (denoted as Sim2 in Table 2.1). System with two YF_3 NCs at a distance of ~7 Å showed, in MD simulation performed at 100 °C, the spontaneous formation of a citrate mediated ionic bridge between two different adsorbed ammonium cations (Figure 2.10). Concerning to MD simulation performed at 5 °C, we did not observe the formation of citrate mediated ionic interactions and any kind of interaction between NCs. This interaction, only observed at 100 °C, is compatible with a mechanism where NCs tend to aggregate following a self-assembly procedure mediated by citrate ions when thermal energy is higher than a determinate barrier value.
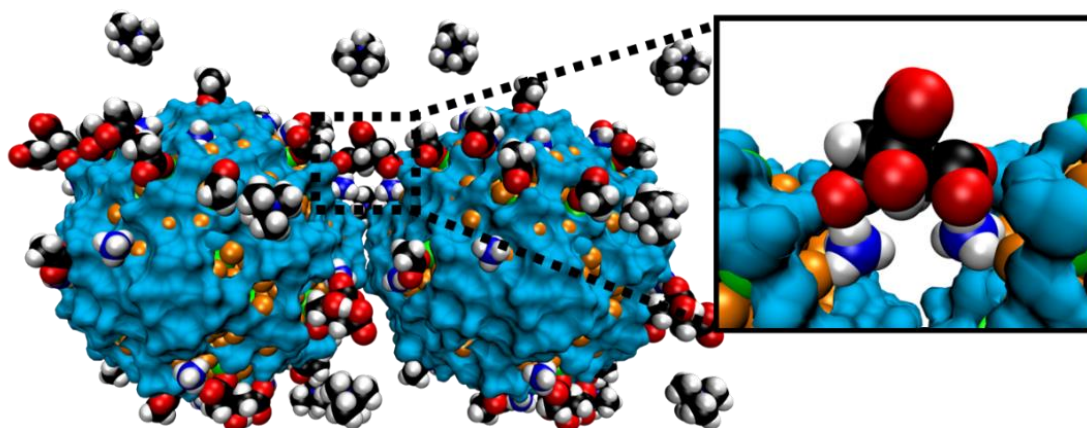
Figure 2.10. Snapshot of Sim2 simulation at 100 °C in which it can be observed an ionic interaction between the two NCs. In enlarged image is represented the self-assembly interaction mediated by citrate ionic bridge between two different attached ammoniums.

But, is the energy of this interaction higher enough to stabilise large assembled particles? To know this, we performed Adaptive Biasing Force (ABF) MD free energy calculation to know the energy value of the cleavage of citrate mediated ionic interaction. Simulation was performed in the same system as Sim 2 (maintaining YF$_3$ particle fixed) and with the restraining of citrate (which is doing the bridge) at different distances of its equilibrium minimum to perform the Gibbs free energy diagram (Figure 2.11). A final value of 25 Kcal/mol is higher enough to stabilise big supraparticles as to define this new interaction as one of the strongest ionic-based interaction ever described for colloidal systems. Just to recall, the normal values for ions strongly adsorbed onto the surface of colloids are ~10 times the thermal energy (k$_B$T),[38] we are in a range of ~40 k$_B$T, four times more than the normal energies observed in these kind of systems.

Thus, we propose a mechanism based on the self-assembly of YF$_3$ NCs into supraparticles where the pivotal factor is the formation of these citrate mediated ionic bridges. Consequently, self-assembly is triggered by the cooperative effect of temperature and ions present in the system (e.g. adsorbed ammoniums and free citrates). Due to the high affinity of ammonium to NC surface observed during the MD simulations (~1.4 ions/nm^2 at 100 °C, corresponding to ~200 ammoniums in a 7 nm NC), these bridges are postulated to be formed between several NCs in all directions allowing a spherical supraparticle.
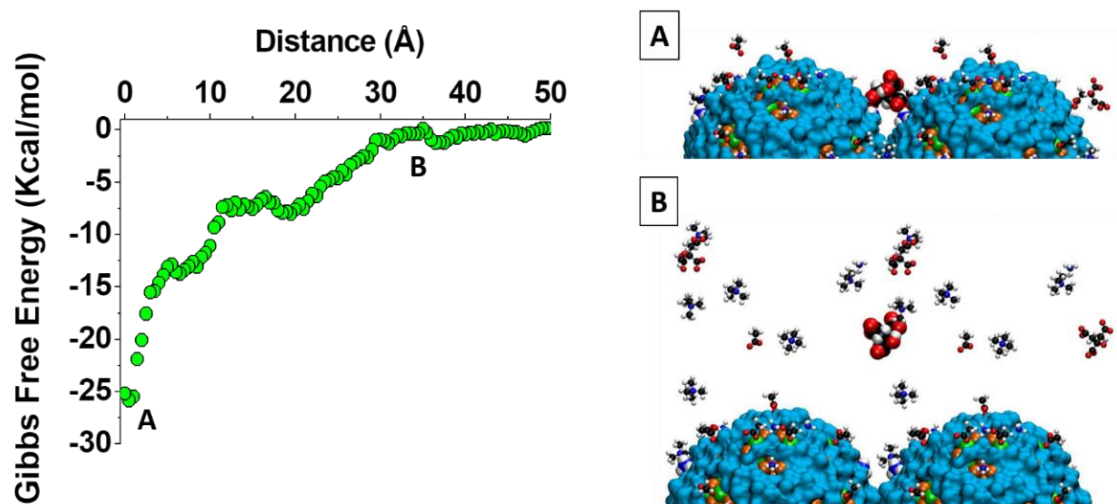
Figure 2.11. Gibbs free energy (obtained as PMF in ABF-MD simulation) associated to a single citrate self-assembled cleavage at 100 °C. (A) Initial step in ABF-MD simulation in which the bridge is formed. (B) Point of simulation where citrate bridge is totally pulled out.

Once the ionic self-assembly mediated by citrate bridges were ensured as the key factor of supraparticle formation, we wanted to know if this interaction is also possible at 5 °C. To this aim, we started from the equilibrium position of citrate bridge (the same of ABF at 100 °C), but in this case, the MD was carried out at 5 °C. Gibbs free energy diagram is shown in Figure 2.12, in which is clearly observed a value of ~37 Kcal/mol (~ 60 k_BT), higher than the obtained by ABF MD simulation at 100 °C (~ 40 k_BT).
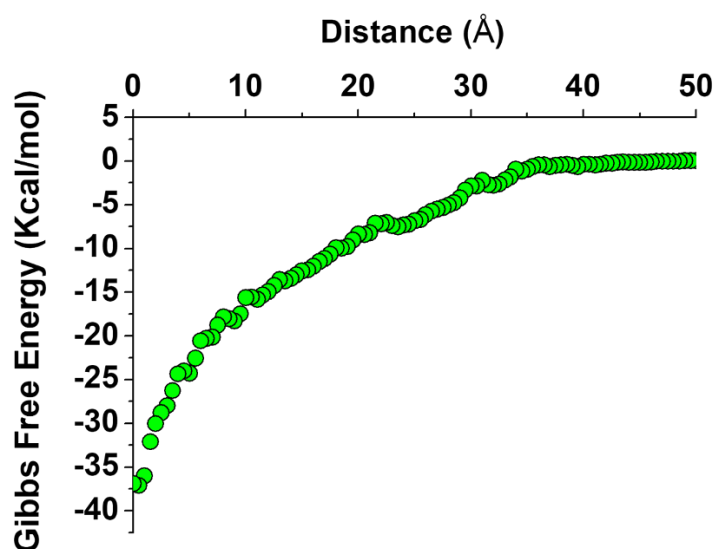
Figure 2.12. Hypothetical Gibbs free energy (obtained as PMF in ABF-MD simulation) associated to a single citrate self-assembled cleavage at 5 °C.

Values indicate that the unravelled citrate bridge interaction is more effective at low temperatures, but it needs a certain temperature to be formed. We postulate a thermal barrier energy between 5 – 25 °C in which the thermal energy is enough to promote citrate bridge interaction. It is possible that the

high charge density around NCs avoids the approximation of citrate by charge hindrance, while if the temperature increase, the higher movement of citrates allows them to cross the barrier to be able to form these interactions between different NCs.

2.3.6 Is ammonium a crucial ion in this ionic interaction?

During the effect of precursor section has been stated that these supraparticles are also obtained without the presence of ammonium cation in the media. In the synthesis carried out with tetramethylammonium and tetrabutylammonium, we obtained supraparticles produced by the same kind of self-assembly.

To study if other cation could adopt the role of ammonium, we performed a simple approximation to know if tetramethylammonium is able to be adsorbed onto NC surface if there are not more cations in the system. Due to the simplicity of the question compared with the complex simulations that we performed before, we employed a simple surface containing some atomic layers with citrates and tetramethylammoniums in the water box. The surface contains 96 Y atoms and 384 F atoms, with the F occupancy correction mentioned before. We use two citrate molecules neutralised by six tetramethylammonium cations in a water box of 897 water molecules. Simulation has 3,309 total atoms and has been simulated for 10 ns approximately (Sim3).

To obtain the maximum information with the minimum computational cost, we adapt the system to our necessities. If we perform a crystal surface, we need to cut the system by one plane and select if we prefer yttrium exposed surface or fluorine exposed surface (note that this drawback is avoided in the spherical NC simulation). To avoid the choosing of one plane, we perform a system in which we are able to analyse both planes at the same time. Crystals were introduced in the upper part (fluorine-exposed surface) and in the bottom part (yttrium-exposed surface), and finally the ions and water were introduced between these two crystals.

In Figure 2.13 is shown the equilibrium configuration of each surface, where it is confirmed the affinity of cations to fluorine-exposed faces and anions to yttrium-exposed faces. Considering the radial pair correlation functions, we demonstrate that, in absence of a more hydrophilic cation in the media, tetramethylammoniums are adsorbed onto fluoride-exposed surface stabilising NC surface. In addition, we observed as citrates are adsorbed onto NC surface as we expect, due to the results of all performed simulations.

After these results combined with the formation of supraparticles without ammonium (see section 2.3.2.2 Effect of the ionic precursors), we propose that the most hydrophilic/ less hydrophobic cation present in the system will play the role of ammonium cations. The change in the cation affects the size of the NCs and supraparticles but the self-assembly mechanism mediated by the citrate bridge is preserved.
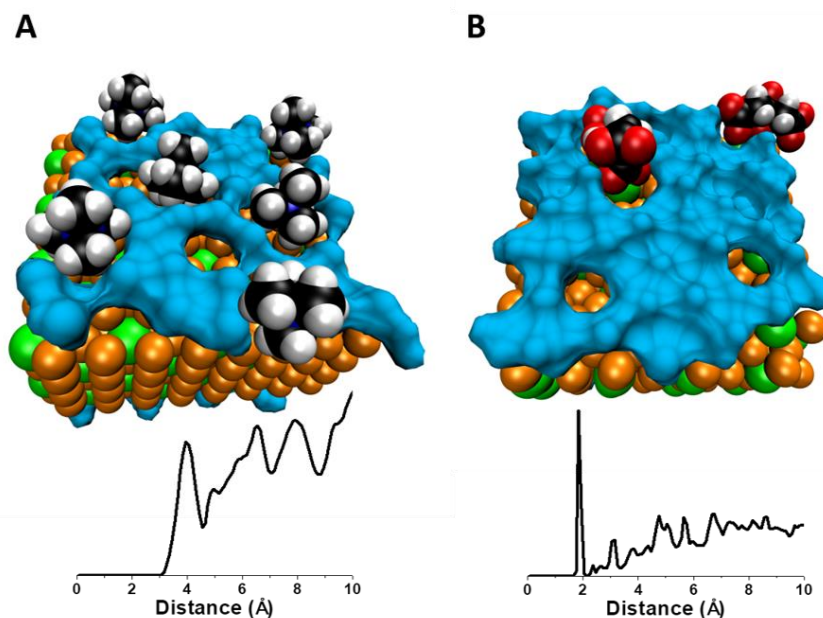

Figure 2.13. Snapshots of the MD simulation corresponding to Sim3 in van der Waals representation and adsorbed water with the surface algorithm of VMD. Radial pair correlation function of (A) tetramethylammonium with fluorine and (B) citrate with yttrium is represented below each snapshot.

2.3.7 Is citrate the key ion in these bridges?

The results of simulations and experimental evidences claim that this ionic mediated interaction can be applied to NCs able to adsorb ions onto their surface and the interaction of a multidentate anion (at least two carboxylic moieties to produce the bridge). To assess these evidences, we test the formation of YF$_3$ supraparticles using two new stabilisers: citraconic acid (Figure 2.14A) and maleic acid (Figure 2.14B), both containing a double bond and two carboxylic moieties.

In both cases, we observed the formation of YF$_3$ supraparticles at 100 °C, demonstrating that the citrate mediated ionic interaction is extensible to other multidentate anions such as the presented citraconate and maleate anions. The presence of two different carboxylate moieties is able to form an ionic mediated bridge interaction between two adsorbed ammoniums onto different NC surfaces (Figure 2.14C). Concerning stability, we postulate the

necessity of a free anionic moiety (e.g. carboxylate) to enhance the stability of final colloidal suspensions in water. YF_3 NCs obtained with citrate show a stable colloidal solution during months, while the citraconate and maleate cases show a short stability of few hours. This effect could be easily explained considering the ionic moieties of the anionic specie. Citrate uses two carboxylic moieties to produce the bridge interaction and the thirst one is enhancing the stabilisation by charge in water. However, citraconic acid and maleic acid only have two carboxylic groups, used in the bridge interaction, while the double bound and the -H or $-CH_3$ groups are more hydrophobic, avoiding a large stability in water media.
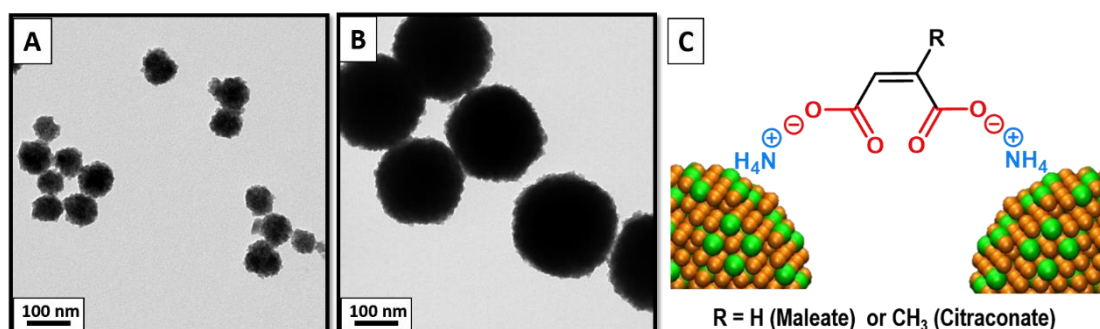

Figure 2.14. TEM images of YF_3 supraparticles formed using citraconic acid (a) and maleic acid (b) instead of citric acid. (c) Schematic representation of the ionic mediated bridge interaction with maleate and citraconate.

The mechanism presented here is based on the ionic mediated interaction between two cations with a multidentate anion acting as bridge. The minimum number of dentate positions has been stated to be two (one for each cation) as the maleate and citraconate cases. Likewise, this mechanism is reminiscent if we use tridentate anions as citrate, which uses two carboxylic groups to promote the bridge while the free carboxylate is enhancing the stability in water as commented before.

2.3.8 Could these results be applied in other NC systems?

To do extensible the applicability of the described interaction in other systems, we evaluated the formation of citrate mediated bridges in other NCs. In consequence with some considerations, we chose SmF_3 (hexagonal structure), EuF_3 (orthorhombic structure) and LuF_3 (cubic structure, isostructural with YF_3) to test this interaction in different crystalline structures and hence, in different surface distribution (Figure 2.15).

In all three cases, we obtained single NC dispersions if the synthesis is carried out at low temperatures (5 °C) and big supraparticles at high

temperatures (100 °C). Concerning the shape of the final assembled systems, this will be discussed in Chapter 3, but here it is noted the spherical behaviour of the single dispersions at 5 °C, which means that the preferential organisation in the self-assembly is promoted by thermodynamics onto the surface. The used metal and the high energy exposed planes combined with the citrate bridge interactions determine the final shape of the assembled system.
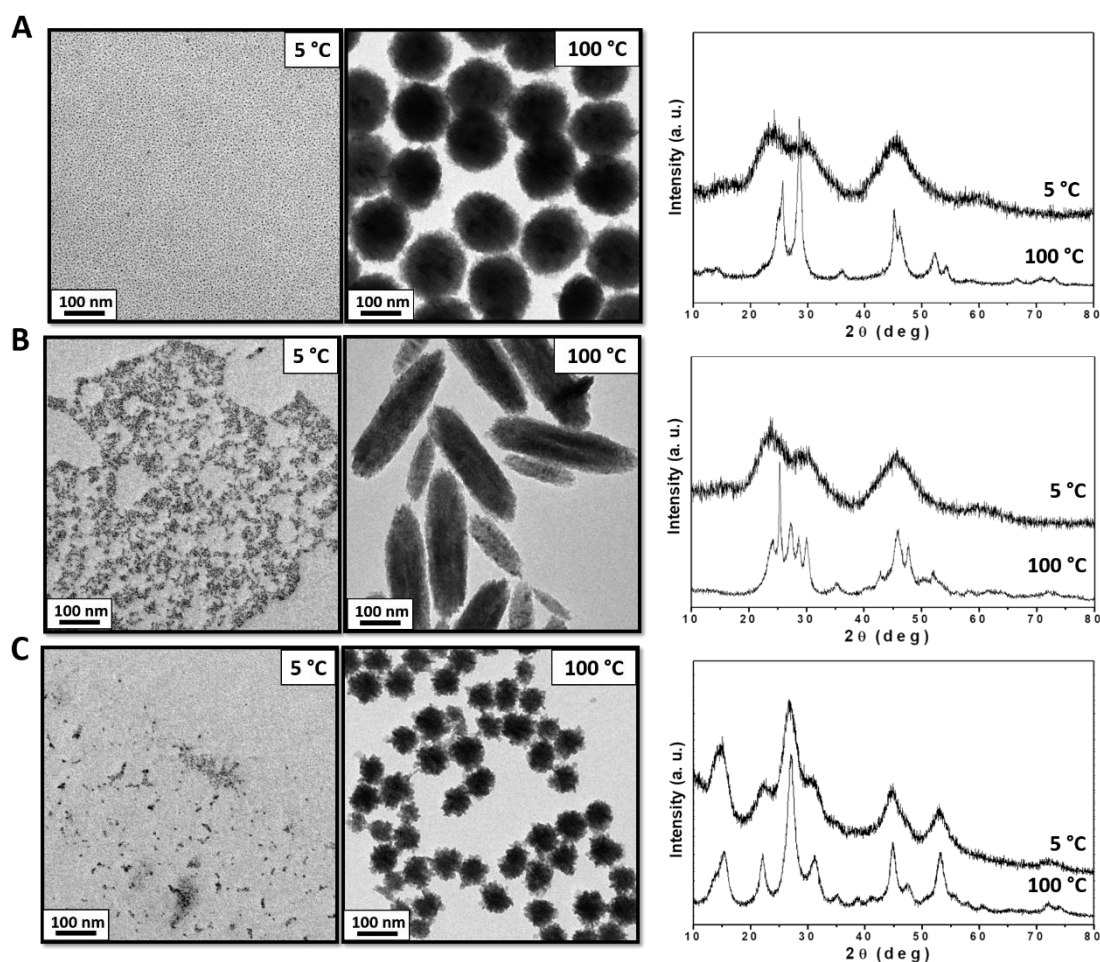

Figure 2.15. TEM images and XRD patterns obtained for a set of LnF$_3$ NCs at 5 °C and 100 °C. (A) SmF$_3$, (B) EuF$_3$ and (C) LuF$_3$ NCs/supraparticles.

If we analyse the crystalline structure, we observed that, at 5 °C, SmF$_3$ and EuF$_3$ (Figures 2.15A and 2.15B) show a mixture of orthorhombic and hexagonal structure due to their close lattice energies and their small size, explaining their broad pattern.[39] In their analogous at 100 °C, we observed the formation of a pure hexagonal phase in SmF$_3$ NCs, while EuF$_3$ show a mixture between orthorhombic and hexagonal structure, being the first one the predominant. In contrast, LuF$_3$ (Figure 2.15C) show a pure cubic crystalline structure in both cases, single NCs at 5 °C and supraparticles at 100 °C.

After all detailed studies concerning the self-assembly process and its applicability in other systems, we identify as key aspects of the self-assembly mechanism the requirement of a NC with a surface able to adsorb cations and the presence of multidentate anions in solution. This indicates that this new ion mediated self-assembly mechanism is not specific of YF_3 and citrate anions, as supported here and in section 2.3.7.

2.3.9 Adsorbed water, the last stabiliser

To end the surface chemistry picture, the role of water in the stabilisation of YF_3 NCs and supraparticles must be studied. To this aim, we performed MD simulations with implicit water (without the presence of water but applying a dielectric constant in the simulation box).

To study at the same time NCs and supraparticles behaviour with the implicit water, we chose the model used in Sim2 (with two NCs close to contact at a distance of ~7 nm), to see the interface between them (x and y axis), as well as, the overall surface that is not close to another NC (z axis). In Figure 2.16 is represented the equilibrium configuration of the simulation carried out at 100 °C, where is observed a massive ionic condensation in the interface of the two NCs. After this result, water is postulated as other stabiliser adsorbed onto NC surface, allowing their stabilisation in water avoiding the ionic condensation that will produce an agglomerated system. It seems that the hydrophilic interactions of water are crucial in the final stabilisation of these particles, due to the dielectric constant ($\varepsilon = 80$) is not enough to avoid the agglomeration via ionic condensation.
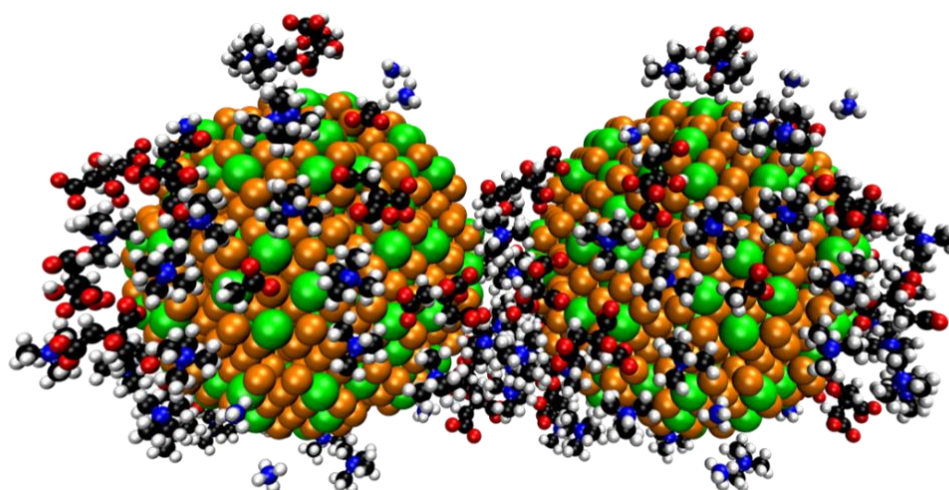

Figure 2.16. Snapshot of the MD simulation with implicit water (described as Sim2B) at 100 °C. It is clearly observed the condensation of all ions (concretely tetramethylammonium cations) in the interface between two YF_3 NCs.

Concerning the hydrophilicity of these particles, in absence of water, tetramethylammonium is adsorbed onto NC surface and it is the principal cation producing the ionic condensation in the interface.

2.4 Conclusions

In this chapter,[13] we propose a mechanism for the self-assembly of NCs into colloidal stable supraparticles, which size is tuneable by temperature or/and the ionic media. The mechanism is based on the formation of an ionic bridge interaction between two different NCs, involving the cooperative interaction of free multidentate anion with adsorbed cations onto the NC surface. Specifically, we studied in deeply detail the particular case of citrate mediated bridges, in which we have proved that the self-assembled citrate bridge is governed by two key factors: (i) temperature and (ii) the particular cations adsorbed onto the surface of NCs. The self-assembly of NCs by multidentate ionic bridges can be considered a generic mechanism for the self-assembly of inorganic NCs, different than the mechanisms usually considered for the self-assembly of inorganic NCs as reported by Min et al. in a review concerning nanocrystal assemblies.[40]

Temperature controls the supraparticle formation, as well as, the size of the final NCs. In our YF_3 system at 5 °C, the formation of single dispersed NCs are observed in experimental results, in addition in our simulation was not presence of ionic interactions between NCs. At 25 °C, we observed formation of stable supraparticles and at 100 °C this citrate-bridge self-assembly mechanism was more efficient, giving rise to larger supraparticles. In consequence with our free energy calculation, the value for a single citrate self-assembled bridge (~40k_BT at 100 °C) is large enough to claim it as one of the strongest ionic interactions ever described for colloidal systems in solution.

Concerning the role of cations, we observed that the effect produced by the adsorbed ions is not only related with electrostatic stabilisation, but it also plays a key role in the self-assembly mechanism. As shown experimentally and by MD simulations, YF_3 NCs are covered by adsorbed ions (with an excess of anions over cations), giving a negative surface charge. Adsorbed cations of different NCs interact with citrate ions in solution to form citrate bridges between NCs. As we have observed experimentally (by DLS and TEM), if we change the employed cation (e.g. using tetrabutylammonium instead of ammonium), we obtained different supraparticle sizes. This evidence is also uncovered using citraconic or maleic acid instead of citric acid. Finally, water and solvation effects also play an essential role in the self-

assembly process. Considering our MD simulations, solvated molecules act as stabiliser avoiding the massive ionic condensation onto the NCs surface.

2.5 References

[1]   S. Fischer, N. D. Bronstein, J. K. Swabeck, E. M. Chan, A. P. Alivisatos, *Nano Lett.* **2016**, *16*, 7241–7247.

[2]   B. Ingham, T. H. Lim, C. J. Dotzler, A. Henning, M. F. Toney, R. D. Tilley, *Chem. Mater.* **2011**, *23*, 3312–3317.

[3]   N. T. K. Thanh, N. Maclean, S. Mahiddine, *Chem. Rev.* **2014**, *114*, 7610–7630.

[4]   M. A. Ramin, K. R. Sindhu, A. Appavoo, K. Oumzil, M. W. Grinstaff, O. Chassande, P. Barthélémy, *Adv. Mater.* **2017**, *29*, 1605227.

[5]   M. Abbas, Q. Zou, S. Li, X. Yan, *Adv. Mater.* **2017**, *29*, 1605021.

[6]   L. Xiong, B. Shen, D. Behera, S. S. Gambhir, F. T. Chin, J. Rao, *Nanoscale* **2013**, *5*, 3253–3256.

[7]   M. Zhang, H. Fan, B. Xi, X. Wang, C. Dong, Y. Qian, *J. Phys. Chem. C* **2007**, *111*, 6652.

[8]   C. Lorbeer, J. Cybi, A. Mudring, *Cryst. Growth Des.* **2011**, 1040–1048.

[9]   X. Wang, J. Zhuang, Q. Peng, Y. Li, T. U. V, *Inorg. Chem.* **2006**, *45*, 6661–6665.

[10]   S. Zhong, S. Wang, H. Xu, C. Li, Y. Huang, S. Wang, R. Xu, *Mater. Lett.* **2009**, *63*, 530–532.

[11]   L. Zhu, Q. Li, X. Liu, J. Li, Y. Zhang, J. Meng, X. Cao, *J. Phys. Chem. C* **2007**, *111*, 5898–5903.

[12]   D. Lin, S. D. Story, S. L. Walker, Q. Huang, W. Liang, P. Cai, *Environ. Pollut.* **2017**, *228*, 35–42.

[13]   J. Martinez-Esain, J. Faraudo, T. Puig, X. Obradors, J. Ros, S. Ricart, R. Yáñez, *J. Am. Chem. Soc.* **2018**, *140*, 2127–2134.

[14]   M. Yang, H. Chan, G. Zhao, J. H. Bahng, P. Zhang, P. Král, N. a. Kotov, *Nat. Chem.* **2017**, *9*, 287–294.

[15]   K. Salorinne, S. Malola, O. A. Wong, C. D. Rithner, X. Chen, C. J. Ackerson, *Nat. Commun.* **2016**, *7*, 10401.

[16]   X. Ye, J. Chen, M. Engel, J. A. Millan, W. Li, L. Qi, G. Xing, J. E. Collins, C. R. Kagan, J. Li, et al., *Nat. Chem.* **2013**, *5*, 466–473.

[17]   E. V. Shevchenko, D. V. Talapin, N. A. Kotov, S. O'Brien, C. B. Murray, *Nature* **2006**, *439*, 55–59.

[18] Z. Nie, A. Petukhova, E. Kumacheva, *Nat. Nanotechnol.* **2010**, *5*, 15–25.

[19] C. B. Murray, C. R. Kagan, M. G. Bawendi, *Annu. Rev. Mater. Sci* **2000**, *30*, 545–610.

[20] A. D. MacKerell, D. Bashford, R. L. Dunbrack, J. D. Evanseck, M. J. Field, S. Fischer, J. Gao, H. Guo, S. Ha, D. Joseph-McCarthy, et al., *J. Phys. Chem. B* **1998**, *102*, 3586–3616.

[21] A. D. Mackerell, M. Feig, C. L. Brooks, *J. Comput. Chem.* **2004**, *25*, 1400–1415.

[22] S. Bernal, F. J. Botana, J. J. Calvino, C. López, J. a. Pérez-Omil, J. M. Rodríguez-Izquierdo, *J. Chem. Soc. Faraday Trans.* **1996**, *92*, 2799–2809.

[23] S. Bernal, F. J. Botana, J. J. Calvino, C. López-Cartes, J. A. Pérez-Omil, J. M. Rodríguez-Izquierdo, *Ultramicroscopy* **1998**, *72*, 135–164.

[24] G. Busker, A. Chroneos, R. W. Grimes, I.-W. Chen, *J. Am. Ceram. Soc.* **1999**, *82*, 1553–1559.

[25] W. Humphrey, A. Dalke, K. Schulten, *J. Mol. Graph.* **1996**, *14*, 33–38.

[26] J. C. Phillips, R. Braun, W. Wang, J. Gumbart, E. Tajkhorshid, E. Villa, C. Chipot, R. D. Skeel, L. Kalé, K. Schulten, *J. Comput. Chem.* **2005**, *26*, 1781–1802.

[27] U. Holzwarth, N. Gibson, *Nat. Nanotechnol.* **2011**, *6*, 534–534.

[28] S. A. MacPherson, G. B. Webber, R. Moreno-Atanasio, *Adv. Powder Technol.* **2012**, *23*, 478–484.

[29] B. Mukherjee, J. W. Weaver, *Environ. Sci. Technol.* **2010**, *44*, 3332–3338.

[30] K. Nakamoto, *Infrared and Raman Spectra of Inorganic and Coordination Compounds, Part B: Applications in Coordination, Organometallic, and Bioinorganic Chemistry*, **2009**.

[31] Q. Chen, J. B. Lynch, L. Que, P. Gomez-Romero, A. Ben-Hussein, G. B. Jameson, C. J. O'Connor, *Inorg. Chem.* **1988**, *27*, 2673–2681.

[32] D. M. Kim, S. H. Lee, W. B. Alexander, K. B. Kim, Y. S. Oh, S. M. Lee, *J. Am. Ceram. Soc.* **2011**, *94*, 3455–3459.

[33] P. Maślankiewicz, J. Szade, A. Winiarski, P. Daniel, *Cryst. Res. Technol.* **2005**, *40*, 410–418.

[34] J. F. Moulder, W. F. Stickle, P. E. Sobol, K. D. Bomben, *Handbook of X-Ray Photoelectron Spectroscopy*, Perkin-Elmer Corporation, Waltham, **1992**.

[35] M. A. Boles, D. Ling, T. Hyeon, D. V. Talapin, *Nat. Mater.* **2016**, *15*, 141–153.

[36] Danylo Zherebetskyy, M. Scheele, Y. Zhang, N. Bronstein, C. Thompson, D. Britt, M. Salmeron, P. Alivisatos, Lin-WangWang, *Science.* **2014**, *346*, 1380–1384.

[37] N. C. Anderson, M. P. Hendricks, J. J. Choi, J. S. Owen, *J. Am. Chem. Soc.* **2013**, *135*, 18536–18548.

[38] C. Calero, J. Faraudo, D. Bastos-González, *J. Am. Chem. Soc.* **2011**, *133*, 15025–15035.

[39] C. Dong, F. C. J. M. van Veggel, *ACS Nano* **2009**, *3*, 123–130.

[40] Y. Min, M. Akbulut, K. Kristiansen, Y. Golan, J. Israelachvili, *Nat. Mater.* **2008**, *7*, 527–538.

3

Tailoring LnF₃ nanocrystals via mechanistic study
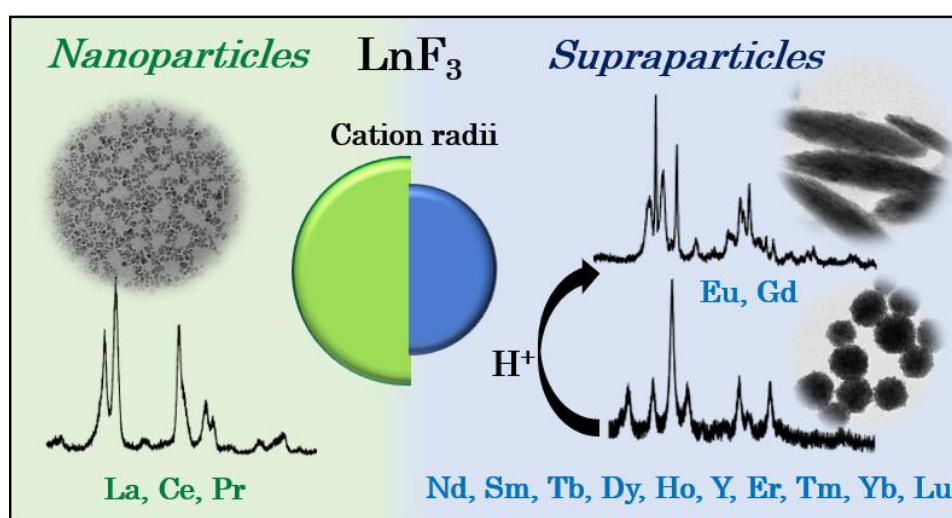
Fifteen LnF₃ nanocrystals are synthesised using co-precipitation method with citrate stabilisation, to allow the fast, easy and reproducible synthesis of several nanoscaled structures in water. General trends related to the behaviour of LnF₃ nanocrystals are unveiled due to their broad range of application in several fields (e.g. medical applications). We found that the use of different lanthanide element is crucial in the final size, shape, assembly and crystalline structure. In addition, we can tune the cubic crystalline phase to pure orthorhombic by modifying the pH of the system using HBF₄ instead of tetramethylammonium citrate. NMR and IR techniques were performed to unravel the picture of the surface chemistry. HRTEM and SAED were performed to uncover the shape of the obtained nanocrystals and the preferential orientation of the assembled particles, giving crucial information of the involved mechanisms. This study reveals the dependence of the crystalline structure with the employed metal and pH, forming nanocrystals, supraparticles or mesocrystals.

3.1 Introduction

When reading about the chemistry of lanthanide (Ln) compounds, it is easy to see that they are commonly summarised as Ln^{3+} cations with similar chemical properties.[1] This generality is close related with the internal role of f-orbitals and the $4f^x\ 5d^1\ 6s^2$ electronic configuration of Ln metals. In consequence, Ln^{3+} are considered formally as $5d^0\ 6s^0$, with the increasing addition of electrons into the 4f-orbitals. In contrast with 4f-orbitals (lanthanoids), 5f-orbitals (actinoids) seem to play an important role in coordination bonds.[2] However, the participation of the orbital $4f_{y(3x^2-y^2)}$ in the bonding role has been recently demonstrated by Lukens et al.[3] but its participation (in terms of energy) is not enough to expect changes. In consequence, it seems that the addition of electrons in 4f-orbitals should not modify the physicochemical properties of the formed compounds.

Concerning the general trends of lanthanides, although the participation of 4f-orbitals in the chemical bond is not expected, incrementing the number of electrons in these orbitals promotes differences in their cation sizes. Due to the low effectivity of f-electrons to shield the outer shell when the nuclear charge is increased, metal cations decrease in size when increasing the nuclear charge. In consequence, the radii of these metal cations are compressed between 103.2 and 86.1 pm (Table 3.1). The difference in cation size is directly observed in the metal coordination, allowing 11-coordinated compound to big cations while the smaller ones prefer 9-coordinated systems.[1] Consequently, LnF_3 present three stable crystalline phases: hexagonal, orthorhombic and cubic. From La to Sm is reported the preference of the hexagonal crystalline structure and from Eu to Lu the orthorhombic structure is the most reported.[4,5] The cubic crystalline structure is observed for YF_3 and for smaller cation-sized LnF_3 nanocrystals (NCs), which could also allow this crystallographic structure.[6]

After these considerations, we can conclude that the exchangeable role depending on the cation size allows the formation of different crystalline phases. Some modifications to study the behaviour of each lanthanide cation must be performed to extract periodical relation. The knowledge of these modifications is highlighted to design and apply the obtained LnF_3 NCs. If we examined the reported modifications performed in water following a co-precipitation method, some general trends could be extracted. Fluorinated precursors are claimed to tune the final crystalline structure,[7] the amount of stabiliser and the metal:stabiliser molar ratio seem to promote a preferential shape and also modify the size.[8–11] Finally, in some synthetic approaches, some lanthanide metals tend to aggregate forming big assembled systems.[12–14]

Table 3.1. Ionic radii of lanthanide elements and the most stable coordination number encountered for these cationic elements.[15]

11-Coordinated Cations		9-Coordinated Cations	
Cations	Size (ppm)	Cations	Size (pm)
La^{3+}	103.2	Sm^{3+}	95.8
Ce^{3+}	102.0	Eu^{3+}	94.7
Pr^{3+}	99.0	Gd^{3+}	93.8
Nd^{3+}	98.3	Tb^{3+}	92.3
Pm^{3+}	97.0	Dy^{3+}	91.2
		Ho^{3+}	90.1
		Y^{3+}	90.0
		Er^{3+}	89.0
		Tm^{3+}	88.0
		Yb^{3+}	86.9
		Lu^{3+}	86.1

In this chapter,[16] the synthesis and characterization of all non-radioactive LnF_3 NCs are stated, including YF_3, in a well-known synthetic approximation, the co-precipitation method with citrate as stabiliser. ESI-MS was used to unveil the precursor solution (metal-stabiliser) before the formation of the NCs. The mechanisms related to the use of a covalent or ionic fluorinating source were unravelled, as well as, the role played by an acidic media in the final obtained crystal phases. In addition, we found that crystal phase transformation is not directly related with the fluorinating agent.[7] We demonstrate that the pivotal parameter to achieve a determinate crystalline structure is the pH, normally induced by the fluoride source. We rationalised the formation of highly oriented rod-like mesocrystals depending on the crystalline structure using SAED images of single supraparticle. Finally, preliminary studies demonstrated that the shape of the obtained NCs affect directly the final colloidal solution, observing single NC dispersions or big assembled particles.

3.2 Experimental

3.2.1 Particle synthesis

❖ **Particle Synthesis. Standard Procedure:** Citric acid (2.25 mmol) in 16 mL of Milli-Q water was neutralised with tetramethylammonium hydroxide (6.75 mmol), followed by the addition of $Ln(CH_3COO)_3 \cdot H_2O$ (1.5 mmol), in a 50 mL round-bottomed flask equipped with a condenser, magnetic stirrer and heater. The initial solution was heated until 100 °C, then NH_4F (4.5 mmol) in 4 mL of Milli-Q water was injected dropwise. After 2 h of reaction, the final mixture was cooled down to room temperature. LnF_3 NCs were separated from the reaction medium by the addition of 10 mL of ethanol or acetone as non-solvent (depending on the used metal), followed by centrifugation at 10,000 rpm for 20 minutes. Separated NCs were re-dispersed in 20 mL Milli-Q water as solvent forming a room temperature stable dispersion.

❖ **Acidic method with fluoride injection:** $Ln(CH_3COO)_3 \cdot H_2O$ (1.5 mmol) in 16 mL of Milli-Q water was introduced into a 50 mL round-bottomed flask equipped with a condenser, magnetic stirrer and heater. The initial solution was heated until 100 °C, then HBF_4 (2.52 mmol) or $HClO_4$ (2.52 mmol) was injected followed by the dropwise addition of NH_4F (4.5 mmol) in 4 mL of Milli-Q water. After 2 h of reaction, the final mixture was cooled down to room temperature. LnF_3 NCs were separated from the reaction medium by the addition of 10 mL of ethanol as non-solvent, followed by centrifugation at 10,000 rpm for 20 minutes. Separated NCs were re-dispersed in 20 mL Milli-Q water as solvent.

❖ **Acidic method without fluoride injection:** $Ln(CH_3COO)_3 \cdot H_2O$ (1.5 mmol) in 20 mL of Milli-Q water was introduced into a 50 mL round-bottomed flask equipped with a condenser, magnetic stirrer and heater. The initial solution was heated until 100 °C, then HBF_4 (2.52 mmol) was injected. After 2 h of reaction, the final mixture was cooled down to room temperature. LnF_3 NCs were separated from the reaction medium by the addition of 10 mL of ethanol as non-solvent, followed by centrifugation at 10,000 rpm for 20 minutes. Separated NCs were re-dispersed in 20 mL Milli-Q water as solvent.

3.2.2 Characterisation

High-resolution Electrospray Ionisation Mass Spectrometry (ESI-MS) measurements were recorded from water solution in a BRUKER Apollo microTOF system (Bruker Daltonics GmbH, Bremen, Alemanya) with

electrospray ionisation, autosampling and equipped with an HPLC pump (Series 1100, Agilent Technologies) at the Servei d'Anàlisi Química at the UAB. Transmission electron microscopy (TEM) micrographs were obtained on a 120 kV JEOL 1210 TEM, which has a resolution point of 3.2 Å. High Resolution Transmission Electron Microscopy (HRTEM) micrographs were obtained on a 200 kV JEOL 2011 TEM, which has a resolution point of 1.8 Å at 200 kV. Samples for TEM analysis were prepared by spreading a drop of as-prepared NCs diluted dispersion on amorphous carbon-coated grids and then dried in air. Powder X-ray diffraction (XRD) patterns of the samples were recorded using a Phillips XPert diffractometer equipped with a two circle diffractometers and Cu tube. Infrared spectroscopy (IR) analyses have been carried out in the Servei d'Anàlisi Química with the Bruker spectrophotometer IR Tensor 27. Nuclear Magnetic Resonance (NMR) analyses were recorded with a Bruker Advance II 400 spectrometer in D_2O at 298 K. Samples for ^{1}H NMR were prepared by washing the colloidal solution five times before drying NCs. Finally, the powder was dispersed in D_2O. In the case of ^{11}B NMR, samples were lyophilised and then dispersed in D_2O. Freeze-drying was performed on a Telstar Lyoquest 80 freeze-dryer. Samples were first frozen at -80 °C in the same freeze-dryer, then dried at 0.05 mbar at room temperature for 24 hours.

3.3 Results and discussion

3.3.1 Particles

A set of fifteen LnF_3 NCs were synthesised with the aim to know if they present the same behaviour, as it is expected in coordination chemistry. We used a modified co-precipitation method[10] to achieve the fast, easy and reproducible synthesis of nanoscaled systems. Citrate was used to be one of the most reported NC stabiliser in aqueous media, allowing a biocompatible system.[17–19] In fact, biomedical applications based on citrate-stabilised NCs are of interest for their biocompatibility and their high water-stability.[20,21]

3.3.1.1 Precursor solution

Method consist of the dissolution of tetramethylammonium citrate and lanthanide (III) acetate in water, following a molar ratio metal:citrate of 1:1.5. Then, the system is heated up 100 °C, and finally ammonium fluoride is injected to start the nucleation step. To allow a homogeneous and reproducible synthesis, we need to be sure of the dissolution of all precursors before the nucleation step. To this aim, we performed Electrospray Ionisation with Mass Spectrometry (ESI-MS), identifying the precursors in our system

(see Figure 3.1 as example). A dynamic equilibrium between different coordination ionic complexes was observed, being the most abundant complexes (a), (b) and (c) showed in Scheme 3.1. To assess the presence of these complexes, we performed ESI-MS positive and negative to avoid the drawback of the ionisation process and to ensure the presence of complexes at both ionisation charges.
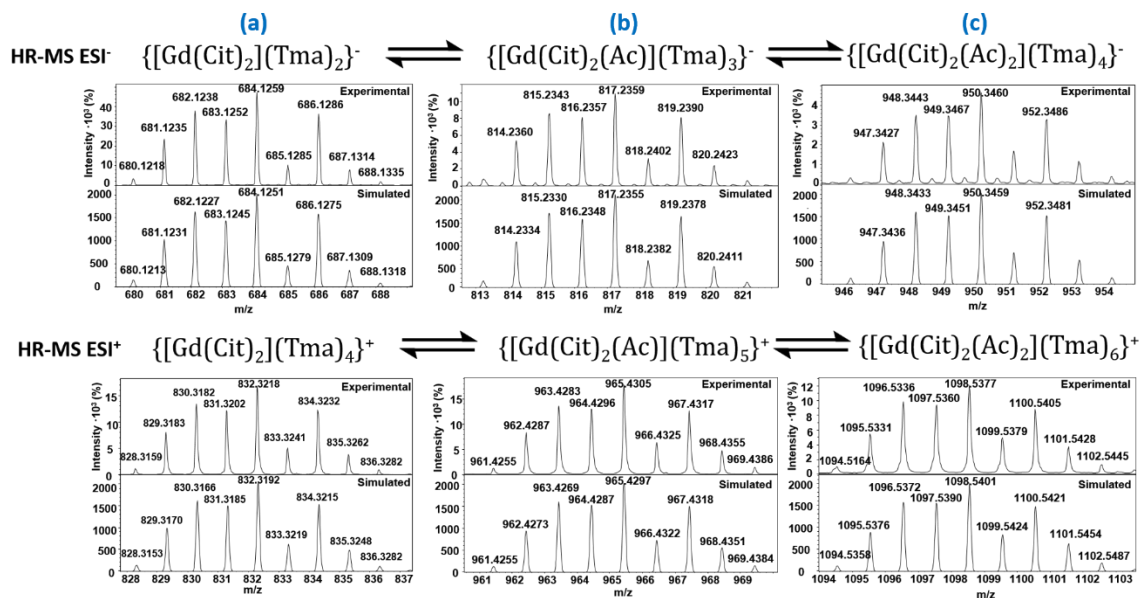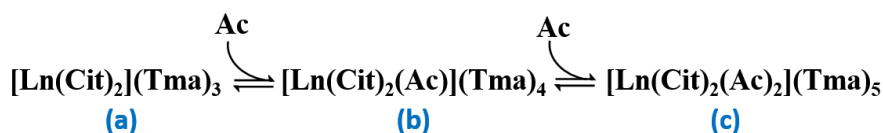

Figure 3.1. As an illustration, negative and positive HR-MS ESI of the precursor solution formed with gadolinium (III) acetate and tetramethylammonium citrate. Here, complexes are assigned as identified in the MS, to clarify we note the assignation of (a), (b) and (c) compounds.

This technique was performed to Gd and Y complexes (see SI for all ESI-MS spectra), allowing the match between these two-precursor solutions. However, due to the different coordination of lanthanide cations depending on the radius size, we expect ionic complexes with a higher coordination number for the first lanthanides in de series, those with big cation size. Interestingly, in Scheme 3.1 is observed the lability of acetate in contrast with the stability of citrate in the most abundant complexes.

Scheme 3.1. Dynamic equilibrium between the different observed species in ESI-MS. Ln is the lanthanide (Ln³⁺), Cit is citrate anion ($C_6H_5O_7^{3-}$), Tma is tetramethylammonium cation ($C_4H_{12}N^+$) and Ac is acetate anion ($C_2H_3O^{2-}$).

$$\text{[Ln(Cit)}_2\text{](Tma)}_3 \xrightleftharpoons{\text{Ac}} \text{[Ln(Cit)}_2\text{(Ac)](Tma)}_4 \xrightleftharpoons{\text{Ac}} \text{[Ln(Cit)}_2\text{(Ac)}_2\text{](Tma)}_5$$

(a)   (b)   (c)

After the injection of ammonium fluoride and a reaction time of 2 h, formed NCs were washed with the help of a non-solvent (acetone or ethanol) to remove the excess of free ions.

3.3.1.2 LnF₃ NCs

Obtained NCs show a variety of sizes and shapes depending on the used metal and their position in the lanthanide series (Figure 3.2). In Table 3.2, we try to summarise the size of NCs obtained by Transmission Electron Microscopy (TEM) histograms and the behaviour observed in TEM (e.g. NCs, supraparticles, …). To complete the table, the results of the X-Ray Diffraction (XRD) technique (see Figure 3.2 in section 3.3.2) are also shown, as well as, Scherrer size and observed crystalline structure.

Table 3.2. Information of the NCs by the standard methodology. Size by histograms in TEM and Scherrer equation using XRD obtained patterns (see section 2.3.2 Crystalline structure). Observed crystalline structure and behaviour of the final colloidal suspensions by TEM. NCs are ordered by their metal cation radii from bigger to smaller one.

	TEM size (nm)		XRD		NCs
NCs	Length	Width	Scherrer (nm)	Crystalline Structure	Behavior
LaF_3	8.2 ± 1.8	2.2 ± 0.5	5.4	Hexagonal	Hexagonal nanoplatelets
CeF_3	7.6 ± 2.3	2.4 ± 0.5	6.6		
PrF_3	8.8 ± 1.6	3.4 ± 0.8	4.7		
NdF_3	43 ± 5	-	5.2		Spherical supraparticles
SmF_3	151 ± 13	-	11.1		
EuF_3	346 ± 96	103 ± 22	8.0	Orthorhombic and Hexagonal	Rod-like supraparticles
GdF_3	469 ± 51	128 ± 15	10.1		
TbF_3	137 ± 11	-	17.8	Cubic	Spherical supraparticles
DyF_3	130 ± 10	-	12.8		
HoF_3	105 ± 12	-	9.4		
YF_3	83 ± 13	-	7.4		
ErF_3	107 ± 12	-	7.6		
TmF_3	58 ± 8	-	6.2		Star-like spherical supraparticles
YbF_3	90 ± 12	-	6.1		
LuF_3	72 ± 12	-	5.7		

Considering the observed behaviours of the obtained NCs, we can arrange them into three different general groups: (i) hexagonal nanoplatelets, (ii) spherical supraparticles (formed by self-assembly of small NCs) and (iii) rod-like supraparticles.

First group (i) is formed by LaF₃, CeF₃ and PrF₃, which show the homogeneous dispersion of single hexagonal nanoplatelets, observed in TEM and DLS. They have a size of ~8 nm in length with a width of ~3 nm, showing these nanoplatelets with a clear hexagonal habit. Group (ii) presents some spherical self-assembled particle organisations, which is formed by NdF₃,
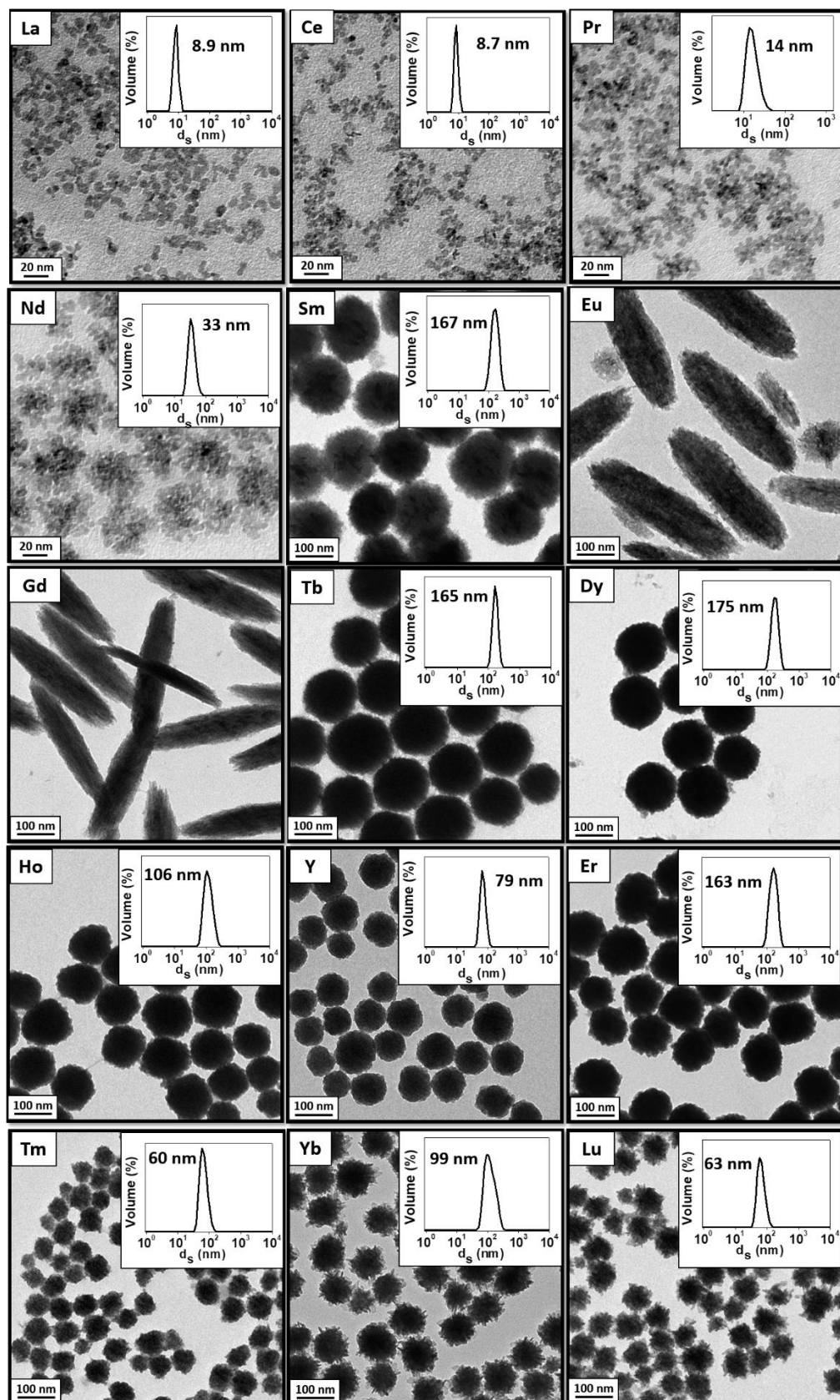
Figure 3.2. TEM and DLS of synthesised LnF₃ particles at 100 °C in a co-precipitation method. All LnF₃ images are ordered from left to right considering their cation size. From La to Nd, scale bar of 20 nm (50,000 mag.) while the rest have a scale bar of 100 nm (15,000 mag.).

SmF_3 and from TbF_3 to LuF_3, being the last ones (TmF_3, YbF_3 and LuF_3) star-like spherical supraparticles. This star-like shape seems to be formed by preferential organisation onto the surface of worm-like NCs located perpendicular to the surface. Finally, group (iii) is composed by EuF_3 and GdF_3, formed by the organisation of small NCs in supraparticles showing a rod-like shape. Group (ii) and (iii) are formed by the assembly of small NCs into supraparticles allowing big homogeneous systems, while group (i) prefers the formation of single faceted NCs.

We try to rationalise the observed groups considering two key factors: (i) the size of the metal cation and (ii) the final shape of the NCs. (i) The radii of the metal cations are claimed to affect directly the crystalline structure, metal coordination and hence the final behaviour of NCs.[22,23] Concerning factor (ii), the shape of the NCs could affect the selective distribution of organic molecules of the NC shell. This effect could promote or avoid the different chemical interactions between NCs, stabilising them electrostatically hampering the aggregation or promoting the formation of self-assembled systems. In our systems, we found that the presence of a big metal cation forms single LnF_3 hexagonal nanoplatelets without aggregation. The final shape seems to be consequence of their hexagonal crystalline structure. In addition, their faceting seems to be able to avoid self-assembly to big supraparticles. When metal cation decreases in size, also decrease the faceted shape forming spherical NCs, promoting the aggregation. In consequence, we obtained big assembled systems formed by the interaction of small particles.

3.3.1.3 Molar ratio study

The molar ratio metal:stabiliser is the common studied parameter to optimise the synthesis in nanoscaled systems. High amounts of stabiliser are attributed to a decrease in the final size of obtained NCs, due to the presence of an excess of capping agent to stabilise NC surface, hampering the growth.[10] However, we found that, in our system, we have two different effects when modifying molar ratio, depending on the studied NCs. We chose LaF_3 NCs and YF_3 supraparticles to perform this study because La represents the 11-coordinated group and Y is the representative element of 9-coordination group. In addition, LaF_3 forms single dispersed nanocrystals while YF_3 forms self-assembled NCs in a spherical shape.

After the synthesis of these NCs in molar ratios metal:citrate of 1:3 and 1:5, we found that in the case of LaF_3 NCs, there are not difference between these new synthesis and those performed at 1:1.5 metal:citrate molar ratio (Figure 3.3A and 3.3B). However, when the same approximation is performed with YF_3 supraparticles, we observe that at a molar ratio 1:3 we obtained the same kind of supraparticles, but if we used higher molar ratios 1:5

metal:citrate, we observed bigger assembled particles (~200 nm), compared with those obtained with a molar ratio of 1:1.5 and 1:3 (~ 80 nm).
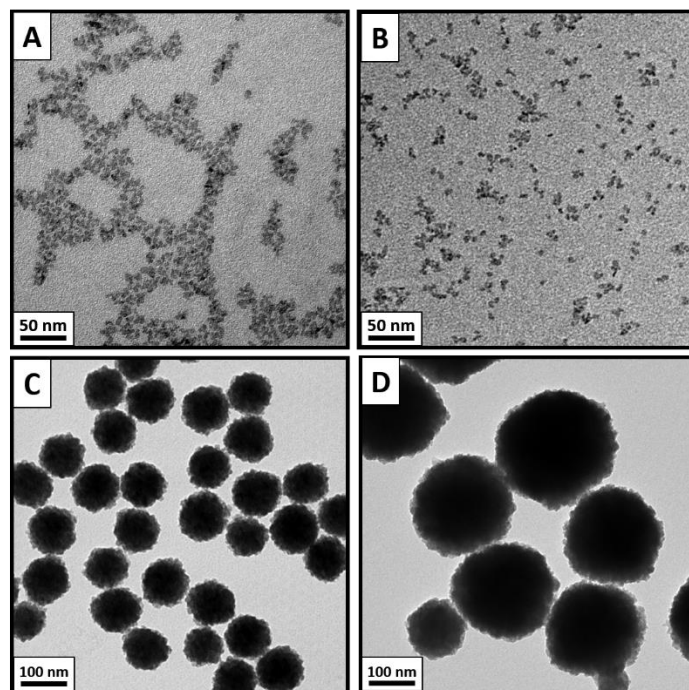

Figure 3.3. TEM of LnF₃ particles at 100 °C in a co-precipitation method using different molar ratios. LaF₃ at (A) 1:3 and (B) 1:5 metal:citrate molar ratios and YF₃ at (C) 1:3 and (D) 1:5 metal:citrate molar ratios.

After this study, we can conclude that the modification of the molar ratio metal:citrate has not effect in those metals that form NC dispersions (LaF₃, CeF₃ and PrF₃). However, if we work at high molar ratios metal:citrate in those NCs that form spherical assemblies, we observed an increase of their size. This effect could be rationalised with the ionic strength of the medium, affecting directly the surface chemistry and hence promoting the formation of big assembled systems. In addition, the presence of more citrate in the system with the high ionic strength could promote citrate mediated interactions increasing the size of the self-assembled particles.

In all synthesis, we chose a molar ratio metal:citrate of 1:1.5 for two main reasons: (i) the observed behaviour if we increase this molar ratio in the supraparticles systems and (ii) considering that metal citrate precursors start to be soluble in water at this molar ratio.[24]

3.3.2 Crystalline structure

After the TEM and DLS analysis, all samples were dried to perform the XRD patterns to know if the crystalline structure is directly related with the

different observed behaviours by TEM. The most common crystalline structures were detected (Figure 3.4). Hexagonal crystalline structure from LaF_3 to SmF_3, the pure cubic structure from TbF_3 to LuF_3 and a mixture of hexagonal and orthorhombic crystalline structures for EuF_3 and GdF_3.
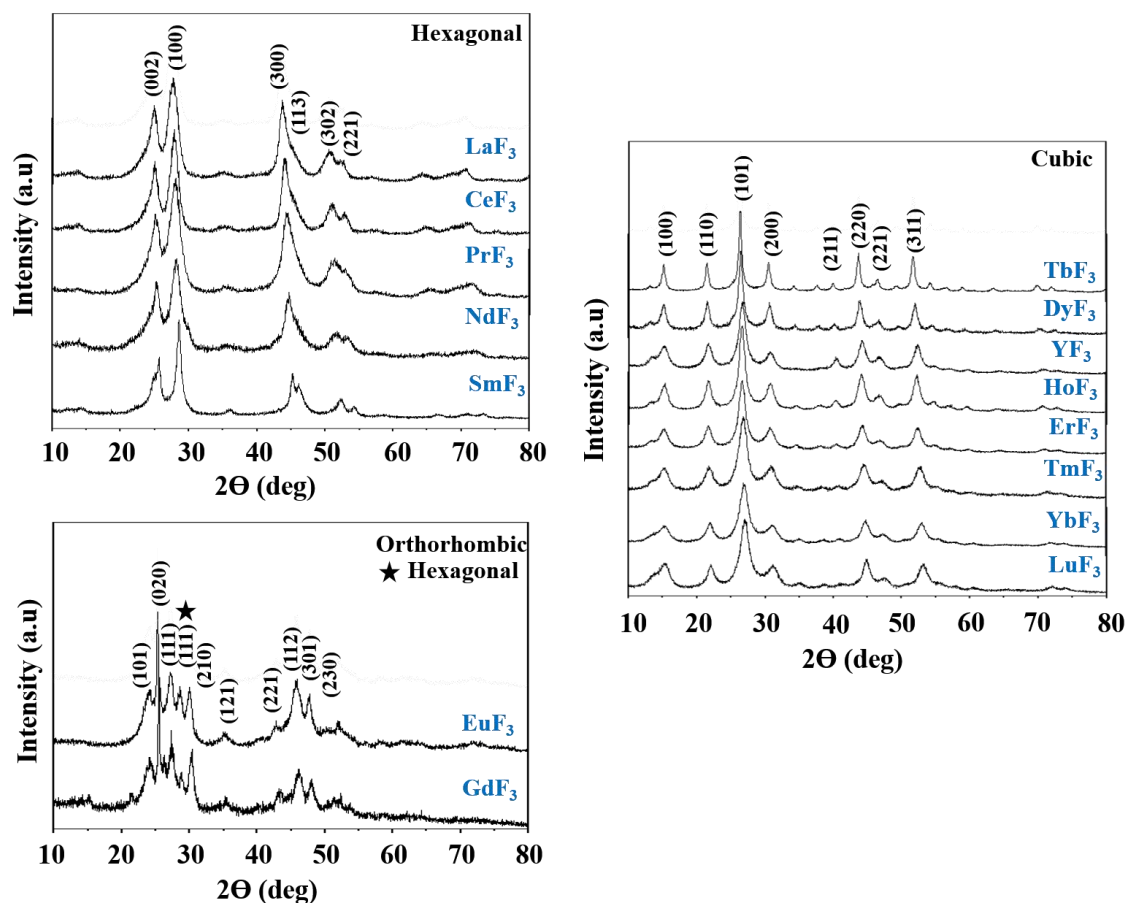

Figure 3.4. XRD patterns obtained for each LnF_3 NC in their powder form. To summarise, diffractograms show the assignation of principal peaks considering the structure that the NCs present. The star in EuF_3 and GdF_3 shows the main peak of their hexagonal structure, the other peaks are overlapped with the orthorhombic structure. Reference patterns: (04-007-2483), (00-032-0483), (00-008-0045), (00-046-1167), (00-009-0416), (00-032-0373), (00-033-0542), (04-006-9968) and (00-012-0788) from the International Centre for Diffraction Data. All cubic structures were identified as isostructural with YF_3 cubic pattern and assigned with this card.

We could observe the effect of the cation radii, which modify progressively the crystalline structure from hexagonal (big cations) to cubic (small cations). Nevertheless, for the intermediated metals, we found a mixture of hexagonal and orthorhombic structures, the most stable for LnF_3 compounds.[4] In addition, they can adopt different structures depending on the synthetic conditions (e.g. ions present in the synthesis).[8] Finally, in our case we found that the cubic structure is the most stable for the smaller cations, instead of the orthorhombic ones. We postulate that the formation of

rod-like shape in supraparticles of EuF_3 and GdF_3 is promoted by the presence of orthorhombic crystalline structure because these are the unique elements adopting this structure and this shape. Concerning our preliminary hypothesis, we can conclude that the crystalline structure is not directly responsible of the formation of assembled systems. Although, the cubic structure forms aggregated NCs in all cases, we found single particles (LaF_3) and aggregated assemblies (SmF_3) with the hexagonal crystalline structure.

3.3.3 Effect of the pH

Once the size, shape and crystalline structure of LnF_3 NCs were unravelled, we want to know if pH modifications during the synthesis could allow any change in these parameters. To perform this test, we used HBF_4 as acid and possible fluorinating source. The new methodology consists of using tetrafluoroboric acid instead of tetramethylammonium citrate following the acidic method with fluoride injection described in the section 3.2.

Firstly, we want to prove what happens when we synthesise hexagonal-faceted NCs in acidic conditions. CeF_3 and NdF_3 were selected as representative compounds of those crystallised in the hexagonal structure due to, they present intermediated cation radii. After the synthesis, CeF_3 (Figure 3.5A) are formed by a homogeneous dispersion of hexagonal nanoplatelets of ~50 nm in size, showing the corresponding hexagonal crystalline structure. In addition, NdF_3 (Figure 3.5B) are also obtained in a hexagonal nanoplatelet shape of hexagonal-faceted NCs in a range of ~50 nm. Both particles show the same behaviour and size, although in the standard synthesis one presented hexagonal shaped nanoplatelets (CeF_3) and the other one spherical supraparticles (NdF_3). This effect means that acidic conditions allow the achievement of a high-faceted NCs, in consequence we obtained both NCs in the typical hexagonal habit expected by NCs in the hexagonal crystalline structure.

Considering the size of the obtained NCs following the standard method and the acidic method with ammonium fluoride injection, we postulated that citrate anion is better stabilising agent than BF_4^- anions. Working with citrate, particles have a size of ~8 nm while with tetrafluoroboric acid they growth until ~50 nm. Concerning the stability of these NCs in water, while the ones obtained by the standard method (Figure 3.2) show stabilities of months, those obtained with acidic method with ammonium fluoride injection (Figure 3.5) are stable during few days.
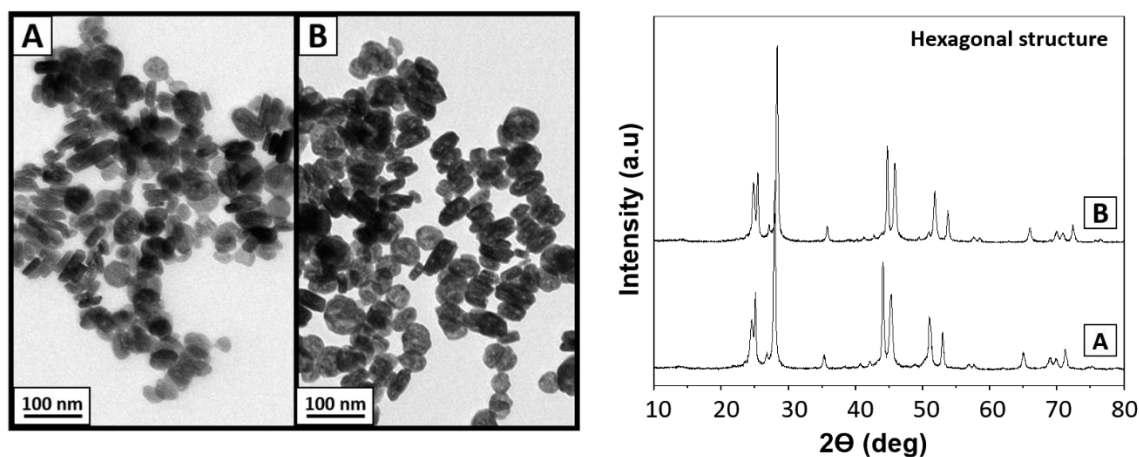
Figure 3.5. TEM and XRD of obtained NCs using the acidic method with ammonium fluoride injection. CeF₃ (A) and NdF₃ (B) hexagonal nanoplatelets in their hexagonal crystalline structure. All TEM images have the same scale bar.

Concerning the NCs obtained in their cubic crystalline phase using the standard method. We also want to test the effect of the pH in these NCs using the acidic method with ammonium fluoride injection. In this case, we used YF₃, DyF₃ and YbF₃ as representative elements of this group. In contrast with NCs in the hexagonal phase, here we observed that cubic NCs (standard method) are obtained in a rod-like shape and orthorhombic structure if they are synthesised under acidic conditions (Figure 3.6).
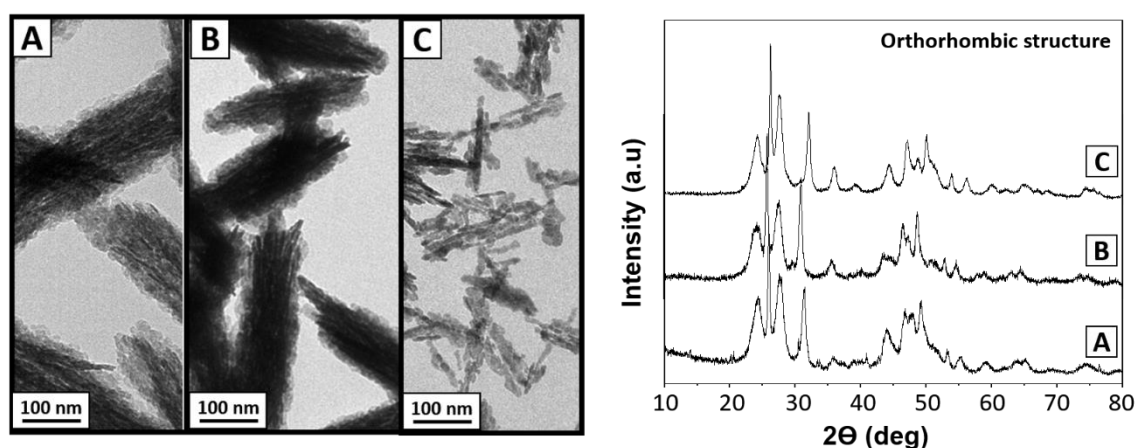

Figure 3.6. TEM and XRD of obtained NCs using the acidic method with ammonium fluoride injection. YF₃ (A), DyF₃ (B) and YbF₃ (C) rod-like NCs in their orthorhombic crystalline phase. All TEM images have the same scale bar.

All three NCs are shown in a rod-like shape with the orthorhombic structure, as in the case of EuF₃ and GdF₃ using the standard method. This means that the orthorhombic phase promotes the ordered self-assembly in a rod-like shape. In addition, we observed as the cubic structure is not stable in acidic condition,[25] obtaining the orthorhombic one in smaller metal cations.

In acidic conditions, the most stable reported crystalline structures (hexagonal and orthorhombic) seem to be the preferred for LnF$_3$ NCs. Concerning the stability of these new rod-like NCs, we observe a less-stable particles than those synthesised by standard method, confirming again the necessity of a strong capping agent to stabilise our system (e.g. citrate anions).

As BF$_4^-$ is also reported as a fluorinating source,[7,26] we want to investigate the effect of using an ionic (NH$_4$F) or covalent (HBF$_4$) source of fluoride ions. To do this, we use the acidic method without the injection of ammonium fluoride. In other words, the use of metal (III) acetate and tetrafluoroboric acid as unique reactants. This test was performed in CeF$_3$ and YF$_3$ obtaining the same results as in the case of ammonium fluoride injection (Figure 3.7A and 3.7B).
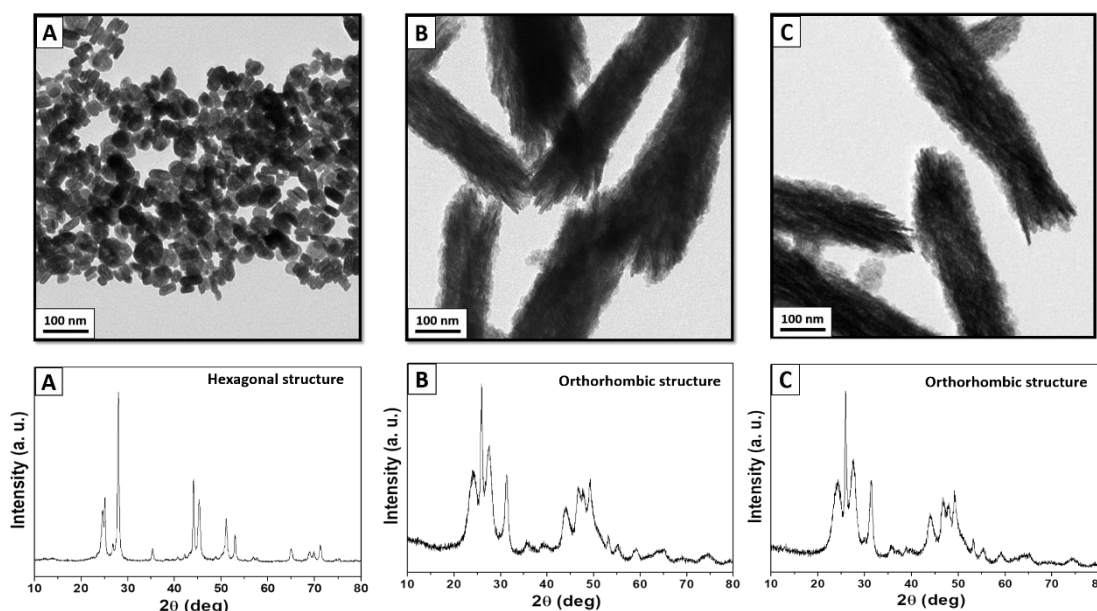

Figure 3.7. TEM and XRD of obtained NCs using the acidic method without ammonium fluoride injection: CeF₃ (A) and YF₃ (B) NCs. In addition, it is shown the TEM and XRD of YF₃ supraparticles synthesised with HClO₄ as acid and NH₄F as fluorinating agent (C). All TEM images have the same scale bar.

Finally, to discard the effect of BF$_4^-$ anions in the preferential crystalline structure formation, we performed the last approximation based on the use of HClO$_4$ instead of HBF$_4$ as acid and with the injection of NH$_4$F as F$^-$ source. The formation of rod-like YF$_3$ supraparticles in their orthorhombic phase (Figure 3.7C) confirms that what is responsible for the crystalline phase transformation is not directly the fluorinating agent. The pH is highlighted to promote the achievement of cubic or orthorhombic crystalline structures.

We also want to know the mechanisms governing these two acidic methodologies to assess the fluoride sources. In the literature,[27] we found the complete hydrolysis of tetrafluoroboric acid in water. Considering the different species of boron depending on the hydrolysis, ^{11}B NMR is an excellent approximation to study accurately these mechanisms.

$$HBF_4 + H_2O \rightleftharpoons HBF_3OH + HF \qquad\qquad 3.1$$

$$HBF_3OH + 2\ H_2O \rightleftharpoons B(OH)_3 + 3\ HF \qquad\qquad 3.2$$

When ammonium fluoride is used as fluorinating agent, we observed the presence of HBF_4 and HBF_3OH in the ^{11}B NMR spectrum (Figure 3.8A), due to the stability of the HBF_3OH species and only a 2% of $B(OH)_3$ was encountered from the complete hydrolysation. The addition of ammonium fluoride into the system avoids the complete hydrolysis of tetrafluoroboric acid and bring enough fluorides to achieve NC synthesis.
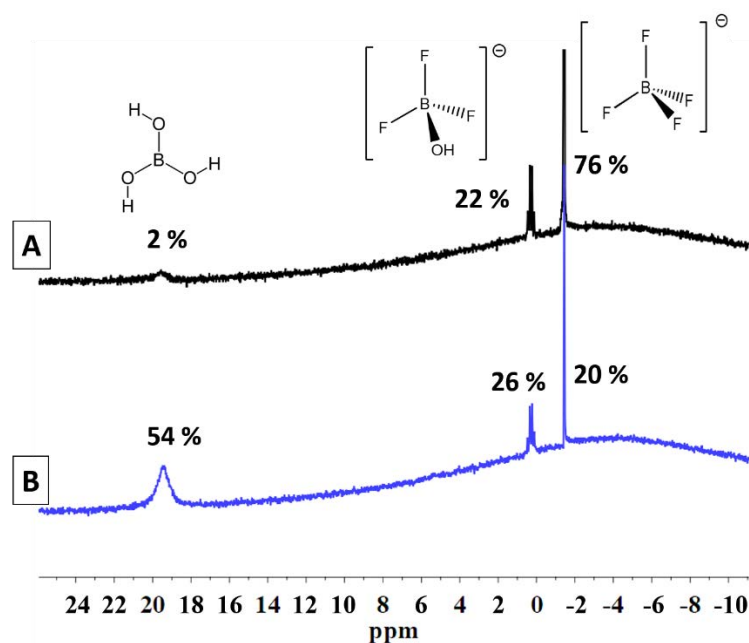

Figure 3.8. ^{11}B NMR of lyophilised YF₃ samples after their synthesis with the acidic methodology using (A) HBF₄ and NH₄F as fluorinating precursors and (B) only using HBF₄.

In contrast, if none additional source of fluoride is introduced into the system (Figure 3.8B), tetrafluoroboric acid hydrolyse completely to boric acid (54%), following reaction 3.1 and 3.2, to contribute to the formation of the NCs by the release of HF. In normal conditions, considering the high stability of HBF_3OH, the formation of $B(OH)_3$ and HF are not promoted by the low displaced 3.2 equilibrium. However, the stability and insolubility of formed LnF_3 displace these equilibria to obtain all the HF necessary to achieve the NCs.

To explain this pH effect (the difference observed in crystalline phase), we postulate an approximation concerning the nature of the first produced seeds in the colloidal solution. When the synthesis is carried out under acidic conditions, lanthanide cations are in their $[Ln(H_2O)_x]^{3+}$ form before the achievement of LnF$_3$. In consequence, acidic medium produces orthorhombic and hexagonal LnF$_3$ NCs, the most stable thermodynamic structures, depending on the metal cation size as we explained before. When NCs are synthesised following the standard method, the pH of the medium is few greater than 7 (by the effect of dissolved ions). At this pH range, the formation of the cubic form of Ln$_2$O$_3$ is promoted forming the first nucleation seeds (kinetic product). After the addition of the fluoride source, the high excess of F$^-$ in the medium, compared with the amount of OH$^-$, allows the formation of LnF$_3$ (thermodynamic product).[28] Seeds of Ln$_2$O$_3$ could predetermine the cubic nature of LnF$_3$, only observed in neutral-basic conditions. The high excess of fluorides in the media, as well as, the insolubility of LnF$_3$ compounds could promote ionic exchanges (substituting O^{2-} by F$^-$) in the first obtained seeds maintaining the crystalline structure adopted by the cubic Ln$_2$O$_3$.[29,30]

3.3.4 Are supraparticles preferentially oriented?

We found that the assembled particles are organised in two main shapes (spherical and rod-like). We want to know if there is a preferential orientation in these supraparticles to understand the mechanism governing these assemblies. We used Selected-Area Electron Diffraction (SAED) of a single supraparticle to see if we observe ordered spots (organised supraparticles) or several spots distributed in circles around the middle with a radius corresponding to the d-spacing of each plane (random NC distribution). Spherical YF$_3$ supraparticles obtained by the standard method shows a SAED pattern (Figure 3.9A) corresponding to a random distribution of NCs into the spherical supraparticles. This evidence agrees with the conclusions obtained in Chapter 2, spherical supraparticles are promoted by the randomly oriented formation of citrate ionic bridges.

Although, we do not observe only rings (pure-random distributed NCs), we need to take into account that we are analysing one single supraparticle and the presence of several spots around circles is considered random distributed NCs.
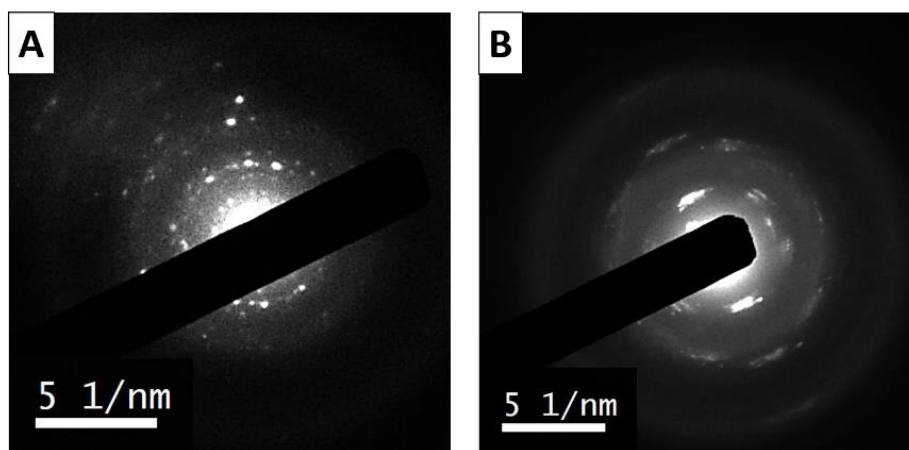
Figure 3.9. SAED by TEM of a single supraparticle of (A) YF₃ spherical supraparticles obtained by standard method and (B) YF₃ obtained by acidic method (HBF₄) with ammonium fluoride.

If we analyse YF$_3$ rod-like supraparticles obtained by the acidic method (using HBF$_4$) with the injection of ammonium fluoride, we observe more ordered SAED pattern composed by spots (Figure 3.9B). This means that the presence of orthorhombic structure or the influence of the pH promote the orientation of NCs in a more ordered supraparticle.

To avoid the effect of the pH, we performed the same study in EuF$_3$ rod-like supraparticles obtained with the standard method. In this case, we analyse also the SAED pattern to know the growth direction of these rods. In Figure 3.10A is shown the image of a single rod-like particle with its SAED pattern. This is a clear example of a highly-ordered NC assembly due to the presence of single spots with defined planes. We simulate the crystalline structure with the three detected planes: (101), (212) and (131) using VESTA software. Detected planes are compatible with electron beam in [101] direction, this was concluded with the cross product of identified planes in SAED pattern. In consequence, growth direction of this rod is the [010] (Table 3.3), considering also SAED analysis of single rods showed in Figure 3.10B and 3.10C.

From these results, we postulate the so-called mesocrystals, an ordered superstructure formed by crystalline NCs with external crystal faces in a scale between hundred nanometres to micrometres.[31] Among the different proposed formation mechanisms of mesocrystals, we postulated a kind of NC alignment by face selective molecules. This mechanism could summarise the behaviour of all obtained LnF$_3$ NCs and their assembled particles depending on the shape of the NC. Particles are interacting between them by ionic interactions due to their high fluoride-cation affinity onto the surface.[32] In high symmetric cubic NCs, this interaction is promoted in all directions allowing spherical assembled systems. However, in orthorhombic NCs the interaction by [010] direction is enhanced due to the high fluoride-cation

interaction, making a selective organisation allowing rod-like supraparticles in the standard synthesis (NH_4^+ promoted interaction) and in acidic method (H_3O^+ mediated interaction), following ionic interactions.
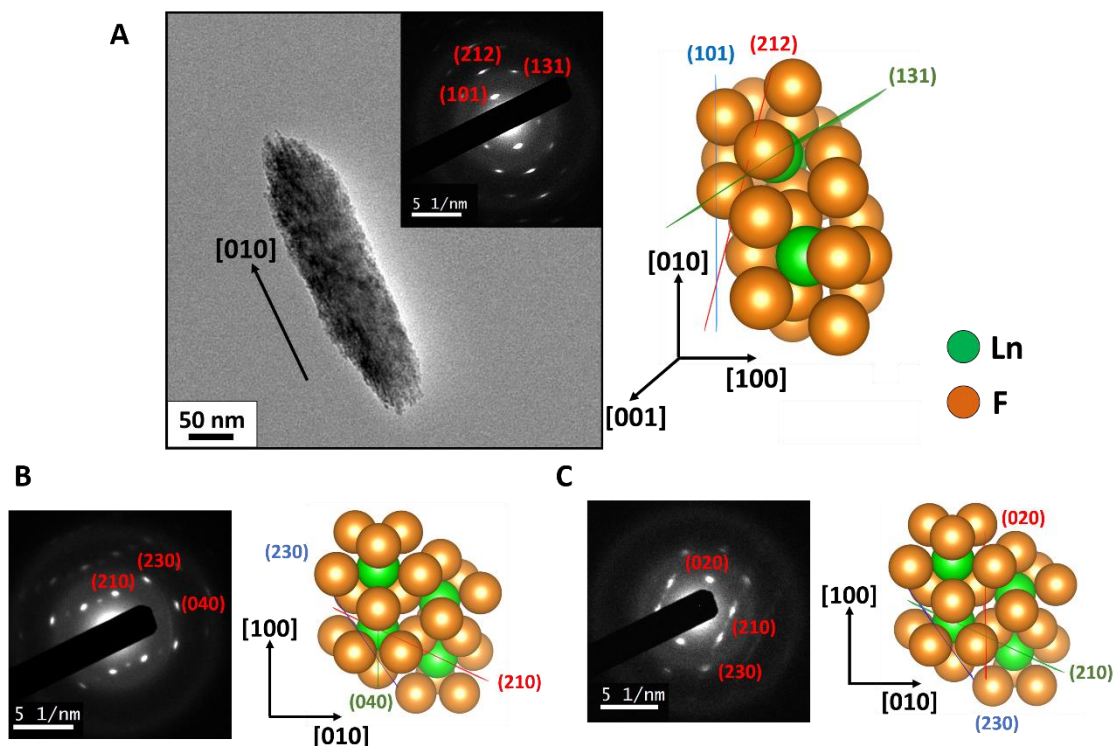

Figure 3.10. Example of some EuF₃ rod-like supraparticle with its respective SAED and the observed planes. At the right of SAEDs, the representation of orthorhombic crystalline structure, made with VESTA software, with the planes found in SAED pattern.

Table 3.3. Planes observed in SAED patterns of the different indexed images with their cross products, direction family and electron beam direction.

	Figure 3.10A	Figure 3.10B	Figure 3.10C
Observed planes	(101), (212) and (131)	(230), (040) and (210)	(020), (230) and (210)
Cross products	(101) x (212) = [$\bar{1}$01] (101) x (131) = [$\bar{3}$03] (131) x (212) = [$\bar{5}$05]	(230) x (040) = [00$\bar{8}$] (230) x (210) = [00$\bar{4}$] (040) x (210) = [00$\bar{8}$]	(020) x (230) = [00$\bar{4}$] (020) x (210) = [00$\bar{4}$] (230) x (210) = [00$\bar{4}$]
Direction family	<101>	<001>	<001>
Electron beam	[101]	[001]	[001]

3.3.5 Shape and preliminary surface chemistry image

After the modifications to study the crystalline structure dependence, we try to identify the surface insights. Combining NMR analysis and HRTEM

images, we will be able to know if the different behaviour of the particles (NCs or supraparticles) is related with the organic attached onto the surface.

^{1}H NMR spectroscopy was performed to those NCs with a diamagnetic behaviour (LaF$_3$ and YF$_3$). Note that in addition of their paramagnetic behaviour, La and Y are the representative elements of the two-different coordination and La shows NCs dispersions while Y forms big assembled particles. Although in Chapter 2, we did not find significant differences between YF$_3$ NCs and supraparticles, here we want to compare YF$_3$ supraparticles with LaF$_3$ NCs. Both spectra show the presence of tetramethylammonium, citrate and acetate (Figure 3.11). We conclude that the ions are attached onto NC surface, due to their broad signals and their different chemical shifts. Citrate should present different chemical shifts depending on at which metal it is attached, as in the case of acetate. In the square of the Figure 3.11 it is shown the comparison between citrate-La and citrate-Y signals, showing different chemical shifts, as well as, different behaviour in the broad signals.
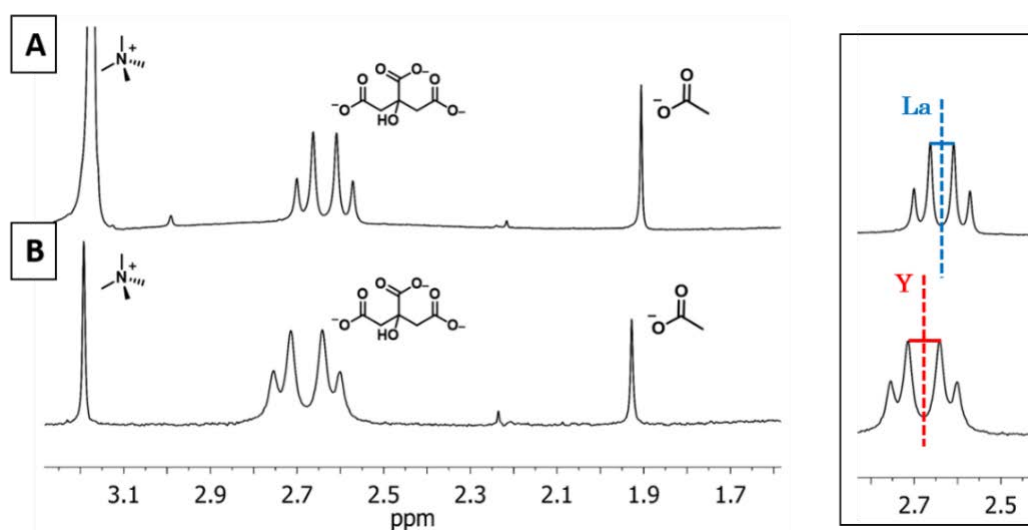

Figure 3.11. ^{1}H NMR of the synthesised (A) LaF$_3$ NCs and (B) YF$_3$ supraparticles, washed five times before their redispersion in D$_2$O. In addition, it is shown the chemical shift comparison between citrate-metal signals in both cases.

We observed citrate-Y signal at lower fields than citrate-La signal, this is because both metals have the same charge but different cation size. As Y is smaller produce more shift to citrate signal in NMR and a broader signal compared with citrate-La signal. From ^{1}H NMR results, we can postulate the same surface composition in both NCs and expand this conclusion to NCs and supraparticles. As the images of the surface chemistry seem to be similar in all NCs, we need to see the shape of the NCs to know if a different surface chemical distribution is possible depending on the metal.

HRTEM was performed to know the NC shape in the three observed groups described in the standard method: (i) hexagonal nanoplatelets, (ii) spherical supraparticles and (iii) rod-like supraparticles. We select LaF_3 of group (i), YF_3 of group (ii) and EuF_3 of group (iii). In addition, due to the spherical assembly obtained by NdF_3 and SmF_3, we decided to perform HRTEM to these samples to understand why NCs with hexagonal crystalline structure tend to form spherical assemblies. We found that LaF_3 shows a hexagonal faceted NC dispersion (Figure 3.12A) while YF_3 and EuF_3 show spherical crystalline NCs. From these observations we can conclude that big assembled particles are formed by the organization of small spherical NCs (Figure 3.12B and 3.12C).

Concerning to those spherical supraparticles formed by NCs in their hexagonal crystalline structure, HRTEM images did not reveal evidences of the presence of hexagonal nanoplatelets neither faceted NCs. Although, we should expect the formation of hexagonal faceted NCs because of their hexagonal crystalline structure, we found spherical NCs (Figure 3.12D and 3.12E). This could mean that at this conditions NdF_3 and SmF_3 form non-defined NCs that are considered spherical by HRTEM.
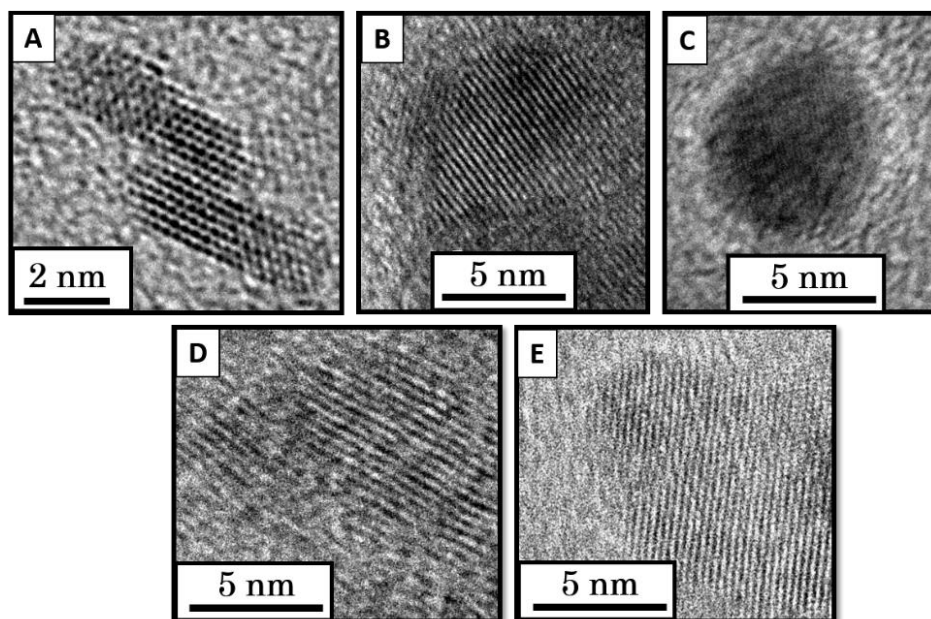

Figure 3.12. HRTEM of (A) single LaF_3 NCs, (B) single NC of YF_3 supraparticles system, (C) a spherical NC of EuF_3 rod-like supraparticles, (D) single NC of NdF_3 assembled system and (E) a spherical NC of SmF_3 spherical supraparticle.

With the obtained results, we postulate that hexagonal shape NCs avoid supraparticle formation by their two exposed faces while spherical NCs tend to organize themselves to form high stable supraparticle systems. As surface characterisation shows the same ions attached onto NC surface, we postulate

that the different behavior of the exposed faces allows the preferential attachment of the ions in one plane instead of the other one. In contrast, the spherical behavior of the rest of metals with the random coordination of the ions could allow ionic interactions easily between NC surfaces, producing these assembled systems.

3.3.6 General role in LnF₃ NCs

After the overview of all-LnF₃ NCs, we found that these particles cannot be considered with similar behaviours. In Scheme 3.2 is shown a graphic summary of the most important trends unravelled here.

Firstly, we found that there are two general behaviour in these particles: (i) the formation of big assembled particles (spherical o rod-like) and (ii) the formation of single NCs dispersion by hexagonal-faceted particles.

Metals in blue, those included in group (i), show aggregated particles by the self-assembly interaction mediated by ionic citrate bridges as shown in Chapter 2. Here, we rationalise as the detailed mechanism described by YF₃ (and postulated to SmF₃, EuF₃ and LuF₃) is extensive to all metal in blue showed in Scheme 3.2.

Scheme 3.2. Summary of the obtained results in this chapter showing the two different uncovered behaviours. NC formation (promoted by green elements) shows a hexagonal faceted shape while supraparticles (denoted as blue elements) are formed by the self-assembly of spherical shape NCs.
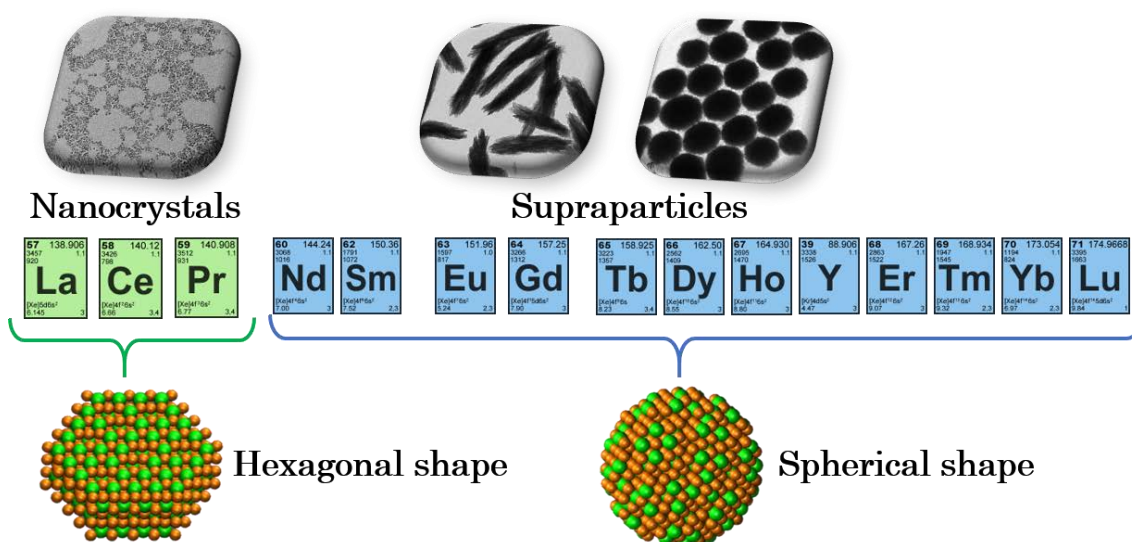
Concerning group (ii) of hexagonal nanoplatelets dispersions (metals in green), we saw clearly that these NCs do not form big assembled particles. We postulated that their two exposed faces avoid the aggregation in big NCs

compared with those with spherical shape. Is the hexagonal shape directly responsible of the non-aggregation of these NCs? Have we any ligand-surface interaction avoiding the aggregation? The insights of these particles and the mechanism responsible to stabilise these NCs are accurately described in Chapter 4.

3.4 Conclusions

In this chapter,[16] we investigated the synthesis and behaviour of all LnF₃ NCs, postulating the general rules concerning these kinds of compounds. Metal cation size has been stated as the key factor to englobe each lanthanide in a defined crystalline structure. We obtained high-crystalline and homogeneous LnF₃ dispersions in NC or supraparticle forms. The crystalline structure and the crystal habit have been tuned in a set of particles via an easy pH modification.

The effect of a strong acid during the synthesis was stated to play a crucial role in the reaction mechanism to form different crystalline phases. We found that LnF₃ NCs, which have hexagonal crystalline structure, could be obtained with a pure hexagonal shape if they are synthesised with the presence of strong acid. However, if the reaction is carried out in a neutral condition, only the first three lanthanides (La, Ce and Pr) show the hexagonal shape. In contrast, cubic structure was only allowed in neutral conditions, while orthorhombic was the stable in acidic conditions for small cation-sized lanthanides (from Tb to Lu). Cross-border elements, Eu and Gd, show a mixture of hexagonal and orthorhombic structures due to their polymorphic behaviour produced by their frontier cation sizes.

Citrate is stated as high-effective stabiliser because of, all-LnF₃ colloidal solution synthesised in the presence of this polydentate carboxylic ion, show more stability than their analogous without it.

The pH modification allows us to obtain LnF₃ NCs with different sizes, shapes and crystalline structures making them suitable for a wide range of applications. The influence of the acidic medium was also stated to tune the crystalline structure. The use of ionic or covalent (NH₄F or HBF₄) fluorinating precursors show the same results, although the mechanism involved is different. The use of NH₄F hampers the hydrolysis of HBF₄ while if HBF₄ is used as fluorinating agent and acid, this is forced to hydrolyse to B(OH)₃ and HF to obtain the final LnF₃ NCs.

The final surface study reveals the presence of the same organic ions attached to NC surface in single NCs and assembled particles. Due to, the

different shape of LnF$_3$ NCs, we postulate that the hexagonal-shape NCs avoid the aggregation by their two different exposed faces. In the case of spherical NCs, they tend to aggregate following a surface-surface interaction mechanism that it seems to be related to their spherical shape.

Two different behaviours were uncovered:

- ❖ Single hexagonal nanoplatelets dispersions (biggest metal cations).
- ❖ Spherical and rod-like supraparticles (smallest and cross-border metal cations).

3.5 References

[1]   F. A. Atkins, P.W. Overton, T.L. Rourke, J.P. Weller, M.T. and Armstrong, *Inorganic Chemistry*, Oxford University Press, **2010**.

[2]   F. T. Edelmann, *Coord. Chem. Rev.* **2017**, *338*, 27–140.

[3]   W. W. Lukens, M. Speldrich, P. Yang, T. J. Duignan, J. Autschbach, P. Kögerler, *Dalt. Trans.* **2016**, *45*, 11508–11521.

[4]   C. Li, J. Yang, P. Yang, H. Lian, J. Lin, *Chem. Mater.* **2008**, *20*, 4317–4326.

[5]   A. and Zalkin, D. H. Templeton, *J. Am. Chem. Soc.* **1953**, *75*, 2453–2458.

[6]   S. Zhong, S. Wang, H. Xu, C. Li, Y. Huang, S. Wang, R. Xu, *Mater. Lett.* **2009**, *63*, 530–532.

[7]   P. P. Fedorov, A. A. Luginina, S. V. Kuznetsov, V. V. Osiko, *J. Fluor. Chem.* **2011**, *132*, 1012–1039.

[8]   Z.-L. Wang, Miao; Huang, Qing-Li; Hong, Jian-Ming; Chen, Xue-Tai and Xue, *Cryst. Growth Des.* **2006**, *9*, 2169–2173.

[9]   T. Paik, A.-M. Chacko, J. L. Mikitsh, J. S. Friedberg, D. A. Pryma, C. B. Murray, *ACS Nano* **2015**, *9*, 8718–8728.

[10]   L. Xiong, B. Shen, D. Behera, S. S. Gambhir, F. T. Chin, J. Rao, *Nanoscale* **2013**, *5*, 3253–3256.

[11]   G. Murali, R. K. Mishra, J. M. Lee, Y. C. Chae, J. Kim, Y. D. Suh, D. Lim, S. H. Lee, *Cryst. Growth Des.* **2017**, *17*, 3055–3061.

[12]   D. Zhang, T. Yan, H. Li, L. Shi, *Microporous Mesoporous Mater.* **2011**, *141*, 110–118.

[13]   S. Rodriguez-liviano, N. O. Nun, S. Rivera-ferna, J. M. De Fuente, M. Ocan, *Langmuir* **2013**, *29*, 3411–3418.

[14] A. I. B. D. Gonzalez-mancebo, M. Ocan, *J. Nanoparticle Res.* **2015**, *17*, 58.

[15] S. Cotton, *Lanthanide and Actinide Chemistry*, Inorganic Chemistry (Wiley), **2006**.

[16] J. Martínez-Esaín, J. Ros, J. Faraudo, S. Ricart, R. Yáñez, *Langmuir* **2018**, *34*, 6443–6453.

[17] A. Abdukayum, J. T. Chen, Q. Zhao, X. P. Yan, *J. Am. Chem. Soc.* **2013**, *135*, 14125–14133.

[18] D. A. Gonzalez-Carter, B. F. Leo, P. Ruenraroengsak, S. Chen, A. E. Goode, I. G. Theodorou, K. F. Chung, R. Carzaniga, M. S. P. Shaffer, D. T. Dexter, et al., *Sci. Rep.* **2017**, *7*, 42871.

[19] Z. R. Tian, J. a Voigt, J. Liu, B. McKenzie, M. J. McDermott, M. a Rodriguez, H. Konishi, H. Xu, *Nat. Mater.* **2003**, *2*, 821–826.

[20] C. Cantarutti, S. Raimondi, G. Brancolini, A. Corazza, S. Giorgetti, M. Ballico, S. Zanini, G. Palmisano, P. Bertoncin, L. Marchese, et al., *Nanoscale* **2017**, *9*, 3941–3951.

[21] S. Moise, E. Céspedes, D. Soukup, J. M. Byrne, A. J. El Haj, N. D. Telling, *Sci. Rep.* **2017**, *7*, 39922.

[22] C. Dong, F. C. J. M. van Veggel, *ACS Nano* **2009**, *3*, 123–130.

[23] J. Xie, Z. Gao, E. Zhou, X. Cheng, Y. Wang, X. Xie, L. Huang, W. Huang, *Nanoscale* **2017**, *9*, 15974–15981.

[24] M. Bobtelsky, B. Graus, *J. Am. Chem. Soc.* **1955**, *77*, 1990–1993.

[25] K. De Keukeleere, J. De Roo, P. Lommens, J. C. Martins, P. Van Der Voort, I. Van Driessche, *Inorg. Chem.* **2015**, *54*, 3469–3476.

[26] L. Zhu, Q. Li, X. Liu, J. Li, Y. Zhang, J. Meng, X. Cao, *J. Phys. Chem. C* **2007**, *111*, 5898–5903.

[27] C. A. Wamser, *J. Am. Chem. Soc.* **1948**, *304*, 1209–1215.

[28] A. Garzón-Manjón, E. Solano, M. de la Mata, R. Guzmán, J. Arbiol, T. Puig, X. Obradors, R. Yáñez, S. Ricart, J. Ros, *J. Nanoparticle Res.* **2015**, *17*, 1–11.

[29] Z. Xu, C. Li, P. Yang, C. Zhang, S. Huang, J. Lin, *Cryst. Growth Des.* **2009**, *9*, 4752–4758.

[30] M. Niederberger, H. Cölfen, *Phys. Chem. Chem. Phys.* **2006**, *8*, 3271–3287.

[31] E. V. Sturm (née Rosseeva), H. Cölfen, *Chem. Soc. Rev.* **2016**, *45*, 5821–5833.

[32] J. Martinez-Esain, J. Faraudo, T. Puig, X. Obradors, J. Ros, S. Ricart, R. Yáñez, *J. Am. Chem. Soc.* **2018**, *140*, 2127–2134.

4

Uncovering charged-surface patchy nanocrystals
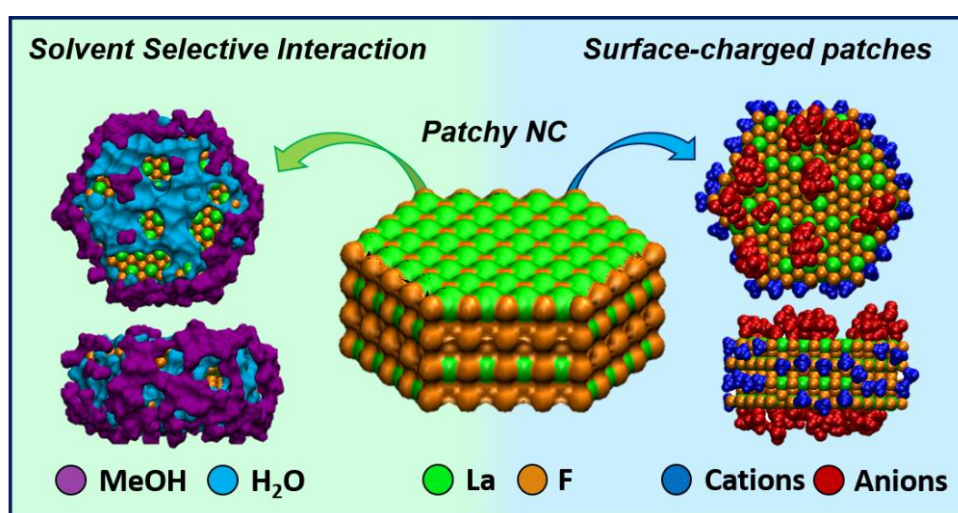
The fast and single-step synthesis of patchy LnF$_3$ (Ln= La, Ce and Pr) NCs is presented in this chapter. In contrast with the common discussion of the thermodynamic instability to form patches onto the surface, here is presented faceted hexagonal NCs in which the different exposed planes show different properties by the exposed atoms. These faceted NCs allow the spontaneous and selective adsorption of anions and cations in their different faces (patches). The final faceted-charge NC system was demonstrated by experimental techniques and MD simulations allowing the complete surface image. In addition, these NCs interact different with the used solvents due to the hydrophobic/hydrophilic behaviour of the faceted NC. Finally, hydrothermal and microwave treatments were used to obtain different sized patchy NCs in two pathways: directly applying the high-thermal methods and in combination with co-precipitation method.

4.1   Introduction

Patchy NCs were first described by Zhang and Glotzer[1] as a new way to decorate NCs, obtaining their different surface behaviours. This computational work explains different models of patchy NCs and how they can organise selectively in self-assembled structures. Conceptually, patchy NCs had been introduced concerning patches in the core. This process is performed by the selective bonding of different group of atoms onto the surface, forming different chemical areas on the surface (patches). Nowadays, the high interest in self-assembly mechanisms has promoted a deep investigation of patchy NCs of different nature that are able to form bigger tuneable structures.[2–8] Experimentally, this approximation is unsatisfactory concerning the thermodynamic instability of creating artificially these patches or considering the multistep processes to achieve it.[9] Currently, the concept of patchy NCs have been extended including the attached ligands. In other words, the selective organisation of different ligands onto the same core-composition.[10,11] In addition, linking two kinds of NCs by the interaction of an organic ligand is also considered a type of patchy NC.[12]

In contrast with the common reported works where NC surface is covered with one or two ligands forming patchy NCs, we are focused to achieve thermodynamically stable patchy NCs (Figure 4.1A). Our model is based on faceted LnF_3 NCs in which the exposed atoms in these faces will play the patches role, forming areas where different ligands or ions could be attached spontaneously and selectively (Figure 4.1B).
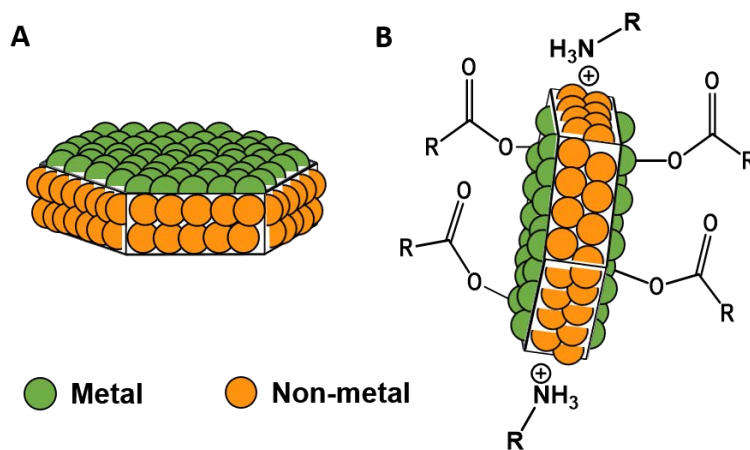

Figure 4.1. Schematic model system of the LnF_3 faceted-charge hexagonal NCs. (A) Here, we shown our faceted model with different exposed atoms in the faceted planes. (B) Stabilised NC in which carboxylate anions are attached to metal-exposed faces and ammonium-based cations are interacting electrostatically with fluoride-exposed faces.

The use of carboxylates and nitrogen-based cations as ionic precursors in aqueous media allows an exchangeable organic-surface with pH modifications (Scheme 1). In cases A and B, carboxylic acid is deprotonated with a direct carboxylic-to-metal interaction (X-type ligand) while in cases B and C, the ammonium salt is in its ionic form, interacting electrostatically with non-metal atoms (X'-type ligand). The amine in the case A is acting as

L-type ligand (neutral donor of free pair electrons), while carboxylic acid is non-interacting with NC surface in case C. With the aim of achieving a dual functionalisation onto the surface, situation B is preferable due to the dual interaction of metal and non-metal atoms with different binding motifs. Two different ligand-NC interactions allow the selective exchange if it is required to be applied in different areas.

Scheme 1. Different scenarios adopted by carboxylate and amine type ligands: (A) In basic conditions, (B) at neutral pH and (C) in acidic conditions.
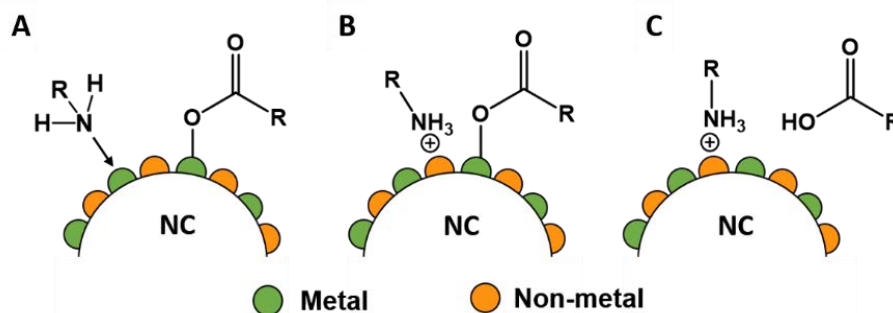
In this chapter,[13] we demonstrate a model of faceted-charge patchy NCs in which the NC surface possess the dual face characteristic of these kind of compounds but maintaining the same core. Exposed atoms in each face allows a core with different patches (hydrophobic or hydrophilic) depending on if metal or fluorine are more exposed. Negative charged faces in combination with positively charged faces give novel charged-surface patchy NCs. Additional studies showed their selective solvent interaction role due to the different distribution of the molecules onto the faceted surface, which promotes a preferential adsorption of the solvent onto hydrophilic or hydrophobic surfaces. Finally, some growing processes and first trials to functionalise NC surface are presented using high-temperature methods.

4.2   Experimental

4.2.1 Particle synthesis

❖ Co-precipitation method

In a 50 ml round-bottom flask equipped with a condenser and a magnetic stirrer, citric acid (2.25 mmol) in 16 ml of MilliQ water was neutralised with tetramethylammonium hydroxide (6.75 mmol), followed by the addition of $Ln(CH_3COO)_3 \cdot H_2O$ (1.5 mmol). The initial solution was heated until 100 °C, then NH_4F (4.5 mmol) in 4 ml of MilliQ water, was injected dropwise. After 2 h of reaction, the final mixture was allowed to reach room temperature. LnF_3 particles were separated from the reaction media by the addition of 10 ml of acetone, followed by centrifugation at 10,000 rpm for 20 minutes. Separated NCs were re-dispersed in 20 ml of MilliQ water or methanol forming stable colloidal dispersions.

❖ Post-hydrothermal treatment

Final washed colloidal suspensions in water are added into a Teflon vessel, then the reactor is sealed and with vigorous stirring the solution is heated up at 170 or 210 °C during 2 h. Final solutions are washed with acetone at 10,000 rpm for 20 minutes. Separated NCs were re-dispersed in 20 ml of MilliQ water or methanol forming stable colloidal dispersions.

In the case of amino acid functionalisation with post-hydrothermal treatment, 40 mg of amino acid has been added in each reaction. In these cases, NCs were re-dispersed in ethanol achieving stable colloidal dispersions during days.

❖ Hydrothermal method

In a Teflon vessel, citric acid (2.25 mmol) in 16 ml of MilliQ water was neutralised with tetramethylammonium hydroxide (6.75 mmol), followed by the addition of $Ln(CH_3COO)_3 \cdot H_2O$ (1.5 mmol). Then NH_4F (4.5 mmol) in 4 ml of MilliQ water was injected dropwise. After the addition, reactor was sealed and heated up at 210 °C. After 2 h of reaction, the final mixture was allowed to reach room temperature. LnF_3 particles were separated from the reaction media by the addition of 10 ml of acetone, followed by centrifugation at 10,000 rpm for 20 minutes. Separated NCs were re-dispersed in 20 ml of MilliQ water or methanol forming stable colloidal dispersions.

❖ Microwave reaction

In a Teflon vessel, citric acid (2.25 mmol) in 16 ml of MilliQ water was neutralised with tetramethylammonium hydroxide (6.75 mmol), followed by the addition of $Ln(CH_3COO)_3 \cdot H_2O$ (1.5 mmol). Then NH_4F (4.5 mmol) in 4 ml of MilliQ water was injected dropwise. After the addition, vessel has been introduced in a Microwave (MW) to be heated up at 200 °C. After 20 min of reaction, LnF_3 particles were separated from the reaction media by the addition of 10 ml of acetone, followed by centrifugation at 10,000 rpm for 20 minutes. Separated NCs were re-dispersed in 20 ml of MilliQ water or methanol forming stable colloidal dispersions.

4.2.2 Characterisation

Dynamic Light Scattering (DLS) and ζ-Potential analyses have been carried out in Characterisation of Soft-Materials Services at ICMAB using a Zetasizer Nano Zs with measurement range of 0.3 nm – 10.0 µm and sensitivity of 0.1 mg/mL. X-ray powder diffraction (XRD) patterns of the samples were recorded using a Phillips XPert diffractometer equipped with a two circle diffractometers and Cu tube. Transmission electron microscopy (TEM) micrographs were obtained on a 120 kV JEOL 1210 TEM, which has a resolution point of 3.2 Å. High Resolution Transmission Electron

Microscopy (HRTEM) micrographs were obtained on a 200 kV JEOL 2011 TEM, which has a resolution point of 1.8 Å at 200 kV. Samples for TEM analysis were prepared by spreading a drop of as-prepared NCs diluted dispersion on amorphous carbon-coated grids and then dried in air. All images have been obtained at Servei de Microscòpia of UAB. Cryo-TEM was performed with 3 µL amount of the sample blotted onto holey carbon grids (Quantifoil Micro Tools, Großloübichau, Germany) previously glow discharged in a PELCO easiGlow glow discharge unit. They were subsequently plunged into liquid ethane at −180 °C using a Leica EM GP cryo workstation and observed in a Jeol JEM 2011 TEM electron microscope operating at 200 kV. During imaging, the samples were maintained at −181 °C, and pictures were taken using a CCD ultrascan camera (Gatan). NMR analyses were recorded with a Bruker Advance II 400 spectrometer in D_2O at 298 K. Samples for NMR were prepared washing the colloidal solution five times before drying NCs. Finally, the powder was dispersed in D_2O. For ^{1}H MAS NMR has been used a Bruker 400 MHz – Avance II equipment with dual ^{1}H/BroadBand, sample was spinning at 10KHz and sample was packed into 4mm diameter rotors of ZrO_2 with plugs of Kel-F. Microwave (MW) oven of Milestone model FlexiWAVE has been used to heat up at 200 °C. Infrared spectroscopy (IR) analyses have been carried out in the Servei d'Anàlisi Química with the Bruker spectrophotometer IR Tensor 27.

4.2.3 Computer simulations

All basic computational details used during this chapter are the same of Chapter 2, using in this case a LaF_3 hexagonal nanoplatelet of 3 nm per 1 nm, since larger particle will need the use of extremely large simulation box (including ions and water). This particle has been simulated using the P63cm space group of reference pattern of hexagonal LaF_3, using Eje-Z[14] and Rhodius[15] software.

As the obtained crystal was not neutral, NC obtained by cutting the bulk material has 724 atoms (192 La and 532 F) resulting in a final charge of +44e, we decide to randomly release some surface atoms to create defects until the neutrality. Final NC contained 177 La atoms and 531 fluoride atoms, forming a neutral LaF_3 hexagonal nanoplatelet with 708 atoms. In the simulations was assigned a partial charge of +3e to the lanthanum atoms and a partial charge of -1e to the fluorine atoms. The model of the obtained NC in this way had a zero-net charge. The generated NC has a total exposed surface of 25.28 nm^2; which corresponds to two exposed hexagonal faces of 7.15 nm^2 (14.30 nm^2 in total) and six rectangular faces of 1.83 nm^2 (10.98 nm^2). During the MD simulations, the atomic positions of La and F atoms were maintained fixed at their initial values, avoiding the need of considering explicitly the interaction between lanthanum and fluorine. The interaction of lanthanum and fluorine atoms with all other atoms of the system (atoms from water or the ions) was modelled with the CHARMM force-field with electrostatic interactions (due to particle charges) and Lennard-Jones interactions. The

Lennard-Jones parameters employed for fluorine were standard CHARMM values. For lanthanum, we have considered a previous work using the same parameters.[16] Table 4.1 shows the summary of ions and molecules introduced in each system.

Table 4.1. Number of organic molecules, total number of atoms (including NC atoms) and size of the water box in each simulation.

	Sim1	Sim2
Citrate	20	13
Acetate	40	10
Ammonium	40	37
Tetramethylammonium	60	12
Water	24,648	264
Methanol	-	2,496
Total Atoms	76,512	17,169
Box size (Å)	98.1 x 104.3 x 80.8	77.9 x 61.8 x 57.7

❖ Preparation of Sim1

We prepared a system for MD simulations, summarised in Table 4.1 corresponding to a LaF_3 particle in ionic solution with an excess of ions. We considered 20 trivalent citrate anions with 60 monovalent tetramethylammonium counter ions and 40 monovalent acetate anions with 40 monovalent ammonium counter ions. These numbers were selected after trials with smaller number of ions, with the goal of obtaining a NC saturated of ions while at the same time, having ions in solution with a high concentration similar to that of the experimental conditions. The ions were randomly placed in the simulation box containing a NC and the whole system was solvated with water using the VMD program.[17] In this way, we generated a big simulation box (~10 nm size in each direction) containing approximately 75,000 atoms. This system (Sim1) was suitable for the study of ion-NC interactions.

❖ Preparation of Sim2

For the Sim2 system, we started from the equilibrium configuration of Sim1 in which we released all water and ions of the diffuse layer. In other words, we maintain the NC and ions/water directly adsorbed onto NC surface (Stern layer). After this, we added a methanol solvating box as it is indicated in Table 4.1, Sim2.

For each case, simulation times were selected to achieve the maximum information with the minimum computational consume. Sim1 at 100 ºC in water (20 ns) and Sim2 at 25 ºC in methanol (60 ns).

4.3 Results and discussion

4.3.1 Nanocrystal characterisation

In this Chapter,[13] we are focused on those NCs obtained in a homogeneous dispersion of ~8 nm particles via co-precipitation method using citrate as stabiliser (presented in Chapter 3). After observing the spontaneous faceting of these NCs, the main goal at this point is to obtain thermodynamically stable faceted patchy NCs, in which the different patches (faceted exposed planes) present different behaviours. In consequence with Figure 4.1, the use of quaternary ammonium compounds and carboxylates allowed a dual surface functionalisation. This combined effect (used ions and faceted surface) will promote the spontaneous adsorption of anions and cations distributed in the different patches (exposed faces). Although this chapter is focused on La, Ce and Pr NCs, the complete study has been performed for the case of LaF_3 to be the cation with the biggest size and diamagnetic (compatible with NMR). However, in some cases we will compare the results of the three metals trying to extract information about the effect of the used metal and the dependence of faceting with the metal cation radius (postulated in Chapter 3).

In Figure 4.2 and Table 4.2 are shown the TEM results of LaF_3, CeF_3 and PrF_3 respectively, showing the formation of hexagonal nanoplatelet shape NCs. Preliminary, LaF_3 and CeF_3 seem to form a homogeneous dispersion of small NCs without presence of aggregation. However, in the case of PrF_3 (Figure 4.2C), NCs seem to start to aggregate in TEM grid forming small supraparticles. This effect will be investigated in detail in the following subsections of this chapter. All NCs show a homogeneous dispersion in water as it can be observed in Figure 4.3A, where LaF_3 and CeF_3 show a hydrodynamic size of ~9 nm. PrF_3 shows also a homogeneous dispersion (one single peak in DLS) but bigger in size (~16 nm), explaining the partial aggregation of some NCs in TEM.

Table 4.2. Size of the as-synthesised NCs obtained using different techniques. DLS in volume, TEM histogram size and Scherrer equation applied on powder XRD.

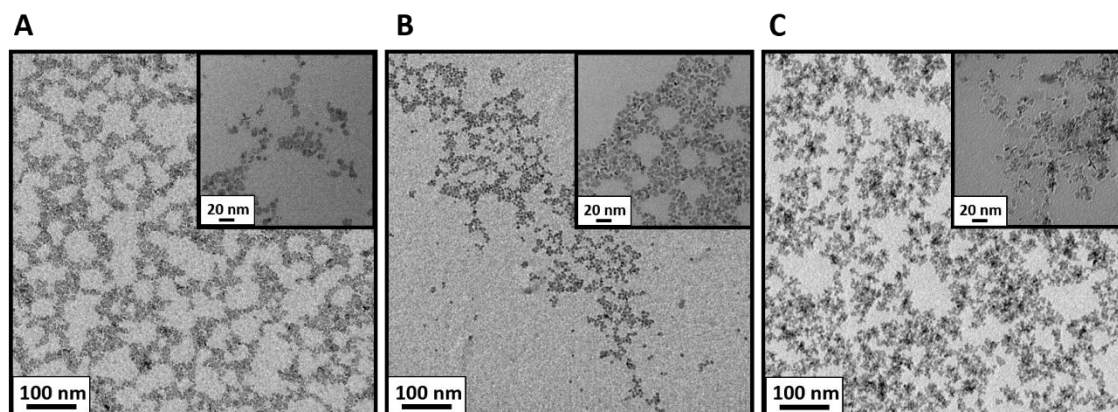| NC	DLS (% volume)	TEM size (length)	TEM size (width)	Scherrer size
LaF_3	9 nm	8.2 ± 1.8 nm	2.2 ± 0.5 nm	5.4 nm
CeF_3	9 nm	7.6 ± 2.3 nm	2.4 ± 0.5 nm	6.6 nm
PrF_3	16 nm	8.8 ± 1.6 nm	3.4 ± 0.8 nm	4.7 nm

Figure 4.2. TEM images of the obtained LnF₃ NCs at 100 °C at two different magnifications. (A) LaF₃, (B) CeF₃ and (C) PrF₃.

Concerning their crystallinity, all NCs show the typically hexagonal crystalline structure (Figure 4.3B) explaining their faceted hexagonal shape.
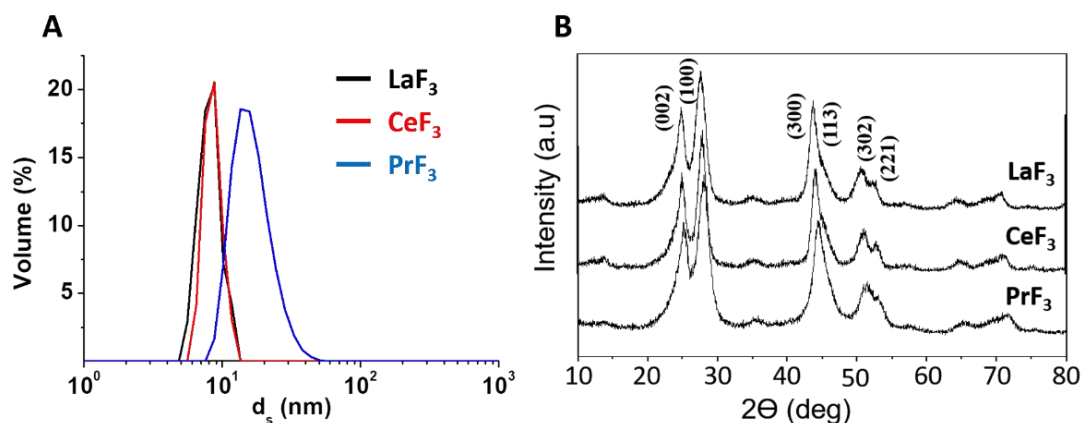

Figure 4.3. DLS in volume (A) and powder XRD with the plane assignation of hexagonal crystalline structure (B) of the obtained NCs.

To see in more detail this faceting, high resolution transmission electron microscopy (HRTEM) was performed (Figure 4.4). LaF₃ NCs show clearly the faceted exposed planes: hexagonal {0001} (Figure 4.4A) and rectangular {1$\bar{1}$00} (Figure 4.4B). In consequence, we obtained faceted hexagonal nanoplatelet expected for NCs with hexagonal crystalline structure, typical for these NCs.
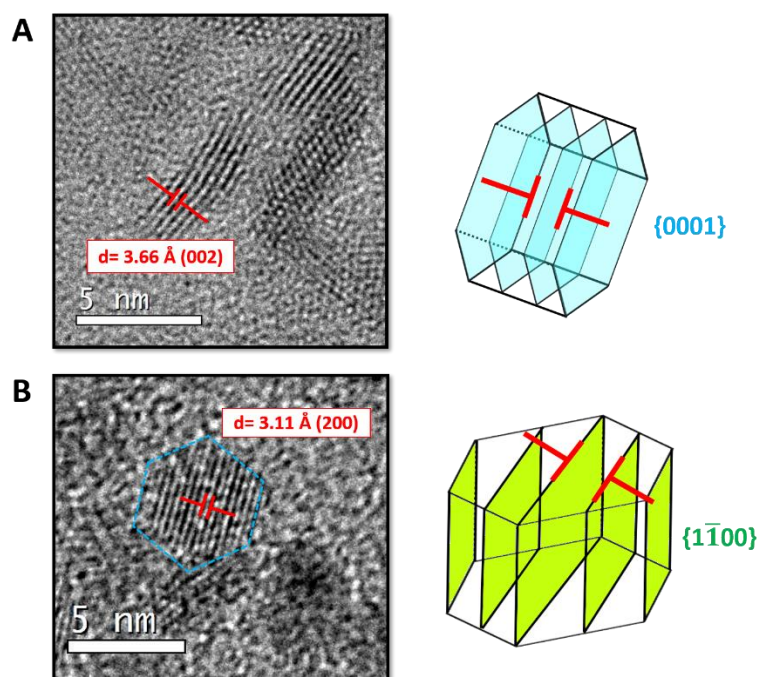
Figure 4.4. HRTEM indexed images of the different exposed faces. (A) Unravelling the faceting of hexagonal {0001} faces and (B) faceting of rectangular {1$\bar{1}$00} faces.

Preliminary characterisation is compatible with our model exposed in Figure 4.1A, obtaining a hexagonal faceted NCs with two different exposed planes hexagonal {0001} and rectangular {1$\bar{1}$00}. However, are the ions (cations an anions) selectively adsorbed onto the different patches? To this end, we firstly characterised experimentally the surface chemistry of LaF_3 NCs.

4.3.2 Surface image

To characterise experimentally the surface of LaF_3 NCs, ^{1}H NMR, IR and ξ-Potential were used. Using ^{1}H NMR, we found the presence of tetramethylammonium, citrate and acetate ions onto NC surface (Figure 4.5A) as in the case of YF_3 NCs. To perform NMR analysis, NCs are washed five times and then dried obtaining a white powder. Considering the neutrality of this powder and the integration of NMR peaks, six ammoniums are necessary to achieve a neutral powder (see SI)

As NMR in D_2O does not allow to observe ammonium protons due to the fast deuterium-proton exchanges, IR measurement was performed trying to confirm the presence of observed ions and the presence of ammonium. Figure 4.5B shows the complete IR spectrum of LaF_3 powder NCs, with the most relevant peaks. Considering that the carboxylic bands of acetate and citrate are located at the same wavenumber, bands at 1397 and 1569 cm^{-1} were assigned to be produced from both anions. In addition, we could observe the bending mode of ammonium cation (N^+-H) at 1488 cm^{-1} and the broad band at ~3258 cm^{-1}, which could be assigned to $\nu(N^+$-H) and $\nu(O$-H).
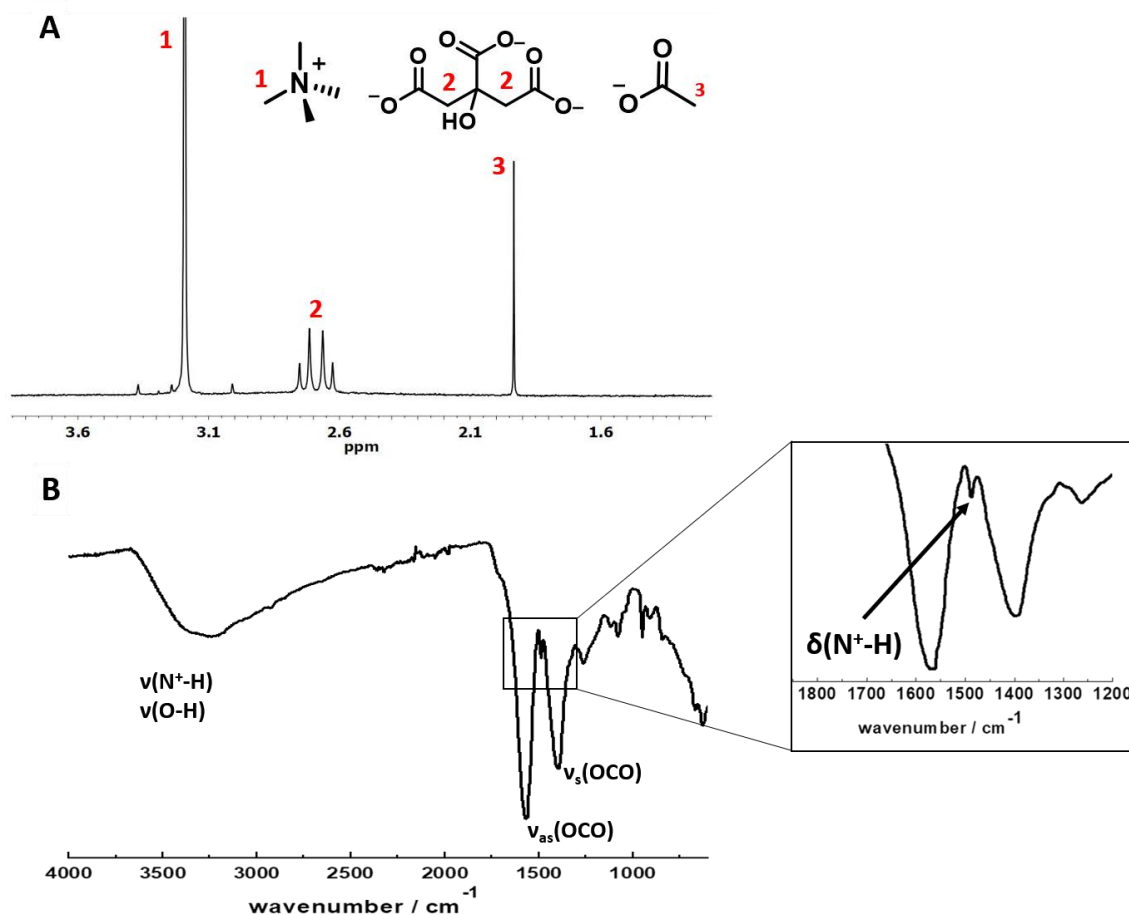
Figure 4.5. Surface characterisation with experimental techniques. (A) ¹H NMR of LaF₃ NCs washed five times and re-dispersed in D₂O with the corresponding assignation and (B) FTIR-ATR spectroscopy of LaF₃ NCs washed five times with the band assignation.

Considering the results of NMR and IR, we postulate that citrate, acetate and ammonium (the most hydrophilic cation) are attached onto NC surface (Stern layer), while tetramethylammonium is playing a counter ion role in the diffuse layer. Obviously, these characterisation techniques do not allow us to know if these ions are attached in preferential exposed planes, due to the measure is performed in the overall sample.

Finally, ξ-Potential measurements were performed to know the global charge of these NCs. In Table 4.3 is shown the values obtained by Hückel equation (Equation 1.4), where it can be observed a high negative charge onto NC surface. These results confirm our postulation of a negatively-charged system neutralised with tetramethylammonium (the more hydrophobic/less hydrophilic cation). In addition, values between -40 to -60 mV are higher enough to guarantee colloidal stability of the synthesised NCs in water.

ξ-Potential is optimised for spherical particles that diffuse equal in all directions, showing their global surface charge. In this case we have hexagonal faceted NCs, which have different diffusion rates by their different exposed surfaces. It is postulated that hexagonal faceted NCs diffuse by one

preferential orientation during the ξ-Potential measurement. In consequence the value obtained by this measure is only considering some exposed planes (hexagonal {0001}). Considering this effect, the high value for the ξ-Potential (~ -60 mV) could be explained by the selective adsorption of anions (citrate and acetate) onto these planes, while the other planes, those with ammoniums attached onto their surfaces, are not analysed. In contrast with YF$_3$ NCs (Chapter 2), which show values of ξ-Potential around -40 mV, due to the spherical shape of the NCs, we obtain here higher values because the charge of ammoniums attached onto NC surface are not considered.[18]

Table 4.3. ζ-Potential values of as-synthesised NCs using the corresponding equation (Hückel) considering their size.

NCs	ζ-Potential	Equation
LaF$_3$	-58.05 mV	Hückel
CeF$_3$	-54.80 mV	Hückel
PrF$_3$	-42.30 mV	Hückel

From these results, we can postulate that scheme showed in Figure 4.1B is achieved and observable by experimental surface techniques. However, to see clearly the surface distribution, we performed all-atomic MD simulations to analyse dually this system, using experimental and computational techniques.

4.3.3 Surface distribution by MD simulations

Simulation box was performed with one LaF$_3$ NC in a water box with all involved ions in the synthesis (acetate, citrate, ammonium and tetramethylammonium) in excess, to ensure the saturation of the surface. The excess has been investigated trying with less amounts of ions until the surface was covered ionically and some ions of each species remained free in diffuse layer. In Figure 4.6A, it is shown a snapshot of the system after reaching equilibrium, in which can be observed the attachment of acetate, citrate and ammonium ions (tetramethylammonium is found only in the diffuse ionic layer surrounding the NC). Interestingly, the ionic distribution observed in Figure 4.6B is compatible with our model presented in Figure 4.1B.

After applying the radial pair correlation function (see section 1.3.5) between La^{3+} cations with oxygens of carboxylates (citrate and acetate) and F$^-$ anions with nitrogen of cations, we obtain the plots of Figure 4.7. Citrates and acetates up to 2.65 Å (carboxylic oxygen – La distance) were accepted as attached. In the case of ammonium, 3.55 Å (nitrogen – fluoride) was accepted at ammonium adsorbed onto NC surface. Tetramethylammonium did not show a correlation with the atoms of the NC.
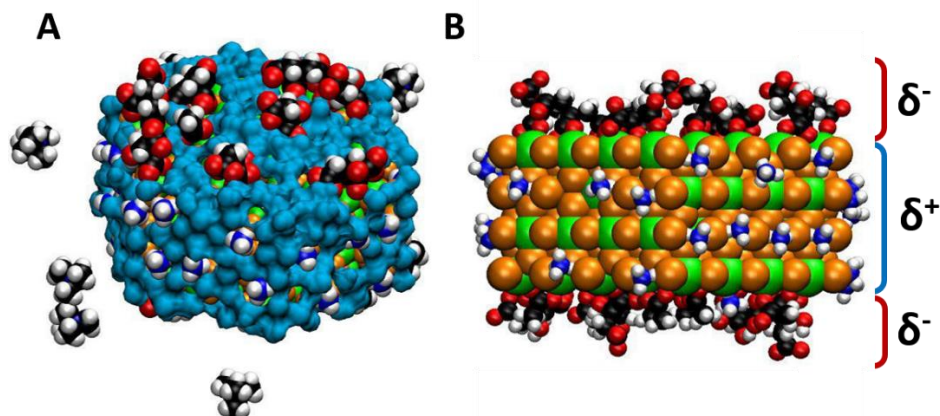
Figure 4.6. (A) Snapshot (made with VMD)[17] from MD simulation at 100 °C of LaF$_3$ NC, showing the surface composition of the NCs. LaF$_3$ atoms and adsorbed ligands are shown in Van der Waals representation. Green spheres correspond to La, orange are F, black are C, red are O, blue are N and white are H. Water molecules adsorbed to the NC surface are shown in blue as a molecular contour surface (calculated using the surface algorithm implemented in VMD). (B) Snapshot without adsorbed water showing clearly the surface charge distribution of LaF$_3$ patchy NC.

In hexagonal exposed faces ({0001} planes), are only present anions (acetate and citrate) with a direct carboxylic-to-metal interaction (13 citrates and 10 acetates, ~1.6 ions/nm^2). However, rectangular faces (exposed {1$\bar{1}$00} planes) are full of ammonium cations (37 ammoniums for the simulated NC, ~3.4 ions/nm^2), interacting electrostatically with exposed fluorine atoms. Also, in our simulation the neutral LaF$_3$ NC acquires a global negative charge due to the ionic adsorption, as in the case of YF$_3$ simulations performed in Chapter 2.
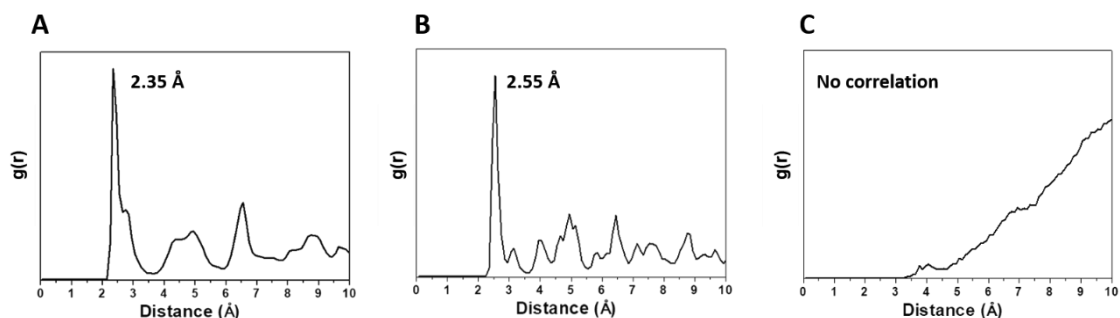

Figure 4.7. Radial pair correlation function g(r) of ions with the respective NC element in water simulation (Sim1). (A) g(r) between lanthanum and all carboxylic oxygens (acetate or citrate). (B) g(r) between fluorine and the nitrogen of ammonium cation. (C) g(r) between fluorine and the nitrogen of tetramethylammonium cation.

Results obtained in MD simulations agree with the high negative value measured experimentally for the ξ-Potential, concerning the non-spherical shape of the NCs. Our results confirm that hexagonal {0001} planes, those measured by ξ-Potential, are covered by anions (citrate and acetate) with a density of ~ -3.4 charge/nm^2. However, rectangular {1$\bar{1}$00} planes, those covered by ammonium, have a density of ~ +3.4 charge/nm^2, but they are not measured during ξ-Potential. Experimental and computational studies

confirm the presence of charged-surface patchy NCs as we postulated in Figure 4.1B.

In addition, these results also show the presence of strongly adsorbed hydration water molecules on the LaF_3 surface. This effect is reminiscent to results obtained with the different models for water (implicit and explicit) in Chapter 2, we concluded that adsorbed water molecules have a substantial role in stabilising charged surfaces of NCs, avoiding a massive ionic condensation onto the surface. For this reason, here it can be also postulated that adsorbed water plays a similar role in LaF_3 NCs preventing a massive ionic condensation onto NC surface.

4.3.4 How are these NCs stabilised in other solvent?

After the complete surface characterisation of LaF_3, we want to test two major changes in the obtained patchy NCs. The effect of changing the crystal structure by changing the metal by another lanthanide cation with different radius and the behaviour of the faceted-charge patchy NCs in other polar solvent (e.g. methanol). These effects must be tested due to in Chapter 3 we postulate the dependence of the faceting with the size of the metal cation, giving the reduction of the size and the different facets, patches should be change if decreasing the cation radius.[19] Additionally, it has been postulated that the presence of patches with different behaviour allows the NC stabilisation because of the selective interaction of solvents in the patches.[20]

To this end, LaF_3, CeF_3 and PrF_3 NCs were re-dispersed in water and methanol after the synthesis. To analyse the behaviour in solution of these NCs, cryo-TEM has been used in both solvents, water and methanol, with the same concentrations for all samples (~ 30 mM). Figure 4.8 shows the image obtained for all NCs in water and methanol, in which can be observed that there is not significance difference between stabilise NCs in water or methanol. In other words, despite of the essential role of ionic ligands in our system, we do not observe any significant effect in moving from water to methanol due to the decreasing polarity of the solvent.

However, if we compare between the different lanthanides, some conclusions can be obtained considering the decreasing of the radius of the used lanthanide. It can be observed an increasing of aggregation (LaF_3 < CeF_3 < PrF_3) as function of the decrease of lanthanide cation radius, being PrF_3 (Figure 4.8C) the most aggregate showing families of supraparticles containing some NCs.
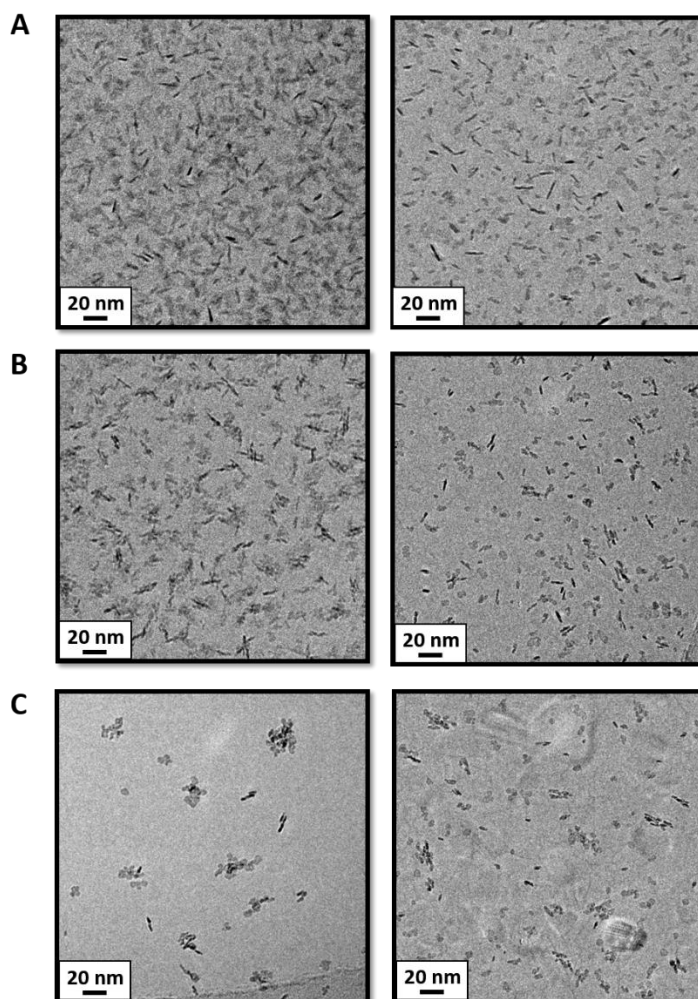
Figure 4.8. Cryo-TEM images obtained from colloidal solutions in water (left) and methanol (right) of (A) LaF₃ NCs, (B) CeF₃ NCs and (C) PrF₃ NCs. All of them performed in holly-carbon grids at ~30 mM concentrations.

The observed aggregation can be related with the decrease in the faceting when decreasing the cationic radius. PrF$_3$ NCs seem to be more spherical/less hexagonal than LaF$_3$ and CeF$_3$, giving a system where the patches are less-defined. As these NCs lose the faceting, they become more spherical with a random distribution of cations and anions onto NC surface, as in the case of YF$_3$. This allows ionic interactions mediated by the self-assembly of citrate bridges,[21] but in this case, forming smaller aggregates because NCs are not totally spherical and they maintain some patches that avoid the formation of big assembled systems.

Nevertheless, the size of the lanthanide cation does not explain why these NCs show the same behaviour in water and methanol. To investigate the role of the patches in this effect, MD simulations are used again to rationalise the surface chemistry of this system after being stabilised in methanol solution.

4.3.5 Selective-solvent interaction

The simulations were performed by starting from the equilibrium configuration of MD simulation carried out in water. Firstly, all water molecules and ions remaining in the diffuse layer were removed. LaF_3 NC with the ions (acetate, citrate and ammonium) and water molecules present in Stern layer have been neutralised with the addition of tetramethylammoniums to achieve a neutral system in diffuse layer. Finally, all system was covered by a methanol box (described in section 4.2.3).

Results of MD simulations show and exchange of water for methanol in rectangular $\{1\bar{1}00\}$ planes while water molecules adsorbed onto hexagonal $\{0001\}$ planes remain anchored onto NC surface in all simulation times (Figure 4.9). Interestingly, NC surface has a dual behaviour as we predict in Figure 4.1A, allowing the exchange of water for methanol in a preferential planes (patches). Patches formed by fluoride exposed atoms in $\{1\bar{1}00\}$ planes show a more hydrophobic/less hydrophilic behaviour which allows the fast exchange between both solvents. Consequently, solvation water is replaced by methanol over these planes, being stable in the new solvent. However, $\{0001\}$ exposed planes, those stabilised by citrates and acetates, present a more hydrophilic/less hydrophobic role and they maintain their adsorbed water in the presence of the new solvent (methanol). Here, it is proposed that this dual water/methanol solvation promoted by the patches of these NCs is the key factor to explain the same role of cryo-TEMs in water and methanol. These patchy NCs can interact selectively with the added solvent modifying their surface chemistry to remain stable in less polar solvents.
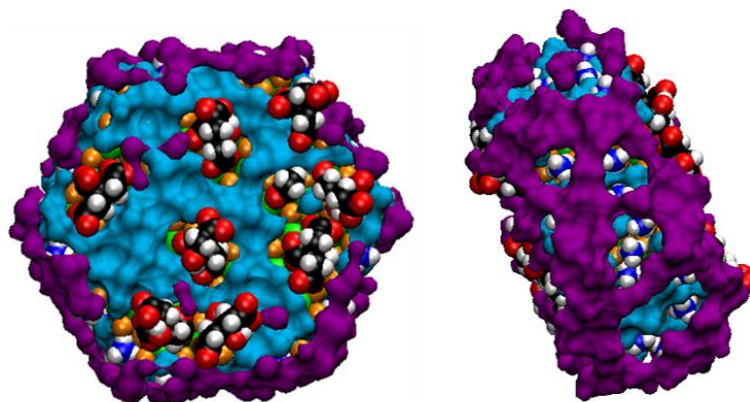

Figure 4.9. Snapshots (made with VMD)[17] from MD simulation carried out in methanol of LaF₃ NC showing the surface distribution of water (blue) and methanol (purple) made using surface algorithm of VMD. Other atoms are showed in Van der Waals representation.

Moreover, the selective exchange between water for methanol is not the unique phenomenon when changing the solvent. In methanol solvent simulations, some tetramethylammonium cations adsorb onto the NC on $\{1\bar{1}00\}$ exposed planes (see Figure 4.10A) as indicates also its radial pair correlation functions (Figure 4.11). This big cation (as compared with ammonium) did not show correlation with NC surface in our simulations

carried out in water because NC surface was full-covered by ammonium cations in $\{1\bar{1}00\}$ planes (Figure 4.6). Additionally, tetramethylammonium shows substantial interaction with the free carboxylic moieties of citrate ligands adsorbed onto the NC surface (Figure 4.10B). However, if methanol is used as solvent, $\{1\bar{1}00\}$ exposed planes become more hydrophobic allowing the adsorption of tetramethylammonium reducing the negative charge of the global NC. Concerning the observed electrostatic citrate-tetramethylammonium interactions (Figure 4.10B), they seem to be induced by an increased counterion condensation at the lower dielectric constant of methanol
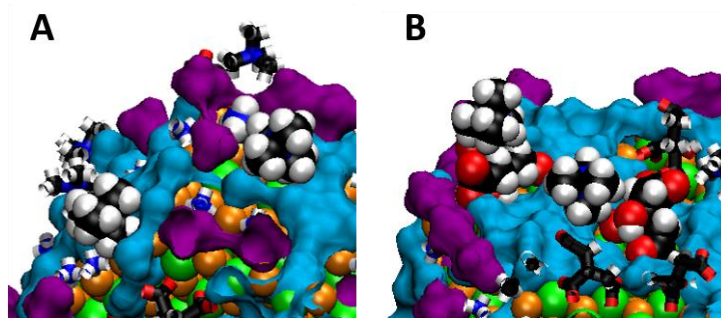
Figure 4.10. Snapshots (made with VMD)[17] from MD simulation carried out in methanol of LaF₃ NC showing (A) tetramethylammonium in Van der Waals representation adsorbed onto NC surface and (B) tetramethylammonium interacting electrostatically with adsorbed citrates both in Van der Waals representation.
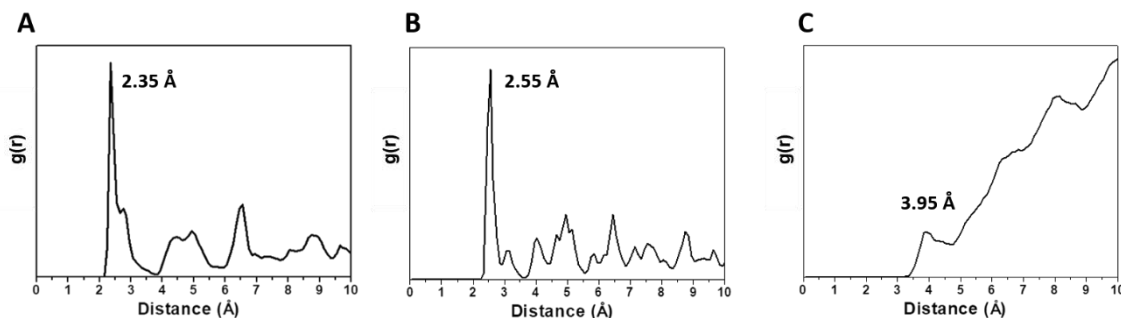

Figure 4.11. Radial pair correlation function g(r) of ions with the respective NC element in methanol simulation (Sim2). (A) g(r) between lanthanum and all carboxylic oxygens (acetate or citrate). (B) g(r) between fluorine and the nitrogen of ammonium cation. (C) g(r) between fluorine and the nitrogen of tetramethylammonium cation.

All these observed effects when changing the solvent to a less-polar as methanol, confirm the presence of patches, onto NC surface, able to adsorb selectively one solvent or other to be stable in the new conditions.

4.3.6 Postulating the mechanism for water-methanol swapping

Once the water-methanol swapping was observed onto selective faces when NCs are moved from water to methanol, we wanted to study preliminary this interesting effect. Firstly, [1]H Magic Angle Spinning (MAS) NMR was performed to both samples, as-synthesised NCs and those stabilised in methanol before the drying process. In Figure 4.12 is shown the spectra in which some differences could be observed.
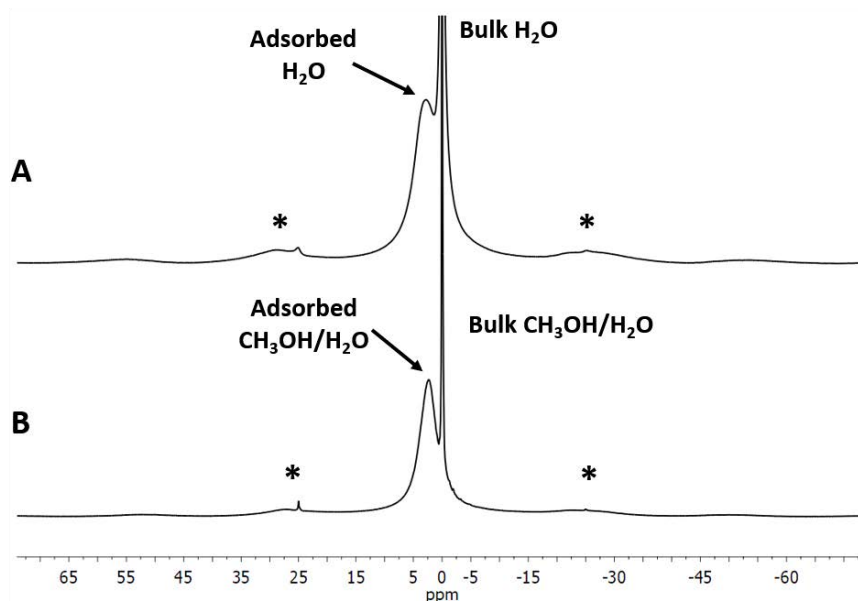

Figure 4.12. ^{1}H MAS NMR spectra of (A) LaF$_3$ NCs stabilised in water before the drying process and (B) LaF$_3$ NCs re-dispersed in methanol before the drying process. * indicates spinning sidebands. Bulk water/methanol has been referenced to 0 ppm.

In Figure 4.12A, a broad peak at 2.78 ppm has been assigned to adsorbed water onto NC surface, while in Figure 4.12B (sample with methanol treatment) shows a narrower peak at 2.37 ppm. This difference could be understood considering the behaviour of methanol, allowing the stabilisation through -OH group, but avoiding the formation of hydrogen bonding interactions with the system due to -CH$_3$ group. In contrast, if water is interacting with NC surface (La-OH$_2$ or F-HOH), these water molecules could interact via hydrogen bonding interactions with other molecules or ions onto NC surface, being its peak broader compared with the mixture of water/methanol. To extract more information about the mechanism of the swapping water-methanol, more studies must be performed to unravel experimentally the insights of this mechanism.[22,23]

Concerning MD simulations, we can study the mechanism of the swapping, but firstly we must to analyse the radial pair correlation function between solvents and NC surface (Figure 4.13) to know the distance to consider the solvent adsorbed or not onto NC surface.
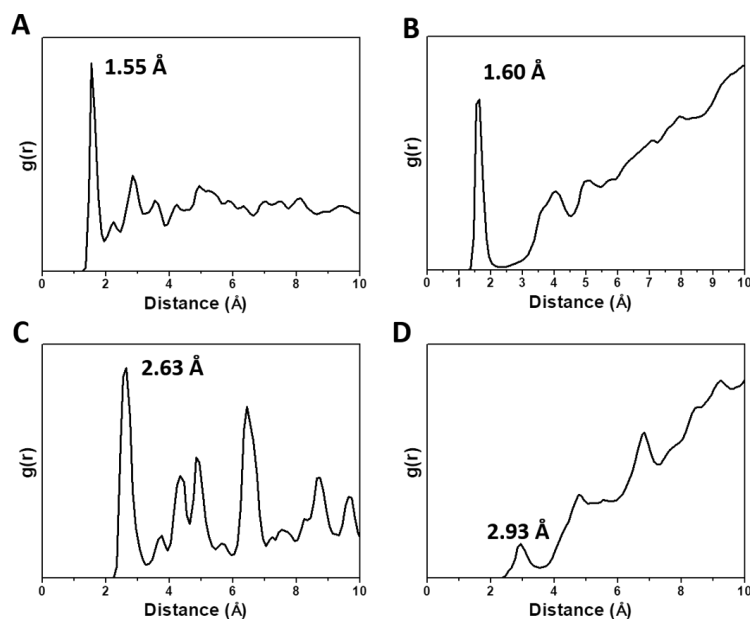
Figure 4.13. Radial pair correlation function g(r) of water/methanol with the respective NC element in methanol simulation (Sim2). (A) g(r) of F with water, (B) g(r) of F with methanol, (C) g(r) of La with water and (D) g(r) of La with methanol.

Considering the radial pair correlation function, the exchange between water and methanol has been represented to see in detail the number of water molecules released, and methanol molecules adsorbed (Figure 4.14). In the graphical representation can be observed the exchange of ~45 water molecules for 35 methanol molecules, all of them exchanged selectively from {1$\bar{1}$00} planes.
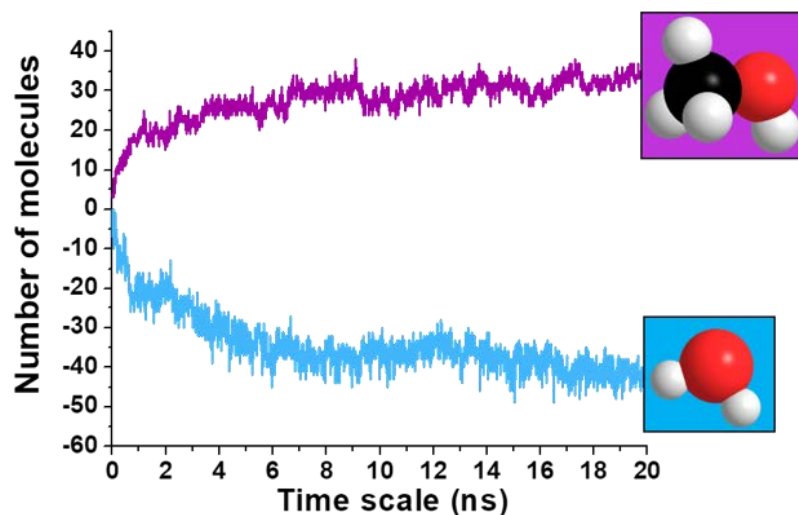

Figure 4.14. Graphical representation of the number of methanol and water molecules adsorbed/released during the simulation performed in methanol per time unit.

Concerning the insights of the mechanism in which methanol release water, we analysed the different steps of water-methanol swapping (Figure 4.15)
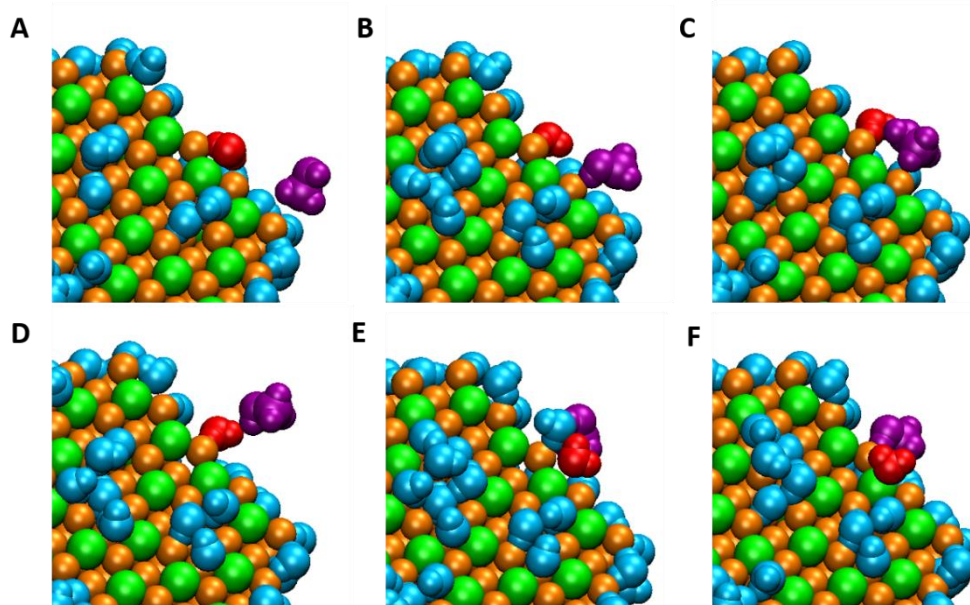
Figure 4.15. Schematic representation of different snapshots to highlight the steps of the water-methanol swapping mechanism. (A) Initial situation, (B) adsorption of methanol onto NC surface, (C) water-methanol-NC interaction, (D) water-methanol hydrogen bonding interaction, (E) water assisted release of methanol and (F) final situation. Adsorbed water molecule is represented in red, methanol molecule in purple, free and adsorbed water in blue, La atoms in green and F in orange.

We postulated here a kind of bimolecular mechanism assisted by one free water molecule, as detailed down below. Figure 4.15A shows the initial configuration in which adsorbed water (red) is interacting via F-HOH onto NC surface, and methanol molecule (purple) remains free in the system. The first approximation is when methanol interacts with NC surface, but not in its thermodynamically stable configuration (Figure 4.15B). At this point, methanol interacts with adsorbed water (red) close to its position, allowing a NC-water-methanol-NC interaction as shown in Figure 4.15C. Due to the high tension of this interaction, the system reach its minimum energetic configuration (Figure 4.15D) via hydrogen bonding interaction between adsorbed water and methanol. The release of water molecule is displayed by the assistance of a free water molecule, helping the attachment of methanol onto NC surface (Figure 4.15E). Final equilibrium configuration (Figure 4.15F) shows the adsorbed methanol (purple) where it was adsorbed water molecule in Figure 4.15A, while this water molecule has been attached onto NC surface, now interacting via La-OH$_2$, close to the first position. As commented before, this mechanism (allowed via MD simulations) must be ensured with further experimental characterisation via NMR.

4.3.7 Growing patchy NCs

After the obtained results for these patchy NCs, we aimed to know if we could modify their size applying post-thermal treatments or synthesising directly the particles using a hydrothermal or microwave (MW) processes. In

addition, due to the insights unravelled onto the NC surface, we tried post-thermal modifications with the addition of amino acids to know if we can growth and modify the surface chemistry of the as-synthesised NCs in a single procedure. In this section is presented the preliminary results of some trials to growth LaF_3 patchy NCs as starting approximation. Currently, this work is under deep investigation by our group to unravel the insights of the surface chemistry concerning the involved processes.

4.3.7.1 Application of a post-hydrothermal treatment

As commented in Chapter 1, hydrothermal synthesis is claimed to allow bigger and more crystalline NCs due to the high temperatures and pressures. To demonstrate this, we performed a growth process of patchy LaF_3 NCs applying the hydrothermal treatment at two different temperatures: 170 and 210 °C after their synthesis by co-precipitation at 100 °C.

In Figure 4.16 can be observed the TEM images of LaF_3 NCs without the post-hydrothermal treatment and with a post-hydrothermal treatment at different temperatures, during 2 h of reaction. Final colloidal suspensions were washed and re-dispersed in water.
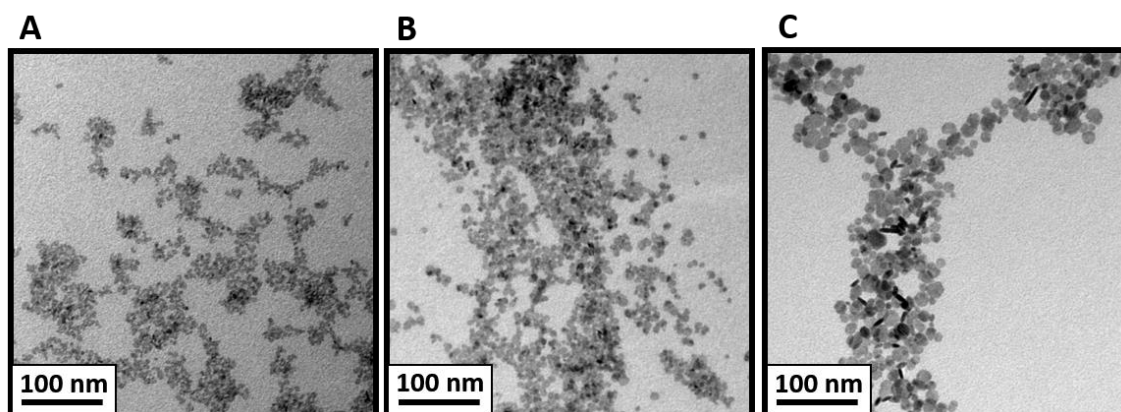

Figure 4.16. LaF_3 NCs obtained via co-precipitation method at 100 °C without post-hydrothermal treatment (A), with a post-hydrothermal treatment at 170 °C during 2 h (B) and a post-hydrothermal treatment at 210 °C during 2 h (C).

After these images, we demonstrate that post-thermal treatment at high temperatures and pressures allow the growth of hexagonal-shape NCs. This effect depends on the temperature of the post-thermal treatment allowing different NC size, obtaining bigger hexagonal NCs at high temperatures (Table 4.4). In addition, it was observed more defined hexagonal shape NCs at bigger temperatures, Thus, temperature in post-synthetic treatments affects directly to the growth and faceting of patchy LaF_3 NCs.

Table 4.4. Comparison between different TEM sizes of LaF$_3$ NCs obtained without and with post-thermal treatment at different temperatures.

LaF$_3$ NCs by co-precipitation	TEM size (length)	TEM size (width)
Without post-thermal treatment	7.9 ± 1.6 nm	2.0 ± 0.5 nm
Post-thermal treatment at 170 °C	10.0 ± 1.4 nm	2.2 ± 0.4 nm
Post-thermal treatment at 210 °C	15.8 ± 2.8 nm	4.2 ± 0.9 nm

4.3.7.2 Post-hydrothermal treatment with amino acids

Recently, Xie et al.[24] reported a synthetic study of citrate-based fluorescent small molecules in which they used citric acid and amino acids (among others) to form dioxo-pyridine ring based dyes. Considering that in our surface chemistry characterisation, we detect the presence of citrate in selective exposed planes, we want to perform a dual approach. Using hydrothermal method as post-synthetic treatment with the addition of amino acids into the system, we want to growth and functionalise the obtained particles in a one-pot reaction. These dioxo-pyridine ring based dyes have been presented as luminescent compounds with excitation around 350 nm and emissions at ~450 nm.

Our postulation is based on mixing citric acid with amino acid at temperatures above 140 °C as it is indicated in Figure 4.17, forming dioxo-pyridine ring based dyes with different terminal functionalisation to our NCs. Considering the results obtained growing NCs at 170 and 210 °C, we select a hydrothermal treatment at 210 °C to form bigger and more shape-defined hexagonal NCs. After the post-thermal treatment, washed NCs were re-dispersed in ethanol instead of water, due to water colloidal suspensions showed poor stability (they precipitated in hours). This evidence could indicate that the surface chemistry has been modified from citrate to the final compounds presented in Figure 4.17, which have a less-hydrophilic behaviour.

In Figure 4.18 is shown the TEM images of LaF$_3$ NCs after the thermal process with Glutamine (LaF$_3$@Glu), Lysine (LaF$_3$@Lys), Threonine (LaF$_3$@Thre) and Arginine (LaF$_3$@Arg). Concerning the final size of NCs after the post-hydrothermal treatment, an homogeneous growth have been achieved in some amino acid functionalised NCs, showing a size of ~14 nm per ~4 nm (Table 4.5). However, LaF$_3$@Arg NCs show a size of ~7 nm per ~2 nm, similar to the NCs synthesised by co-precipitation method without post-hydrothermal treatment. Preliminary results show that the post-hydrothermal treatment allows the growth of these NCs, without significance size effect of the added amino acid. However, in the case of post-hydrothermal treatment with arginine, we found that the addition of this amino acid produces a hampering effect in the NC growth.
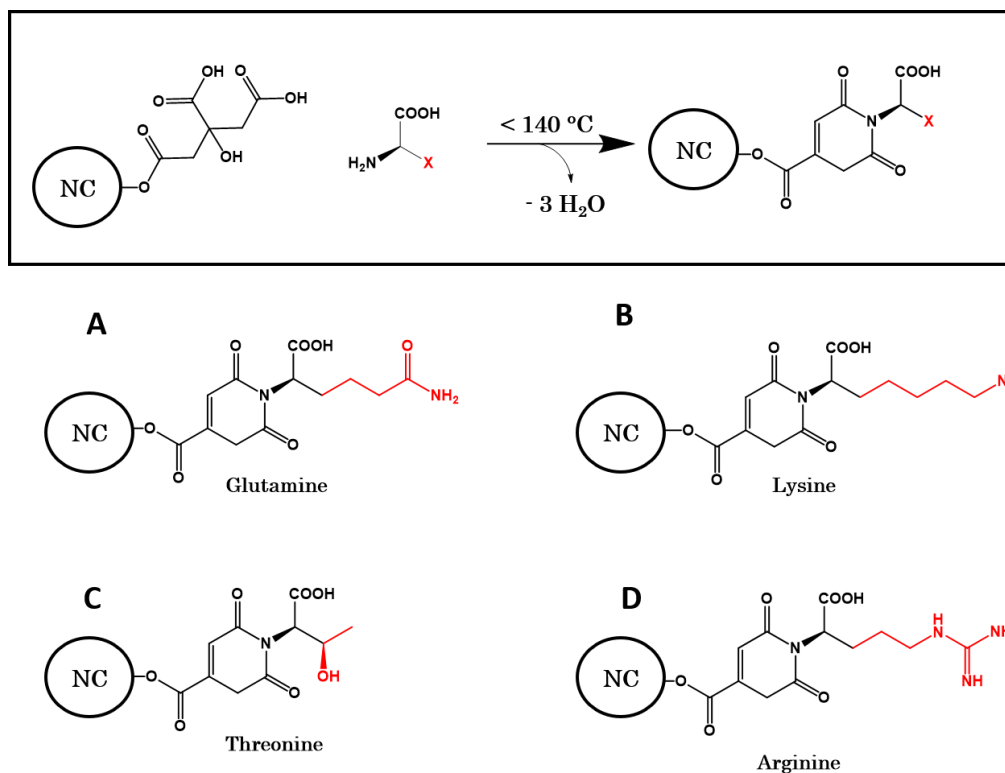
Figure 4.17. Chemical reactions expected between citric acid of citrate stabilised-NCs with different amino acids at temperatures above 140 °C with the corresponding dehydration. (A) Glutamine, (B) Lysine, (C) Threonine and (D) Arginine products.[24]
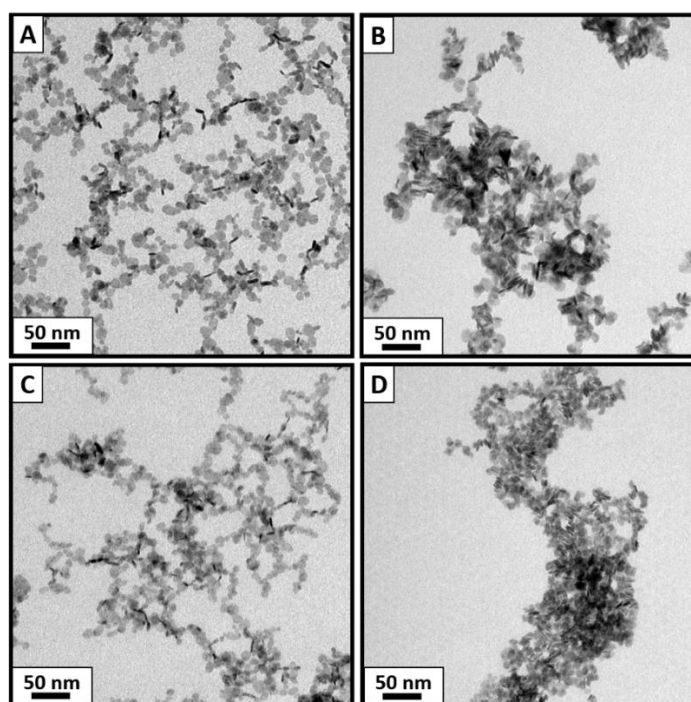

Figure 4.18. LaF₃ NCs obtained via co-precipitation method at 100 °C with a post-hydrothermal treatment at 210 °C during 2 h with: (A) Glutamine, (B) Lysine, (C) Threonine and (D) Arginine.

Table 4.5. Comparison between different TEM sizes of LaF₃ NCs obtained with post-thermal treatment at 210 °C during 2 h with the addition of amino acids.

Amino acid	TEM size (length)	TEM size (width)
Glutamine	14.1 ± 2.3 nm	3.9 ± 0.8 nm
Lysine	14.2 ± 2.5 nm	3.8 ± 0.6 nm
Threonine	13.8 ± 2.3 nm	3.0 ± 0.7 nm
Arginine	7.3 ± 0.9 nm	2.2 ± 0.4 nm

Analysing the different TEM images, it can be observed that LaF₃@Lys and LaF₃@Arg NCs show a clear difference compared with the other ones. NCs are organised in oriented aggregates preferentially by their {0001} planes (see Figure 4.19A), while the other seem to be organised by {1$\bar{1}$00} planes (see Figure 4.19B).
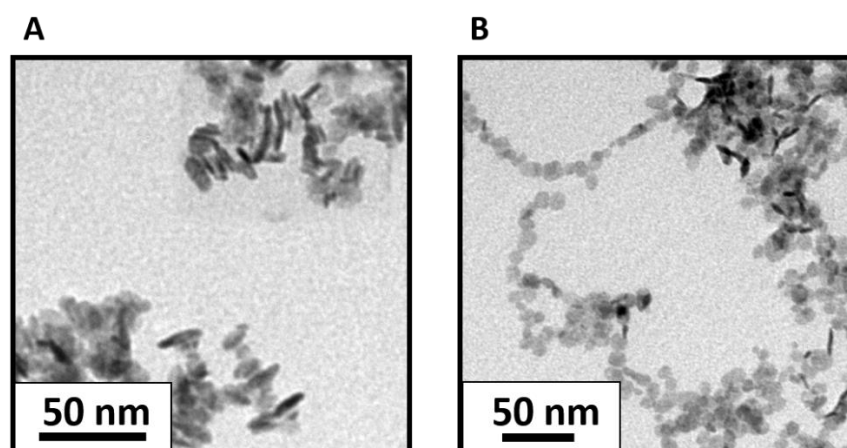

Figure 4.19. Enlarged zones of LaF₃ NCs TEM via co-precipitation method at 100 °C with a post-hydrothermal treatment at 210 °C during 2 h with: (A) Lysine and (B) Threonine as example.

This effect can be directly related with the chemical composition of the x term of the used amino acid and the role of the carboxylate (see Figure 4.17). Considering the functional groups of the used amino acids, threonine and glutamine could be ionised by basic medium via the deprotonation of the free carboxylic acid. However, lysine and arginine present a zwitterionic behaviour due to the presence of carboxylic acid and amine free in the chain (considered as basic amino acids). In neutral pH, lysine and arginine should be in their zwitterionic form (R-COO⁻ and R'-NH₃⁺), showing an ionic behaviour in the colloidal solution. In Figure 4.20 we postulate a kind of ionic-mediated self-assembly responsible of the selectively-oriented aggregation of LaF₃ NCs by their {0001} hexagonal planes. This interaction is also possible for arginine case, due to it has the same basic role than lysine. Preliminary, these results indicate that we are not only be able to growth and functionalise

NC surface, but also promote an ionic self-assembly in those basic amino acids mediated by the postulated interaction described in Figure 4.20. In fact, this postulated self-assembly must be confirmed using other experimental techniques and/or MD simulations in the near future, due to the high interest on self-assembled structures formed by patchy NCs.
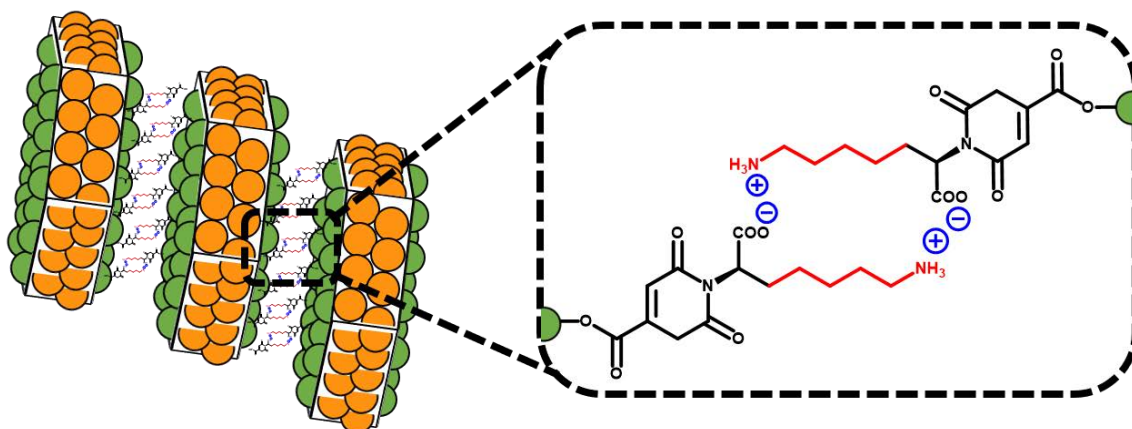

Figure 4.20. Schematic representation of lysine-lysine ionic interactions postulated to promote the selective self-assembly by {0001} hexagonal planes.

Considering the problems to re-disperse these NCs in deuterated solvents after a drying process, we tried to characterise preliminarily the surface chemistry by using IR (in solid state FTIR-ATR). IR spectra of the functionalised LaF$_3$ NCs via post-hydrothermal functionalisation are shown in Figure 4.21.
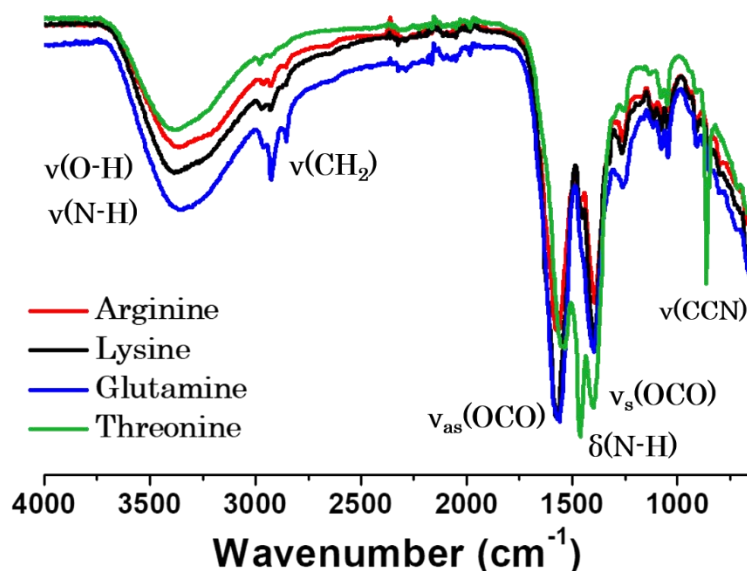

Figure 4.21. FTIR-ATR spectra of powder LaF$_3$ NCs functionalised by a post-hydrothermal treatment with amino acids after two washing steps.

IR spectra are compatible with the formation of the dioxo-pyridine ring based dyes due to the relative increase of $\nu(CH_2)$ compared with the IR of the as-synthesised NCs, which agree with the relative increasing in the number of CH_2 groups. However, the most relevant identification of these products onto NC surface was obtained thanks to threonine. L-threonine has an intense peak in IR at ~900 cm^{-1} produced by $\nu(CCN)$,[25] being highly intense due to the intramolecular hydrogen bonding as shown in Figure 4.22.
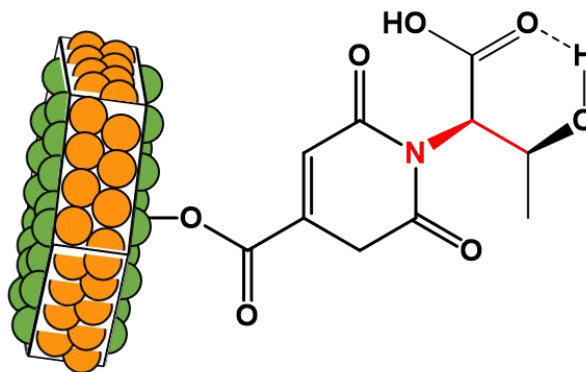

Figure 4.22. Intramolecular hydrogen bonding between the hydroxyl group and the carboxylic acid of the threonine fragment, highlighting in red the stretching mode observed in IR.

In our case, the intensity of this band could be related with the formation of the intramolecular hydrogen bonding interaction, as well as, to the reaction between citrate and threonine. The conformation of the dioxo-pyridine ring based dye observed in Figure 4.22, produces a high tension in the vibration mode producing a highly intense peak. After that, the possible formation of the self-assembly observed in Figure 4.20 and the complete characterisation of dioxo-pyridine ring based dyes postulated before, become in a good starting point as a future perspective concerning the growth and direct functionalisation of these patchy NCs.

4.3.7.3 Applying directly hydrothermal and MW treatments

After the good results of co-precipitation method, we want to test if the synthesis of NCs directly by hydrothermal method is possible following the same methodology. As the hydrothermal treatment is carried out in a sealed Teflon vessel, the injection of ammonium fluoride must be performed at room temperature before introducing the system in the reactor. In addition, as MW method is proposed to be more efficient and to reduce considerably the reaction time with a more homogeneous heating process,[26] we tested the difference of these two high-temperature treatments. These strategies were applied to LaF$_3$ and CeF$_3$ because they are those NCs with a pure patchy behaviour (without evidences of aggregation by citrate mediated bridges with temperature). As expected, LaF$_3$ and CeF$_3$ synthesised by hydrothermal treatment (Figure 4.23) show bigger particles with a more hexagonal-faceted shape.
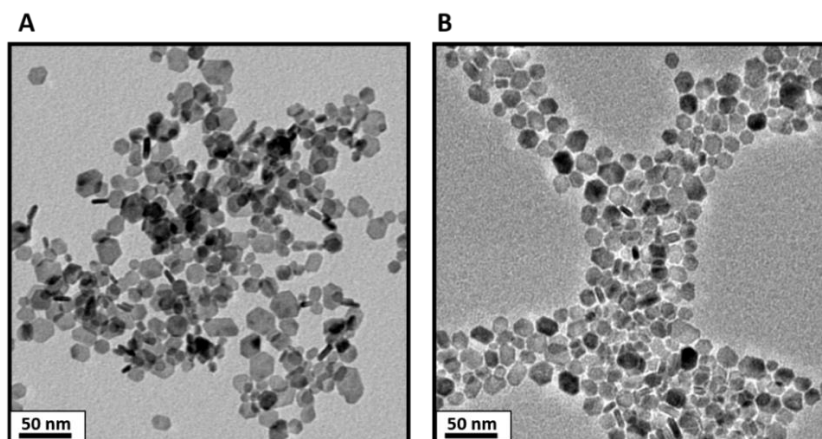
Figure 4.23. (A) LaF₃ and (B) CeF₃ NCs obtained via hydrothermal method at 210 °C during 2 h.

Concerning their sizes, we obtained NCs of ~12 per 4 nm sized particles (smaller than the obtained with a post-hydrothermal treatment from those obtained with co-precipitation method) (Table 4.6). In this case, we postulated that the difference in size could be related considering the growth factors in both approximations. Firstly, if NCs are synthesised by co-precipitation method and then exposed to high temperatures, we are promoting an Ostwald ripening process,[27] in which the smaller obtained NCs are split to grow allowing the homogenisation of the system. In contrast, if NCs are synthesised directly by a hydrothermal treatment, they are prone to grow until the final stabilisation of their surface, allowing smaller NCs (~12 nm) compared with those obtained after the Ostwald ripening (~16 nm).

Table 4.6. Comparison between different TEM sizes of LaF₃ and CeF₃ NCs obtained via hydrothermal and MW treatments.

Particles	TEM size (length)	TEM size (width)
LaF₃ hydrothermal at 210 °C	12.1 ± 2.0 nm	3.9 ± 1.0 nm
CeF₃ hydrothermal at 210 °C	12.6 ± 1.4 nm	4.7 ± 0.9 nm
LaF₃ MW at 200 °C	11.5 ± 3.2 nm	4.0 ± 0.8 nm
CeF₃ MW at 200 °C	12.7 ± 2.5 nm	4.6 ± 0.7 nm

The use of MW allows to obtain hexagonal faceted NCs, homogeneous and dispersible in water as in the case of hydrothermal treatment (Figure 4.24). Final NCs show the same size and stability of those particles obtained by hydrothermal treatment (see Table 4.6 to compare). Analysing in detail the obtained TEM images (Figure 4.23 and 4.24), it seems that NCs obtained using hydrothermal treatment show more hexagonal-faceted shape than those prepared by MW radiation. This effect could be related with the reaction time, the hydrothermal treatment with 2 h of reaction should allow a slow growing process forming hexagonal faceted NCs. Alternatively, a MW reaction allows the fast nucleation and growth of the NCs forming a less-defined shape LaF₃ particles.
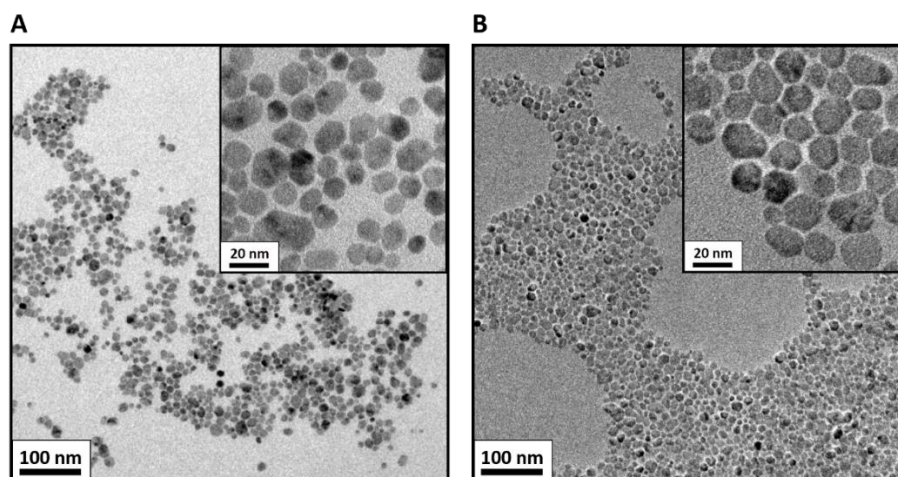
Figure 4.24. TEM images of LaF₃ (A) and CeF₃ (B) NCs obtained via MW process at 200 °C during 20 min.

Concerning the crystallinity of these NCs obtained by high-thermal methods, we performed powder XRD measurements of all powdered samples (Figure 4.25). All samples show the typical hexagonal crystalline structure as those obtained by co-precipitation method. In general terms, we can observe that the samples obtained by an hydrothermal treatment show more relative intensity in the XRD pattern, although their crystallinity is comparable. Concerning the width of the peaks (related with particle crystalline size by Scherrer equation), both samples show the same magnitude, explaining the histogram sizes obtained by TEM (same values for both methodologies).
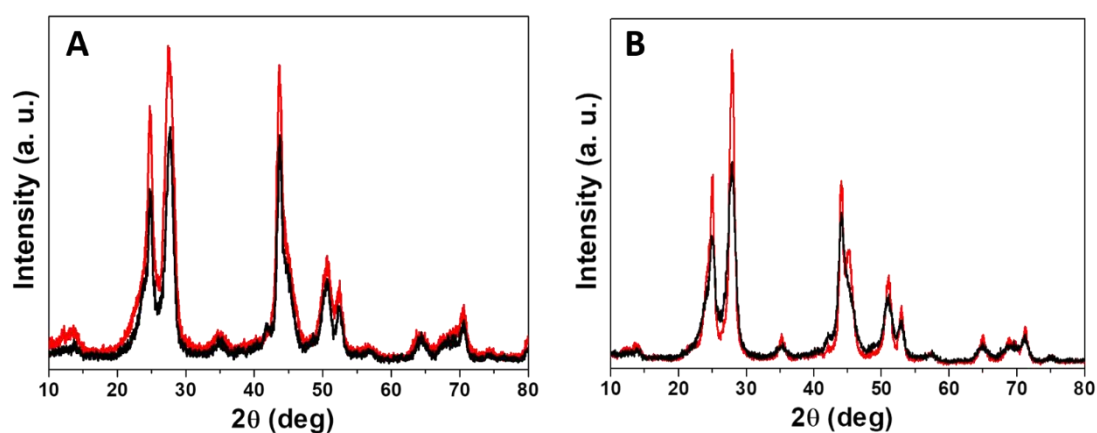

Figure 4.25. Powder XRD of LaF₃ (A) and CeF₃ (B) NCs obtained via hydrothermal treatment at 210 °C during 2 h (red spectra) and via MW process at 200 °C during 20 min (black spectra).

After these results, the two high temperature methods show us compatible results concerning size and crystallinity. The main differences are the reaction time, allowing fast synthesis in MW treatments and the final shape of NCs, obtaining better defined particles at large time reactions.

4.4 Conclusions

In summary, it is presented a model of faceted-charge patchy NCs in which cations or anions are adsorbed selectively onto different NC surfaces. This model has been investigated accurately starting from experimental evidence and finally ensured via MD simulations. NC faceting, promoted by the formation of hexagonal crystalline structure, allows the formation of thermodynamically stable patchy NCs. Interestingly, NC core shows these patches due to the exposed atoms in the different exposed planes. This new approach to create discrete patches onto NC surface allows the easy and fast synthesis of thermodynamically stable patchy NCs.

Consequently, cations and anions are selectively anchored spontaneously in different exposed planes creating ionic stabilised patchy NCs. This functionalisation can be done in the same synthetic process using determinate ions (carboxylates to coordinate the metal and nitrogen-based cations to stabilise fluoride position). The different behaviour of the exposed planes makes possible easily exchanges to be able to functionalise, the obtained NCs, with wished ligands selectively.

When water is replaced for methanol, NC surface releases adsorbed water in specific planes to adsorbed methanol, stabilising NCs in the new medium. This effect produces the adsorption of some tetramethylammonium onto NC surface in contrast with the simulations performed in water. Moreover, cations initially in the diffusion layer move to Stern layer to minimise the negative charge, being the new surface chemistry stable in methanol without observable instability.

The final part of this Chapter (growing processes) opens interesting pathways to be analysed deeply in the near future. We demonstrate that these patchy NCs not only can be synthesised using other thermal methods (MW and hydrothermal), but also it is possible to perform post-hydrothermal treatments to growth and functionalise selectively the NCs. A functionalisation based on the generation of dioxo-pyridine ring based dyes attached onto NCs surface was performed. These systems are able to be doped (by the addition of different lanthanide cations during the synthesis), obtaining a dual fluorometric device.

4.5   References

[1]   Z. Zhang, S. C. Glotzer, *Nano Lett.* **2004**, *4*, 1407–1413.

[2]   I. C. Pons-Siepermann, S. C. Glotzer, *ACS Nano* **2012**, *6*, 3919–3924.

[3]   R. M. Choueiri, E. Galati, A. Klinkova, H. Thérien-Aubin, E. Kumacheva, *Faraday Discuss.* **2016**, *191*, 189–204.

[4]   D. J. Lunn, J. R. Finnegan, I. Manners, *Chem. Sci.* **2015**, *6*, 3663–3673.

[5]   O. D. Velev, *Nat. Nanotechnol.* **2013**, *8*, 620–621.

[6]   C. Singh, A. M. Jackson, F. Stellacci, S. C. Glotzer, *J. Am. Chem. Soc.* **2009**, *131*, 16377–16379.

[7]   W. Fan, L. Liu, H. Zhao, *Angew. Chemie - Int. Ed.* **2017**, *56*, 8844–8848.

[8]   J. R. Finnegan, J. Gwyther, I. Manners, *Angew. Chemie - Int. Ed.* **2017**, *56*, 2842–2844.

[9]   B. Luo, J. W. Smith, Z. Wu, J. Kim, Z. Ou, Q. Chen, *ACS Nano* **2017**, *11*, 7626–7633.

[10]   S. Pothorszky, D. Zámbó, D. Szekrényes, Z. Hajnal, A. Deák, *Nanoscale* **2017**, *9*, 10344–10349.

[11]   R. M. Choueiri, E. Galati, H. Thérien-Aubin, A. Klinkova, E. M. Larin, A. Querejeta-Fernández, L. Han, H. L. Xin, O. Gang, E. B. Zhulina, et al., *Nature* **2016**, *538*, 79–83.

[12]   E. M. See, C. L. Peck, W. L. Santos, H. D. Robinson, *Langmuir* **2017**, *33*, 10927–10935.

[13]   J. Martínez-Esaín, T. Puig, X. Obradors, J. Ros, R. Yáñez, J. Faraudo, S. Ricart, *Angew. Chemie - Int. Ed.* **2018**, DOI: 10.1002/ange.201806273.

[14]   S. Bernal, F. J. Botana, J. J. Calvino, C. López, J. a. Pérez-Omil, J. M. Rodríguez-Izquierdo, *J. Chem. Soc. Faraday Trans.* **1996**, *92*, 2799–2809.

[15]   S. Bernal, F. J. Botana, J. J. Calvino, C. López-Cartes, J. A. Pérez-Omil, J. M. Rodríguez-Izquierdo, *Ultramicroscopy* **1998**, *72*, 135–164.

[16]   C. Calero, J. Faraudo, M. Aguilella-Arzo, *Mol. Simul.* **2011**, *37*, 123–134.

[17]   W. Humphrey, A. Dalke, K. Schulten, *J. Mol. Graph.* **1996**, *14*, 33–38.

[18]   T. Preocanin, A. Abdelmonem, G. Montavon, J. Luetzenkirchen, *Charging Behavior of Clays and Clay Minerals in Aqueous Electrolyte Solutions — Experimental Methods for Measuring the Charge and Interpreting the Results*, **2016**.

[19]   J. Martínez-Esaín, J. Ros, J. Faraudo, S. Ricart, R. Yáñez, *Langmuir* **2018**, *34*, 6443–6453.

[20]   X. Zheng, M. Liu, M. He, D. J. Pine, M. Weck, *Angew. Chemie - Int. Ed.* **2017**, *56*, 5507–5511.

[21]   J. Martinez-Esain, J. Faraudo, T. Puig, X. Obradors, J. Ros, S. Ricart, R. Yáñez, *J. Am. Chem. Soc.* **2018**, *140*, 2127–2134.

[22]   K. Kristinaitytė, L. Dagys, J. Kausteklis, V. Klimavicius, I. Doroshenko,

V. Pogorelov, N. R. Valevičienė, V. Balevicius, *J. Mol. Liq.* **2017**, *235*, 1–6.

[23] T. Tsukahara, A. Hibara, Y. Ikeda, T. Kitamori, *Angew. Chemie - Int. Ed.* **2007**, *46*, 1180–1183.

[24] Z. Xie, J. P. Kim, Q. Cai, Y. Zhang, J. Guo, R. S. Dhami, L. Li, B. Kong, Y. Su, K. A. Schug, et al., *Acta Biomater.* **2017**, *50*, 361–369.

[25] B. L. Silva, P. T. C. Freire, F. E. a. Melo, I. Guedes, M. a. Araújo Silva, J. Mendes Filho, a. J. D. Moreno, *Brazilian J. Phys.* **1998**, *28*, 19–24.

[26] K. De Keukeleere, J. De Roo, P. Lommens, J. C. Martins, P. Van Der Voort, I. Van Driessche, *Inorg. Chem.* **2015**, *54*, 3469–3476.

[27] J. Yao, K. Elder, H. Guo, M. Grant, *Phys. Rev. B* **1993**, *47*, 14110–14125.

5

Selective ligand exchanges in LaF$_3$ nanocrystals
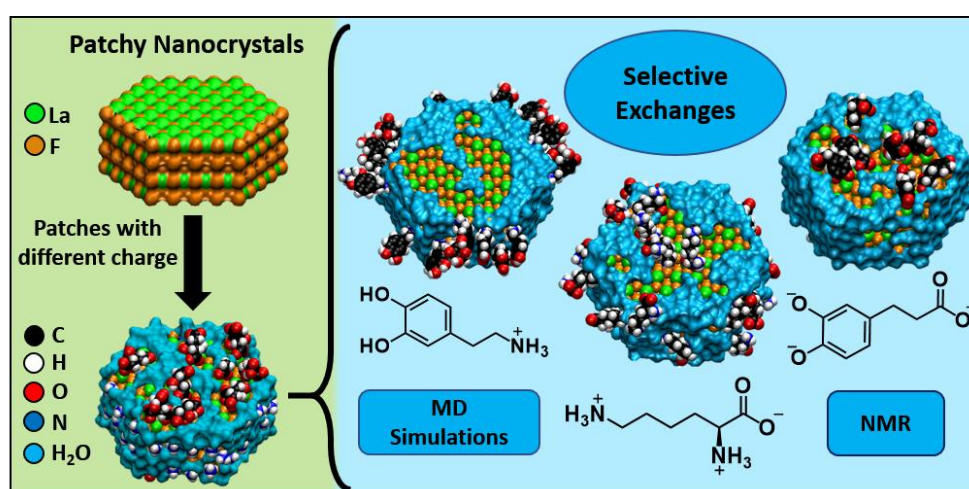
We present an easy method of selective ligand exchange onto faceted patchy LaF$_3$ nanocrystals in aqueous medium. These particles possess hydrophilic exposed faces (stabilised by carboxylates) and more hydrophobic/less hydrophilic faces with attached ammonium cations. We employed experimental techniques (mainly ^{1}H NMR) and MD simulations to unravel the substitution mechanisms and characterise the final systems. Our results demonstrate that it is possible to selectively introduce dopamine with the corresponding release of ammonium cation on rectangular faceted planes. Likewise, we observe how 3,4-dihydroxyhydrocinnamate is able to be adsorbed onto nanocrystal surface releasing citrate in the hexagonal faceted planes, if the ligand is totally deprotonated. Finally, using a zwitterionic molecule (e.g. lysine), we were able to completely modify all surface chemistry, having lysine as the only stabilising molecule of LaF$_3$ nanocrystals. The presented knowledge in this chapter could be considered as proof of concept that nanocrystals can be synthesised by an easy procedure and finally selectively surface modified for specific applications.

5.1 Introduction

Concerning the main goals of this thesis, after the successful synthesis of metal fluoride nanocrystals (NCs) and their complete study, we aimed to functionalise selectively their surface, obtaining different coated NCs. Once patchy LaF$_3$ NCs were obtained and fully characterised in the previous chapter, we want to go one step further in their study. Considering that these patchy NCs show spontaneously different coated faces, we chose LaF$_3$ as starting point to selectively exchange their stabilisers (cationic and anionic). In addition, our motivation is not only related to the switch of the coating ligands, but also in the complete understanding of the processes to make it extensible to other nanoscaled systems.

Currently, two different approximations are emphasised; NMR analysis[1–3] (by 1D and 2D experiments) and computational techniques[4–6] (e.g. all-atomistic MD simulations). NMR experiments are suitable to characterise NC surface to detect the organic molecules attached onto the surface as well as to ensure if they are coordinated or free in the medium. De Roo et al.[1] reported the role played by carboxylic acids and amines onto the surface of metal oxide NCs and their catalytic properties[7] via NMR technique. Concerning MD simulations, the complete screening of the NC interface in all-atomistic detail, gives us the opportunity to explore the behaviour that we are not able to observe using common experimental techniques. In fact, the identification of the citrate mediated ionic bridge (explained in Chapter 2) was possible thanks to MD simulations in metal fluoride NC systems.[6] In addition, the identification of patchy NCs with selective ligand and solvent interactions onto NC surface presented in Chapter 4 was possible thanks to all-atomistic screening via MD simulations.[8]

In this chapter, we used 1D and 2D NMR techniques combined with all-atomic detailed MD simulations to explore deeply the insights of ligand exchange mechanisms in colloidal chemistry. Thanks to the patches obtained in LaF$_3$ NCs and their selective ligand attachment, we tried ligand exchange by modifying cations or anions as desired. Dopamine hydrochloride has been used as nitrogenated ligand to exchange ammonium from NC surface while 3,4-dihydroxyhydrocinnamic acid has been selected as anionic stabiliser to release citrate and acetate ions. Final approximation was the use of a zwitterionic molecule such as lysine to release all ions from the NC surface obtaining at the end lysine-stabilised NCs in which lysine should display two different binding modes; by carboxylate onto {0001} planes and protonated amine stabilising {1$\bar{1}$00} planes as X'-type ligand. Experimentally, these exchanges were studied by ^{1}H NMR to identify the ligand and by NOESY experiments to ensure its attachment onto the NC surface. To disclose the mechanistic insights, MD simulations have been applied in all systems obtaining the full-picture of the surface chemistry of these exchanges.

5.2 Experimental

5.2.1 Synthetic details

❖ **Particle synthesis**

LaF$_3$ NCs were obtained using the synthetic approach explained in the experimental part of Chapter 4 (Co-precipitation method).

❖ **Aqueous ligand exchange**

General procedure to perform the ligand exchange in water consist of the addition of 20 mg of the desired ligand (dopamine hydrochloride, 3,4-dihydroxyhydrocinnamic acid or L-lysine hydrochloride) onto 1 mL of washed LaF$_3$ NCs ~70 mM in water. In the case of 3,4-dihydroxyhydrocinnamic acid ligand, the addition of 3 equivalents of tetramethylammonium hydroxide was required. After that, the solution was treated during 10 min in an ultrasonic bath to promote the exchange. Final solutions were washed twice with acetone and re-dispersed in 1 mL of Milli-Q water.

❖ **Organic ligand exchange**

General procedure to perform the ligand exchange in toluene consist of the previous precipitation of LaF$_3$ NCs from water dispersion using a mixture of ethyl ether and 2-propanol 2:1. After the addition of 1 mL of toluene, 40 mg of the desired ligand (glutaric acid or 3,4-dihydroxyhydrocinnamic acid) was added to a milky dispersion. It is necessary the addition of 200 µL of oleylamine. After that, the solution was treated during 10 min in an ultrasonic bath to promote the exchange. Final solutions were washed twice with 2-propanol and re-dispersed in 1 mL of toluene.

5.2.2 Characterisation

For dynamic light scattering (DLS) and zeta-potential measurements, a Malvern Nano ZS was used in back-scattering mode (173°). Transmission electron microscopy (TEM) images were taken on a JEOL JEM-2200FS TEM with Cs corrector and with a 120 kV JEOL 1210 TEM, which has a resolution point of 3.2 Å. Ultraviolet-Visible (UV-Vis) measurements were run on a spectrophotometer (Cary 500, Varian) equipped with a quartz cell having a path length of 1 cm in the range of 200-600 nm. Nuclear magnetic resonance (NMR) measurements were recorded on a Bruker Avance III spectrometer operating at a ^{1}H frequency of 500.13 MHz and equipped with a BBI-Z probe. For each NMR measurement, 500 µL or 750 µL ampoule of dry deuterated solvent was used. The sample temperature was set to 298.2 K. One-dimensional (1D) ^{1}H and 2D NOESY (nuclear Overhauser effect spectroscopy)

spectra were acquired using standard pulse sequences from the Bruker library.

5.2.3 Computer simulations

All basic computational details used during this Chapter are the same of Chapter 4, using in this case as starting point, the equilibrium configuration of Sim1 explained in Chapter 4. However, in the case of the starting simulation with implicit water, we used the same parameters than Chapter 2.

During the MD simulations, the atomic positions of La and F atoms were maintained fixed at their initial values, avoiding the need of considering explicitly the interaction between lanthanum and fluorine. The interaction of lanthanum and fluorine atoms with all other atoms of the system (atoms from water or the ions) was modelled with CHARMM force-field with electrostatic interactions (due to particle charges) and Lennard-Jones interactions. The Lennard-Jones parameters employed for fluorine were standard CHARMM values. For lanthanum, we have considered a previous work using the same parameters.[9] Parameters of the new used ions (protonated dopamine, trivalent 3,4-dihydroxyhydrocinnamate and protonated lysine), were generated by analogy by CHARMM General Force Field (CGenFF) program version 1.0.0 and detailed in the SI. The composition of each system is described in Table 5.1.

❖ Preparation of Sim1

For the Sim1 system, we started from the equilibrium configuration of Sim1 of Chapter 4 in which we released all water and ions in the diffuse layer. In other words, we maintained the NC and ions/water directly adsorbed onto NC surface (Stern layer). After this, we introduced protonated dopamine and chloride anions as described in Table 5.1. Before the addition of water box, we ran a simulation with implicit water to recreate the effect of the ultrasonic bath, after that we solvated the system in a water box. After that, we ran the system with explicit water.

❖ Preparation of Sim2

For the Sim2 system, we started from the equilibrium configuration of Sim1 of Chapter 4 in which we released all water and ions of the diffuse layer, maintaining the NC and ions/water directly adsorbed onto NC surface (Stern layer). After that, we introduced trivalent 3,4-dihydroxyhydrocinnamate anions and tetramethylammonium cations as described in Table 5.1. Before the addition of water box, we ran a simulation with implicit water to recreate the effect of the ultrasonic bath, after that we solvated the system in a water box. After that, we ran the system with explicit water.

❖ <u>Preparation of Sim3</u>

For the Sim3 system, we started from the equilibrium configuration of Sim1 of Chapter 4 in which we released all water and ions of the diffuse layer, maintaining the NC and ions/water directly adsorbed onto NC surface (Stern layer). After that, we introduced protonated lysine and chloride anions as described in Table 5.1. Before the addition of water box, we ran a simulation with implicit water to recreate the effect of the ultrasonic bath, after that we solvated the system in a water box. After that, we ran the system with explicit water.

Table 5.1. Number of organic molecules, total number of atoms (including NC atoms) and size of the water box in each simulation. Tma is tetramethylammonium and Cin corresponds to 3,4-dihydroxyhydrocinnamate.

	Sim1	Sim2	Sim 3
Citrate	13	13	13
Acetate	10	10	10
Ammonium	37	37	37
Tma	12	72	12
Dopamine	40	-	-
Cin	-	20	-
Lysine	-	-	40
Chloride	40	-	40
Water	62,261	64,628	65,038
Total Atoms	189,144	196,705	197,555
Box size (Å)	125 x 125 x 127	127 x 127 x128	129 x 126 x 128

For each case, simulation times were selected to achieve the maximum information with the minimum computational consume. Sim1 (20 ns), Sim2 (2 ns) and Sim3 (2 ns) all of them performed in water at 25 °C.

5.3 Results and discussion

5.3.1 From stable NCs to stable NCs

Commonly, ligand exchange methodologies have been applied when aggregated NCs are obtained in the synthetic process. Ligand exchange methodologies are used to promote stable colloidal solutions with the desired stabilising agents, even when the system could be aggregated, if particles show good appearance by TEM and high crystallinity by XRD.[10] In our

specific case, LaF$_3$ NCs have been successfully obtained by a simple co-precipitation method allowing the formation of small, homogeneous and well-dispersed NCs (Figure 5.1).
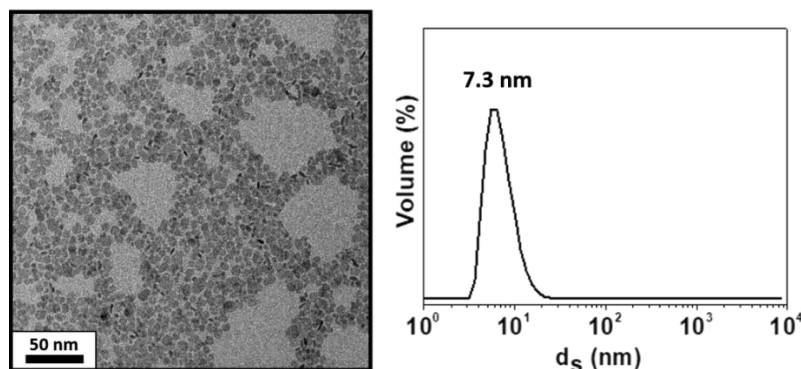

Figure 5.1. TEM and DLS of LaF$_3$ NCs obtained by the co-precipitation method in water at 100 °C.

As we observed in Chapter 4, the surface chemistry of these NCs is composed by acetate, citrate and ammonium directly attached to NC surface and tetramethylammonium cation as counter ion neutralising the global negative charge. By ^{1}H NMR, we could detect tetramethylammonium, citrate and acetate ions in D$_2$O (Figure 5.2). However, ammonium cation is not visible by NMR performed in water due to the fast exchange between deuterium and hydrogen.
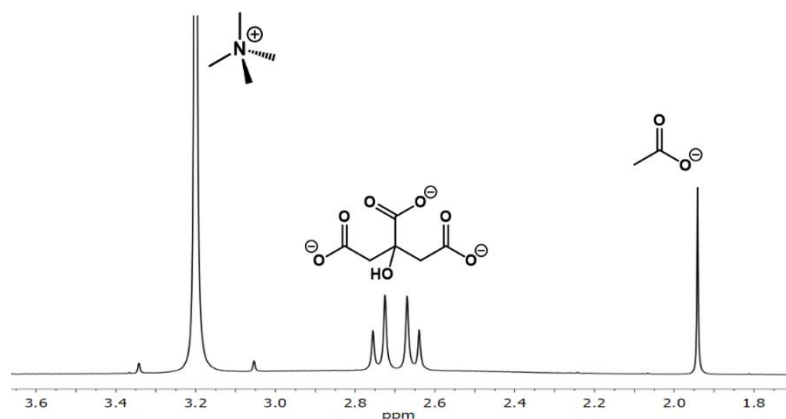

Figure 5.2. ^{1}H NMR spectrum of LaF$_3$ NCs in D$_2$O and the main peak assignation corresponding to the represented ions.

Regarding the General Introduction of this thesis, 2D NMR experiments are used to characterise NC surfaces, to distinguish if the detected ligands are bonded to the surface or are free in the medium. Trying to confirm experimentally if citrate, acetate and tetramethylammonium are attached or not onto NC surface, we performed NOESY experiment at room temperature to the five-times washed NCs (Figure 5.3A). 2D NOESY NMR spectrum shows a notable drawback in our surface chemistry. To see if a molecule shows a negative or positive cross-peak, we need at least two hydrogen signals produced by the same molecule, separated enough to observe the NOE effect.
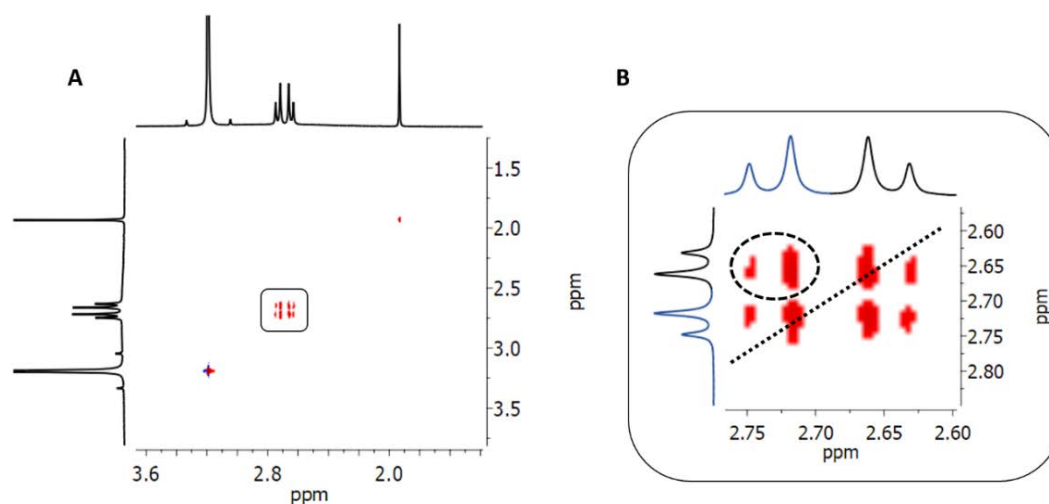
Figure 5.3. (A) Room temperature NOESY spectrum of the resulting suspension of as-synthesised LaF₃ NCs in D₂O and (B) Enlarged zone where it can be observed negative cross-peak effects. Positive NOE effect is represented in blue while negative NOE effect is observed in red.

Only citrate shows more than one peak in ¹H NMR, a doublet for each proton of the -CH₂- groups. In Figure 5.3B, the enlarged zone of the citrate signals is shown, in which the diagonal peaks (self-cross peaks) and a negative cross peak (noted with a discontinuous circle) are observed. This negative NOESY effect between the different signals of citrate could means that this molecule is attached onto NC surface. However, due to the distance between this cross-peak to the diagonal, it could be controversial to be ensured only with NMR technique. As in Chapter 4 where we observed this attachment using several techniques (experimental and MD simulations), we postulate that citrate presents a negative NOESY effect. Considering the surface chemistry of LaF₃ patchy NCs, {0001} planes are stabilised by carboxylate-based anions (citrate and acetate) while exposed {1$\bar{1}$00} planes are stabilised by ammonium cations (Figure 5.4A).
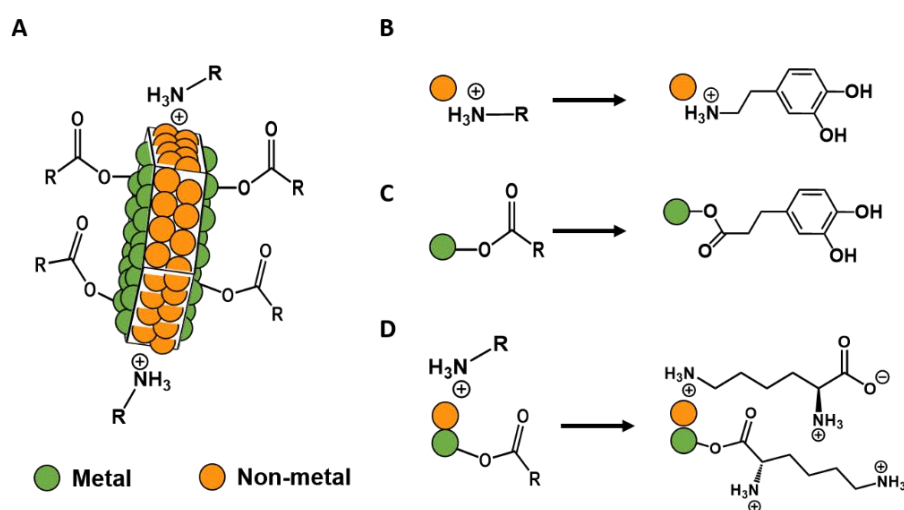

Figure 5.4. (A) Schematic representation of the surface chemistry of LaF₃ patchy NCs. (B) Selective exchanges of ammonium by dopamine, (C) selective exchange of carboxylates by 3,4-dihydroxyhydrocinnamic acid and (D) total ligand exchange using a zwitterionic molecule as lysine.

The first approximation is the exchange of ammonium cations attached onto $\{1\bar{1}00\}$ planes using dopamine hydrochloride (Figure 5.4B). Dopamine has been selected due to its biocompatibility with a terminal -NH_3^+ group with low steric hindrance able to completely substitute ammonium cations from the NC surface. To be able to compare between cationic and anionic exchanges, we used 3,4-dihydroxyhydrocinnamic acid because it has the same chemical structure than dopamine but containing a carboxylic group instead of an amine. This molecule should be able to release carboxylate ligands from the NC surface, as represented in Figure 5.4C.

Finally, we aimed to exchange all the attached ligands onto NC surface by a new unique molecule. To this goal, zwitterionic lysine, in its acidic form was selected because it has a carboxylate and a low-steric hindrance ammonium group in its structure (Figure 5.4D). This molecule should be able to interact with the ammonium group onto $\{1\bar{1}00\}$ planes while carboxylate should interact onto $\{0001\}$ planes.

5.3.2 Selective cationic exchange. Dopamine

Firstly, we used dopamine hydrochloride to exchange ammonium cations from the NC surface, being at the end dopamine stabilised NCs in their $\{1\bar{1}00\}$ planes. Using as-synthesised LaF_3 NCs (see Chapter 4, section 4.3.1), dopamine hydrochloride was added. The resulting colloidal solution was treated in an ultrasonic bath during 10 min to perform the exchange, without visual modifications of the initial solution (Figure 5.5). After this time, the colloidal solution was washed twice with acetone and re-dispersed in MilliQ water.

TEM and DLS analysis were carried out to ensure the stability and the homogeneity of the NCs after the exchange procedure (Figure 5.5). Initial characterisation showed a homogeneous LaF_3 colloidal suspension of ~8 nm size, confirming the no aggregation of NCs after the exchange.

To study in detail the surface chemistry of this colloidal solution and to ensure if the exchange had been carried out successfully, we used ^1H NMR to see the organic stabilisers onto the NC surface and NOESY experiments to ensure their coordination (or not) by the presence (or not) of a negative cross-peak. These NCs were dried with air flow and directly re-dispersed in D_2O, minimising further problems with their re-dispersibility after the drying process.
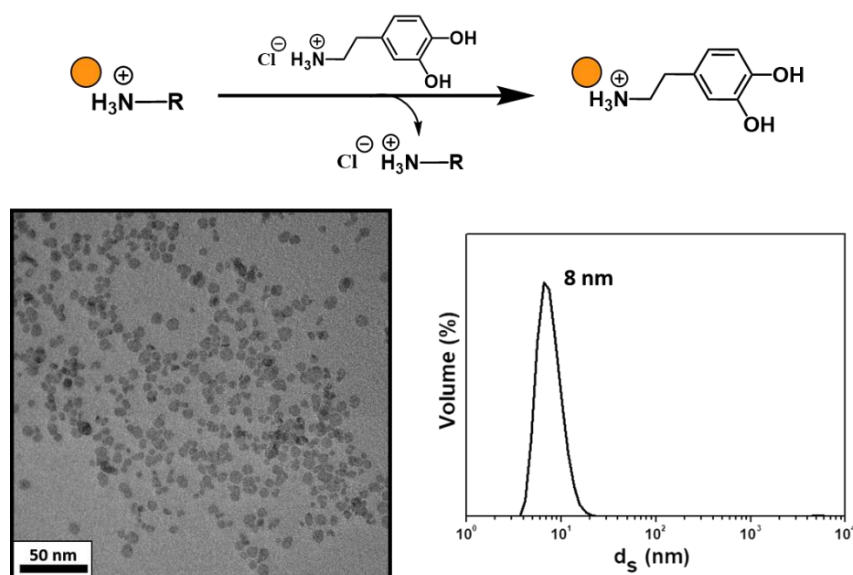
Figure 5.5. Schematic representation of the ligand exchange reaction in cations attached to fluoride atoms onto surface (orange spheres). TEM and DLS of LaF₃ NCs obtained after the ligand exchange with dopamine hydrochloride in water at room temperature.

We observed the main peaks of dopamine in the spectrum after the ligand exchange (Figure 5.6B). All the signals are broader without visible multiplicity, due to the effect explained in Chapter 1 by the equation 1.2, meaning the attachment of dopamine onto NC surface. In the spectrum we also found the presence of citrate and acetate, which should be attached onto {0001} planes. Just to recall, dopamine should promote the exchange of ammonium onto {1$\bar{1}$00} planes (cationic exchange), maintaining the anions in the same positions. To ensure the attachment of dopamine, 2D NOESY spectrum was recorded (Figure 5.7) to see negative cross-peaks between the different dopamine hydrogens.
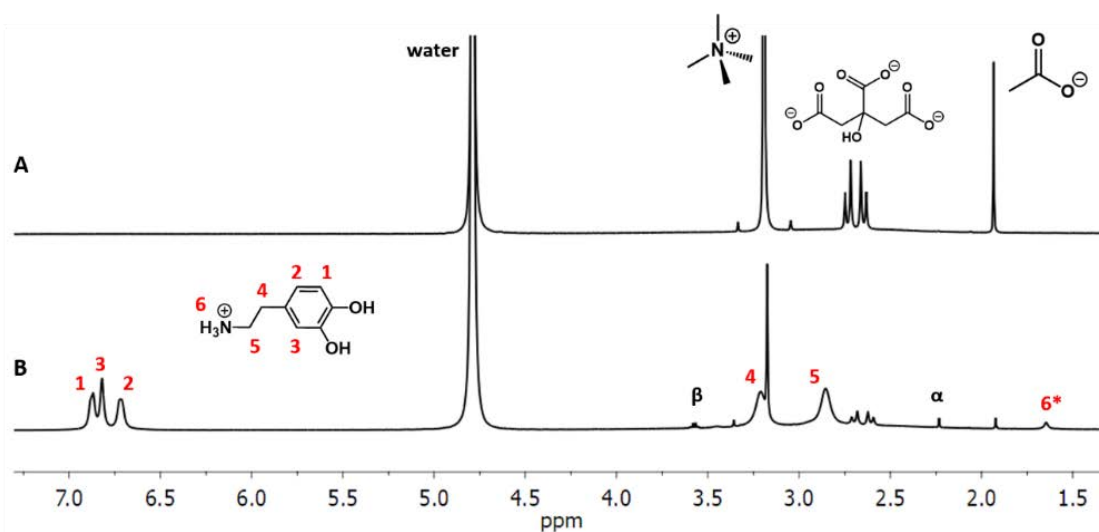

Figure 5.6. (A) ¹H NMR spectrum of LaF₃ NCs in D₂O with its peak assignation. (B) ¹H NMR spectrum of LaF₃ NCs after the ligand exchange with dopamine hydrochloride in D₂O with its peak assignation. *This assignation could be compatible with -NH₃⁺ hydrogens if they are fixed onto NC surface avoiding the H-D exchange.
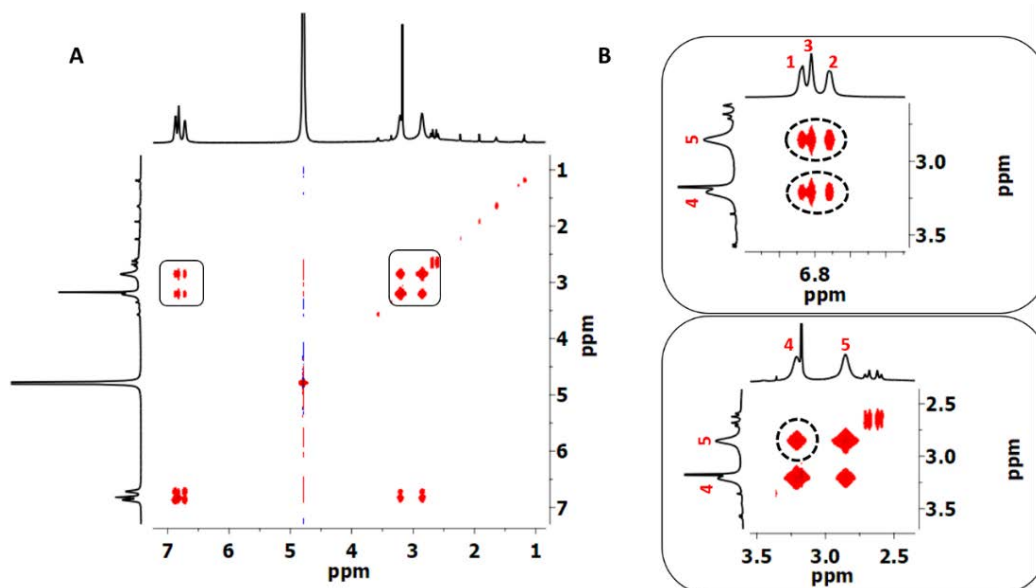
Figure 5.7. (A) Room temperature NOESY spectrum of the resulting suspension of LaF₃ NCs after ligand exchange in D₂O and (B) Enlarged zones where it can be observed negative cross-peak effects. Positive NOE effect is represented in blue while the negative NOE effect is observed in red.

In Figure 5.7A, clear negative NOE cross-peaks are observed for the distinct dopamine signals, allowing us to ensure its coordination onto the NC surface. To easily clarify the cross peaks, in Figure 5.7B an enlarged zone of the NOESY is shown to see the cross peak between aliphatic and aromatic signals and the once between the two different -CH₂- groups (protons 4 and 5). After the 1D and 2D NMR analysis we can conclude that the addition of dopamine hydrochloride allows the selective release of ammonium cations to attach dopamine-based cations. This exchange maintains onto the surface citrate and acetate anions and it seems to be compatible with the presence of tetramethylammonium as counter ion in this colloidal system.

5.3.3 Selective anionic exchange. 3,4-Dihydroxyhydrocinnamic acid

Once the selective exchange of cations from NC surface was achieved, we tried to release the anions by the attachment of 3,4-dihydroxyhydrocinnamate. Here, we focused in to exchange the citrate and acetate onto {0001} planes, maintaining ammonium cations stabilising the {1$\bar{1}$00} planes. In contrast with the dopamine case, 3,4-dihydroxyhydrocinnamic acid must be deprotonated to allow the coordination by the carboxylate moiety.

We added 3,4-dihydroxyhydrocinnamic acid and 1 equivalent of tetramethylammonium hydroxide into washed LaF₃ NCs. The resulting colloidal solution was treated in an ultrasonic bath during 10 min to promote the exchange and solution became coloured (red-brown). After this time, colloidal solution was washed twice with acetone and re-dispersed in MilliQ

water, obtaining a yellow-orange solution. After checking that DLS showed a good colloidal dispersion, the sample was dried and re-dispersed in D_2O to be analysed by NMR (Figure 5.8).
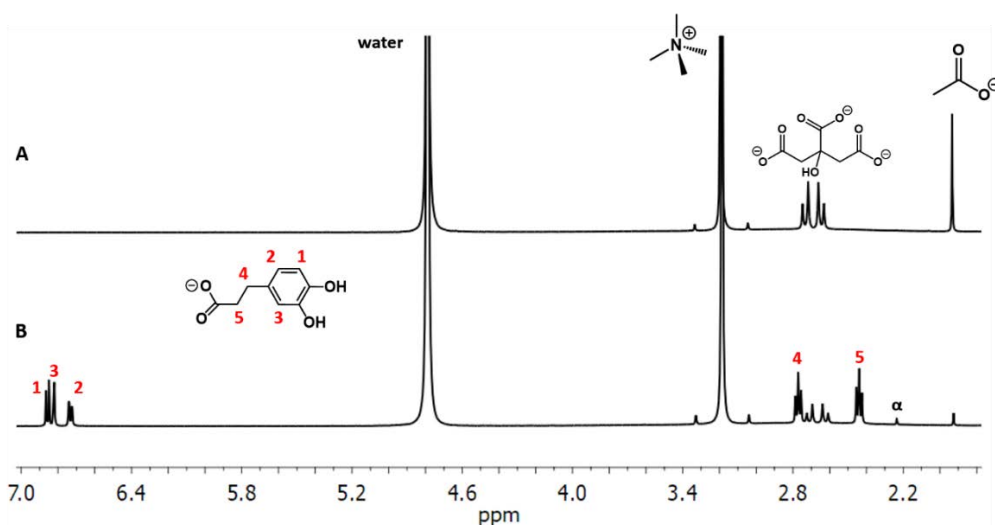

Figure 5.8. (A) ^{1}H NMR spectrum of LaF$_3$ NCs in D$_2$O with its peak assignation. **(B)** ^{1}H NMR spectrum of LaF$_3$ NCs after the ligand exchange with 3,4-dihydroxyhydrocinnamic acid and 1 equivalent of tetramethylammonium hydroxide in D$_2$O with its peak assignation.

Although in the ^{1}H NMR spectrum (after the ligand exchange) the main peaks of 3,4-dihidroxycinnamate were observed, they are narrow and well-defined suggesting that they could be free in the medium. To ensure this postulation, NOESY experiment was performed to see negative NOE cross peaks if the carboxylate is attached onto NC surface. In Figure 5.9 positive cross peaks between aromatic region and -CH$_2$- groups can be observed, confirming that 3,4-dihidroxicinnamate ligands are free into the solution.
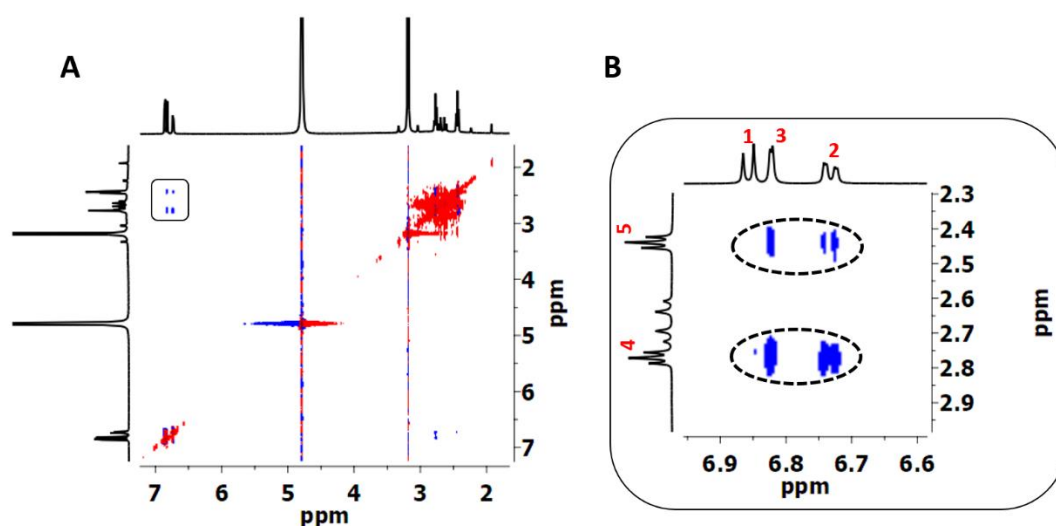

Figure 5.9. (A) Room temperature NOESY spectrum of the resulting suspension of LaF$_3$ NCs after ligand exchange in D$_2$O and **(B)** Enlarged zones where it can be observed positive cross-peak effects, meaning the free behaviour of the ligand. Positive NOE effect is represented in blue while negative NOE effect is observed in red.

To understand why 3,4-dihydroxyhydrocinnamic acid was not attached onto the NC surface, we added 20 µL of tetramethylammonium hydroxide to the NMR tub. The further addition of a base to the system could allow the total deprotonation of carboxylic group and both hydroxyl groups of the 3,4-dihidroxhydroycinnamate, allowing its attachment onto the NC surface. In Figure 5.10, signals concerning 3,4-dihydroxyhydrocinnamate disappeared and citrate is shifted to lower ppm values (meaning that it is released from the NC surface).
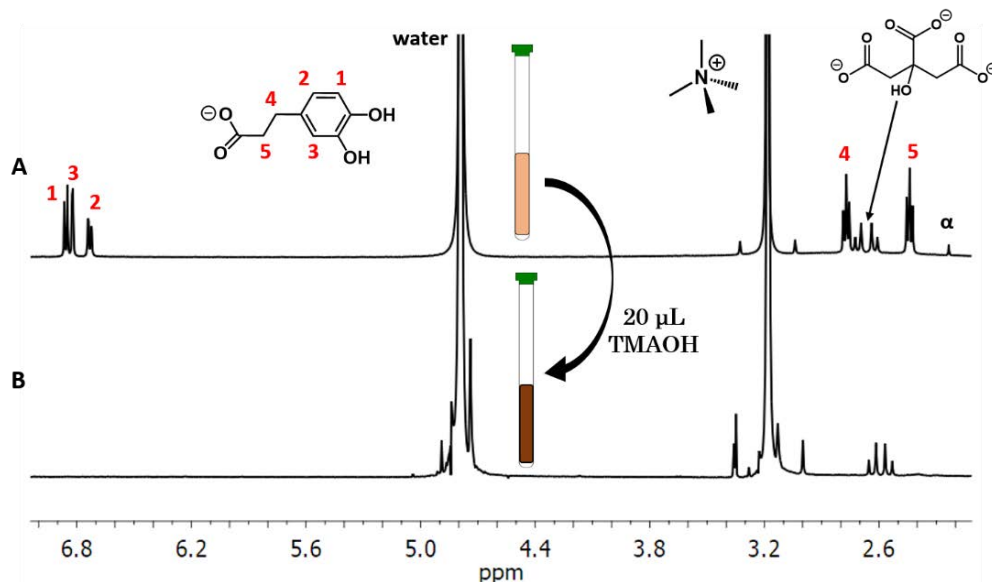

Figure 5.10. (A) ^{1}H NMR spectrum of LaF$_3$ NCs after the ligand exchange with 3,4-dihydroxyhydrocinnamic acid and 1 equivalent of tetramethylammonium hydroxide in D$_2$O with their peak assignations. (B) ^{1}H NMR spectrum after the addition of 20 µl of tetramethylammonium hydroxide to NMR tube.

The most interesting effect of the additional base to the system is the disappearance of the main peaks of 3,4-dihydroxyhydrocinnamate. We interpret this effect as a consequence of the deprotonation of hydroxyls and carboxylic acid with the basification, being the trivalent anion, the new ligand attached onto the NC surface using the 3 moieties. The close distance between the aromatic ring and the NC surface allowed π-interactions (aromatic ring with NC), making this molecule not observable by NMR.

To promote the exchange in one-step, we introduced 3 equivalents of tetramethylammonium hydroxide (Figure 5.11). Following this pathway, 3,4-dihydroxicitraconnic acid should be in its trivalent anionic form allowing the coordination and the exchange thanks to its three moieties. TEM and DLS results after the exchange are shown in Figure 5.11, stating the presence of homogeneous NCs of 9 nm size approximately.

To detect the new ligand onto the NC surface, we did a ^{1}H NMR analysis to observe the main peaks of 3,4-dihydroxyhydrocinnamate ligand onto NC surface (as in the case of dopamine). In Figure 5.12, it can be observed that after the ligand exchange and washing process, only solvent and

tetramethylammonium are identified by NMR. The presence of tetramethylammonium could be easily understood taking into account that the exchange was performed on the anions, releasing trivalent citrate and monovalent acetate to introduce a trivalent anion. As the exchange was carried out using the same counter ion (tetramethylammonium), this remains between the diffuse and Stern layer neutralising the global negative charge of the system.
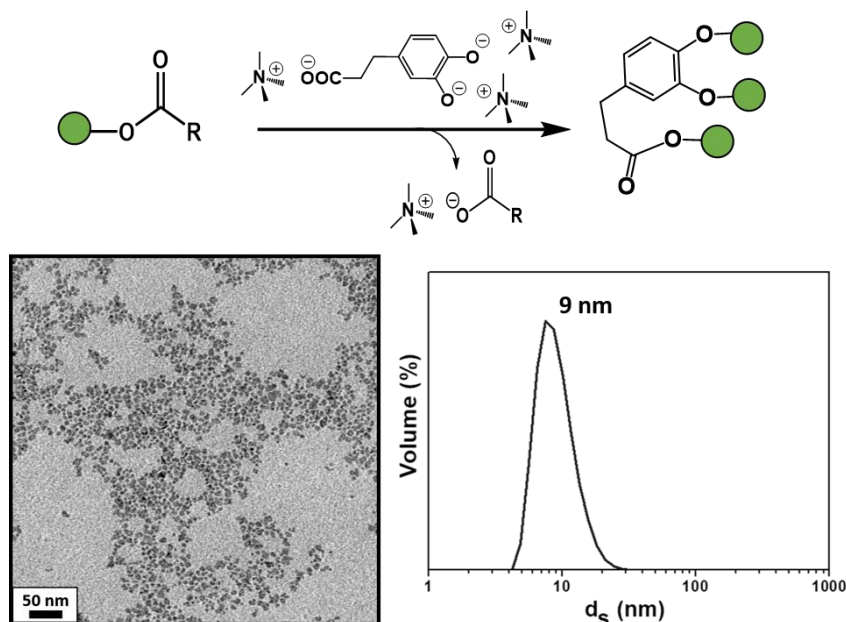

Figure 5.11. Schematic representation of the ligand exchange reaction in anions attached to lanthanum atoms onto surface (green spheres). TEM and DLS of LaF₃ NCs obtained after the ligand exchange with 3,4-dihydroxyhydrocinnamic acid with 3 equivalents of tetramethylammonium hydroxide in water at room temperature.

Concerning 3,4-dihydroxyhydrocinnamic acid, their peaks are not observed in the NMR spectrum, meaning that the new ligand was not attached onto NC surface or it is hardly coordinated through the three moieties, being impossible to detect it by NMR. Interestingly, the absence of 3,4-dihydroxyhydrocinnamic acid onto NC surface was discarded due to the colour of the final colloidal solution (orange-brown), which matches with the deprotonated form of 3,4-dihydroxyhydrocinnamic acid, being the coordination effect the unique plausible reason, for not being observed in NMR.

To detect 3,4-dihydroxyhydrocinnamic acid and considering the final colour of the colloidal solution, we performed UV-Vis measurements to confirm the attachment of the new ligand onto the NC surface. If we observe 3,4-dihydroxyhydrocinnamic acid via UV-Vis, this should be attached because if it will be free in the system, we could detect it via NMR as in the case of Figure 5.8. The broader band at ~270 nm in LaF₃@Cin NCs (Figure 5.13) matches with the narrower one observed in the ligand reference at 272 nm postulating the presence of 3,4-dihydroxyhydrocinnamic acid in its trivalent anionic form (avoiding its detection via NMR technique) onto the NC surface.
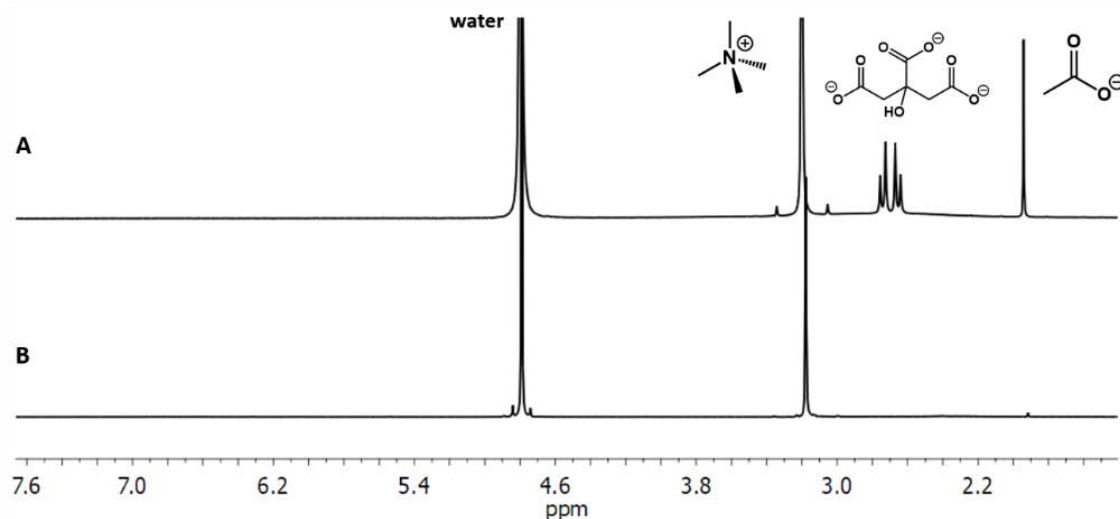
Figure 5.12. (A) ¹H NMR spectrum of LaF₃ NCs in D₂O with its peak assignation. (B) ¹H NMR spectrum of LaF₃ NCs after the ligand exchange with 3,4-dihydroxyhydrocinnamic acid and 3 equivalents of tetramethylammonium hydroxide in D₂O.
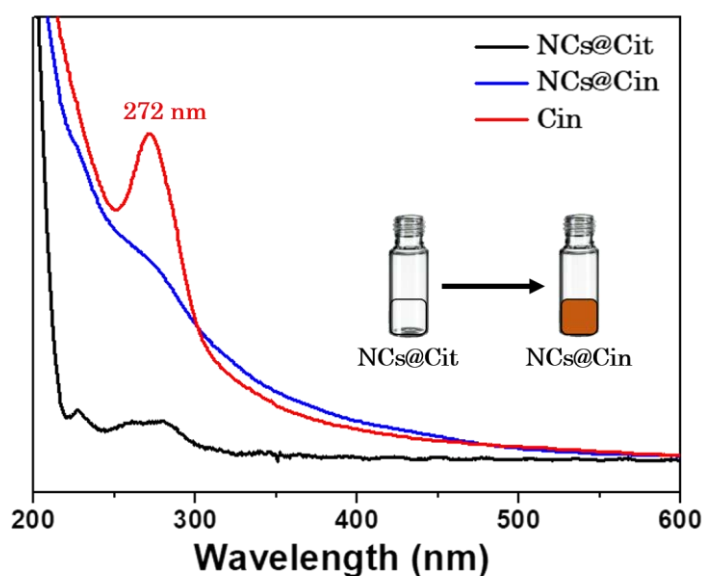
Figure 5.13. UV-VIS measurements of as-synthesised LaF₃ NCs (LaF₃@Cit, in black), LaF₃ NCs after the ligand exchange (LaF₃@Cin, in blue) and a reference of 3,4-dihydroxyhydrocinnamic acid with 3 equivalents of tetramethylammonium hydroxide (red).

The final coloured colloidal dispersion observed after the ligand exchange confirms that it successfully release citrate and acetate anions. In addition, we postulate that 3,4-dihydroxyhydrocinnamic acid is attached onto NC surface by its three different moieties (carboxylate and deprotonated hydroxyls of the catechol).

5.3.4 Homogenisation of the NC surface. L-Lysine

To conclude the postulations displayed in Figure 5.4, we performed the same ligand exchange methodology using L-Lysine which stabilises $\{1\bar{1}00\}$ planes through the protonated amine, while carboxylate should interact onto $\{0001\}$ planes. With the addition of L-lysine hydrochloride we are not only able to stabilise both exposed faces releasing cations and anions, but also replacing tetramethylammonium as counter ion in the system.

To do this, we used washed LaF$_3$ NCs in water adding L-Lysine hydrochloride, after 10 min under sonication, NCs were washed with acetone and re-dispersed in water before their characterisation (Figure 5.14). TEM and DLS measures showed a homogeneous system of nanoplatelets with 10 nm size in water, which means that the ligand exchange procedure did not affect the size and stability of the LaF$_3$ NCs.
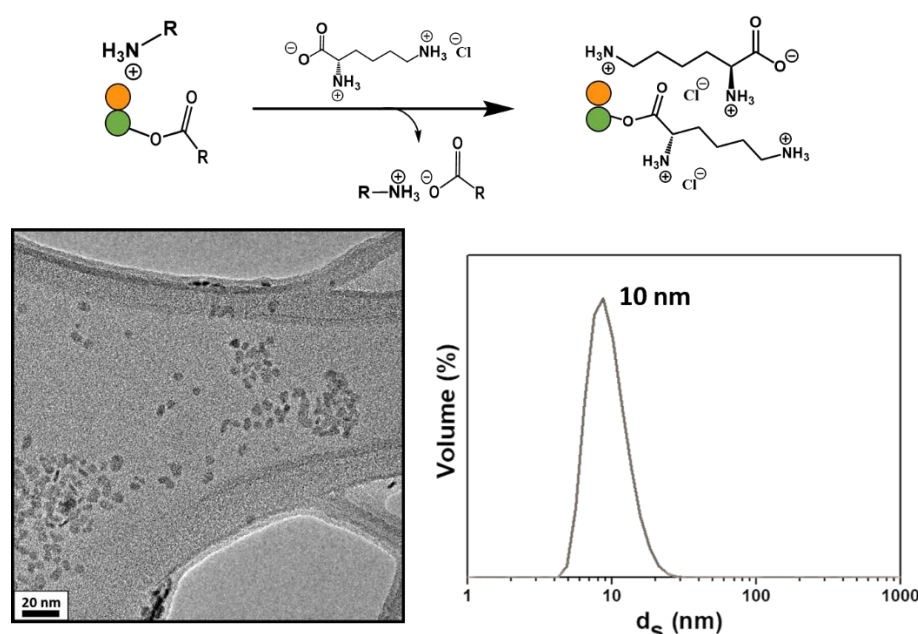

Figure 5.14. Schematic representation of the ligand exchange reaction in anions attached to lanthanum atoms onto surface (green spheres) and cations attached to fluoride atoms onto surface (orange spheres). TEM and DLS of LaF$_3$ NCs obtained after the ligand exchange with L-lysine hydrochloride in water at room temperature.

After the characterisation by TEM and DLS, we performed ^{1}H NMR analysis. In Figure 5.15B, the spectra of LaF$_3$ NCs after the exchange is presented, showing the main peaks of lysine and solvent, without the presence of impurities from the initial ligands (tetramethylammonium, citrate and acetate).

Peaks seem to be broader than the expected signals for free lysine, although their multiplicity could be observed more defined that in the case of dopamine (see Figure 5.6). To unveil if lysine is attached onto NC surface or free in the media, a NOESY experiment was carried out (Figure 5.16).
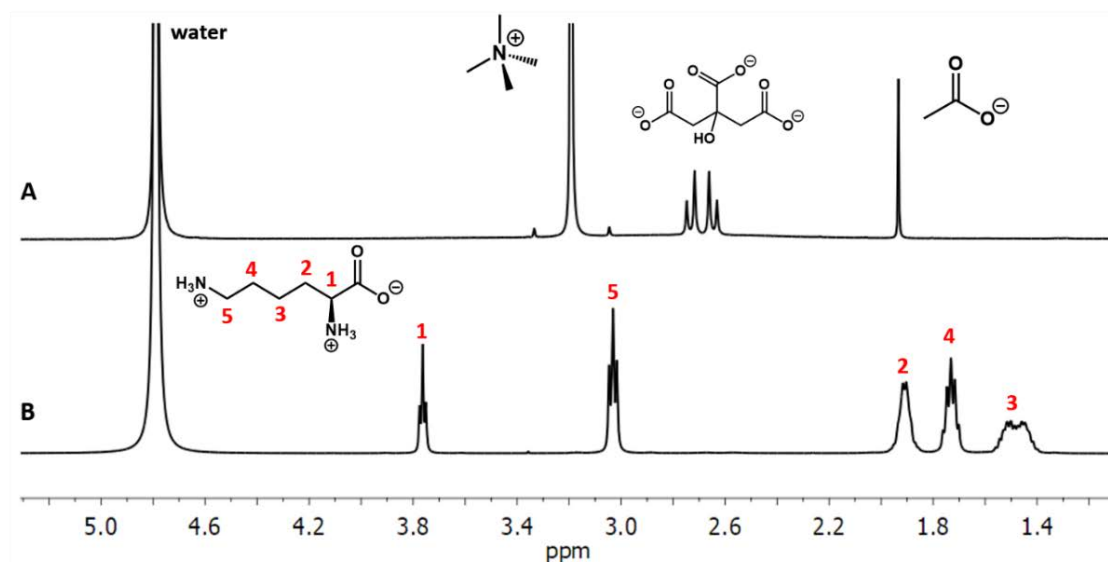
Figure 5.15. (A) ¹H NMR spectrum of LaF₃ NCs in D₂O with its peak assignation. (B) ¹H NMR spectrum of LaF₃ NCs after the ligand exchange with L-lysine hydrochloride in D₂O with its peak assignation.
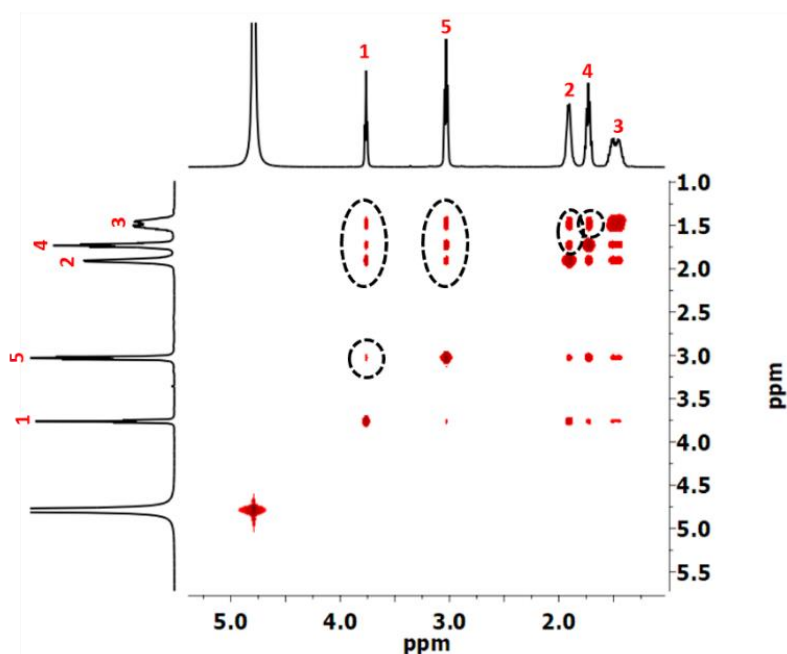
Figure 5.16. Room temperature NOESY spectrum of the resulting suspension of LaF₃ NCs after the ligand exchange with L-lysine hydrochloride in D₂O where negative cross-peak effects can be observed. Positive NOE effect is represented in blue while negative NOE effect is observed in red.

All peaks in NOESY spectrum show negative cross peak NOE effect, which means that lysine is attached onto the NC surface. Considering the NOESY experiment and the release of all the initial surface ions (acetate, tetramethylammonium and citrate), we postulated that the total exchange of NC surface was achieved successfully. Lysine is stated to be able to interact with its amino group onto {1$\bar{1}$00} planes while carboxylate is attached onto {0001} planes.

5.3.5 Mechanistic insights by MD simulations

After all the experimental evidences concerning the ligand exchange procedures, we aimed to understand in detail the mechanistic insights of each exchange using all atomistic MD simulations. Computer details are explained accurately in the experimental section of this Chapter. In fact, we started with the equilibrium configuration of Sim1 carried out in Chapter 4, releasing non-attached ions (maintaining those tetramethylammonium to achieve the neutrality) and releasing also free water. After that, we introduced enough molecules of the desired stabiliser (dopamine, 3,4-dihydroxyhydrocinnamic acid or lysine) with their respective counter ion (chloride, tetramethylammonium and chloride respectively). In the case of dopamine and lysine we used 40 molecules but, as we introduced 3,4-dihydroxyhydrocinnamic acid in its trivalent anionic form (with 3 tetramethylammonium as counter ion), we decided to perform the system with 20 molecules. By this way, all systems have the same number of added ions after the Sim1 template.

The most important consideration in these simulations relies on the best approximation to simulate the effect of the ultrasounds during the exchange. Among the different possibilities, we decided to start with a preliminary MD simulation with implicit water (applying an $\varepsilon = 80$). In previous simulations (see Chapter 2, section 2.3.9), we observed that the use of implicit water promoted the condensation of the ions onto the NC surface. We chose this approximation to force the system to condensate onto NC surface and after that, applying MD simulations with explicit water, the system should achieve its equilibrium configuration maintaining only in the surface the most stable stabilisers.

To corroborate the applicability of this method, we aimed to perform non-equilibrium MD simulations using an external force over all molecules in specific times to simulate the effect of the ultrasounds. Considering the complexity of non-equilibrium MD simulations, in this thesis only those simulations based on the use of implicit and explicit water are presented. These preliminary simulations allowed us to understand the insights concerning ligand exchange methodologies. Although more complex simulations must be performed in the near future, those with implicit/explicit water have been performed to postulate the exchange mechanism and will be corroborated using other approximations.

5.3.5.1 Ligand exchange with dopamine

To build the dopamine simulation box, we were based in the experimental procedure explained in section 5.3.2. As we used dopamine hydrochloride, we introduce 40 protonated dopamine molecules with their corresponding 40 chloride ions randomly distributed through the simulation box. We chose this number of molecules arbitrary to ensure the complete

saturation of the surface and with an excess to have free dopamine molecules in the system.

As commented previously, first we performed few nanoseconds simulations of a system with implicit water (applying an $\varepsilon = 80$). This allowed the system to condensate onto NC surface, reaching a new configuration far enough to the equilibrium configuration expected with explicit water. After that, a water box containing the NC and the ions in their equilibrium configuration for a system without water was built. When the new system was performed, we ran MD simulations at 25 °C considering that this ligand exchange has been carried out at room temperature.

In Figure 5.17A, a snapshot of the equilibrium configuration of the dopamine exchange system is presented, in which the ionic distribution onto the surface could be clearly observed. Rectangular faces ($\{1\bar{1}00\}$ exposed planes) are stabilised by ammonium and dopamine cations electrostatically adsorbed by the ammonium-based group. In contrast, hexagonal faces ($\{0001\}$ exposed planes) are stabilised by citrate and acetate, maintaining the patchy behaviour of the as-synthesised LaF_3 NCs (see Chapter 4).

To see in more detail in which positions dopamine molecules are attached, Figure 5.17B shows two different snapshots where is represented the NC, the adsorbed water and the attached dopamine molecules. We can clearly observed how dopamine is attached only onto $\{1\bar{1}00\}$ faces as we predicted by the release of ammonium cations.

The equilibrium configuration shows a system with citrate, acetate, ammonium and dopamine attached onto NC surface (Table 5.2). Comparing with the equilibrium configuration of LaF_3 NCs (see section 4.3.3 on Chapter 4), we observed the release of several ammonium cations, allowing the attachment of dopamine in their positions (onto $\{1\bar{1}00\}$ faces). The final system has a global charge of -3e produced by the presence of ~1 ions/nm^2 or -2.7 e/nm^2 onto $\{0001\}$ faces and 2.8 ions/nm^2 or +2.8 e/nm^2 onto $\{1\bar{1}00\}$ faces. The remaining negative charge is because the number of monovalent cations is not enough to neutralise this charge, although there are 12 ammonium and 19 dopamine cations onto $\{1\bar{1}00\}$ faces.
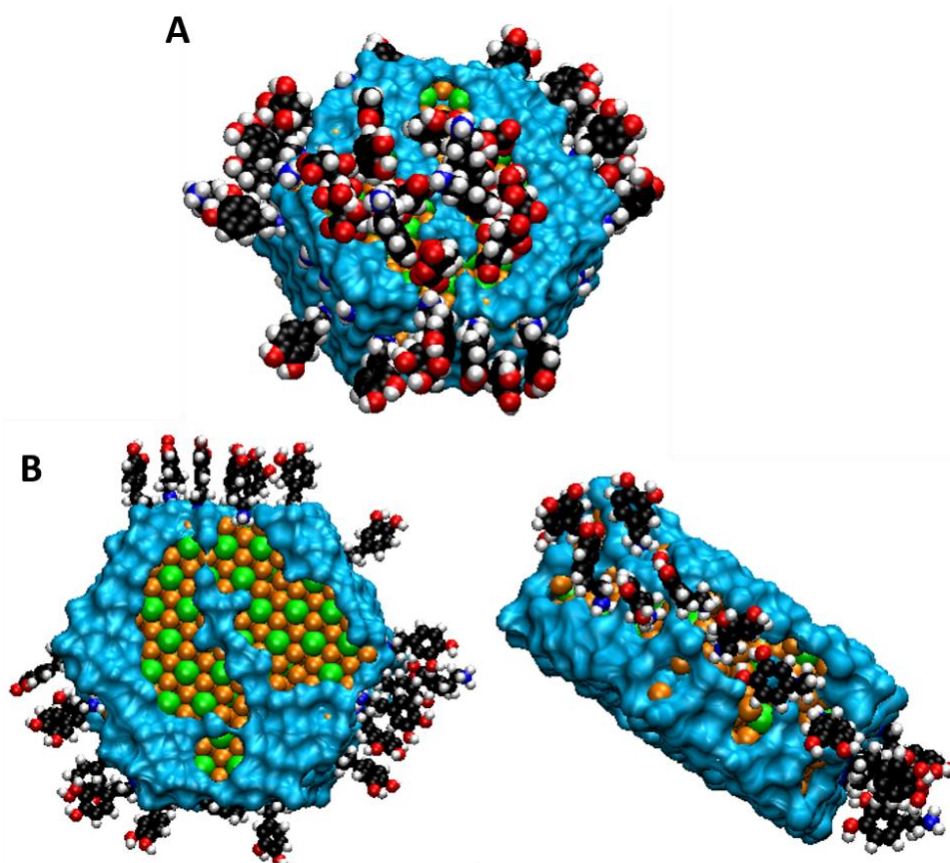
Figure 5.17. Snapshots of the equilibrium configuration corresponding to Sim1. (A) Surface image in which is represented all attached ions and water and (B) snapshots where are represented the NC, adsorbed water and dopamine cations. LaF$_3$ atoms and adsorbed ligands are shown in Van der Waals representation. Green spheres correspond to La, orange are F, black are C, red are O, blue are N and white are H. Water molecules adsorbed to the NC surface are shown in blue as a molecular contour surface (calculated using the surface algorithm implemented in VMD). All MD snapshots have the same colour assignation.

Table 5.2. Number of ions directly attached onto the NC surface at experimental temperature and the charge of each organic molecule. Citrate (Cit), Acetate (Ac), Ammonium (Amm), Tetramethylammonium (Tma) and Dopamine (Dop).

	Cit	Ac	Amm	Tma	Dop	Total
N° molecules	12	2	12	0	19	45
Charge (e)	-36	-2	+12	0	+19	-3

In addition, we can observe that the attached dopamine molecules are interacting with themselves via π-stacking interactions of the aromatic ring (being dopamine-dopamine π-stacking interactions visible in NMR). This effect could be explained by considering the hydrophilic/hydrophobic double-role of dopamine molecules. The two alcohols and the amino group show a hydrophilic behaviour allowing hydrogen interactions between water molecules while aromatic ring shows a hydrophobic role. If dopamine molecules were attached by the amino group and could interact via π-

stacking, they would minimise the hydrophobic role because the alcohol groups are in the other site being exposed to water box. In this way, the organisation of dopamine could be considered similar to liposomes membrane, formed by exposed hydrophilic heads (hydroxyl groups), an internal hydrophobic zone (aromatic ring) and an internal hydrophilic head (amino group). This configuration in our LaF_3 systems, produces a new kind of NC interface, allowing their stabilisation in aqueous solution.

Although in Figure 5.17B, a system without dopamine molecules onto {0001} planes is presented, this is not strictly true. We found some dopamine molecules onto {0001} planes, but we consider this effect as artefact produced by how we built the system. As commented in Chapter 4, we built LaF_3 NC from its bulk hexagonal structure applying the faceting observed by HRTEM technique. This procedure produced a charged LaF_3 NC and considering that NC must be neutral, we randomly release fluoride and lanthanum atoms from different positions. In Figure 5.18, we can observe two different cases of dopamine molecules attached onto {0001} planes of LaF_3 NC in the holes created by the release of lanthanum cations: using hydrogen bonding interactions with the two alcohol groups (Figure 5.18A) or by the adsorption of the ammonium group onto the created hole (Figure 5.18B).

Considering that the attachment of these dopamine molecules has been induced by the defects created to allow the fabrication of a neutral crystal, we decided to release these molecules from the equilibrium configuration before the detailed analysis of adsorbed molecules onto NC surface.
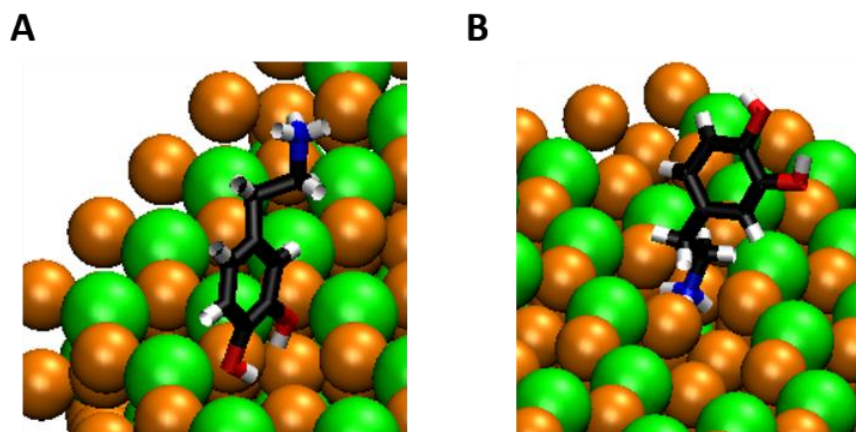
Figure 5.18. (A) Snapshot with dopamine adsorbed onto lanthanum hole by the hydroxyl groups and (B) snapshot with dopamine adsorbed inside lanthanum vacancy by amino based group. LaF_3 NC is shown in Van der Waals representation and dopamine in bond representation. Green spheres correspond to La, orange are F, black are C, red are O, blue are N and white are H.

After the atomistic analysis of NC interface via MD simulations of the dopamine exchange system, we can conclude that experimental and computational approximations give us compatible results to understand the

exchange mechanism. We successfully achieved the selective exchange of ammonium cations for dopamine molecules on $\{1\bar{1}00\}$ faces, due to the stabilisation of these faces by dopamine molecules attached via amino group and interacting themselves via π-stacking interactions.

5.3.5.2 Ligand exchange with 3,4-dihydroxyhydrocinnamic acid

Using the same protocol than with dopamine, we performed MD simulations to understand the ligand exchange carried out by 3,4-dihydroxyhydrocinnamic acid. As in the experimental part we realised the necessity of 3 equivalents of a base to obtain the trivalent anion of 3,4-dihydroxyhydrocinnamic acid, we directly built this system. To maintain equal the number of added ions in the system, we added 20 molecules of trivalent anion of 3,4-dihydroxyhydrocinnamic acid with their 60 respective tetramethylammonium molecules (80 molecules as the case of 40 dopamine molecules with 40 chloride anions). After the few nanoseconds simulation with implicit solvent, we started the simulation with a water box at 25 °C.

The equilibrium configuration of this simulation is showed in Figure 5.19A, where it can be observed that the citrate and trivalent 3,4-dihydroxyhydrocinnamate are attached onto $\{0001\}$ planes while ammonium cations remains stabilising $\{1\bar{1}00\}$ faces. To see in more detail the selective exchange allowed by trivalent 3,4-dihydroxyhydrocinnamate anion, in Figure 5.19B two snapshots of the equilibrium configuration representing only the NC, adsorbed water and trivalent 3,4-dihydroxyhydrocinnamate anions are shown. In this case, ligand exchange process has been performed selectively onto $\{0001\}$ faces, releasing acetate and some citrate to coordinate the new trivalent anion.

The complete covering of ions onto the NC surface revealed a global charge of -33e (Table 5.3) produced by the presence of ~1.3 ions/nm² or -3.8 e/nm² onto $\{0001\}$ faces and 1.9 ions/nm² or +1.9 e/nm² onto $\{1\bar{1}00\}$ faces. In contrast to the other systems, in this case we have that the charge per surface area on $\{0001\}$ and $\{1\bar{1}00\}$ is not neutralised. Additionally, we found that $\{0001\}$ faces have the double surface charge per area than $\{1\bar{1}00\}$ faces, explaining the high negative global energy of -33e.
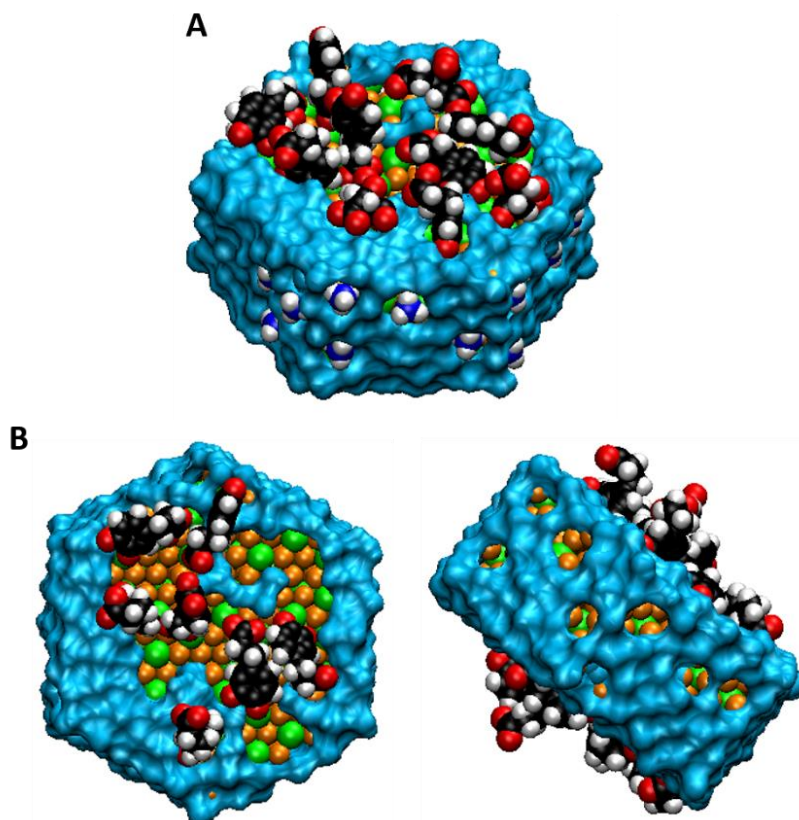
Figure 5.19. Snapshots of the equilibrium configuration corresponding to Sim2. (A) Surface image in which is represented all attached ions and water and (B) snapshots where are represented the NC, adsorbed water and trivalent 3,4-dihydroxyhydrocinnamate anions. LaF$_3$ atoms and adsorbed ligands are shown in Van der Waals representation. To see colour assignation, see Figure 5.17.

Table 5.3. Number of ions directly attached onto the NC surface at experimental temperature and the charge of each organic molecule. Citrate (Cit), Acetate (Ac), Ammonium (Amm), Tetramethylammonium (Tma) and 3,4-dihydroxihydrocinnamic acid (Cin).

	Cit	Ac	Amm	Tma	Cin	Total
N° molecules	6	0	16	5	12	39
Charge (e)	-18	0	+16	+5	-36	-33

Considering the possible NC-ligand interaction after the ligand exchange with trivalent 3,4-dihydroxyhydrocinnamate anions, through a tridentate mode, we cannot confirm the presence of this ligand using ^{1}H NMR technique. To confirm this, we examined the behaviour of attached trivalent 3,4-dihydroxyhydrocinnamate anions via MD simulations (Figure 5.19 and Table 5.3), obtaining a 67% of the 3,4-dihydroxyhydrocinnamate anions in the tridentate attached mode. Via ^{1}H NMR we did not observe the presence of citrate while in the simulations was present, being necessary the application of non-equilibrium MD simulations explained before to have a more representative system. Although these simulations based on the use of

implicit/explicit water are only a preliminary approximation, they provide relevant information to unravel the general insights of the selective ligand exchanges. Thus, we postulate that in the case of carrying out more accurate and complexes simulations, we will find a system in which the tridentate attached mode will be majority, better explaining the NMR results.

In consequence with the high surface charge density onto {0001} faces, we examined the system in more detail, if the presence of a high charge could promote ionic condensations onto the interfaces. Interestingly, we found a stable ionic interaction onto the surface promoted by the interaction of ammonium cations, citrate and trivalent 3,4-dihydroxyhydrocinnamate anions (Figure 5.20).
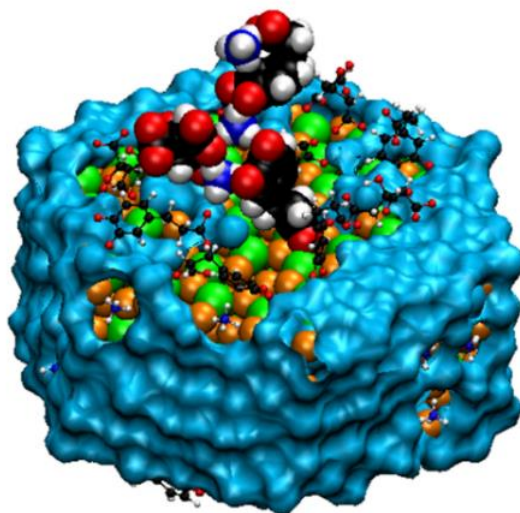

Figure 5.20. Snapshot of ionic interactions unravelled onto surface in the equilibrium configuration of Sim2. LaF₃ atoms and ions involved in the ionic interaction are shown in Van der Waals representation while the other adsorbed ions are represented in CPK. To see colour assignation, see Figure 5.17.

Trying to summarise this complex interaction, we divided it into two different major interactions, as it can be observed in Figure 5.21. Firstly, we have the as-mentioned citrate bridge interaction (described in Chapter 2) as it is represented in Figure 5.21A. In this case, citrate electrostatic interaction between two different ammonium cations is not promoting the self-assembly of different NCs, but it is promoting a bridge between two trivalent 3,4-dihydroxyhydrocinnamate anions. This evidence confirms the strong interaction produced by citrate to form ionic bridge electrostatic interactions observed in NCs (Chapter 2) and in ordered ionic interactions as it is observed in Figure 5.21A.
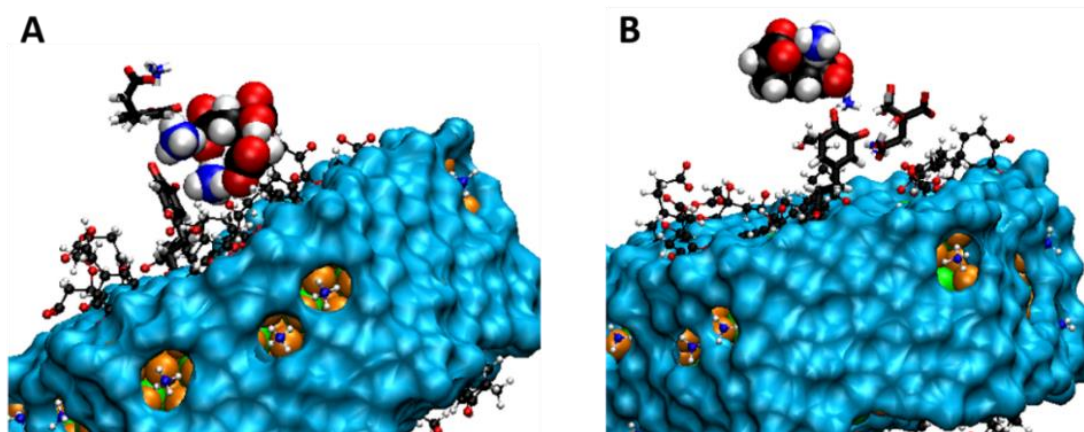
Figure 5.21. Snapshot of ionic interactions unravelled onto surface in the equilibrium configuration of Sim2. (A) Citrate mediated ionic interaction and (B) 3,4-dihydroxyhydrocinnamate anion displaying tridentate chelate coordination mode with an ammonium cation. LaF₃ atoms and ions involved in the ionic interaction are shown in Van der Waals representation while the other adsorbed ions are represented in CPK. To see colour assignation, see Figure 5.17.

In the same ionic interaction, we found a trivalent 3,4-dihydroxyhydrocinnamate anion displaying tridentate chelate coordination mode with an ammonium cation. This interaction was also encountered free in the medium (through the water box), indicating the coordination preference of trivalent 3,4-dihydroxyhydrocinnamate anions (Figure 5.21B).

All these observed interactions could be promoted by the high charge density onto {0001} faces, allowing ionic condensations and different kind of interactions in aqueous systems. Concerning the role of aromatic ring in this case, we observed that they are not interacting themselves via π-stacking, so {0001} faces become more hydrophobic. This increased hydrophobicity is observed by the attachment of tetramethylammonium (see Figure 5.22) preferentially onto {0001} faces (80% of tetramethylammonium attached cations). Although some of these tetramethylammonium cations are attached onto the lanthanum vacancies created during the construction of the NCs, in this case we considered this attachment so important because we only saw the attachment of tetramethylammonium in methanol simulations of Chapter 4. These preliminary results could be understood considering the hydrophilic/hydrophobic behaviour of the different systems. Tetramethylammonium cation could be attached onto NC surface when the hydrophobicity of the interfaces increases (e.g. using methanol as solvent or by the presence of aromatic rings).
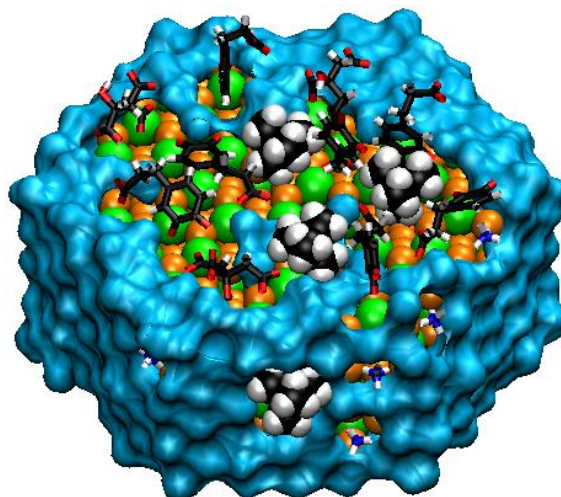
Figure 5.22. Snapshot of the adsorption of tetramethylammonium cations onto NC surface in the equilibrium configuration of Sim2. LaF₃ atoms and tetramethylammonium cations are shown in Van der Waals representation while the other adsorbed ions are represented in bond representation. To see colour assignation, see Figure 5.17.

After the computational study of the exchange performed with trivalent 3,4-dihydroxyhydrocinnamate anions, we can observe that this exchange was carried out selectively onto {0001} faces, releasing some citrate and acetate from their equilibrium positions. In addition, the use of trivalent anion, in combination with the presence of citrate (another tridentate anion), produces a highly charged system with a high ionic density onto {0001} faces. This allows the formation of several ionic interactions between the different ions onto these surfaces. In contrast to the dopamine case in which aromatic rings formed π-stacking interaction minimising the hydrophobicity of NC, in this case, the presence of aromatic rings onto {0001} faces promote the attachment of tetramethylammonium onto the NC surface.

5.3.5.3 Ligand exchange with lysine

In the last case, lysine was chosen as exchange molecule as it contains containing a carboxylate and amino groups able to interact with fluorine and lanthanum atoms. In the experimental characterisation of this exchange, we found that lysine was the unique stabiliser onto the NC surface after the ligand exchange. This effect was postulated to be related with the double role of lysine, stabilising both exposed faces.

In this case, we added 40 protonated lysine molecules with their respective 40 chlorides, applying the same implicit/explicit method to simulate the effect of the ultrasonic bath. In Figure 5.23A, it is shown the equilibrium configuration of lysine exchange simulation in which citrate and lysine (42%) are attached onto {0001} faces while ammonium, tetramethylammonium and lysine (58%) are anchored onto {1$\bar{1}$00} faces. As it

can be observed in Figure 5.23B in which NC, adsorbed water and lysine are presented, being the latter attached in both exposed faces in almost equal proportions.
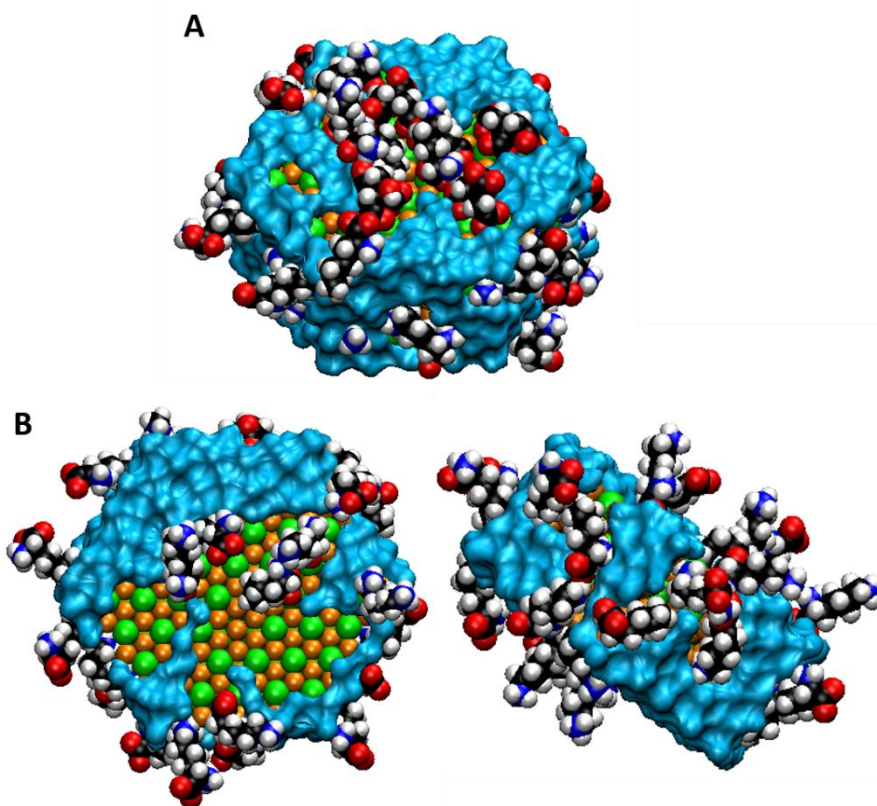

Figure 5.23. Snapshots of the equilibrium configuration corresponding to Sim3. (A) Surface image in which is represented all attached ions and water and (B) snapshots where are represented the NC, adsorbed water and L-lysine in its cationic form. LaF$_3$ atoms and adsorbed ligands are shown in Van der Waals representation. To see colour assignation, see Figure 5.17.

Concerning the final charge of the NC, its surface revealed a global charge of -9e (Table 5.4) produced by the presence of ~1.6 ions/nm^2 or -2.0 e/nm^2 onto {0001} faces and 1.8 ions/nm^2 or +1.8 e/nm^2 onto {1$\bar{1}$00} faces. Given the few differences between both charge per surface area, in this case we could consider that the charge per surface area on {0001} and {1$\bar{1}$00} is almost neutralised.

Here, we have demonstrated as the use of a zwitterionic molecule (e.g. lysine) in its acidic form (lysine hydrochloride) could allow the total release of the cations or anions from patchy LaF$_3$ NCs. As previously commented, the use of non-equilibrium MD simulations could promote the release of all ions from NC surface to be exchanged by lysine molecules. In the present case (Figure 5.23), some of the initial ions remain onto the surface in contrast with our experimental evidences in which only lysine was visible by NMR technique.

Table 5.4. Number of ions directly attached onto the NC surface at experimental temperature and the charge of each organic molecule. Citrate (Cit), Acetate (Ac), Ammonium (Amm), Tetramethylammonium (Tma) and Lysine (Lys).

	Cit	Ac	Amm	Tma	Lys	Total
N° molecules	13	0	5	1	24	43
Charge (e)	-39	0	+5	+1	+24	-9

5.3.6 First steps in non-aqueous solvents

After the achievement of the selective functionalisation of the NC surface in water, we aimed to perform the ligand exchange methodology to be able to transfer NC from water to organic solvents (e.g. toluene). The synthetic process to promote the exchange was based on the work of De Keukeleere et al.[10]

Our first trials to obtain a stable colloidal solution in toluene using oleic acid with/without oleylamine were unsuitable for our colloidal suspensions. After several experiments with different combinations of acids and amines, we found that, to promote the exchange, we need the combination of a hydrophilic molecule containing one or more carboxylic acid moieties and oleylamine as hydrophobic base.

Considering that the ligand exchange methodologies in toluene are currently under study, in this thesis, two examples of ligand exchange carried out in toluene are presented as overview of this upcoming work.

5.3.6.1 Ligand exchange with glutaric acid and oleylamine

The exchange with glutaric acid was carried out starting from the precipitation of LaF$_3$ NCs with diethyl ether and 2-propanol. Without drying the precipitate, it was re-dispersed in toluene forming a milky colloidal suspension. After the addition of glutaric acid and oleylamine, the solution was treated by an ultrasonic bath for 10 minutes obtaining a transparent colourless colloidal solution, meaning that the exchange to toluene was performed successfully. To confirm this, sample was analysed using TEM and DLS techniques (Figure 5.24).

Both techniques reveal a homogeneous colloidal suspension of NCs of 9 nm size approximately, without aggregation observed by TEM, showing the same morphology that the citrate stabilised LaF$_3$ NCs. After the preliminary characterisation of the size, morphology and aggregation, we need to ensure that the ligand exchange was performed successfully, knowing which is the new surface image.
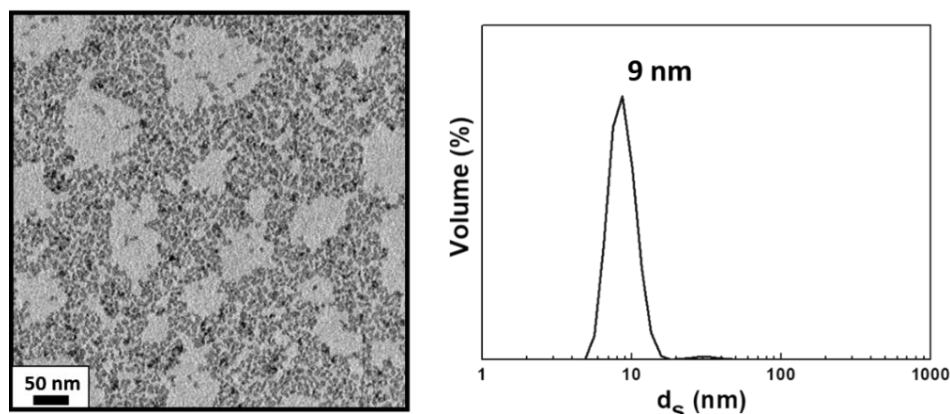
Figure 5.24. TEM and DLS of LaF₃ NCs obtained after the ligand exchange with glutaric acid and oleylamine in toluene at room temperature.

As in the case of water exchanges, ^{1}H NMR was used to characterise the ligands attached onto the NC surface (Figure 5.25). NMR spectrum clearly reveals the presence of oleylamine onto NC surface, showing the characteristic broad peaks of a ligand attached onto a NC.
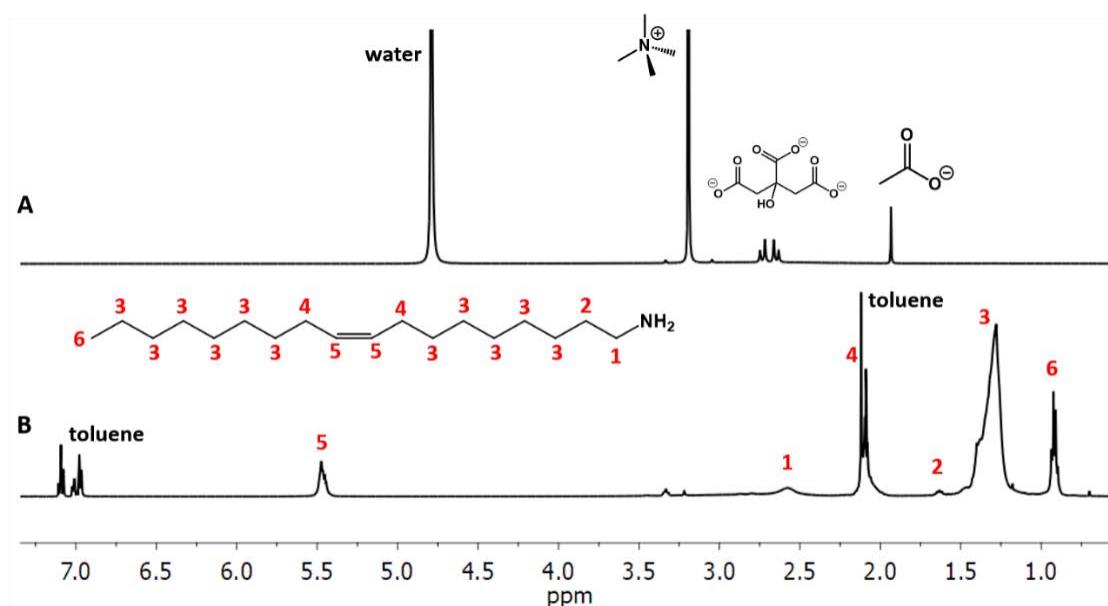
Figure 5.25. (A) ^{1}H NMR spectrum of LaF₃ NCs in D₂O with its peak assignation. (B) ^{1}H NMR spectrum of LaF₃ NCs after the ligand exchange with glutaric acid and oleylamine in toluene-d₈ with its peak assignation.

Once ^{1}H NMR was used to see the presence of the desired molecules in the system, a NOESY experiment was carried out to ensure the attachment of the molecules onto NC surface (Figure 5.26). The presence of negative NOE cross-peaks indicates that oleylamine is attached onto NC surface, stabilising the particles in toluene through the hydrophobic chain. Likewise, if we only observed the presence of oleylamine onto NC surface, it could be possible to think that with the addition of only oleylamine we would obtain the same stabilised system.

Figure 5.26. Room temperature NOESY spectrum of the resulting suspension of LaF₃ NCs after ligand exchange in toluene-d₈ where the negative NOE cross-peaks have been highlighted. Positive NOE effect is represented in blue while negative NOE effect is observed in red.
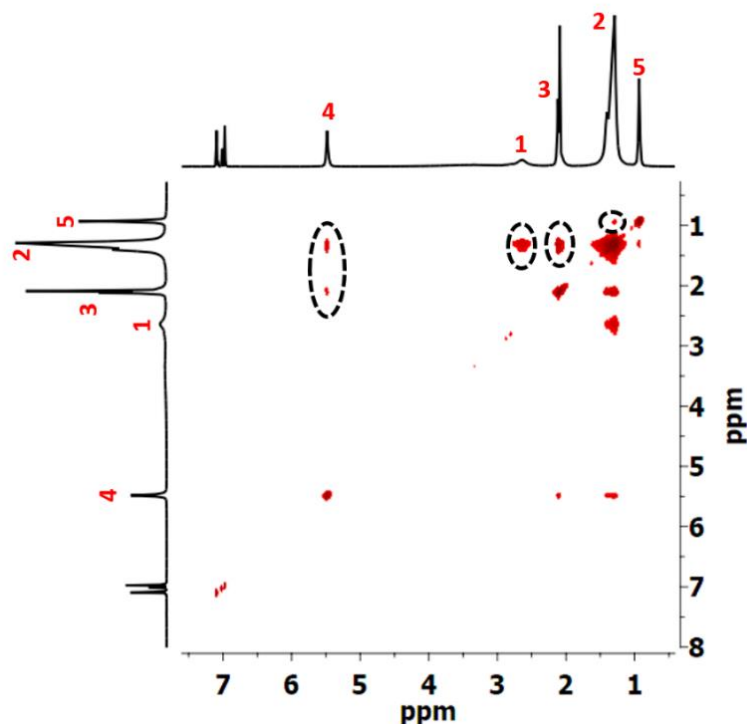
In consequence, we performed ligand exchanges using only oleylamine or octylamine to prove if the addition of a hydrophobic base is enough to carry out the exchange. All colloidal solutions became unstable and milkier after the addition of the base. Thus, the addition of a hydrophilic molecule with carboxylic moieties is required to produce the ligand exchange but it seems to be absent onto the NC surface.

Trying to unravel more about the exchange performed in toluene, we wanted to know the role of the carboxylic acid, if it only protonates oleylamine or it is acting as stabiliser onto the surface. Thus, we used 3,4-dihydroxyhydrocinnamic acid due to its presence onto NC surface produces coloured colloidal dispersions.

5.3.6.2 Ligand exchange with 3,4-dihydroxyhydrocinnamic acid and oleylamine

We performed the same ligand exchange as the ones carried out in the previous section using 3,4-dihydroxyhydrocinnamic acid instead of glutaric acid. After washing the particles with 2-propanol and re-disperse in toluene, we observed a yellow-orange coloured dispersion, indicating the presence of 3,4-dihydroxyhydrocinnamate onto the surface or free in the system. Firstly, as in the previous cases, TEM and DLS (Figure 5.27) were performed to know the size and behaviour of the final colloidal dispersion. TEM image show a

homogeneous dispersion of NC interacting in small families of 2-4 NCs. In addition, DLS revealed the presence of bigger particles (around 20 nm size), confirming the evidence observed by TEM of the presence of small families of some NCs.
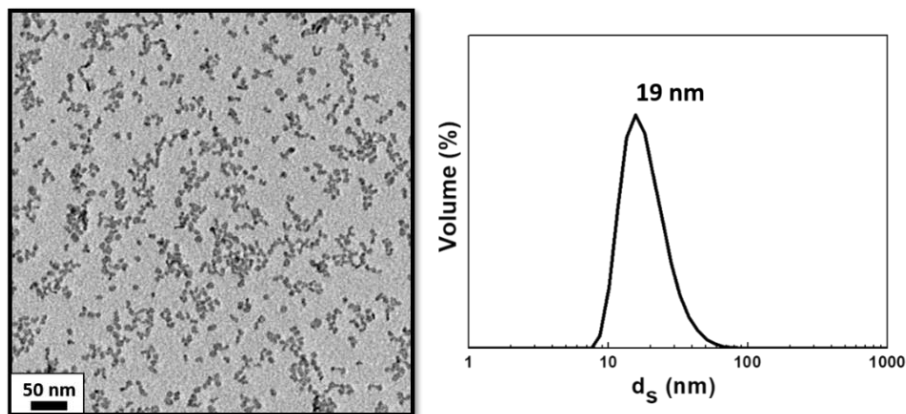

Figure 5.27. TEM and DLS of LaF₃ NCs obtained after the ligand exchange with 3,4-dihydroxyhydrocinnamic acid and oleylamine in toluene at room temperature.

^{1}H NMR analysis (Figure 5.28) was carried out to see the surface image of the new colloidal solution, in which we observed the presence of oleylamine as unique stabiliser in the system. The broad behaviour of the signals indicates that oleylamine is attached onto NC surface as stabiliser, but we need to confirm this with a NOESY experiment.

Considering 3,4-dihydroxyhydrocinnamic acid, it seems not to be present in the system, but the colloidal solution shows a yellow-orange colour indicating the presence of 3,4-dihydroxyhydrocinnamate onto NC surface as in the case of ligand exchange carried out in water. As it can be observed in section 5.3.3, ligand exchanges with 3,4-dihydroxyhydrocinnamic acid produce a coloured colloidal dispersion (with the ligand coordinated or free in the medium). Thus, if we do not observe the presence of 3,4-dihydroxyhydrocinnamic acid in ^{1}H NMR (to compare see Figure 5.8B) and the solution has this characteristic colour, we could postulate that 3,4-dihydroxyhydrocinnamate is anchored onto NC surface stabilising hydrophilic faces. In addition, and with the results of ligand exchange in water (experimentally and by MD simulations), we could also postulate that 3,4-dihydroxyhydrocinnamate is adsorbed by its three moieties, avoiding its detection via NMR technique.
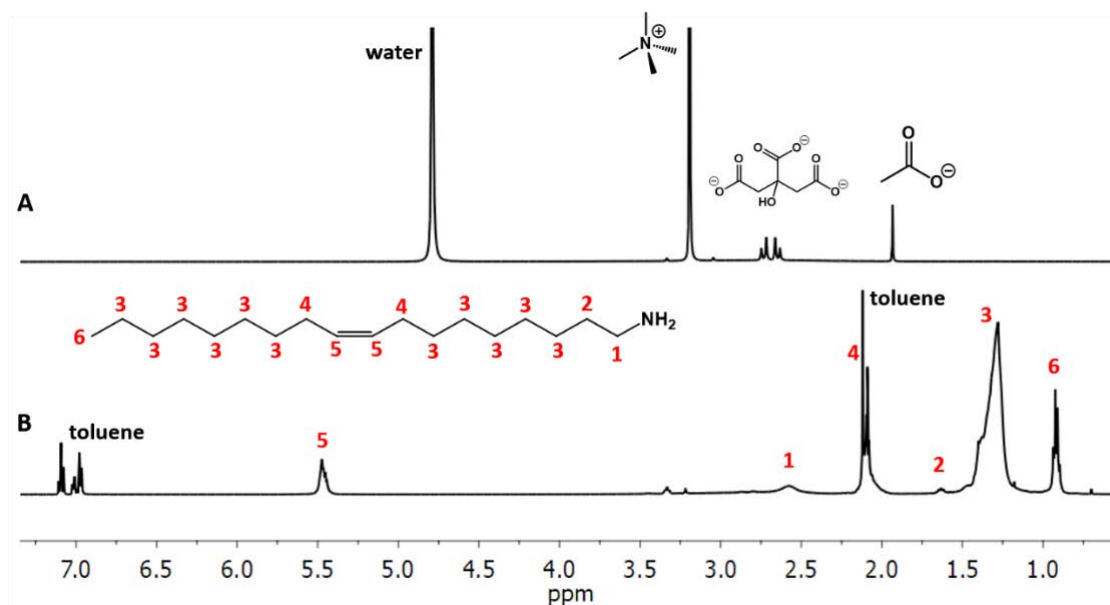
Figure 5.28. (A) ¹H NMR spectrum of LaF₃ NCs in D₂O with its peak assignation. (B) ¹H NMR spectrum of LaF₃ NCs after the ligand exchange with 3,4-dihydroxyhydrocinnamic acid and oleylamine in toluene-d₈ with its peak assignation.

To confirm if oleylamine is attached onto the NC surface, a NOESY experiment (Figure 5.29) was performed revealing negative NOE cross-peaks. As in the case of glutaric acid, oleylamine is attached onto NC surface stabilising particles in toluene.
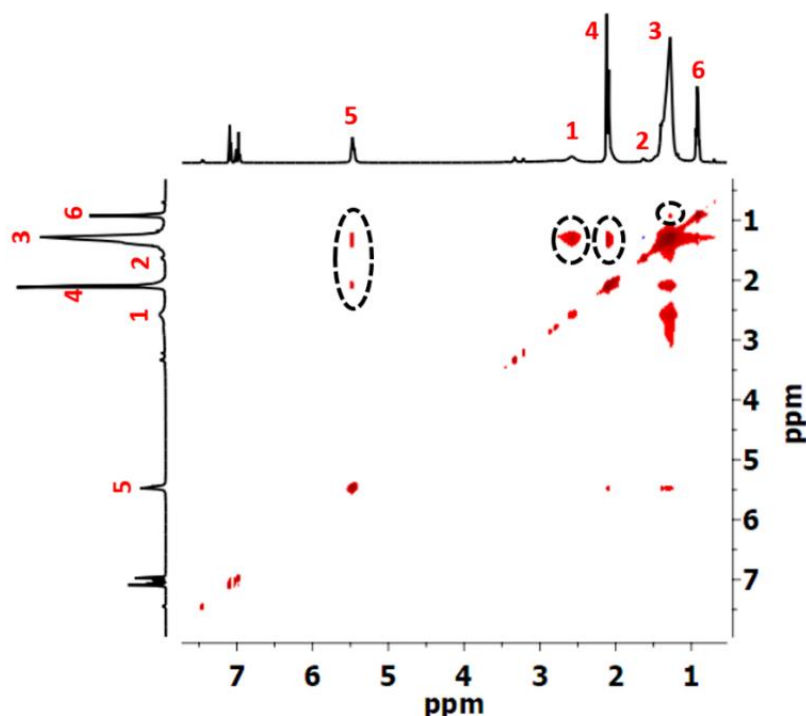
Figure 5.29. Room temperature NOESY spectrum of the resulting suspension of LaF₃ NCs after ligand exchange in toluene-d₈ where the negative NOE cross-peaks have been highlighted. Positive NOE effect is represented in blue while negative NOE effect is observed in red.

Once oleylamine was identified as stabiliser in LaF₃ NCs in toluene, we aimed to know if 3,4-dihydroxyhydrocinnamate could be removed from NC surface with the addition of another molecule able to be adsorbed onto the surface. To see clearly the release of 3,4-dihydroxyhydrocinnamate, we worked in the same NMR tube adding some microliters of oleic acid and ^{1}H NMR analysis was performed again. In the bottom part of Figure 5.30, it is shown the spectrum performed after the addition of oleic acid, showing clearly the new peaks (1,2 and 3 in blue) corresponding to oleic acid.
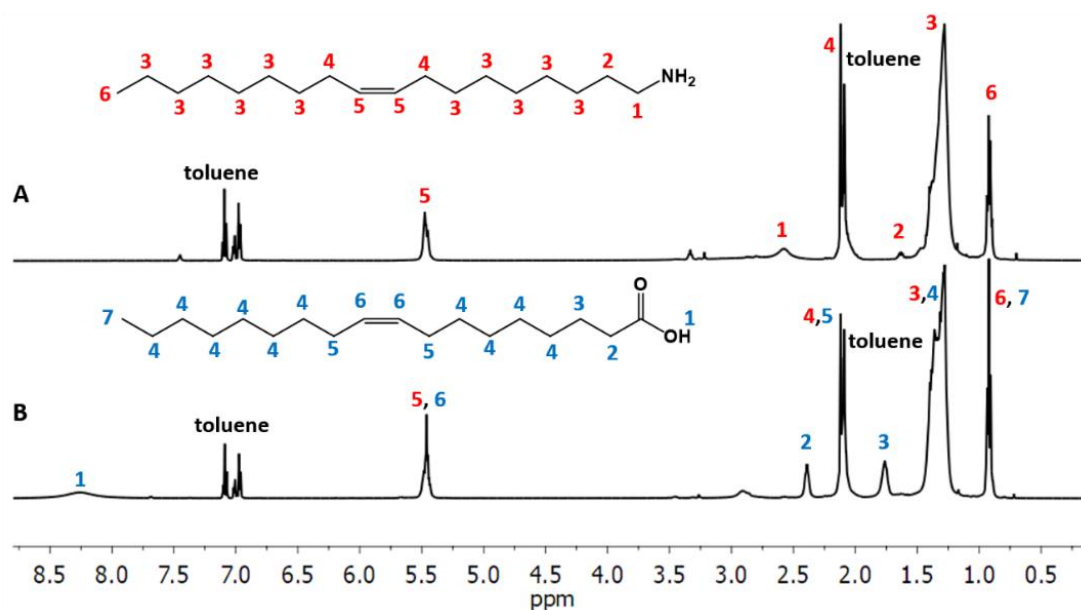
Figure 5.30. (A) ^{1}H NMR spectrum of LaF₃ NCs after the ligand exchange with 3,4-dihydroxyhydrocinnamic acid and oleylamine in toluene-d₈ with its peak assignation. (B) ^{1}H NMR spectrum of LaF₃ NCs after the addition of 20 µl of oleic acid in toluene-d₈ with its peak assignation.

The broad signals, corresponding to oleic acid suggest that the carboxylic moiety has been attached onto NC surface. Interestingly, we did not observe evidence of the release of 3,4-dihydroxyhydrocinnamate in the NMR spectrum. In addition to ^{1}H NMR, we performed again a NOESY experiment to ensure if oleic acid was attached onto the NC surface or free in the medium (Figure 5.31).

In this case, we observe two different molecules attached onto NC surface (oleylamine and oleic acid), in contrast to the other analysed system that we were only able to see one molecule in NOESY experiment. Both molecules, oleic acid and oleylamine, show negative NOE cross-peaks because they are attached onto NCs surface. In addition, in Figure 5.31B we can observe that hydrogen 1 of oleylamine shows a negative NOE effect with hydrogen 2 and 3 of oleic acid. This means that both molecules are close enough to present NOE effect, showing a negative cross-peak between them because they are both attached onto the NCs surface.
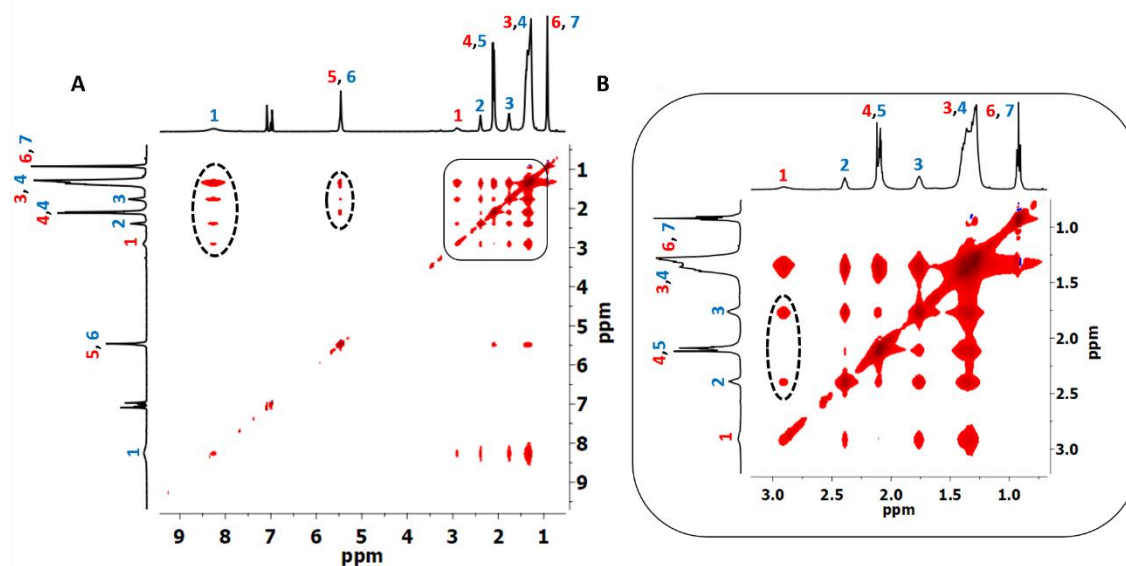
Figure 5.31. (A) Room temperature NOESY spectrum of the resulting suspension of LaF₃ NCs after the addition of oleic acid in toluene-d₈ where the negative NOE cross-peaks have been highlighted. (B) Enlarged zone of aliphatic peaks to clarify the interactions between oleic acid and oleylamine. Positive NOE effect is represented in blue while negative NOE effect is observed in red.

After the complete characterisation via NMR analysis, we wanted to know if the morphology of NC changed after the addition of oleic acid. To do this, we performed TEM analysis with the deuterated toluene NC dispersion (Figure 5.32), showing a different behaviour compared with Figure 5.27 corresponding to colloidal solution before the addition of oleic acid.
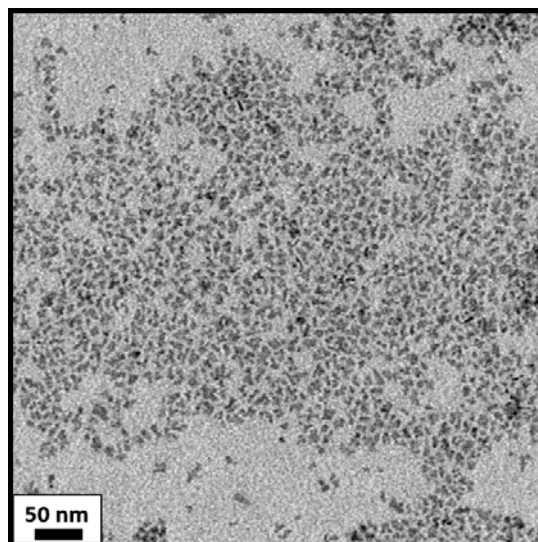
Figure 5.32. TEM and DLS of LaF₃ NCs obtained after the ligand exchange with 3,4-dihydroxyhydrocinnamic acid and oleylamine after the addition of oleic acid in deuterated toluene at room temperature.

Finally, we postulated that after the titration with oleic acid, trying to release 3,4-dihydroxyhydrocinnamate, oleic acid is able to absorb onto NC

surface stabilising better NCs in toluene. This evidence suggests that NC surface was not saturated and oleic acid replace solvated molecules instead of 3,4-dihydroxyhydrocinnamate. After the addition of higher amounts of oleic acid and base (to promote the deprotonation of oleic acid), we observe the precipitation of NCs without evidence of 3,4-dihydroxyhydrocinnamate release.

First trials of ligand exchange in non-aqueous solvents (e.g. toluene) revealed promising effects and mechanisms to be studied in the near future. Compared to ligand exchange in water, toluene exchange seems more complex and requires deep investigations from experimental and computational point of view.

5.4 Conclusions

In this Chapter, we analysed deeply the insights of the ligand exchange reaction performed in aqueous medium, summarised in Figure 5.33. Starting with the patchy LaF$_3$ NCs, which selectively adsorb anions and cations in their different faces, we were able to promote selectively ligand exchange strategies. Our main goal was successfully accomplished using different ionic molecules to promote cationic, anionic or total exchanges onto NC surface. We investigated in detail the final system via NMR technique (1D and 2D experiments) and using MD simulations to analyse in all-atomistic detail the mechanism and/or the selectivity of the exchanges.
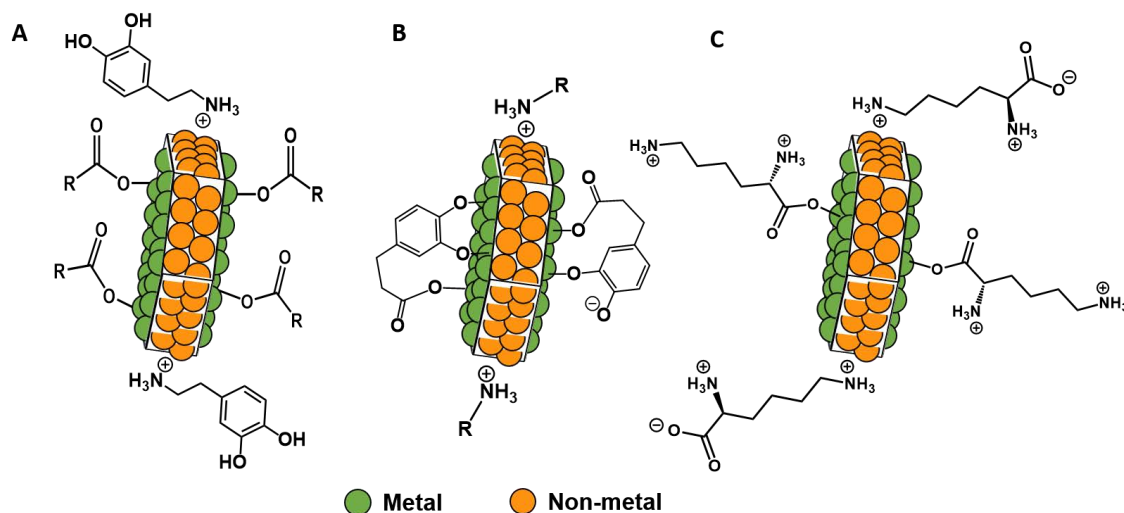
Figure 5.33. Schematic representation of the three systems after the ligand exchange with (A) dopamine hydrochloride, (B) 3,4-dihydroxyhydrocinnamic acid and (C) L-lysine hydrochloride.

Cationic release from {1$\bar{1}$00} faces was promoted by the addition of dopamine hydrochloride, being dopamine the new stabiliser in these planes. To reduce the hydrophobic effect of the aromatic ring, dopamine interacts with themselves via π-stacking interactions, creating hydrophobic interactions to reduce their exposition to water molecules. To release anions

from {0001} faces, we used 3,4-dihydroxyhydrocinnamic acid in their trivalent anionic form. Although the new molecule was not observed by NMR technique, UV-Vis technique allowed its detection onto NC surface. In addition, using MD simulations, we observe that their coordination via tridentate mode could be the main reason for the non-detection of this attached molecule by NMR technique. In this case, the hydrophobic effect produced by the presence of aromatic rings onto {0001} faces, allows the formation of ionic interactions (e.g. citrate ionic bridge) and the attachment of tetramethylammonium cations.

Finally, we demonstrate that the addition of a zwitterionic molecule (e.g. lysine), with the presence of a carboxylate and amino based groups, could allow the total exchange of ligands onto NC surface, being the new added one the unique stabiliser. First tests in toluene open pathways to use these NCs not only in aqueous media but with several insights that must be unravelled in the near future.

This Chapter is the proof of concept that, we can use an easy, reproducible and fast methodology to synthesise NCs with a desired core. After that, these NCs could be functionalised selectively to be applied in a deep range of fields without the necessity to modify the initial synthetic methodology. Here, we highlight the importance of the surface chemistry as the bridge between the NC design and their final applications, to enable the commonly intricate protocols to obtain the desired systems.

5.5 References

[1]   J. De Roo, F. Van Den Broeck, K. De Keukeleere, J. C. Martins, I. Van Driessche, Z. Hens, *J. Am. Chem. Soc.* **2014**, *136*, 9650–9657.

[2]   J. De Roo, K. De Keukeleere, Z. Hens, I. Van Driessche, *Dalt. Trans.* **2016**, *45*, 13277–13283.

[3]   J. De Roo, Y. Justo, K. De Keukeleere, F. Van den Broeck, J. C. Martins, I. Van Driessche, Z. Hens, *Angew. Chemie - Int. Ed.* **2015**, *54*, 6488–6491.

[4]   Danylo Zherebetskyy, M. Scheele, Y. Zhang, N. Bronstein, C. Thompson, D. Britt, M. Salmeron, P. Alivisatos, Lin-WangWang, *Science.* **2014**, *346*, 1380–1384.

[5]   M. A. Boles, D. Ling, T. Hyeon, D. V. Talapin, *Nat. Mater.* **2016**, *15*, 141–153.

[6]   J. Martinez-Esain, J. Faraudo, T. Puig, X. Obradors, J. Ros, S. Ricart, R. Yáñez, *J. Am. Chem. Soc.* **2018**, *140*, 2127–2134.

[7]   J. De Roo, I. Van Driessche, J. C. Martins, Z. Hens, *Nat. Mater.* **2016**,

15, 517–521.

[8]   J. Martínez-Esaín, T. Puig, X. Obradors, J. Ros, R. Yáñez, J. Faraudo, S. Ricart, *Angew. Chemie - Int. Ed.* **2018**, DOI 10.1002/ange.201806273.

[9]   C. Calero, J. Faraudo, M. Aguilella-Arzo, *Mol. Simul.* **2011**, *37*, 123–134.

[10]   K. De Keukeleere, J. De Roo, P. Lommens, J. C. Martins, P. Van Der Voort, I. Van Driessche, *Inorg. Chem.* **2015**, *54*, 3469–3476.

6

EGA-MS as useful nanocrystal surface technique
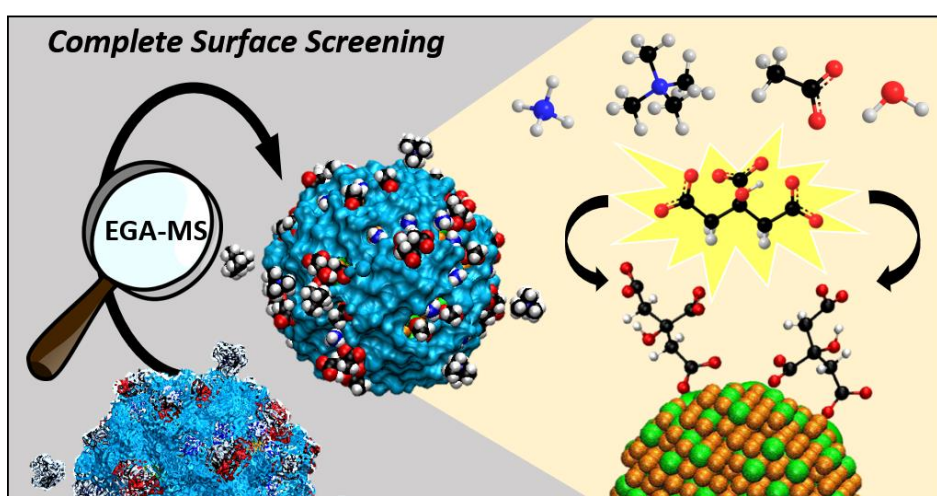
EGA-MS was performed to obtain the complete image of the nanocrystal-solvent interface, unravelling the molecules present onto surface. Using YF_3 nanocrystals/supraparticles and LaF_3 nanocrystals as model systems, we performed the complete surface characterisation by using EGA-MS as unique experimental technique. This study was applied to previous fully characterised nanoscaled systems via experimental techniques and MD simulations. We demonstrated the applicability of this technique in two systems with different sizes (e.g. YF_3 nanocrystals of ~8 nm vs YF_3 supraparticles of 80 nm size) and in two systems composed by the same ions onto their surface but containing different inorganic cores (e.g. LaF_3 and YF_3 nanocrystals). Our results agree with the previously unravelled surface chemistry, allowing us to postulate this technique as a new pathway to elucidate the intricate surface of nanoscaled systems. This technique not only revealed the ions attached onto nanocrystal surface but also their coordination (e.g. citrate attached by one or two carboxylate moieties).

6.1 Introduction

The complete characterisation of a nanocrystal (NC) surface is currently performed with the combination of several techniques to know the complete system image.[1] Surface chemistry has arisen as a new multidisciplinary approach to unravel and study the surface-to-ligand interactions in nanoscaled systems.[2,3] Complete knowledge of the NC surface composition is sometimes a complex task in nanoscience, due to the intricacy of the applied synthetic methodologies, which use several reactants and/or stabilisers. Previously used techniques suffer from some drawbacks like fast H-D exchanges and re-dispensability problems in nuclear magnetic resonance (NMR), or the overlapping of different ligands containing the same functional group in infrared spectroscopy (IR), among others. These drawbacks in combination with the impossibility of using a single technique to detect all attached molecules, make necessary to use different techniques to ensure their presence. The large-scale applicability of nanoscaled systems highlights the use of an efficient technique to extract surface information without the necessity of combining several techniques.

Evolved Gas Analysis (EGA) by mass spectrometry (MS) is a key technique for the identification of volatile products during thermal degradation of substances. EGA is a technique that identifies the volatile species thanks to the mass of molecule fragments (via MS) or their vibrational spectra (via IR). Often EGA is coupled to a thermobalance or thermogravimetric analysis (TGA). Among the vast number of applications (periodically reviewed by Mareratzzi et al. since 2006),[4] pyrolysis and thermal stability studies of organic materials,[5,6] metallorganic[7] and inorganic salts[8] are the most usual. EGA is also used to identify absorbed gases in polymers,[9] the surface structure of catalysts,[10] the functionalisation of nanocrystals[11,12] and carbon nanotubes to prepare graphene nanoribbons.[13] In vacuum, EGA-MS offers a very high sensitivity and reduces the chance of secondary reaction between volatiles. Consequently, it is very suitable to decomposition processes where several radicals evolve from the surface of nanocrystals. Classically, EGA-MS gives us the mass of the organic molecules lost as a function of temperature and the mass spectrum of each detected volatile in the system. We aimed to use the decomposition pattern of the attached molecules onto NC surface to ensure not only their presence as capping agent, but also to extract crucial information about their behaviour (e.g. coordination onto NC surface).

In this Chapter, a simple and effective pathway to fully characterise the surface chemistry of NCs containing several adsorbed ions/molecules onto their surface via EGA-MS technique is shown. To this aim, we applied the methodology to three different reported colloidal systems: (i) YF_3 nanocrystals of ~5 nm, (ii) YF_3 supraparticles of ~80 nm and (iii) LaF_3 nanoplatelets of ~7 nm size. The use of (i) and (ii) allows the comparison between compounds of different size, maintaining the composition. Group (iii) allows to observe the effect of different metals in the LnF_3 compounds. The obtained results

perfectly agree with the previous experimental and computational characterisations performed to obtain the real surface image of these systems. Using a single technique, we were able to identify all ions attached onto the NC surface and to know the coordination of a multidentate ligand (e.g. citrate), observing if it is adsorbed by one or two carboxylate moieties. This new approximation is prone to rationalise the shell composition in nanoscaled systems, as well as, to full-identify all ligand-to-surface interactions.

6.2 Experimental

6.2.1 Synthetic details

YF$_3$ and LaF$_3$ NCs have been obtained using the synthetic approach explained in the experimental part of Chapter 2 and Chapter 4 (Co-precipitation method).

6.2.2 Characterisation

Dynamic Light Scattering (DLS) and ζ-Potential analyses have been carried out in Characterisation of Soft-Materials Services at ICMAB using a Zetasizer Nano Zs with a measurement range of 0.3 nm – 10.0 μm and sensitivity of 0.1 mg/mL. Transmission electron microscopy (TEM) micrographs were obtained on a 120 kV JEOL 1210 TEM, which has a point resolution of 3.2 Å. The EGA-MS setup consists in a quartz tube that is kept at a pressure of 10^{-6} mbar. To measure the sample temperature, samples are placed directly on a platinum sheet that is in a tight thermal contact with a K thermocouple. Gases evolving from the sample are analysed by means of a quadrupole mass spectrometer, MS, (model Microvision Plus from MKS). The MS is placed next to the quartz tube so the distance from the sample to the gas analyser is about 40 cm. The quartz tube is place inside a tubular furnace. Experiments are performed at a constant temperature rise of 5 K per minute. This setup allows monitoring the evolution of the volatiles and their fragments as a function of the sample temperature.

Concerning other experimental techniques (^{1}H NMR, IR and XPS) and MD simulations mentioned during this chapter, see Chapters 2 and 4 to obtain more details.

6.3 Results and discussion

6.3.1 Overview of analysed systems

Particles were obtained following the standard protocol based on a modified co-precipitation method in water, as described in Chapter 2 (YF$_3$ supraparticles[14]) and Chapter 4 (LaF$_3$ patchy NCs[15]). To obtain YF$_3$

nanocrystals of small size (~ 5 nm), we used a kinetic control during the synthesis at a temperature of 5 °C (as explained in Chapter 2).[14] Used NCs are shown in Figure 6.1, presenting monodispersed colloidal systems in water. During the synthesis, several ionic species were introduced in the system: acetate (from metallic precursor), tetramethylammonium citrate (stabiliser) and ammonium (counter ion of fluorinating source). The final composition of the system contains two carboxylate species and two nitrogen-based compounds, being difficult their direct identification by one classical experimental technique.
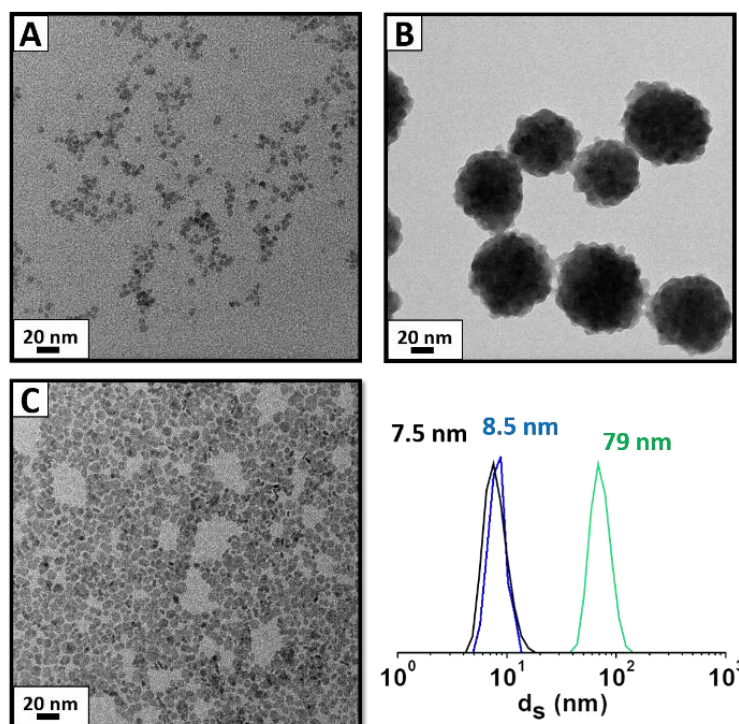
Figure 6.1. DLS and TEM brightness images of the selected particles for the EGA-MS study. (A) YF₃ nanocrystals synthesised at 5 °C (DLS in black), (B) YF₃ supraparticles obtained at 100 °C (DLS in green) and (C) LaF₃ nanocrystals obtained at 100 °C (DLS in blue). All of them via a co-precipitation method in water.

As mentioned before, the complete study of the surface chemistry requires sometimes the combination of several techniques. In Chapter 2, the shell of YF₃ nanocrystals/supraparticles was completely unravelled by experimental techniques and MD simulations. Using a computational approach (Figure 6.2A), we were able to know that the NC surface was covered by acetate, citrate and ammonium while tetramethylammonium played the counter ion role. This information was difficult to be clarified by using only conventional experimental techniques. However, using NMR and XPS (Figure 6.2B) characterisation, all these ions have been detected onto NC surface. Due to, the fast H-D exchange of ammonium cations, these cations were not visible by ^{1}H NMR and the full-analysis of the surface by XPS was required. Concerning the coordination observed in tridentate citrate anions, we postulated that in YF₃ NCs, citrate is preferentially attached by one carboxylic moiety while, in YF₃ supraparticles, the coordination by two carboxylic groups is observed. This evidence was detected only experimentally

(by the broad signals of ¹H NMR), but MD simulations showed a similar behaviour in both systems in water.
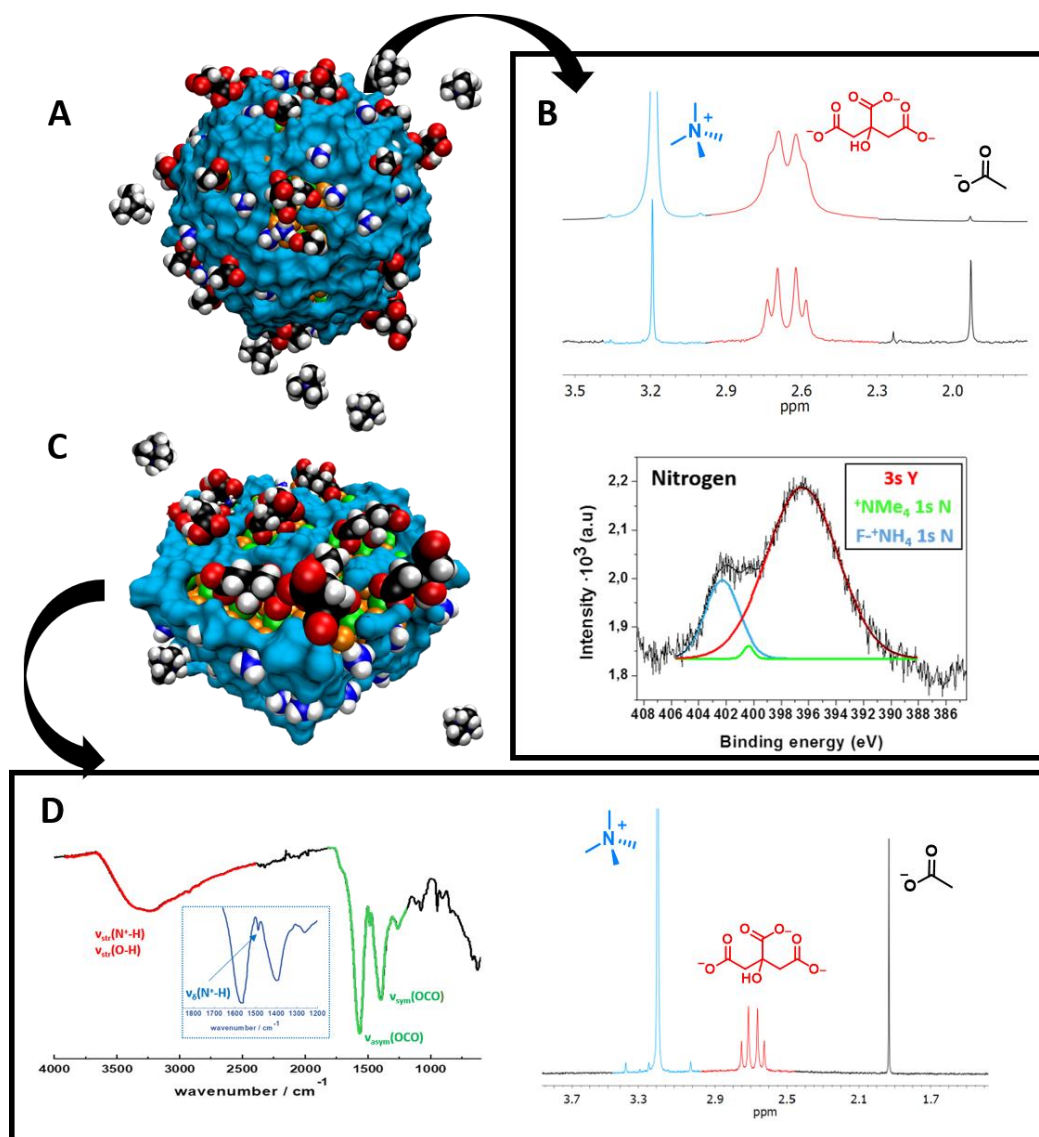
Figure 6.2. Summary of the experimental characterisation and MD simulations performed to unravel the surface image of YF₃ and LaF₃ NCs. (A) Snapshot of equilibrium configuration obtained in MD simulation of YF₃ at 100 °C, (B) ¹H NMR (upper YF₃ synthesised at 5 °C and bottom synthesised at 100 °C) and XPS of YF₃ supraparticles synthesised at 100 °C (C) Snapshot of equilibrium configuration obtained in MD simulation of LaF₃ at 100 °C and (D) IR and ¹H NMR characterisation of LaF₃ NCs washed five times.

LaF₃ NCs presented in Chapter 4 were also characterised by MD simulations (Figure 6.2C), unravelling patchy NCs where ions were selectively attached onto the different exposed faces. To observe this surface chemistry, NMR and IR were carried out (Figure 6.2D), showing acetate, citrate and tetramethylammonium by NMR and the bending mode of ammonium in IR.

Considering all exposed drawbacks in the surface chemistry study by commonly used experimental techniques and MD simulations, the

implementation of a general protocol to full-characterise the surface of colloids is required. As we presented in the introduction, EGA-MS is a suitable technique to detect all volatiles released from NC surface during a thermic process. The high sensibility and limited drawbacks of MS make it an excellent technique to be applied to colloidal systems containing inorganic NCs.

6.3.2 Monovalent species by EGA-MS

Firstly, we aimed to detect water and ammonium adsorbed onto the NC surface because they were very difficult to uncover by experimental techniques in previous chapters. Considering these molecules, we expect to see the fragmentation patterns of water and ammonia by the detection of fragments showed in Scheme 6.1.

Scheme 6.1. Expected mass of the fragments produced from water and ammonium cation.

$$H_2O \longrightarrow OH^+ + H_2O^+$$
$$\quad\quad\quad\quad M/Z = 17 \quad M/Z = 18$$

$$NH_4^+ \longrightarrow NH_2^+ + NH_3^{+\cdot}$$
$$\quad\quad\quad\quad M/Z = 16 \quad M/Z = 17$$
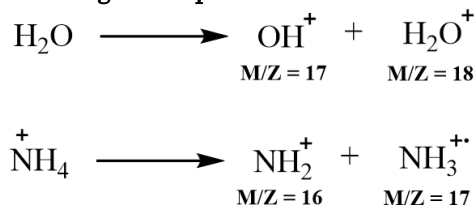
We started the study of EGA-MS comparing YF_3 NCs with YF_3 supraparticles (Figure 6.3). The use of EGA-MS allowed us to observe easily the presence of NH_4^+ onto the surface of the NCs, as well as, the strongly adsorbed water, playing also a stabiliser role.

Figure 6.3. EGA-MS analysis of YF₃ supraparticles (upper) and YF₃ NCs (bottom) with detected M/Z peaks for water and ammonia, corresponding to water and ammonium cation adsorbed onto NC surface.

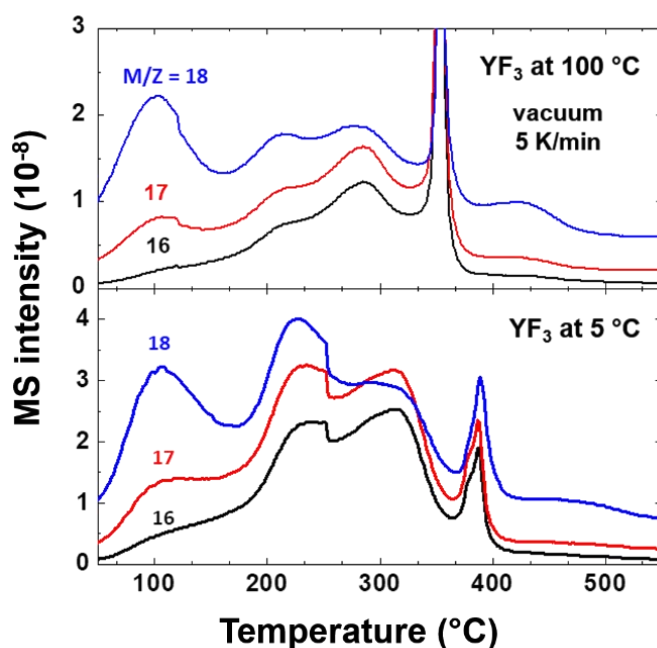The EGA-MS curves of fragments M/Z = 16, 17 and 18 can be interpreted as arising from H_2O and NH_3. Their relative intensities should be compared to the defragmentation pattern of H_2O ($I_{16}/I_{17}/I_{18}$ = -/0.22/1) and NH_3 ($I_{16}/I_{17}/I_{18}$ = 0.8/1/-). The peak at 100 °C corresponds mainly to water desorption with a non-negligible contribution of NH_3 revealed by the M/Z = 16 signal. As temperature increases above 200 °C, two additional processes at around 220 and 290-310 °C are detected in which the contribution of NH_3 dominates (higher I_{17}/I_{18} ratio). Finally, the sharp peak between 350 and 400 °C can be attributed to a combustion process. It does not provide any relevant information as most measured M/Z curves contain this peak.

We also detect the presence of both molecules in the case of LaF_3 NCs (Figure 6.4), using the main peak in M/Z = 18 to water and M/Z = 16 to ammonia. However, the main peaks in this case were at lower temperatures ~80 °C for water and ~220 and ~290 °C for ammonia. From these results, the same role of water and ammonium have been postulated in all NCs, those with the same core but different sizes and those containing different metal in the core.
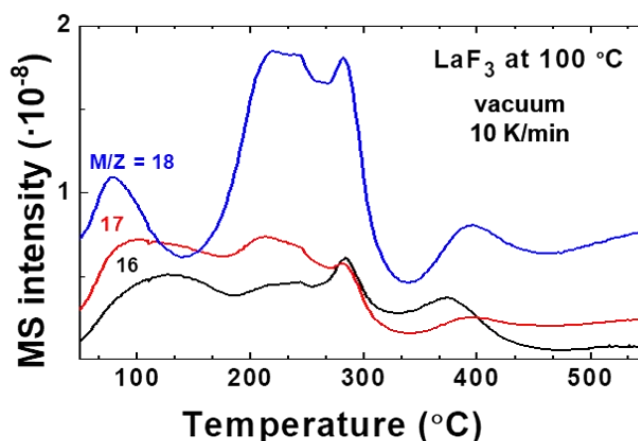
Figure 6.4. EGA-MS analysis of LaF₃ particles with detected M/Z peaks for water and ammonia, corresponding to water and ammonium cation adsorbed onto NC surface.

Concerning the obtained releasing temperatures, ammonium cation (postulated to be adsorbed in fluorine position), shows the same temperature in all EGA-MS plots. However, water molecules (postulated to be adsorbed onto fluoride and metal positions) show little displacement depending on the used metal. This effect is not surprising considering the size of the metal cation, in which bigger sized cations should show lower binding energy and hence, lower temperature of releasing (i.e. water onto LaF_3 NCs).

Using EGA-MS, water and ammonium were easily identified to be adsorbed onto the NC surface. These two molecules showed some drawbacks when we tried to detect them with simple experimental techniques. In addition, the presence of other nitrogenated compound made it difficult the direct application of techniques based on nitrogen detection (e.g. elemental analysis). In Figure 6.2 is shown an overview of the required techniques to

unveil the presence of ammonium in our two previous works,[14,15] while using EGA-MS we detected it easily.

To identify tetramethylammonium in our system, we expect the detection of the trimethylamine release with main peaks at M/Z = 58, 59, 30 and 42 as shown in Scheme 6.2.

Scheme 6.2. Expected mass of theoretical fragmentations produced by tetramethylammonium cation.

$$C_4H_{12}N^+ \longrightarrow CH_2NH_2^+ + C_2H_4N^+ + C_3H_8N^+ + C_3H_9N^+$$
$$\text{M/Z = 30} \quad \text{M/Z = 42} \quad \text{M/Z = 58} \quad \text{M/Z = 59}$$

The presence of tetramethylammonium in our system was also stated, in both cases (NCs and supraparticles), thanks to the M/Z = 58 and 59 fragments at ~300 °C with an experimental ratio of ($I_{58}/I_{59} \approx 2.5$) fragments observed in Figure 6.5. The main peaks for the trimethylamine identification are M/Z = 58, 59, 30 and 42 with theoretic ratios of ($I_{58}/I_{59}/I_{30}/I_{42} = 1/0.70/0.35/0.27$). The higher relative intensity of fragment 58 obtained experimentally could be understood because this M/Z value can receive contribution from other volatiles like acetone (see below). Experimental fragments at M/Z = 30 and 42 also contain the contribution of other volatiles, which difficult matching the theoretical ratios.

Figure 6.5. EGA-MS analysis of YF₃ particles at 100 °C (upper) and 5 °C (bottom) with detected M/Z peaks for tetramethylammonium release.

Considering the analysis in LaF₃ NCs, the same peaks have been detected at ~280 °C, which corroborate the presence of tetramethylammonium onto the surface of the particles (Figure 6.6).
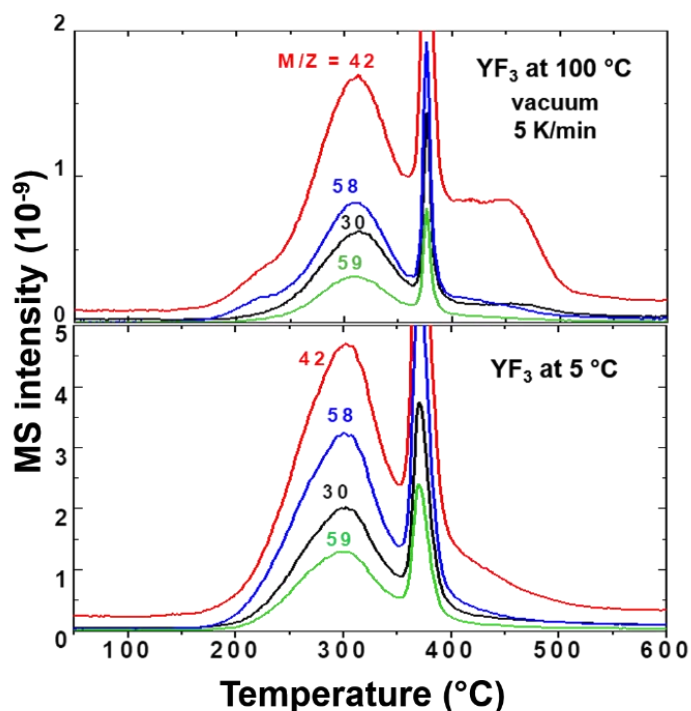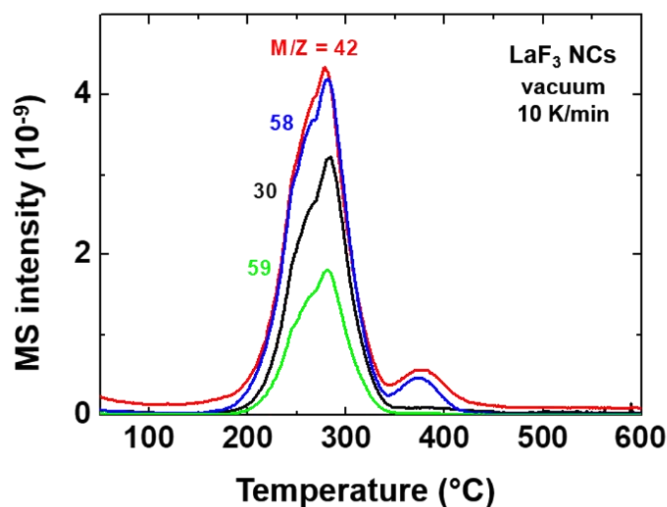
Figure 6.6. EGA-MS analysis of LaF₃ particles with detected M/Z peaks for tetramethylammonium release.

Here, we observed that tetramethylammonium is released at lower temperatures in LaF₃ than in both YF₃ cases. This behaviour could be explained considering that tetramethylammonium is playing the counter ion role in these systems, being interacting with free carboxylate moieties of citrate. In consequence, releasing temperature of tetramethylammonium could be modified by the metal-citrate interaction as we explain in section 6.3.3.

Finally, the last monovalent specie identified was the acetate anion arising from the metallic precursor. Considering the conditions of the experiment, we expect to observe the releasement of acetate in acetone form following Scheme 6.3.[16,17]

Scheme 6.3. Expected mass of theoretical fragmentations produced by the acetate anion.

$$C_2H_3O_2^- \longrightarrow C_2H_3O^+ + C_3H_6O^{+\bullet}$$
$$\text{M/Z = 43} \qquad \text{M/Z = 58}$$
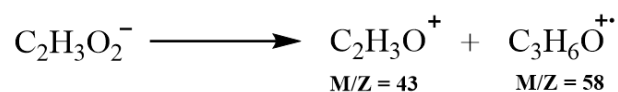
Acetone can be detected by the presence of M/Z = 58 and 43 at ~300 °C with a theoretical ratio of $I_{43}/I_{58} = 4$. Peak observed at M/Z = 58 is assigned to two different species (tetramethylammonium and acetate), in consequence we expect that the experimental ratio intensities will differ to the theoretical ones in the case of acetate identification. In Figure 6.7, the EGA-MS results of both YF₃ NCs and supraparticles are shown. The presence of acetate onto NC surface is confirmed although the relative intensities of the M/Z peaks cannot be decisive to a clear assignation due to the overlapping of other volatiles.
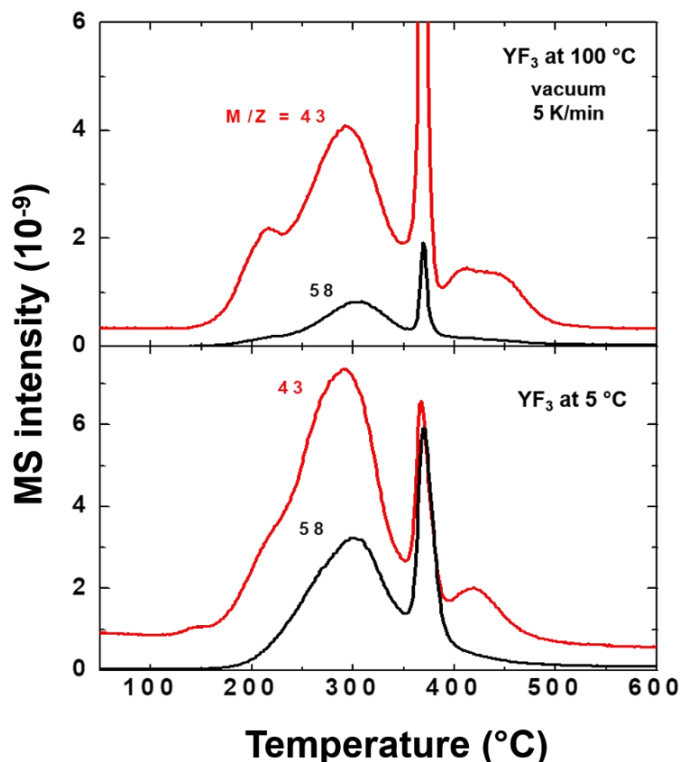
Figure 6.7. EGA-MS analysis of YF₃ particles at 100 °C (upper) and 5 °C (bottom) with detected M/Z peaks for acetate release as acetone.

Concerning the results of EGA-MS for LaF₃ NCs (Figure 6.8), the presence of acetate onto NC surface can also be postulated at ~250 °C. In this case the difference in temperature for the release of acetate is clearly observed. In the case of YF₃ NCs, a temperature of ~300 °C is observed while, in the case of LaF₃ NCs, acetate is released at ~250 °C.
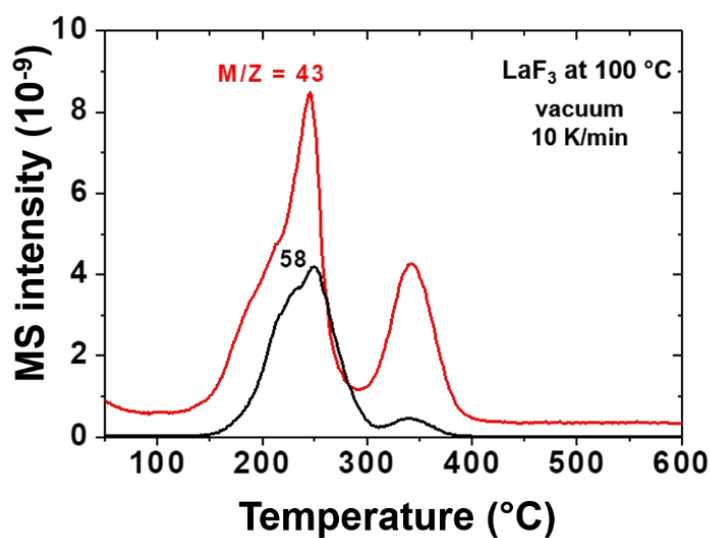

Figure 6.8. EGA-MS analysis of LaF₃ particles with detected M/Z peaks for acetate released as acetone.

For the acetate anion, a high difference of 50 °C in releasing temperatures between YF_3 and LaF_3 particles was observed. Considering the negative charge of acetate, we expect the highest interaction in carboxylic-to-metal binding. This behaviour is explained in more detail for the citrate case in section 6.3.3.

In summary, we found the presence of adsorbed water, ammonium, acetate and tetramethylammonium as molecules or monovalent ions onto the NC surface. All these species were detected in the three studied systems (YF_3 NCs/supraparticles and LaF_3 NCs), with difference in the release temperatures in which the volatiles were detected (Table 6.1).

We observed as ammonium cation shows the same released temperatures in all systems. This could be explained considering that ammonium cation is adsorbed onto fluoride positions. The two different observed peaks for ammonium in each sample could be explained considering different ionic behaviours onto NC surface although no more information could be extracted from EGA-MS analysis.

Table 6.1. Temperatures in which monovalent ions/molecules are released from NC surface in their corresponding volatile form.

	YF_3 NCs	YF_3 suprap.	LaF_3 NCs
Water	100 °C	100 °C	80 °C
Ammonium	220/310 °C	220/290 °C	220/290 °C
Tetramethylammonium	300 °C	300 °C	280 °C
Acetate	300 °C	300 °C	250 °C

The other species show larger differences between YF_3 and LaF_3 inorganic cores, being the releasing temperature higher in the case of YF_3 particles. This effect could be closely related with the cation radii of the different lanthanides, having higher energy interaction the smaller one (Y^{3+}), as is shown in the case of water and acetate detection.

6.3.3 Unravelling the coordination of citrate

To detect citrate attached to the NC surface, firstly we need to know the decomposition path of this molecule. Two decomposition pathways are highlighted for citric acid;[17] one at 175 °C with the formation of citraconic anhydride and the other at 250 °C with the formation of 1,3-acetonedicarboxylic acid. In our conditions, we expect the formation of citraconic anhydride because it takes place at lower temperature, showing the fragmentation pattern described in Scheme 6.4.

Scheme 6.4. Expected mass of theoretical fragmentations produced by citraconic anhydride acid after its decomposition from citrate.

$$C_6H_5O_7{}^{3-} \longrightarrow C_3H_3{}^{+} + C_3H_4{}^{+\bullet} + C_4H_4O{}^{+\bullet}$$
$$\phantom{C_6H_5O_7{}^{3-} \longrightarrow } M/Z = 39 \qquad M/Z = 40 \qquad M/Z = 68$$
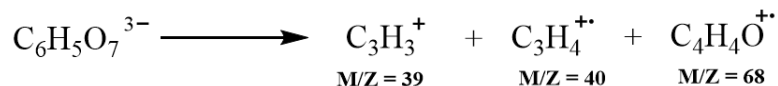
In consequence, it is crucial the detection of citraconic anhydride that was identified through fragments with M/Z = 39, 40 and 68 (Figure 6.9). The intensity ratios of fragments 39 and 40 agree with the fragmentation pattern of citraconic anhydride ($I_{39}/I_{40}/I_{68}$ = 1/0.7/0.7). The discrepancy between their intensity and that of M/Z = 68 can be attributed to the more likely generation of small fragments inside the furnace due to thermal decomposition, in addition to the fragmentation in the quadrupole itself; a phenomenon we have recently observed during decomposition of metal organic salts.[18]
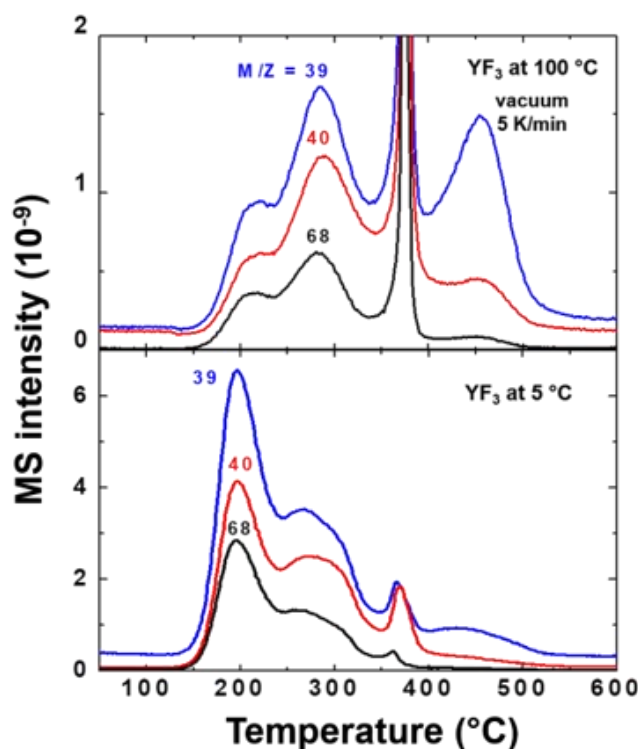
Figure 6.9. EGA-MS analysis of YF₃ particles at 100 °C (upper) and 5 °C (bottom) with detected M/Z peaks for citraconic anhydride release.

From EGA-MS plot, we can identify the presence of two peaks related to citraconic anhydride in YF₃ particles at 200 and 285 °C. The peak at 200 °C is more intense in particles obtained at 5 °C (Figure 6.9 bottom) while the peak at 285 °C is predominant for those synthesised at 100 °C (Figure 6.9 upper). The evolution of citraconic anhydride reveals a temperature-dependent coordination to the NC surface and can be attributed to a different coordination of citrate onto NC surface. At 5 °C, the energy of the system allows the preferential coordination by one carboxylic group. This interaction

could be broken by a mechanism that starts from citrate to form citraconic anhydride, releasing water and carbon dioxide (Figure 6.10A). Finally, citraconic anhydride is released from the surface of NCs at a temperature (T_1) of 200 °C approximately. In contrast, for particles synthesised at 100 °C, the coordination by two different carboxylic moieties accounts for the most intense peak at a higher temperature ($T_2 = 285$ °C), as it can be observed in Figure 6.10B. These citrate coordination of YF_3 NCs and supraparticles were postulated in our previous work via ^1H NMR analysis.[14] In this study, we observed a coordination by one carboxylic moiety in those YF_3 NCs synthesised at 5 °C while in those synthesised at 100 °C presented a predominant stabilisation of citrate attached by two carboxylic moieties.
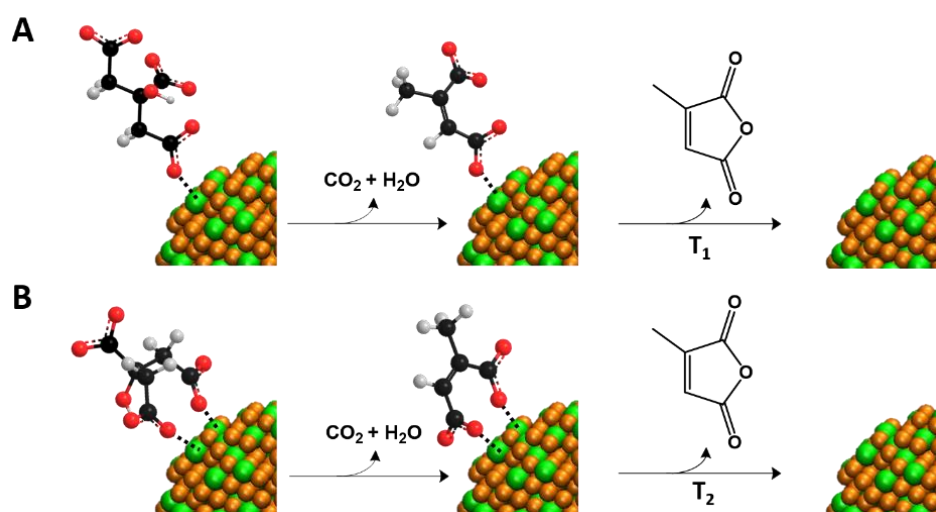
Figure 6.10. Mechanism involved during the decomposition and release of citrate from NC surface. (A) Citrate is attached by one carboxylic acid and is released at temperature T_1 and (B) citrate is adsorbed by two different carboxylic moieties and is released at T_2 as citraconic anhydride.

From these observations, we stablish a surface chemistry containing ammonium, acetate, citrate and tetramethylammonium; i.e. the same composition than that was identified using several experimental techniques and MD simulations. In addition, giving the two different volatilisation temperatures for the same molecule, we postulate a surface with two different kind of coordination. NCs obtained at 5 °C revealed more citrate attached to one carboxylic group (Figure 6.11A) while those obtained at 100 °C present more citrate attached to two carboxylic groups (Figure 6.11B). In this case, EGA-MS gave us the detailed surface composition of our NCs and it allowed us to know the coordination of a multidentate molecule to the NC surface.

A **B**
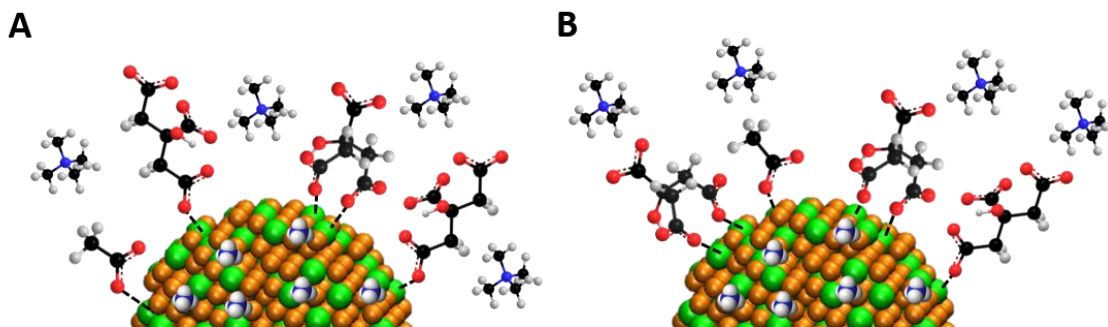
Figure 6.11. Schematic representation of the particle surface for (A) YF₃ NCs synthesised at 5 °C and (B) YF₃ supraparticles synthesised at 100 °C.

In LaF₃ particles EGA-MS plot, we can observe a single peak showing the three main fragments of citraconic anhydride at 210 °C (Figure 6.12). This means that we have one kind of citrate coordination to the NC surface, but it cannot be directly assigned to a monovalent coordination. Results obtained by YF₃ are not extensible to other metals because of their different radius and/or affinity with the organic molecule. La^{3+} is bigger than Y^{3+} and we should expect that citraconic anhydride will be released from NC surface at lower temperatures than their YF₃ analogues (as observed in water and acetate release).
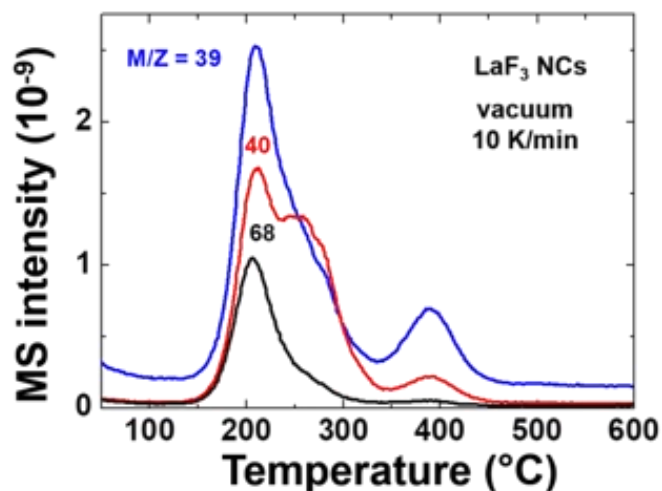
Figure 6.12. EGA-MS analysis of LaF₃ particles with detected M/Z peaks for citraconic anhydride release.

To this aim, we used the results obtained during our MD simulations performed in recently published works, making it possible the comparison of this experimental information with all-atomic MD simulations. From Arrhenius equation:

$$p \sim e^{-\frac{\Delta(\Delta G)}{k_B T}}$$

(6.1)

it can be stated that for LaF$_3$ NCs that the temperature of 210 °C corresponds to T$_2$ showed in Figure 6.10.

In the equilibrium configurations, we can compare the correlation functions of LaF$_3$ and YF$_3$ NCs with oxygens of carboxylic groups of citrates of our previous MD simulations observed in Figure 6.13. The intensity of the first peak give us the affinity of citrate with the metal of our system and hence, an estimation of the Gibbs free energy of this interaction in equilibrium. If the quotient between the temperature of the citraconic anhydride release observed in EGA-MS by LaF$_3$ and YF$_3$ NCs obtained at 100 °C is comparable, we could assess that the difference observed in temperature is produced by the effect of the metal. A ratio value of 0.869 obtained by the correlation function quotient (106/122 from Figure 6.13) is compatible with the 0.866 obtained by the temperature quotient (483/558 from Figure 6.9 and 6.12 in Kelvin units). Thus, we demonstrate that the peak of citraconic acid at 210 °C in LaF$_3$ NCs is produced by the attachment by two different carboxylic groups following the process described in Figure 6.10B.
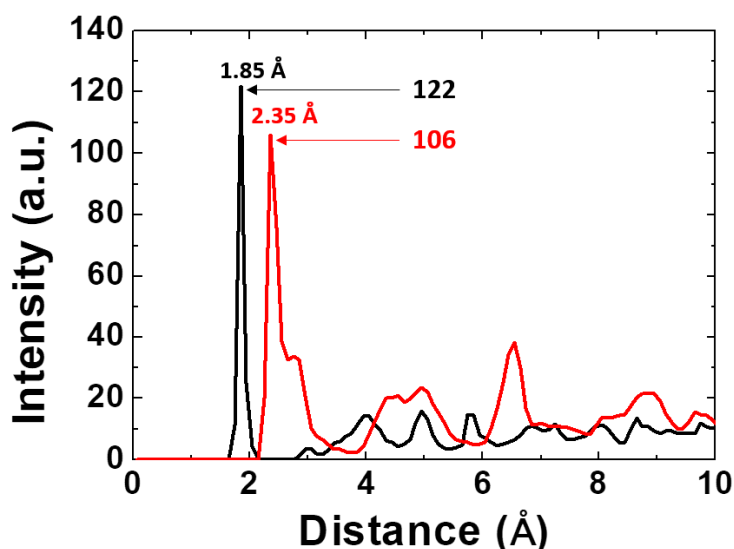
Figure 6.13. Correlation function of Citrate-Metal performed in the equilibrium for YF$_3$ and LaF$_3$ MD simulations.

6.4 Conclusions

In this Chapter is reported an easy, fast and complete surface characterisation applied to nanoscaled systems that allows the accurate identification of all attached species onto a NC surface. Using EGA-MS as principal technique we unravelled the complete surface composition of a set of three kinds of NCs (YF$_3$ NCs, big YF$_3$ supraparticles and LaF$_3$ NCs). Surface chemistry is composed by the combination of acetate, citrate,

ammonium and tetramethylammonium, obtaining the same composition in all cases with some difference related to coordination and the used metal cation in NC core.

Considering the coordination differences, we concluded that in YF_3 nanocrystals (those obtained at 5 °C), present a preferential coordination by one carboxylate moiety. On the other hand, YF_3 supraparticles (synthesised at 100 °C) and LaF_3 NCs show a preferential coordination by two carboxylate moieties. The effect of metal used in NC core (YF_3 or LaF_3) was claimed to affect directly the releasing temperature of those ions attached onto these atoms (water, acetate and citrate). We found that ions attached to lanthanum were released at lower temperature than those adsorbed onto yttrium atoms. This behaviour is expected considering their cationic radii (La^{3+} is bigger than Y^{3+}), in consequence the binding energy of the same molecule with different sized-atoms decrease as bigger the metal radius is.

The present study is of interest not only for metal fluoride nanocrystals, but in general for all kind of nanoscaled system in which their surface composition is the key parameter to control and design stable colloidal suspensions. The use of EGA-MS as main technique to fully characterise nanoscaled systems avoids the necessity of performing several experimental characterisation and/or MD simulations to unravel a real surface image. Although it is interesting the use of different techniques to uncover specific insights of the obtained systems, here we demonstrate the efficiency of EGA-MS in NC surface characterisation.

6.5 References

[1]   H. Al-Johani, E. Abou-Hamad, A. Jedidi, C. M. Widdifield, J. Viger-Gravel, S. S. Sangaru, D. Gajan, D. H. Anjum, S. Ould-Chikh, M. N. Hedhili, et al., *Nat. Chem.* **2017**, *9*, 890–895.

[2]   M. A. Boles, D. Ling, T. Hyeon, D. V. Talapin, *Nat. Mater.* **2016**, *15*, 141–153.

[3]   J. De Roo, Y. Justo, K. De Keukeleere, F. Van den Broeck, J. C. Martins, I. Van Driessche, Z. Hens, *Angew. Chemie - Int. Ed.* **2015**, *54*, 6488–6491.

[4]   S. Materazzi, R. Risoluti, *Appl. Spectrosc. Rev.* **2014**, *49*, 635–665.

[5]   L. Sanchez-Silva, D. López-González, J. Villaseñor, P. Sánchez, J. L. Valverde, *Bioresour. Technol.* **2012**, *109*, 163–172.

[6]   M. Brebu, T. Tamminen, I. Spiridon, *J. Anal. Appl. Pyrolysis* **2013**, *104*, 531–539.

[7]   J. Farjas, J. Camps, P. Roura, S. Ricart, T. Puig, X. Obradors, *Thermochim. Acta* **2013**, *556*, 58–62.

[8]   C. Maton, N. De Vos, C. V. Stevens, *Chem. Soc. Rev.* **2013**, *42*, 5963.

[9]   T. Shimoaka, C. Wakai, T. Sakabe, S. Yamazaki, T. Hasegawa, *Phys. Chem. Chem. Phys.* **2015**, *17*, 8843–8849.

[10] I. Murillo Leo, M. López Granados, J. L. G. Fierro, R. Mariscal, *Appl. Catal. B Environ.* **2016**, *185*, 141–149.

[11] D. Celik, M. Krueger, C. Veit, H. F. Schleiermacher, B. Zimmermann, S. Allard, I. Dumsch, U. Scherf, F. Rauscher, P. Niyamakom, *Sol. Energy Mater. Sol. Cells* **2012**, *98*, 433–440.

[12] C. Slostowski, S. Marre, O. Babot, T. Toupance, C. Aymonier, *Langmuir* **2012**, *28*, 16656–16663.

[13] B. Genorio, W. Lu, A. M. Dimiev, Y. Zhu, A. R. O. Raji, B. Novosel, L. B. Alemany, J. M. Tour, *ACS Nano* **2012**, *6*, 4231–4240.

[14] J. Martinez-Esain, J. Faraudo, T. Puig, X. Obradors, J. Ros, S. Ricart, R. Yáñez, *J. Am. Chem. Soc.* **2018**, *140*, 2127–2134.

[15] J. Martínez-Esaín, T. Puig, X. Obradors, J. Ros, R. Yáñez, J. Faraudo, S. Ricart, *Angew. Chemie - Int. Ed.* **2018**, DOI: 10.1002/ange.201806273.

[16] J. Farjas, J. Camps, P. Roura, S. Ricart, T. Puig, X. Obradors, *Thermochim. Acta* **2011**, *521*, 84–89.

[17] I. A. Farbun, I. V. Romanova, S. A. Kirillov, *J. Sol-Gel Sci. Technol.* **2013**, *68*, 411–422.

[18] S. Rasi, S. Ricart, X. Obradors, T. Puig, P. Roura, J. Farjas, *J. Anal. Appl. Pyrolysis* **2018**, *133*, 225–233.

7

General conclusions and Perspectives
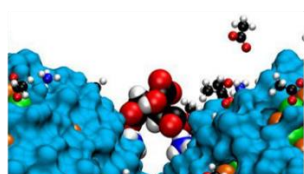
Citrate-mediated Ionic bridges
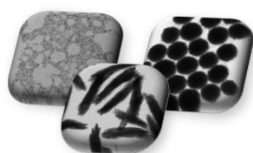
LnF₃ NCs
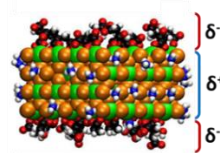
Patchy NCs
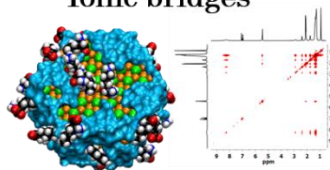
Selective ligand exchanges
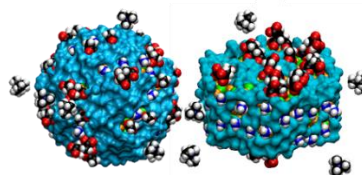
New Surface Technique

"Everything should be made as simple as possible, but not simpler."

Albert Einstein

"The history of science shows that theories are perishable. With every new truth that is revealed we get a better understanding of Nature and our conceptions and views are modified."

Nikola Tesla

"We must not forget that when radium was discovered no one knew that it would prove useful in hospitals. The work was one of pure science. And this is a proof that scientific work must not be considered from the point of view of the direct usefulness of it. It must be done for itself, for the beauty of science, and then there is always the chance that a scientific discovery may become like the radium a benefit for humanity."

Marie Curie

7.1 General conclusions

In our quest for the insights of the synthesis of LnF$_3$ NCs and the study of their surface chemistry, we found not only a deep understanding of their synthetic parameters and their general properties, but also interesting conceptually new systems which focused our attention to be explored in detail. This led to extract several conclusions in each step carried out during this PhD. study. As in each chapter has been explained the main conclusions of this work, here we summarised the most relevant as an overview of the main ones.

Firstly, we unravelled a new kind of ionic self-assembly based on the formation of citrate mediated ionic bridges tuneable with temperature. This self-assembly was postulated not only for a specific system of YF$_3$ and citrate but extended to other NC systems (e.g. SmF$_3$) and with other carboxylic acids (e.g. citraconic acid). During this study, the use of experimental techniques and MD simulations allow us to postulate the complete mechanism of this self-assembly. We unravelled the effect of using different cations and anions, as well as, the important role of water as stabiliser onto the NC surface.

Second, aimed by the results obtained with YF$_3$, SmF$_3$, EuF$_3$ and LuF$_3$, we investigated in detail the mechanistic insights on the synthesis of all-LnF$_3$ NCs via co-precipitation method. We found that LnF$_3$ NCs could be divided in two different groups, (i) homogeneous NC dispersions that avoid the self-assembly thanks to their facets and (ii) supraparticles formed by citrate mediated bridges due to the spherical role of their NCs. In addition, we found that the faceting of LnF$_3$ is directly associated with their crystalline structure and the size of the used lanthanide cation, being the first three classified in the group (i) and the rest in group (ii). Finally, it was demonstrated that the pH modifies the crystalline structure of those NCs formed with the smaller lanthanide cation, from cubic in neutral-basic conditions to orthorhombic in acidic conditions.

Third, we found patchy NCs in those metals of group (i), due to the hexagonal faceting of the NCs. The faceting allows thermodynamically stable patches during the synthetic process in contrast with the reported methods to obtain patchy NCs. During the synthetic process, cations and anions are spontaneously adsorbed in the different patches. In addition, patches show different affinity with the used solvent, producing a swapping between water and methanol in determinate faces. Finally, we open a pathway to growth the obtained patchy NCs and different synthetic routes to obtain bigger and more shape defined systems (hydrothermal and MW treatments).

Fourth, we performed several ligand exchange methodologies to modify partially and completely the interface of LaF$_3$ patchy NCs. In water media, we found that dopamine hydrochloride releases ammonium cations while 3,4-dihydroxyhydrocinnamic acid replaces the attached anions if we used 3 equivalents of a base. Likewise, using L-lysine hydrochloride, we were able to

exchange cations and anions from NC surface. All these exchanges have been studied using experimental techniques (e.g. NMR) and MD simulations to understand the mechanisms concerning the exchanges. Finally, we used the same methodology applied to non-aqueous systems (e.g. toluene). Although the exchanges have been successfully achieved, the main insights of the new surface chemistry, in toluene, must be unravelled.

Fifth, EGA-MS was proved as useful technique not only for the complete screening of the ligands onto NC surface but also for unravelling the coordination of multidentate ions (e.g. citrate). Obtained results match with the previous characterisation via experimental techniques and MD simulations.

Finally, during all this thesis, experimental techniques have been used in combination with all-atomic detailed MD simulations to provide the complete image of the main problem in each situation. Although experimental characterisation provides us relevant and complete information about our systems, this thesis would not have been possible without the use of MD simulations. In other words, citrate mediated ionic bridges and patchy NCs would not have been appropriately unveiled without the use of MD simulations. In consequence, the last conclusion of this thesis is the importance of combining experimental techniques and computational approaches to obtain all details in the studied systems.

7.2 Perspectives

Once this thesis is concluded, we realised that not all the goals have been concluded properly, in other words, there are more insights to be uncovered.

Concerning Chapter 2, after the unravelling of citrate mediated interactions in YF$_3$ NCs, we observed the same behaviour in other systems and using other multidentate carbonylated ions. A deep investigation of several kind of ligands to promote this ionic self-assembly could be an interesting continuation of this chapter. Is a carbonylated ion mandatory to promote this self-assembly? Could be used other kind of anion to promote the bridges? Is this self-assembly only applicable to metal fluoride NCs? Are there other factors (instead of temperature) to tune this self-assembly? All these questions could be a starting point to extract more information about this tailored ionic self-assembly of NCs.

Chapter 3 was performed as a systematic study of the co-precipitation method and the modification of some parameters to extract the maximum information. Obviously, more parameters could be studied to know deeply more insights concerning this methodology, as well as, the complete study of the hydrothermal treatment to all metals (as introduced in Chapter 4 for lanthanum). In a more ambitious project, it could be studied the same kind of

systematic and mechanistic process to lanthanide (III) oxide NCs, being a new pathway to study the surface chemistry of NCs based on lanthanides.

After the synthesis of thermodynamically stable patchy NCs and their experimental and computational study, Chapter 4 open the way to growth and functionalise NCs in one step. In addition, in this chapter is opened the hydrothermal and MW treatments, which as said before, could be applied in all lanthanide series. The most relevant perspective in this chapter is the functionalisation with amino acids forming dioxo-pyridine ring based dyes and the possible self-assembly produced when using basic amino acids during this functionalisation.

In Chapter 5, we opened non-aqueous ligand exchanges in toluene using a similar methodology of those performed in water. But the direct identification of the carboxylic acid on the system was not achieved, although this seems present in the system (coloured colloidal solution in the case of 3,4-dihydroxyhydrocinnamic acid with oleylamine). A deep study of the exchanges in non-aqueous solvents could be carried out to see the complete picture of these patchy NCs in non-polar solvents, understanding better the interface of these NCs.

Finally, the use of EGA-MS technique to explore the surface chemistry of metal fluoride NCs in Chapter 6, should be tested in other system (e.g. metal oxide NCs) and with other kind of stabilisers (e.g. triethylene glycol coated NCs). The use of this technique in other systems should allow a deep understanding of this technique, being after that, extensible to all-nanoscaled systems as useful technique in a wide range of NCs.

Concerning the use of these NCs, it will be open some ways to apply the knowledge obtained during this thesis. As commented during some chapters, LnF_3 NCs are prone to be applied in several fields due to their exceptional properties, specifically when they are doped with other lanthanide elements. Currently, three different pathways have been opened to apply these NCs: (i) as pinning NCs in the enhancement of superconducting layers, (ii) as medical carriers to the detection and treatment of several diseases and (iii) as up-converting devices in materials science and medical purposes.

In the following sections, it will be explained a summary of the current work of these NCs trying to be useful for a wide range of applications. Although all results are preliminary, they seem promising in material science and medical purposes.

7.2.1 Application as pinning centres in $YBa_2Cu_3O_{7-\delta}$

This part has been carrying out in collaboration with Superconducting Materials and Large Scale Nanostructures group of ICMAB-CSIC.

Among the different ceramic superconductors, $YBa_2Cu_3O_{7-\delta}$ (YBCO) is currently one of the most studied high-temperature superconductor. Given its high critical current temperature ($T_c \approx 92$ K), makes YBCO an excellent candidate for a deep range of applications.

The generation of vortices through the YBCO matrix and their movement under the effect of Lorentz forces are the two main drawbacks. Concerning power applications, it is necessary to improve the YBCO performances at high magnetic fields by the pinning of these vortices. First approximation to solve this was the in situ generation of NCs through the YBCO matrix.[1,2] Thanks to the pinning of these vortices produced by the incorporation of defects allows the enhancement of the superconductivity properties of YBCO.

Currently, the ex situ process has been performed because it allows more control in the size, homogeneity and stability of NCs during the synthesis of YBCO.[3] As commented in the introduction of this thesis, a fluorine source is needed during the process of YBCO to produce BaF_2 instead of $BaCO_3$. Here, we use CeF_3 NCs (Figure 7.1A) to carry on a pyrolysis with a precursor solution containing the trifluoroacetate metallic salts of yttrium, barium and copper in methanol. After the pyrolysis (Figure 7.1B), layer seemed good to be growth, obtaining an epitaxial YBCO nanocomposite.
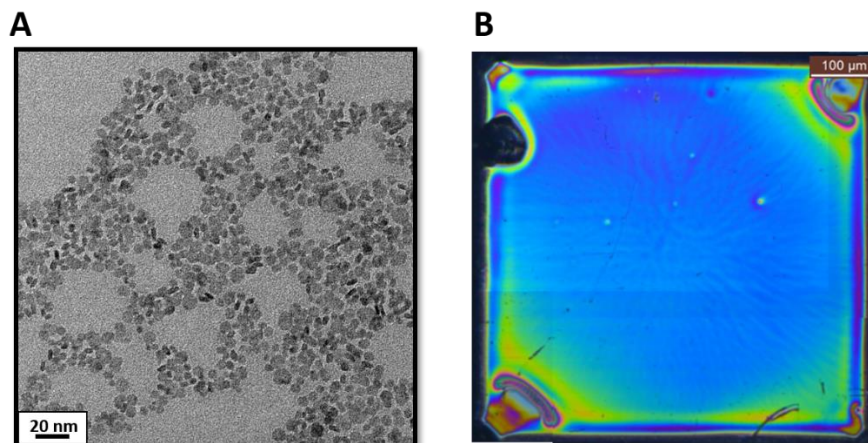
Figure 7.1. (A) TEM image of as-synthesised CeF_3 NCs and (B) YBCO layer after the pyrolysis treatment without cracks and inhomogeneities.

After the growing process and using a Superconducting Quantum Interference Device, M(T) and H(T) curves can be obtained (Figure 7.2). From these curves, we obtained a value of Jc = 3.3 MA/cm² at 77 K and T_c = 89.5 K, good enough to study in more detail further the incorporation of metal fluoride NCs in YBCO matrix. These values have been obtained from the graphs of Figure 7.2 by interpolating 77 K, for the case of J_c, while T_c value was obtained from the derived of the M(T) curve to obtain the inflexion point.
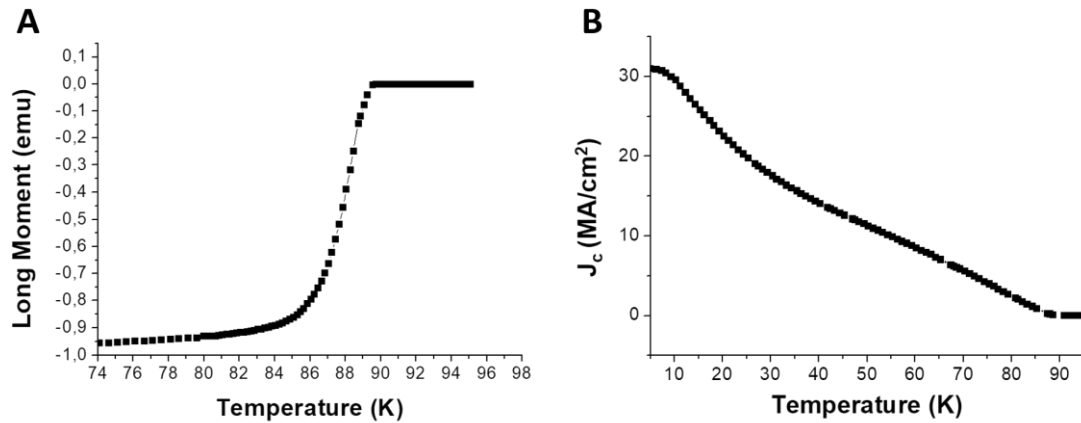
Figure 7.2. (A) M(T) and **(B)** H(T) obtained via superconducting quantum interference device magnetometry to calculate T_c and J_c parameters for layer showed in Figure 7.1.

Finally, we want to know if CeF_3 NCs are present in YBCO matrix distributed randomly. General Area Detector Diffraction System X-ray diffraction pattern was recorded (Figure 7.3), in which is clearly observable the epitaxial peaks of YBCO and the substrate (LAO), but NCs do not seem to be present in the matrix, maybe for their low concentration (8 % molar) or because they reacted forming oxides and they are not visible for their low concentration.
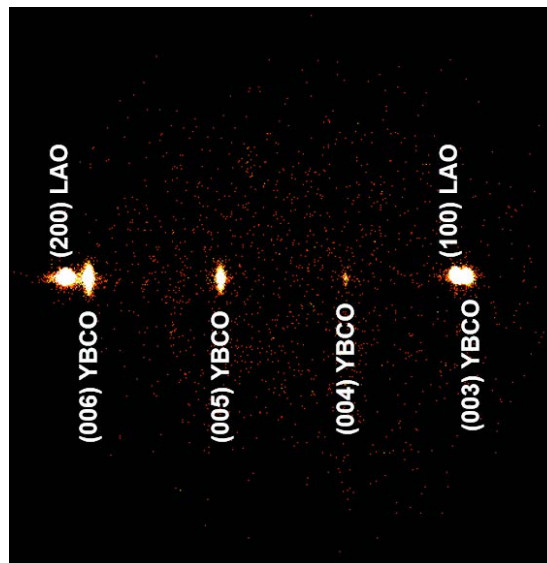
Figure 7.3. 2D General Area Detector Diffraction System X-ray diffraction pattern of TFA-YBCO nanocomposite films with 8 % mol CeF_3 (film thickness of ~150 nm) grown on a LAO substrate.

In this pathway, we are aimed to produce high concentrated layers to detect NCs onto YBCO and study their enhancement of the superconducting properties.

7.2.2 Preliminary toxicity assays in cancer cells

Results explained in this section have been performed with a current collaboration with Drug Delivery and Targeting group of Molecular Biology and Biochemistry Research Centre for Nanomedicine (CIBBIM-Nanomedicine) in Vall d'Hebron research Institute (VHIR).

The possibility to tune our systems (citrate mediated self-assembly), as well as, the selective functionalisation of patchy LaF_3 NCs have been the main factors to start this collaboration with Vall d'Hebron group. They used polymeric-based nanoparticles[4] in a drug delivery onto breast cancer cells, being interesting to expand this drug delivery to inorganic NCs with the possibility to selectively functionalise their different facets.

Aimed by the patchy behaviour of LaF_3 NCs (LaF_3@Cit) and the possibility to selective functionalise NC surface with cations or anions as desired, we tested their toxicity effect in MCF-7 linear cells of breast cancer. To this end, we tested the toxicity of the as-synthesised LaF_3 NCs and the ones after the ligand exchange with lysine (LaF_3@Lys), being presented in Figure 7.4.
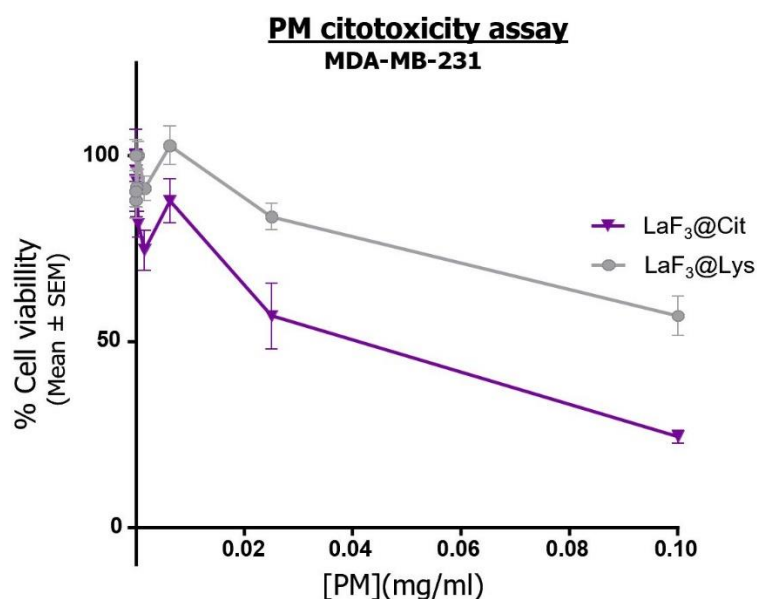
Figure 7.4. In vitro cytotoxicity of different capped NCs: as-synthesised, LaF₃@Cit (purple) and after the exchange with lysine, LaF₃@Lys (grey) in MCF-7 linear cells of breast cancer.

Results show a significant different between the different coated NCs, being those stabilised with lysine less toxic than the as-synthesised with citrate. Here, we have two different effects: (i) NC core toxicity and (ii) stabiliser toxicity, being the most relevant for our purpose to know the toxicity of the core.

To compare easily between the toxicity of both systems, we represented the values in 50 % of cell viability, also called IC50 value. In Figure 7.5 is clearly observed the high difference between both shells, being lysine (the homogenised surface) the less toxic for the system. It is mandatory to remember that, when we said citrate stabilised NCs, we are referring to the previous mentioned system in which there are citrate, acetate, ammonium and tetramethylammonium.
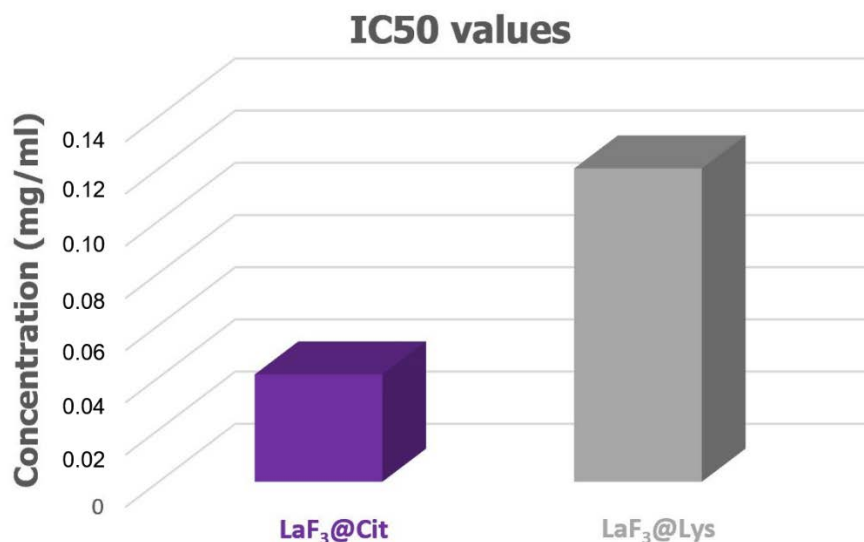
Figure 7.5. IC50 values of different capped NCs: as-synthesised, LaF$_3$@Cit (purple) and after the exchange with lysine, LaF$_3$@Lys (grey) in MCF-7 linear cells of breast cancer.

Preliminary results are promising because the toxicity seems to depend on the capping ligand more than NC. Considering the work reported by Rafael et al.[4], they used long length polymers to stabilise polymeric nanoparticles, the steric hindrance of these polymers could protect the cell of the toxicity of the core. In consequence, our next goal is to prove to stabilise our LaF$_3$ NCs with their polymers to see again the toxicity values.

7.2.3 Up-converting luminescent properties

This work is currently under study in collaboration with the Centre for Nanoscale BioPhotonics (CNBP) - Macquarie University (Sidney).

Finally, our most recent collaboration is to achieve NCs with up-converting properties to apply our systems in material science and medical fields (e.g. drug delivery in collaboration with Vall d'Hebron). To this aim, we started doping our LaF$_3$ NCs and YF$_3$ supraparticles with 20 % Yb^{3+} and 8 % Tm^{3+} as theoretically values as their recent work.[5]

Following the co-precipitation method described in Chapter 2 (YF$_3$ supraparticles) and the hydrothermal treatment explained in Chapter 4 (LaF$_3$ NCs), we prepared both systems of Figure 7.6 with a 20 % Yb^{3+} and 8

% Tm^{3+} (using in all cases acetate precursors). Particles showed the same behaviour than those without doping with some differences, YF$_3$ supraparticles have a size of ~50 nm instead of the ~80 nm obtained in Chapter 2. In contrast of LaF$_3$ NCs synthesised via hydrothermal treatment in Chapter 4, those obtained here have not the defined hexagonal shape. This less faceted behaviour could be explained considering the presence of two metals (Yb and Tm), which crystallise in the cubic form instead of hexagonal crystalline structure.
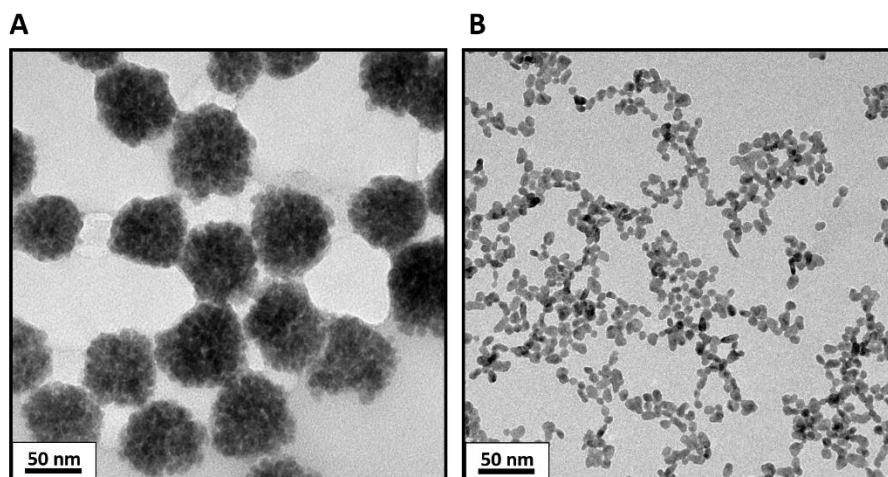
Figure 7.6. (A) TEM image of YF$_3$:Yb,Tm supraparticles and (B) LaF$_3$:Yb,Tm NCs.

After the achievement of homogeneous colloidal suspensions, we need to know if these systems have been properly doped with the desired % weight. To this aim, we used energy-dispersive X-ray spectroscopy to know the values of doping elements as shown in Table 7.1.

Table 7.1. EDX values for LaF$_3$:Yb,Tm and YF$_3$:Yb,Tm samples analysed via TEM.

Weigh (%)	LaF$_3$:Yb,Tm	YF$_3$:Yb,Tm
Lanthanum	51.90 ± 0.22	-
Yttrium	-	51.66 ± 0.85
Fluoride	19.04 ± 0.15	25.91 ± 0.62
Ytterbium	19.08 ± 0.20	13.92 ± 0.64
Thulium	9.99 ± 0.18	8.52 ± 0.57

Results are compatible with the expected values for the case of LaF$_3$:Yb,Tm NCs, but in the case of YF$_3$:Yb,Tm NCs, the amount of Yb was less than the expected. Considering that these syntheses have been the first trials to know if these NCs show up-converting properties, we tested them under a wavelength of 980 nm (Figure 7.7).
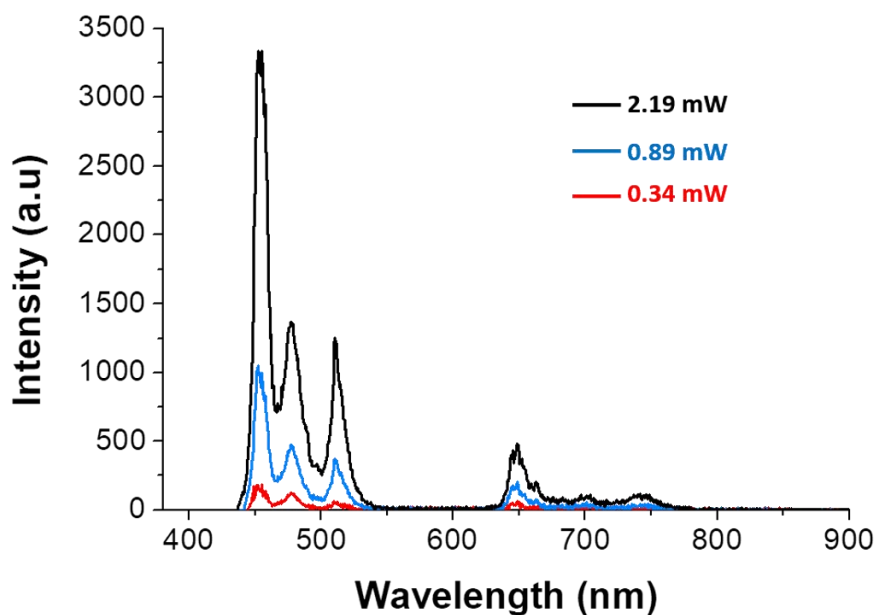
Figure 7.7. As example, YF$_3$@ Yb^{3+};Tm^{3+} spectra of the up-converting properties of this particles. Emission spectra were recorded under an exciting wavelength of 980 nm.

We observe how NCs absorb at 980 nm, emitting then at ~450, 475, 520 and 650 nm. This demonstrate the up-converting behaviour of doped metal fluoride NCs, allowing the adsorption at low energies (980 nm) with several emissions at high energies (e.g. 450 nm).

These results are promising to apply these NCs in several fields, due to in the first trials we obtain similar results than the reported for NaYF$_4$:Yb,Tm.[5] In our case, using YF$_3$ and LaF$_3$ NCs, we are obtaining similar results than the postulated as one of the best host to up-converting systems (NaYF$_4$).

7.3 References

[1]   A. Llordés, A. Palau, J. Gázquez, M. Coll, R. Vlad, A. Pomar, J. Arbiol, R. Guzmán, S. Ye, V. Rouco, et al., *Nat. Mater.* **2012**, *11*, 329–336.

[2]   J. Gutiérrez, A. Llordés, J. Gázquez, M. Gibert, N. Romà, S. Ricart, A. Pomar, F. Sandiumenge, N. Mestres, T. Puig, et al., *Nat. Mater.* **2007**, *6*, 367–373.

[3]   X. Obradors, T. Puig, Z. Li, C. Pop, B. Mundet, N. Chamorro, F. Vallés, M. Coll, S. Ricart, B. Vallejo, et al., *Supercond. Sci. Technol.* **2018**, DOI: 10.1088/1361-6668/aaaad7.

[4]   D. Rafael, F. Martínez, F. Andrade, J. Seras-Franzoso, N. Garcia-Aranda, P. Gener, J. Sayós, D. Arango, I. Abasolo, S. Schwartz, *Chem. Eng. J.* **2018**, *340*, 81–93.

[5]   Y. Liu, Y. Lu, X. Yang, X. Zheng, S. Wen, F. Wang, X. Vidal, J. Zhao, D. Liu, Z. Zhou, et al., *Nature* **2017**, *543*, 229–233.

Supporting Information

Chapter 2

Powder XRD of YF$_3$ supraparticles with Bu$_4$NF as precursor used to calculate Scherrer crystalline domain
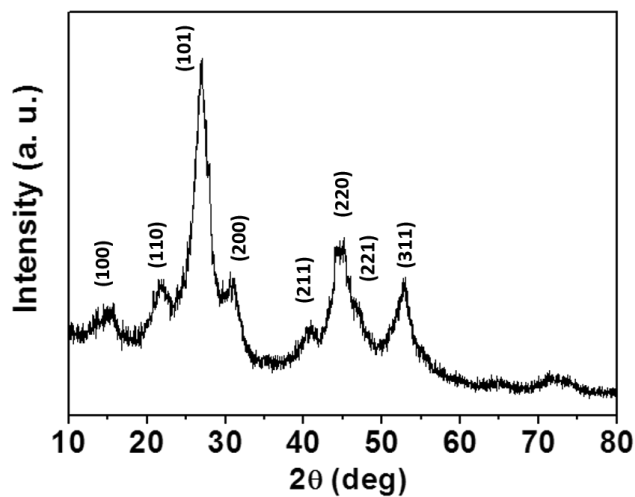
Figure SI.1. Powder XRD of the obtained YF$_3$ supraparticles using Bu$_4$NF instead of NH$_4$F as fluorinating precursor.

TEM images corresponding to the effect of the free ions with temperature
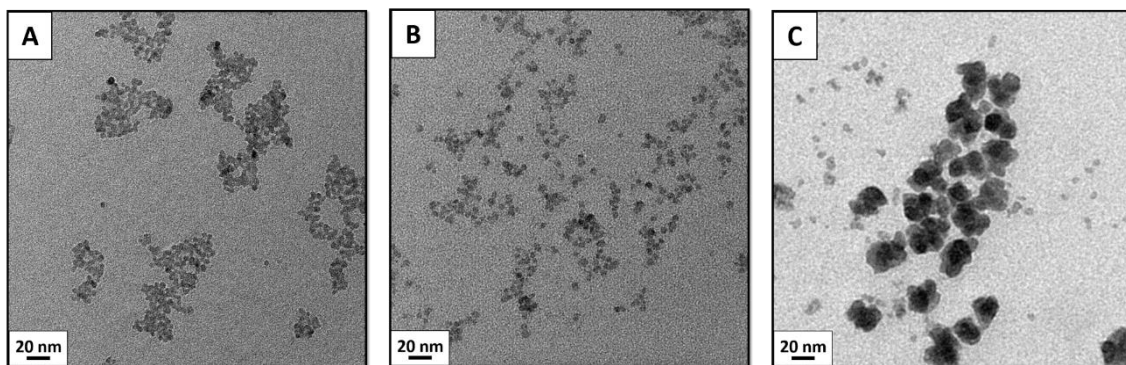
Figure SI.2. TEM images of free ions test of section 2.3.2.3 corresponding to Figure 2.4 samples. (A) is solution A, (B) is solution B and (C) is solution C.

Effect of the washing process in YF$_3$ supraparticles obtained at 100 °C

^{1}H NMR spectra show the different surface composition of the ionic ligands on the synthesised supraparticles after one washing step (Figure SI.3A) and after five steps (Figure SI.3B). Results reveal different integrations in citrate and tetramethylammonium signals while acetate was used as reference in this study, giving an integration value of 3.

The relative amounts obtained by the integration of the peaks showed the presence of an excess of tetramethylammonium and citrate, compatible with the combination of attached ions and free ones. After five washing steps, considerable number of citrates remains onto the surface while most of the tetramethylammonium was washed away. We must consider a neutral system, so the negatively charged NCs should have cations in the diffusion layer to neutralise the colloidal system. We have a negative formal charge of -71e in one washing step that needs to be neutralised by the presence of ammonium onto particle surface or free in the system. After several washing steps, the NC's surface become neutral (Stern layer) and they did not need tetramethylammonium as counter ion (Table SI.1).

In Figure SI.4A it is clearly shown how NCs start from a ζ-Potential value of -32 mV which is keep in the first washing-up step. After five washing-up, this ζ-Potential value became ~0 mV, considering only the Stern layer. NPs, after several washing steps, reorganise their surface and become neutral. These measurements are compatible with the release of tetramethylammonium postulated by analysis of ^{1}H NMR spectrum. In this case, we have also detected the presence of ammonium anchored onto the particle surface due to the necessity to achieve a neutral system. The formal

charge of -43e after five washing steps inspire to propose the presence of 43 ammoniums onto the particle surface to produce a neutral system.
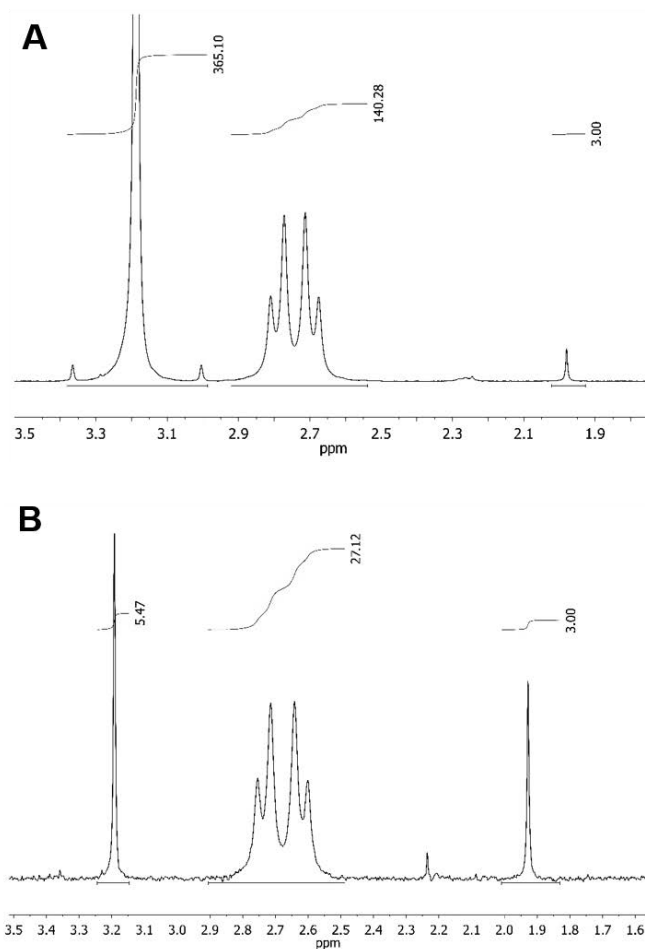
Figure SI.3. Study of the washing process by ^{1}H NMR: (A) ^{1}H NMR of YF$_3$ as-synthesised supraparticles washed once. (B) ^{1}H NMR of YF$_3$ as-synthesised supraparticles washed five times.

Table SI.1. Results obtained by the integration of the ^{1}H NMR of Figure SI.3 and the corresponding relative number of molecules referenced with acetate. Acet is acetate, Tma is tetramethylammonium and Cit is citrate.

	One washing step		Five washing steps	
	Integration	Rel. amount	Integration	Rel. amount
Acet	3	1	3	1
Tma	365.10	30	5.47	0.5
Cit	140.28	35	27.12	7

The last study performed in this section was the measurement of the supraparticle size by DLS to observe their stability during the washing processes (Figure SI.4B). We could observe that one washing step did not change the size of the supraparticles and produce a narrower signal compared with the unwashed NCs. After one washing step, supraparticles start to aggregate increasing in size. These results are compatible with ζ-Potential measurements, where it is observed after one washing step that supraparticles start to destabilise, releasing the ions attached onto their surface. This produces the aggregation of the colloidal system due to the high reactivity of the uncoordinated surface.
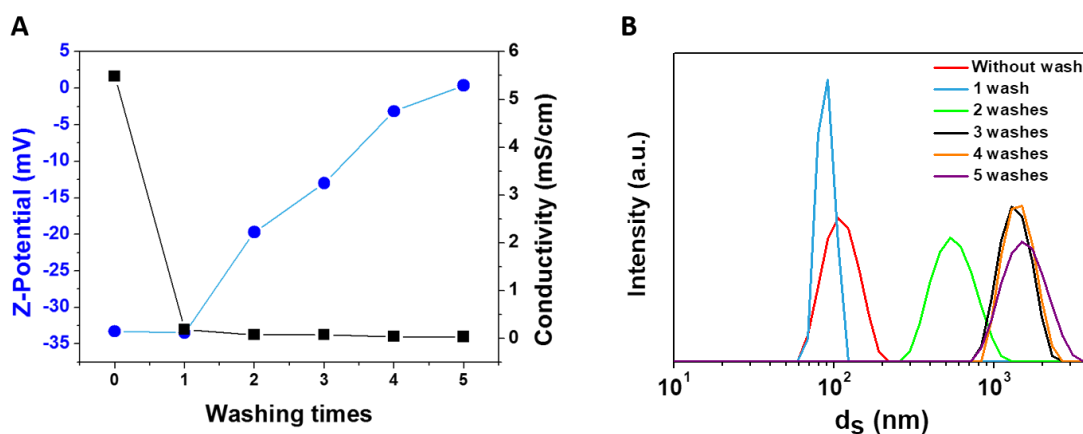
Figure SI.4. The study of the washing process by Zeta-sizer. (A) ζ-Potential and conductivity measurements of YF₃ supraparticles after each washing process (B) DLS measurements of YF₃ supraparticles after each washing process performed in water.

Chapter 3

High Resolution Electrospray Ionization Mass Spectrometry (HR ESI-MS) in GdF₃ precursor solution
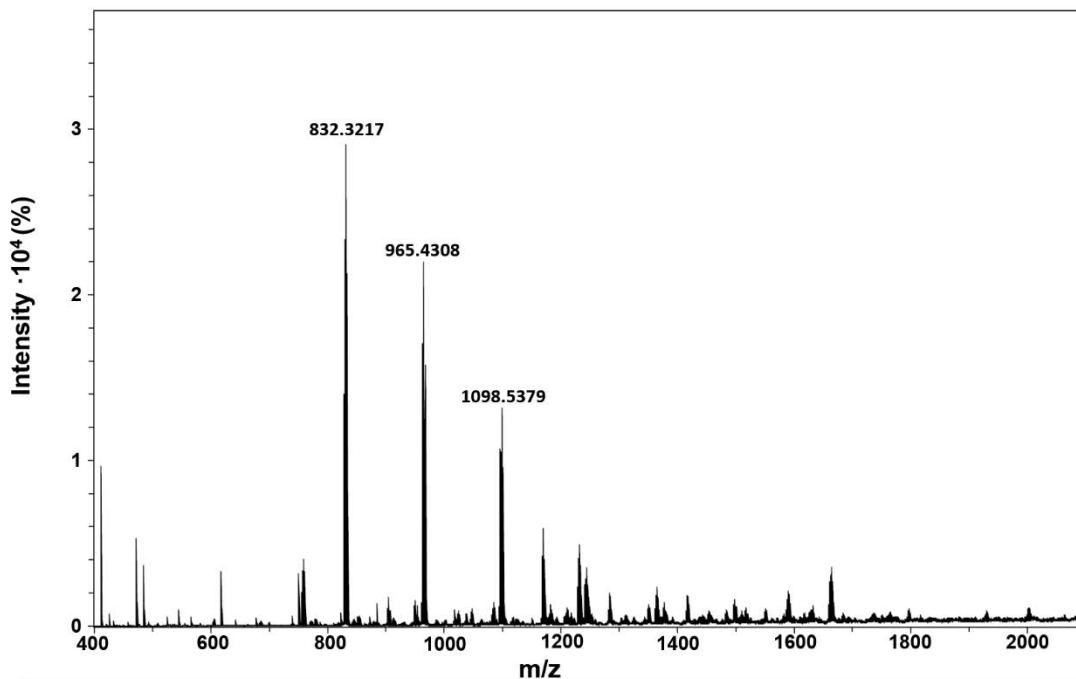
Figure SI.5. As illustration, the complete ESI(+)-MS spectrum of gadolinium (III) acetate precursor with tetramethylammonium citrate as example of composition of the precursor solution before ammonium fluoride injection.
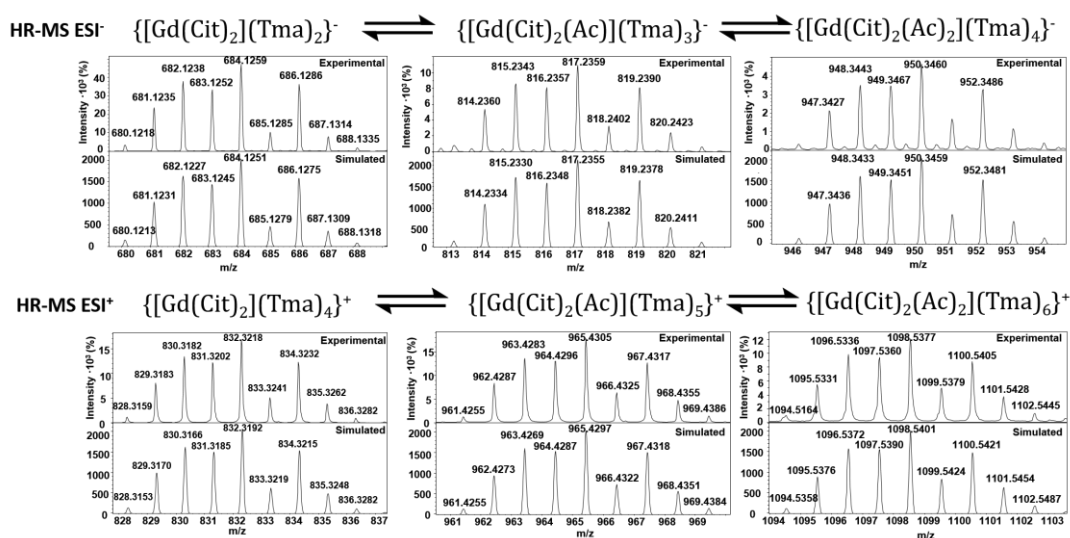
Figure SI.6. Assignation of the three main peaks observed in Figure SI.5 of ESI-MS of gadolinium (III) acetate with tetramethylammonium citrate showing observed the dynamic equilibrium. In the upper part HR-MS ESI negative and in the bottom HR-MS ESI positive. Species are indicated as observed in the technique, with their corresponding charge.

High Resolution Electrospray Ionization Mass Spectrometry (HR ESI-MS) in YF₃ precursor solution
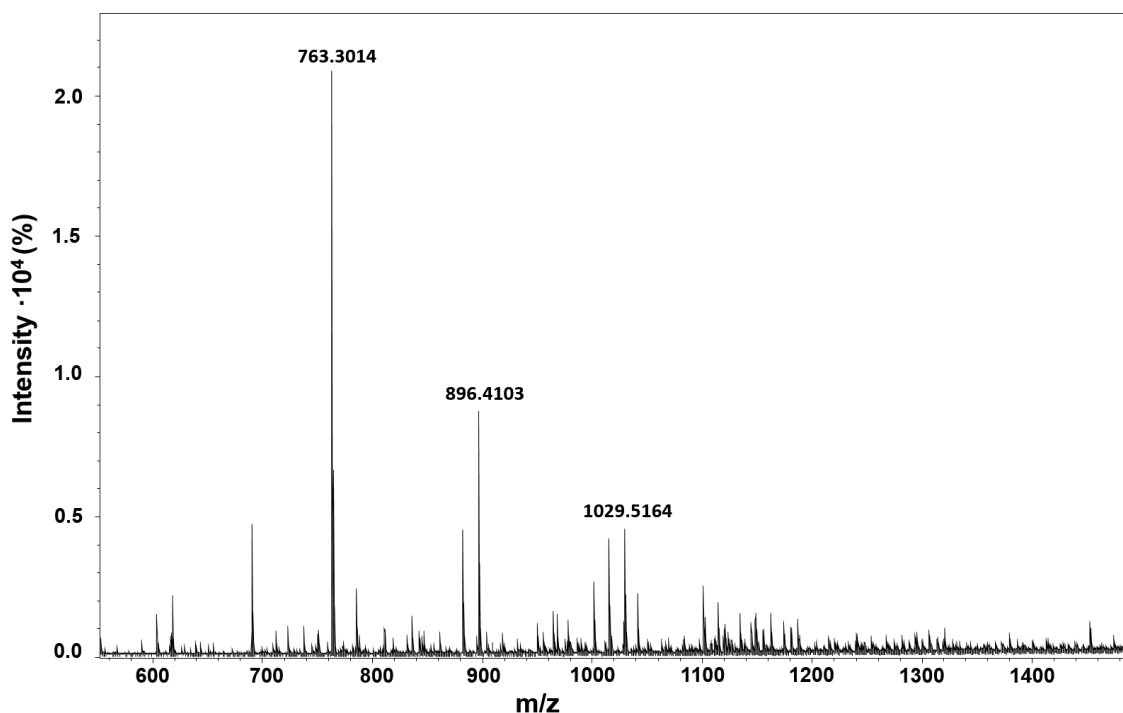
Figure SI.7. As illustration, the complete ESI(+)-MS spectrum of yttrium (III) acetate precursor with tetramethylammonium citrate as example of composition of the precursor solution before ammonium fluoride injection.
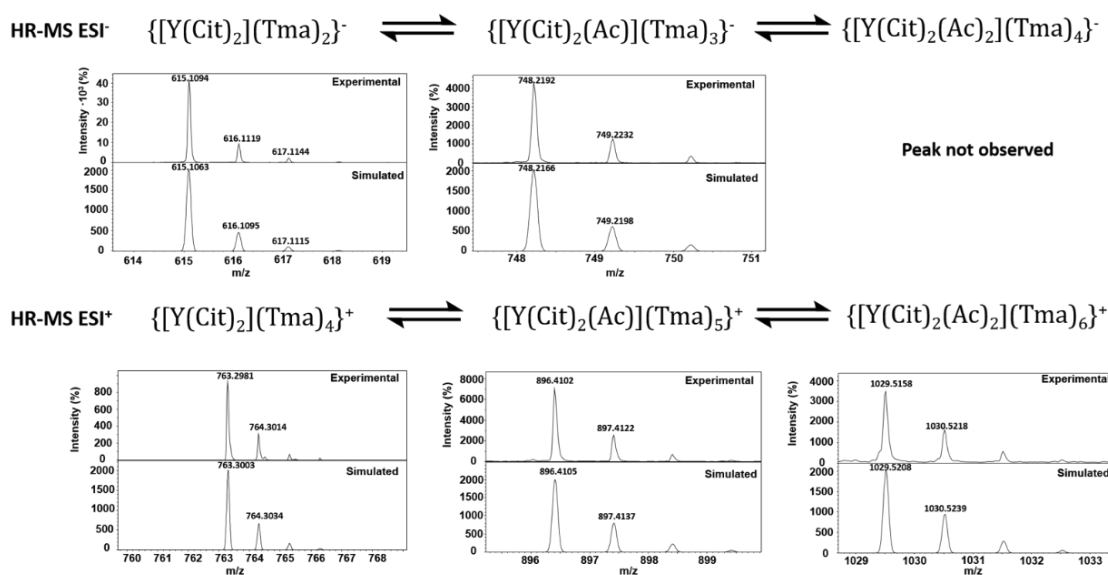
Figure SI.8. Assignation of the three main peaks observed in Figure S3 (also detected in Figure SI.5) of ESI-MS of yttrium (III) acetate with tetramethylammonium citrate showing the observed dynamic equilibrium. In the upper part HR-MS ESI negative and in the bottom HR-MS ESI positive. Species are indicated as observed in the technique, with their corresponding charge.

Chapter 4
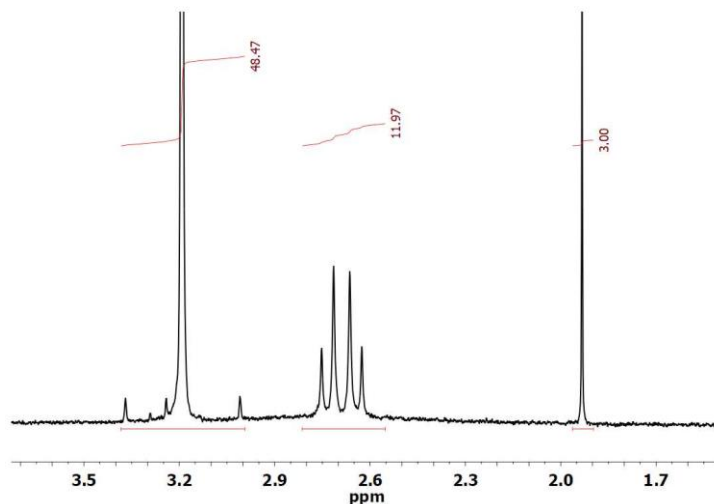
Figure SI.9. ^{1}H NMR of LaF$_3$ NCs after five washing steps with the corresponding integration to obtain a relative amount of the different species.

Table SI.2. Relative amounts of tetramethylammonium, citrate and acetate obtained in the integration of Figure S6. Finally, the relative amount assignation of ammonium to achieve neutral NCs.

	Tetramethylammonium	Citrate	Acetate	Ammonium
Integration	48.47	11.97	3.00	-
R. Amount	4	3	1	6

Chapter 5

Parameters for cationic dopamine

- **Topology field**

```
RESI DOP    1.000
GROUP
ATOM C1    CG2R61    -0.115
ATOM C2    CG2R61    -0.115
ATOM C3    CG2R61     0.11
ATOM C4    CG2R61     0.11
ATOM C5    CG2R61    -0.115
ATOM C6    CG2R61     0.00
ATOM C7    CG321     -0.18
ATOM C8    CG331      0.13
ATOM N1    NG3P3     -0.30
ATOM O1    OG311     -0.53
ATOM O2    OG311     -0.53
ATOM H1    HGR61      0.115
ATOM H2    HGR61      0.115
ATOM H3    HGR61      0.115
ATOM H4    HGA2       0.09
ATOM H5    HGA2       0.09
ATOM H6    HGA2       0.09
ATOM H7    HGA2       0.09
ATOM H8    HGP2       0.33
ATOM H9    HGP2       0.33
ATOM H10   HGP1       0.42
ATOM H11   HGP1       0.42
ATOM H12   HGP2       0.33
BOND C1    C6
BOND C1    C2
BOND C1    H1
BOND C2    C3
BOND C2    H2
BOND C3    C4
BOND C3    O2
BOND C4    C5
BOND C4    O1
BOND C5    C6
BOND C5    H3
BOND C6    C7
BOND C7    C8
BOND C7    H4
BOND C7    H5
BOND C8    N1
BOND C8    H6
BOND C8    H7
BOND N1    H8
BOND N1    H9
BOND N1    H12
BOND O1    H10
BOND O2    H11
IMPH C1    C2    C6    H1
```

```
IMPH C2    C3    C1    H2
IMPH C3    C4    C2    O2
IMPH C4    O1    C3    C5
IMPH C6    C5    C1    C7
IMPH C7    C8    C6    H4
IMPH C7    C8    C6    H5
IMPH C8    N1    C7    H6
IMPH C8    N1    C7    H7
IMPH C5    C6    C4    H3
IMPH N1    H8    C8    H9
IMPH N1    H8    C8    H12
IC C1    C2    C3    C4    1.38   119.96     0.05  119.90  1.39
IC C1    C2    C3    O2    1.38   119.96   179.99  120.02  1.36
IC C1    C6    C5    C4    1.38   120.15    -0.05  120.00  1.39
IC C1    C6    C5    H3    1.38   120.15   179.99  120.00  1.08
IC C1    C6    C7    C8    1.38   119.93    89.99  109.47  1.53
IC C1    C6    C7    H4    1.38   119.93  -149.99  109.47  1.09
IC C1    C6    C7    H5    1.38   119.93   -29.99  109.43  1.09
IC C2    C1    C6    C5    1.38   120.13     0.05  120.15  1.38
IC C2    C1    C6    C7    1.38   120.13  -179.97  119.93  1.51
IC C2    C3    C4    C5    1.39   119.90    -0.04  119.85  1.39
IC C2    C3    C4    O1    1.39   119.90   179.99  120.10  1.36
IC C2    C3    O2    H11   1.39   120.02    90.02  113.98  0.97
IC C3    C2    C1    C6    1.39   119.96    -0.05  120.13  1.38
IC C3    C2    C1    H1    1.39   119.96   179.74  119.93  1.08
IC C3    C4    C5    C6    1.39   119.85     0.04  120.00  1.38
IC C3    C4    C5    H3    1.39   119.85  -179.99  120.00  1.08
IC C3    C4    O1    H10   1.39   120.10    89.95  114.02  0.97
IC C4    C3    C2    H2    1.39   119.90  -179.99  120.08  1.08
IC C4    C3    O2    H11   1.39   120.08   -90.03  113.98  0.97
IC C4    C5    C6    C7    1.39   120.00   179.97  119.92  1.51
IC C5    C4    C3    O2    1.39   119.85  -179.99  120.08  1.36
IC C5    C4    O1    H10   1.39   120.05   -90.02  114.02  0.97
IC C5    C6    C1    H1    1.38   120.15  -179.74  119.94  1.08
IC C5    C6    C7    C8    1.38   119.92   -90.02  109.47  1.53
IC C5    C6    C7    H4    1.38   119.92    30.00  109.47  1.09
IC C5    C6    C7    H5    1.38   119.92   150.00  109.43  1.09
IC C6    C1    C2    H2    1.38   120.13   179.98  119.96  1.08
IC C6    C5    C4    O1    1.38   120.00  -179.99  120.05  1.36
IC C6    C7    C8    N1    1.51   109.47  -179.99  109.46  1.47
IC C6    C7    C8    H6    1.51   109.47   -59.98  109.53  1.09
IC C6    C7    C8    H7    1.51   109.47    60.01  109.49  1.09
IC C7    C6    C1    H1    1.51   119.93     0.25  119.94  1.08
IC C7    C6    C5    H3    1.51   119.92     0.00  120.00  1.08
IC C7    C8    N1    H8    1.53   109.46   -60.03  109.48  1.01
IC C7    C8    N1    H9    1.53   109.46    60.03  109.47  1.01
IC C7    C8    N1    H12   1.53   109.46  -179.95  109.46  1.01
IC N1    C8    C7    H4    1.47   109.46    60.01  109.49  1.09
IC N1    C8    C7    H5    1.47   109.46   -60.04  109.48  1.09
IC O1    C4    C3    O2    1.36   120.10     0.04  120.08  1.36
IC O1    C4    C5    H3    1.36   120.05    -0.02  120.00  1.08
IC O2    C3    C2    H2    1.36   120.02    -0.04  120.08  1.08
IC H1    C1    C2    H2    1.08   119.93    -0.23  119.96  1.08
IC H4    C7    C8    H6    1.09   109.49  -179.98  109.53  1.09
IC H4    C7    C8    H7    1.09   109.49   -59.99  109.49  1.09
IC H5    C7    C8    H6    1.09   109.48    59.97  109.53  1.09
```

```
IC H5    C7    C8    H7     1.09   109.48  179.96  109.49   1.09
IC H6    C8    N1    H8     1.09   109.45  179.91  109.48   1.01
IC H6    C8    N1    H9     1.09   109.45  -60.03  109.47   1.01
IC H6    C8    N1    H12    1.09   109.45   59.99  109.46   1.01
IC H7    C8    N1    H8     1.09   109.47   59.99  109.48   1.01
IC H7    C8    N1    H9     1.09   109.47 -179.96  109.47   1.01
IC H7    C8    N1    H12    1.09   109.47  -59.94  109.46   1.01
IC C2    C6   *C1    H1     0.00     0.00  180.00    0.00   0.00
IC C3    C1   *C2    H2     0.00     0.00  180.00    0.00   0.00
IC C4    C2   *C3    O2     0.00     0.00  180.00    0.00   0.00
IC O1    C3   *C4    C5     0.00     0.00  180.00    0.00   0.00
IC C5    C1   *C6    C7     0.00     0.00  180.00    0.00   0.00
IC C8    C6   *C7    H4     0.00     0.00  120.00    0.00   0.00
IC C8    C6   *C7    H5     0.00     0.00 -120.00    0.00   0.00
IC N1    C7   *C8    H6     0.00     0.00  120.00    0.00   0.00
IC N1    C7   *C8    H7     0.00     0.00 -120.00    0.00   0.00
IC C6    C4   *C5    H3     0.00     0.00  180.00    0.00   0.00
IC H8    C8   *N1    H9     0.00     0.00  120.00    0.00   0.00
IC H8    C8   *N1    H12    0.00     0.00 -120.00    0.00   0.00
```

- Force field

```
BONDS
CG2R61 CG2R61   305.00      1.3750
CG2R61 CG321    230.00      1.4900
CG2R61 OG311    334.30      1.4110
CG2R61 HGR61    340.00      1.0800
CG321  CG324    222.50      1.5300
CG321  HGA2     309.00      1.1110
CG324  NG3P3    200.00      1.4900
CG324  HGA2     284.50      1.1000
NG3P3  HGP2     403.00      1.0400
OG311  HGP1     545.00      0.9600


ANGLES
CG2R61 CG2R61 CG2R61   40.00    120.00   35.00   2.41620
CG2R61 CG2R61 CG321    45.80    120.00
CG2R61 CG2R61 OG311    45.20    120.00
CG2R61 CG2R61 HGR61    30.00    120.00   22.00   2.15250
CG2R61 CG321  CG324    51.80    107.50
CG2R61 CG321  HGA2     49.30    107.50
CG324  CG321  HGA2     26.50    110.10   22.53   2.17900
HGA2   CG321  HGA2     35.50    109.00    5.40   1.80200
CG321  CG324  NG3P3    67.70    110.00
CG321  CG324  HGA2     26.50    111.80   22.53   2.17900
NG3P3  CG324  HGA2     45.00    107.50   35.00   2.10100
HGA2   CG324  HGA2     35.50    109.00    5.40   1.80200
CG324  NG3P3  HGP2     30.00    109.50   20.00   2.07400
HGP2   NG3P3  HGP2     44.00    109.50
CG2R61 OG311  HGP1     65.00    108.00
```

```
DIHEDRALS
CG2R61 CG2R61 CG2R61 CG2R61     3.1000  2   180.00
CG2R61 CG2R61 CG2R61 CG321      3.1000  2   180.00
CG2R61 CG2R61 CG2R61 OG311      3.1000  2   180.00
CG2R61 CG2R61 CG2R61 HGR61      4.2000  2   180.00
CG321  CG2R61 CG2R61 HGR61      2.4000  2   180.00
OG311  CG2R61 CG2R61 OG311      2.5800  2   180.00
OG311  CG2R61 CG2R61 HGR61      2.4000  2   180.00
HGR61  CG2R61 CG2R61 HGR61      2.4000  2   180.00
CG2R61 CG2R61 CG321  CG324      0.2300  2   180.00
CG2R61 CG2R61 CG321  HGA2       0.0020  6     0.00
CG2R61 CG2R61 OG311  HGP1       0.9900  2   180.00
CG2R61 CG321  CG324  NG3P3      0.2000  3     0.00
CG2R61 CG321  CG324  HGA2       0.0400  3     0.00
HGA2   CG321  CG324  NG3P3      0.1950  3     0.00
HGA2   CG321  CG324  HGA2       0.1950  3     0.00
CG321  CG324  NG3P3  HGP2       0.1000  3     0.00
HGA2   CG324  NG3P3  HGP2       0.1000  3     0.00
```

Parameters for trivalent 3,4-dihydroxihydrocinnamate anion

- ## Topology field

```
RESI CIN          -3.000
GROUP
ATOM C1     CG2R61 -0.593
ATOM C2     CG2R61 -0.118
ATOM C3     CG2R61 -0.003
ATOM C4     CG2R61 -0.603
ATOM C5     CG2R61  0.088
ATOM C6     CG2R61  0.081
ATOM O1     OG312  -0.761
ATOM O2     OG312  -0.761
ATOM C7     CG321  -0.179
ATOM C8     CG321  -0.286
ATOM C9     CG2O3   0.620
ATOM O3     OG2D2  -0.760
ATOM O4     OG2D2  -0.760
ATOM H1     HGR61   0.280
ATOM H2     HGR61   0.115
ATOM H3     HGR61   0.280
ATOM H4     HGA2    0.090
ATOM H5     HGA2    0.090
ATOM H6     HGA2    0.090
ATOM H7     HGA2    0.090

BOND C1    C2
BOND C1    C6
BOND C1    H1
BOND C2    C3
BOND C2    H2
```

```
BOND C3    C4
BOND C3    C7
BOND C4    C5
BOND C4    H3
BOND C5    C6
BOND C5    O2
BOND C6    O1
BOND C7    C8
BOND C7    H4
BOND C7    H5
BOND C8    C9
BOND C8    H6
BOND C8    H7
BOND C9    O3
BOND C9    O4
IMPR C9      O4      O3      C8
```

- Force field

```
BONDS
CG2O3  CG321   200.00      1.5220
CG2O3  OG2D2   525.00      1.2600
CG2R61 CG2R61  305.00      1.3750
CG2R61 CG321   230.00      1.4900
CG2R61 OG312   525.00      1.2600
CG2R61 HGR61   340.00      1.0800
CG321  CG321   222.50      1.5300
CG321  HGA2    309.00      1.1110

ANGLES
CG321  CG2O3  OG2D2   40.00   116.00   50.00   2.35300
OG2D2  CG2O3  OG2D2  100.00   128.00   70.00   2.25870
CG2R61 CG2R61 CG2R61  40.00   120.00   35.00   2.41620
CG2R61 CG2R61 CG321   45.80   120.00
CG2R61 CG2R61 OG312   40.00   120.00
CG2R61 CG2R61 HGR61   30.00   120.00   22.00   2.15250
CG2O3  CG321  CG321   52.00   108.00
CG2O3  CG321  HGA2    33.00   109.50   30.00   2.16300
CG2R61 CG321  CG321   51.80   107.50
CG2R61 CG321  HGA2    49.30   107.50
CG321  CG321  HGA2    26.50   110.10   22.53   2.17900
HGA2   CG321  HGA2    35.50   109.00    5.40   1.80200

DIHEDRALS
OG2D2  CG2O3  CG321  CG321    0.0500  6   180.00
OG2D2  CG2O3  CG321  HGA2     0.0500  6   180.00
CG2R61 CG2R61 CG2R61 CG2R61   3.1000  2   180.00
CG2R61 CG2R61 CG2R61 CG321    3.1000  2   180.00
CG2R61 CG2R61 CG2R61 OG312    3.1000  2   180.00
CG2R61 CG2R61 CG2R61 HGR61    4.2000  2   180.00
CG321  CG2R61 CG2R61 HGR61    2.4000  2   180.00
OG312  CG2R61 CG2R61 OG312    2.5800  2   180.00
OG312  CG2R61 CG2R61 HGR61    2.4000  2   180.00
HGR61  CG2R61 CG2R61 HGR61    2.4000  2   180.00
```

```
CG2R61 CG2R61 CG321   CG321        0.2300  2    180.00
CG2R61 CG2R61 CG321   HGA2         0.0020  6      0.00
CG2O3  CG321  CG321   CG2R61       0.0400  3      0.00
CG2O3  CG321  CG321   HGA2         0.1950  3      0.00
CG2R61 CG321  CG321   HGA2         0.0400  3      0.00
HGA2   CG321  CG321   HGA2         0.2200  3      0.00


IMPROPERS
CG2O3  OG2D2  OG2D2   CG321       96.0000  0      0.00
```

Parameters for cationic lysine

- **Topology field**

```
RESI LIS           1.000
GROUP
ATOM C1       CG324   0.125
ATOM C2       CG321  -0.199
ATOM C3       CG321  -0.138
ATOM C4       CG321  -0.182
ATOM C5       CG314   0.342
ATOM C6       CG2O3   0.445
ATOM O1       OG2D2  -0.760
ATOM N1       NG3P3  -0.301
ATOM O2       OG2D2  -0.760
ATOM N2       NG3P3  -0.362
ATOM H1       HGA2    0.090
ATOM H2       HGA2    0.090
ATOM H3       HGA2    0.090
ATOM H4       HGA2    0.090
ATOM H5       HGA2    0.090
ATOM H6       HGA2    0.090
ATOM H7       HGA2    0.090
ATOM H8       HGA2    0.090
ATOM H9       HGA1    0.090
ATOM H10      HGP2    0.330
ATOM H11      HGP2    0.330
ATOM H12      HGP2    0.330
ATOM H13      HGP2    0.330
ATOM H14      HGP2    0.330
ATOM H15      HGP2    0.330

BOND C1    C2
BOND C1    N1
BOND C1    H1
BOND C1    H2
BOND C2    C3
BOND C2    H3
BOND C2    H4
BOND C3    C4
BOND C3    H5
BOND C3    H6
BOND C4    C5
```

```
BOND C4    H7
BOND C4    H8
BOND C5    C6
BOND C5    N2
BOND C5    H9
BOND C6    O1
BOND C6    O2
BOND N1    H10
BOND N1    H11
BOND N1    H12
BOND N2    H13
BOND N2    H14
BOND N2    H15
IMPR C6    O2     O1     C5
```

- Force field

```
BONDS
CG2O3  CG314    200.00    1.5220
CG2O3  OG2D2    525.00    1.2600
CG314  CG321    222.50    1.5380
CG314  NG3P3    200.00    1.4800
CG314  HGA1     309.00    1.1110
CG321  CG321    222.50    1.5300
CG321  CG324    222.50    1.5300
CG321  HGA2     309.00    1.1110
CG324  NG3P3    200.00    1.4900
CG324  HGA2     284.50    1.1000
NG3P3  HGP2     403.00    1.0400

ANGLES
CG314  CG2O3  OG2D2    40.00    116.00    50.00    2.35300
OG2D2  CG2O3  OG2D2   100.00    128.00    70.00    2.25870
CG2O3  CG314  CG321    52.00    108.00
CG2O3  CG314  NG3P3    43.70    110.00
CG2O3  CG314  HGA1     50.00    109.50
CG321  CG314  NG3P3    67.70    110.00
CG321  CG314  HGA1     34.50    110.10    22.53    2.17900
NG3P3  CG314  HGA1     51.50    107.50
CG314  CG321  CG321    58.35    113.50    11.16    2.56100
CG314  CG321  HGA2     33.43    110.10    22.53    2.17900
CG321  CG321  CG321    58.35    113.60    11.16    2.56100
CG321  CG321  CG324    58.35    110.50    11.16    2.56100
CG321  CG321  HGA2     26.50    110.10    22.53    2.17900
CG324  CG321  HGA2     26.50    110.10    22.53    2.17900
HGA2   CG321  HGA2     35.50    109.00     5.40    1.80200
CG321  CG324  NG3P3    67.70    110.00
CG321  CG324  HGA2     26.50    111.80    22.53    2.17900
NG3P3  CG324  HGA2     45.00    107.50    35.00    2.10100
HGA2   CG324  HGA2     35.50    109.00     5.40    1.80200
CG314  NG3P3  HGP2     30.00    109.50    20.00    2.07400
CG324  NG3P3  HGP2     30.00    109.50    20.00    2.07400
HGP2   NG3P3  HGP2     44.00    109.50
```

```
DIHEDRALS
OG2D2  CG2O3  CG314  CG321       0.0500  6   180.00
OG2D2  CG2O3  CG314  NG3P3       3.2000  2   180.00
OG2D2  CG2O3  CG314  HGA1        0.0500  6   180.00
CG2O3  CG314  CG321  CG321       0.2000  3     0.00
CG2O3  CG314  CG321  HGA2        0.2000  3     0.00
NG3P3  CG314  CG321  CG321       0.2000  3     0.00
NG3P3  CG314  CG321  HGA2        0.2000  3     0.00
HGA1   CG314  CG321  CG321       0.1950  3     0.00
HGA1   CG314  CG321  HGA2        0.1950  3     0.00
CG2O3  CG314  NG3P3  HGP2        0.1000  3     0.00
CG321  CG314  NG3P3  HGP2        0.1000  3     0.00
HGA1   CG314  NG3P3  HGP2        0.1000  3     0.00
CG314  CG321  CG321  CG321       0.5000  3     0.00
CG314  CG321  CG321  CG321       0.5000  6   180.00
CG314  CG321  CG321  HGA2        0.1950  3     0.00
CG321  CG321  CG321  CG324       0.1950  3     0.00
CG321  CG321  CG321  HGA2        0.1950  3     0.00
CG324  CG321  CG321  HGA2        0.1950  3     0.00
HGA2   CG321  CG321  HGA2        0.2200  3     0.00
CG321  CG321  CG324  NG3P3       0.1950  3     0.00
CG321  CG321  CG324  HGA2        0.1950  3     0.00
HGA2   CG321  CG324  NG3P3       0.1950  3     0.00
HGA2   CG321  CG324  HGA2        0.1950  3     0.00
CG321  CG324  NG3P3  HGP2        0.1000  3     0.00
HGA2   CG324  NG3P3  HGP2        0.1000  3     0.00

IMPROPERS
CG2O3  OG2D2  OG2D2  CG314      96.0000  0     0.00
```

Scientific output

Conference contributions

1. SolGel2017, Liege (Belgium) (2017). Oral presentation: "Unravelling the ionic self-assembly behaviour of LnF_3 nanoparticles" **Jordi Martínez-Esaín**, Jordi Faraudo, Josep Ros, Ramón Yáñez and Susagna Ricart.

2. Jornades Doctorals 2017 UAB, Barcelona (Spain). Poster: "Uncovering the Surface Chemistry of LnF_3 Nanoparticles" **Jordi Martínez-Esaín**, Jordi Faraudo, Josep Ros, Susagna Ricart and Ramón Yáñez. **Awarded with the Second Prize**

3. Jornades Doctorals 2017 UAB, Barcelona (Spain). Oral presentation: "Uncovering the Surface Chemistry of LnF_3 Nanoparticles" **Jordi Martínez-Esaín**, Jordi Faraudo, Josep Ros, Susagna Ricart and Ramón Yáñez. **Awarded with the Second Prize**

4. SELF2016, Barcelona (2016). Oral presentation: "Exceptional self-assembly by citrate bridge formation in LnF_3 nanoparticles synthesis" **Jordi Martínez-Esaín**, Jordi Faraudo, Josep Ros, Ramón Yáñez and Susagna Ricart.

5. NANOSELECT annual meeting, Sant Feliu de Guíxols (Spain) (2016). Poster: "The role of citrate as self-assembler molecule in LnF_3 nanoparticles synthesis" **Jordi Martínez-Esaín**, Jordi Faraudo, Josep Ros, Ramón Yáñez and Susagna Ricart.

6. EMRS Spring Meeting, Lille (2016). Oral presentation: "Understanding mechanism formation of LnF_3 nanoparticles" **Jordi**

Martínez-Esaín, Jordi Faraudo, Susagna Ricart, Ramón Yáñez and Josep Ros.

7. EMRS Spring Meeting, Lille (2016). Oral presentation: "From colloidal solution to superconducting nanocomposites epitaxial layers of $YBa_2Cu_3O_7$ superconductors" Susagna Ricart, Pablo Cayado, Alba Garzon, **Jordi Martínez-Esaín**, Natalia Chamorro, Josep Ros, Ramón Yáñez, Ferràn Valles, Anna Palau, Jaume Gazquez, Bernat Mundet, Mariona Coll, Xavier Obradors, Teresa Puig.

8. NANOBIOAPP, Barcelona (2015). Poster: "Aqueous Synthesis of LnF_3 Nanoparticles and their Bactericide Effect" **Jordi Martínez-Esaín**, María Pilar Cortés, Jordi Barbé, Susagna Ricart, Ramón Yáñez and Josep Ros.

9. EUCAS 2015, Lyon (2015). Oral presentation: "Solution design for ReBCO CSD-MOD films and nanocomposites" Susagna Ricart, Pablo Cayado, Cornelia Pop, Alba Garzon, **Jordi Martinez-Esain**, Bohores Villarejo, Josep Ros, Ramon Yáñez, Pere Roura, Jordi Farjas, Anna Palau, Jaume Gazquez, Bernat Mundet, Mariona Coll, Xavier Obradors, Teresa Puig.

10. TEM-UCA summer Workshop, Cádiz (2015). Poster: "Aqueous Synthesis of LnF_3 Nanoparticles and their Bactericide Effect" **Jordi Martínez-Esaín**, María Pilar Cortés, Jordi Barbé, Susagna Ricart, Ramón Yáñez and Josep Ros.

11. MRS Spring Meeting, San Francisco (2015). Oral presentation: "Synthesis of metal, metal oxide and metal fluoride nanoparticles. Tunning shape and composition" Susagna Ricart, Alba Garzón-Manjón, **Jordi Martínez-Esaín**, Eduardo Solano, ChangYong Lu, María de la Mata, Roger Guzmán, Jordi Arbiol, Jordi Garcia-Anton, Teresa Puig, Xavier Obradors, Ramón Yáñez, Josep Ros.

12. NANOSELECT annual meeting, Sant Feliu de Guíxols (Girona) (2014). Poster: "Metal Fluoride Nanoparticle Sythesis. DLS Studies" **Jordi Martínez-Esaín**, Alba Garzón-Manjón, Susagna Ricart, Ramón Yáñez and Josep Ros.

Publications in international journals

1. **Martínez-Esaín, J.**; Faraudo, J.; Puig, T.; Obradors, X.; Ros, J.; Ricart, S.; Yáñez, R. Tunable self-assembly of YF_3 nanoparticles by citrate-mediated ionic bridges. **J. Am. Chem. Soc.** 2018, 140, 2127-2134.

2. **Martínez-Esaín, J.**; Ros, J.; Faraudo, J.; Ricart, S.; Yáñez, R. Tailoring the Synthesis of LnF_3 (Ln= La-Lu and Y) Nanocrystals via Mechanistic Study of the Coprecipitation Method. **Langmuir** 2018, 34, 6443–6453.

3. **Martínez-Esaín, J.**; Puig, T.; Obradors, X.; Ros, J.; Yáñez, R.; Faraudo, J.; Ricart, S. Faceted-charge patchy LnF_3 nanocrystals with selective solvent interaction. **Angew. Chemie - Int. Ed.** 2018, DOI: 10.1002/ange.201806273.

4. **Martínez-Esaín, J.**; De Roo, J.; Puig, T.; Obradors, X.; Ros, J.; Van Driessche, I.; De Keukeleere, K.; Yáñez, R.; Ricart, S.; Faraudo, J. Understanding the Selective Ligand Exchange through the Study of LaF_3 Patchy Nanocrystals Functionalization. *In preparation*

5. **Martínez-Esaín, J.**; Puig, T.; Obradors, X.; Ros, J.; Farjas, J.; Roura, P.; Faraudo, J.; Yáñez, R.; Ricart, S. Key role of Evolved Gas Analysis-Mass Spectrometry to generate the surface image in colloidal systems. *In preparation*